MULTIPLE WAVE SCATTERING BY QUASIPERIODIC STRUCTURES

A thesis submitted to the University of Manchester
for the degree of Doctor of Philosophy
in the Faculty of Engineering and Physical Sciences

2014

S. R. Voisey
School of Mathematics

Contents

Word count 63127

List of Figures

The University of Manchester

S. R. Voisey
Doctor of Philosophy
Multiple wave scattering by quasiperiodic structures
June 19, 2014

Understanding the phenomenon of wave scattering by random media is a ubiquitous problem that has instigated extensive research in the field. This thesis focuses on wave scattering by quasiperiodic media as an alternative approach to provide insight into the effects of structural aperiodicity on the propagation of the waves. Quasiperiodic structures are aperiodic yet ordered so have attributes that make them beneficial to explore. Quasiperiodic lattices are also used to model the atomic structures of quasicrystals; materials that have been found to have a multitude of applications due to their unusual characteristics. The research in this thesis is motivated by both the mathematical and physical benefits of quasiperiodic structures and aims to bring together the two important and distinct fields of research: waves in heterogeneous media and quasiperiodic lattices.

A review of the past literature in the area has highlighted research that would be beneficial to the applied mathematics community. Thus, particular attention is paid towards developing rigorous mathematical algorithms for the construction of several quasiperiodic lattices of interest and further investigation is made into the development of periodic structures that can be used to model quasiperiodic media.

By employing established methods in multiple scattering new techniques are developed to predict and approximate wave propagation through finite and infinite arrays of isotropic scatterers with quasiperiodic distributions. Recursive formulae are derived that can be used to calculate rapidly the propagation through one- and two-dimensional arrays with a one-dimensional Fibonacci chain distribution. These formulae are applied, in addition to existing tools for two-dimensional multiple scattering, to form comparisons between the propagation in one- and two-dimensional quasiperiodic structures and their periodic approximations. The quasiperiodic distributions under consideration are governed by the Fibonacci, the square Fibonacci and the Penrose lattices. Finally, novel formulae are derived that allow the calculation of Bloch-type waves, and their properties, in infinite periodic structures that can approximate the properties of waves in large, or infinite, quasiperiodic media.

Declaration

No portion of the work referred to in the thesis has been submitted in support of an application for another degree or qualification of this or any other university or other institute of learning.

Copyright Statement

Acknowledgements

I would like to thank my supervisors, Professor David Abrahams and Dr William Parnell, for their fantastic support, patience and encouragement throughout my time at the University of Manchester. It has been an absolute privilege working with both David and William, I have learnt so much from them and will continue to be inspired by their work and their enthusiasm. I am also grateful to them and to the school of mathematics for giving me the opportunity to attend many conferences and summer schools during my PhD.

I am grateful to the Leverhulme Trust for their financial support of my PhD, and the group at Sheffield University led by Professor Harm Askes and Dr Inna Gitman with whom we have had several fruitful discussions throughout our collaboration. I would like to thank the Knowledge Transfer Network and the Aeroacoustic research team at Dyson Technology Ltd for the opportunity and the amazing experience of the six month internship.

Finally, I would like to thanks my boyfriend, friends, family and peers for all their parts in my journey; it would not have been the same without them.

Chapter 1

Introduction

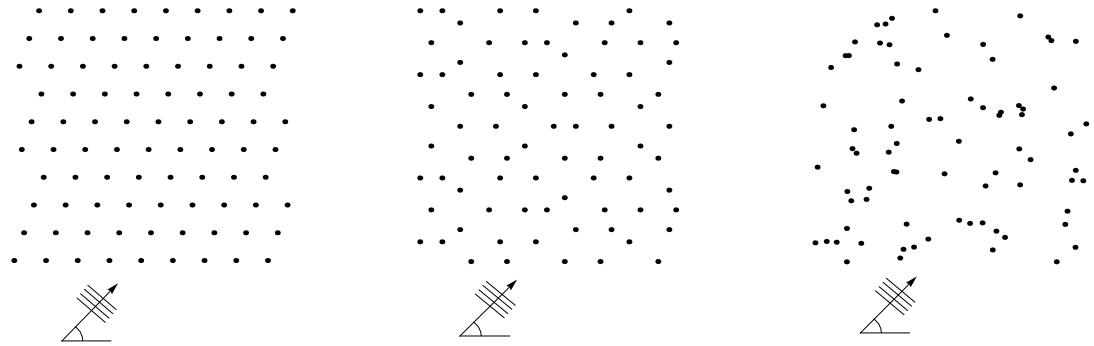

Figure 1.1: Comparison of incident plane wave on arrays of small circular cylinders with periodic, quasiperiodic and random distributions (left to right).

This thesis investigates the propagation of time-harmonic scalar waves in one-dimensional (1D) and two-dimensional (2D) infinite domains with finite or infinite arrays of isotropic scatterers with particular distributions. The main distributions of interest are *quasiperiodic*, roughly defined as patterns that are ordered but not periodic, and are inspired by the global desire to model the effects of structural disorder on wave propagation. The concept of quasiperiodic can be illustrated via the function

$$f(z) = \sin(Az) + \sin(Bz). \tag{1.1}$$

If the ratio A/B is rational, then the function is periodic. If the ratio A/B is irrational then the function is aperiodic. However, the function does have successions of similar "periods". This can also be described as the function having "long-range order" but not "short-range order". That is, from afar the pattern looks to have some "periodicity", but upon closer inspection it can be seen that the pattern is non-repeating,

as depicted in figure 1.2. This ordered yet aperiodic behaviour gives the function the definition of *quasiperiodic*.

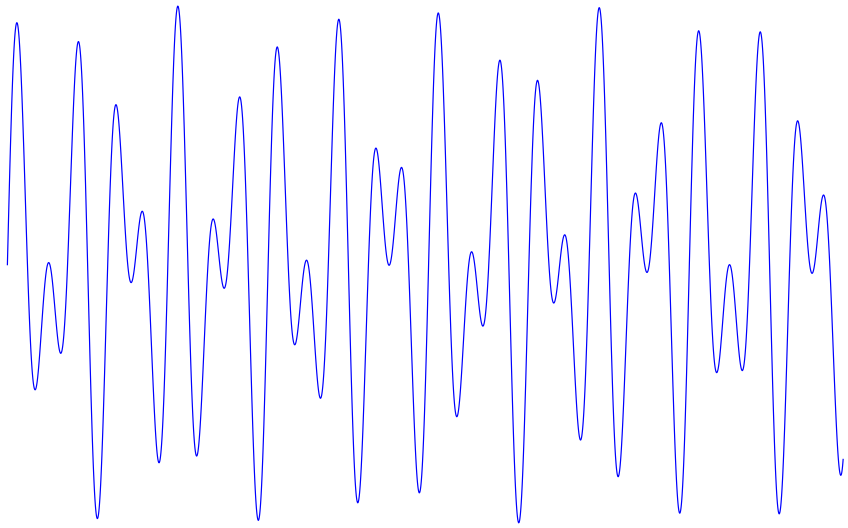

Figure 1.2: The quasiperiodic function $f(z) = \sin(Az) + \sin(Bz)$ with $A = 1$ and $B = \tau = \frac{1+\sqrt{5}}{2}$.

The primary thrust of this thesis can be depicted quite simply, as in figure 1.1. Illustrated here are three different distributions: periodic, quasiperiodic and random. In this research these distributions are used to determine the position of circular cylinders, infinite in the normal direction to the plane, which are treated as inclusions in a 2D acoustic wave scattering problem.

On the left of figure 1.1 is a well understood problem of wave propagation in a periodic medium. Periodic scattering problems can be solved relatively easily in finite and infinite scenarios. On the right however, is a poorly understood problem of wave propagation in a random medium. Random media problems can be tackled using a plethora of techniques, but require approximate approaches. Thus, divert your attention to the centre image: wave propagation in a material which is not completely random, but nor is it periodic, hence it is aperiodic. Such a distribution as depicted here, is known as a *quasiperiodic lattice*. The quasiperiodic structure depicted does not possess translational symmetry, but has long-range order. We hope to bridge the gap between the well-known and the unknown of wave propagation in periodic and random media by gaining an understanding of wave propagation in quasiperiodic media.

With such influential papers as those by Anderson [6] and Foldy [30], people are under the impression that random microstructure within a material can cause acoustic

wave localisation/decay. Anderson's work shows how the interference of coherent, multiple scattered waves from randomly positioned inclusions can cause wave transmission to completely stop. Similarly, Foldy's use of ensemble averaging and the closure condition often results in a complex effective wave number, i.e. exponential decay in the wave field. Both papers are now widely cited with a lot of research still ongoing in this area, so it has become a natural assumption that this attenuation within random media will always occur. Numerous studies and experiments have supported this hypothesis, but what about the counter examples? Is it possible to really have a complex wavenumber?

In an attempt to comprehend this phenomenon, whilst fully appreciating the work of Anderson and Foldy, we seek viable alternative methods that could aid understanding of wave propagation in random media.

Quasiperiodic distributions have an "air" of randomness as they are aperiodic, although they do have a *deterministic* distribution. For a distribution to be deterministic it means that no randomness is involved in the development of the arrangement. Investigating such distributions will reveal how the transition from a periodic structure to a quasiperiodic structure alters the transmitted wave field. The understanding gained will provide insight into how introducing "randomness"/aperiodicity to a structure affects the wave propagation without having to lose any information on the composition through the normal approach for random media of averaging techniques.

Further analysis will be conducted in order to determine periodic or homogeneous structures which have similar scattering properties to the quasiperiodic structures. By accurately modelling quasiperiodicity with periodicity in structures, it will be demonstrated how a "more random" structure does not necessarily cause wave decay, contrary to the beliefs of many. It will also enable one to model a complicated quasiperiodic distribution with one that is simpler to analyse.

A quasiperiodic distribution can also be thought of as a random perturbation from a periodic structure. In fact, the statistics involved with the distribution of the quasiperiodic lattice nodes are similar to that of a random lattice, and a quasiperiodic lattice can represent one realisation of a random lattice. This reiterates why quasiperiodic structures will help in the quest to understand the properties of random media.

There is an additional motivation for considering wave scattering by inclusions with quasiperiodic distributions, and that is due to the quasiperiodic atomic structure of some materials known as *quasicrystals*, [66]. Quasicrystalline materials have been shown to be increasingly useful in applications. Quasicrystalline coatings are being widely used on a multitude of objects due to their hardness, low thermal and electrical conductivity, low friction and high corrosion resistivity, [23]. Therefore, a material with inclusions distributed in the same way as the atomic structure of a quasicrystal may also have interesting characteristics and thus applications, making it a useful structure to look at.

Analysis of large periodic arrays of scatterers is often approached by approximating the finite array as an infinite array and applying the effective properties of the infinite array to the finite. Computations of effective properties of infinite structures is possible for periodic structures and is often much less computationally expensive than calculations for large finite arrays. However, the same analysis is not applicable to aperiodic structures. Therefore, there is no analogous approach to determine effective properties of infinite quasiperiodic or random structures without alternative averaging methods. In this thesis we seek to determine finite periodic structures that provide similar scattering properties to quasiperiodic structures. By establishing an **appropriate** periodic representation of a finite quasiperiodic structure we can justify using the determined infinite periodic structure to model an infinite quasiperiodic structure. In this thesis we conclude with a periodic representation that has not been applied to quasiperiodic structures before in acoustics. We also develop a novel analytic procedure for infinite periodic distributions with a period containing a finite number of scatterers with arbitrary distributions, which can be applied to compute the approximate effective properties of the infinite quasiperiodic structure.

Due to the link with quasicrystals [66] and because of the interest in the "phononics" of quasicrystals, the main quasiperiodic inclusion distribution we aim to consider is the 2D Penrose tiling. However we will build up to this complicated structure with simpler 1D and 2D quasiperiodic lattices, which provide extendible theories and motivational results. We will first consider a 1D quasiperiodic structure determined by the Fibonacci chain which is the 1D analogue of the Penrose tiling. This is then extended to the 2D version, the square Fibonacci lattice, which is an arrangement of the 1D

quasiperiodic Fibonacci chain in two perpendicular directions.

Throughout this thesis we will delve further into the motivation and background briefly mentioned here. The full story is set with the previous influential works in wave scattering by random, quasiperiodic and periodic materials and the history of quasicrystals, their properties and applications, and how one would go about constructing such a quasiperiodic distribution. Only after this, will we be able to discuss the new results for acoustic wave propagation through 1D and 2D quasiperiodic structures and provide solutions to appropriate periodic approximations that one could use to model the aperiodic lattices.

Therefore, we begin in chapter 2 with the general background required for the thesis. Section 2.1 introduces quasicrystals, and how they provide motivation to consider analogous quasiperiodic structures. It is necessary to then discuss the background behind the geometry of these structures, and the complicated method behind their construction. We will then also be able to introduce two different approaches to approximating the quasiperiodic lattices, through a periodic average structure (PAS) and an approximant. The construction methods of the two periodic approximations are then briefly discussed along with reviews of existing literature in the area. In section 2.2 a literature review of existing work within wave propagation in random, quasiperiodic and periodic structures is given. The method of multiple scattering theory in 1D and 2D is discussed in sections 2.3 and 2.4 respectively, in particular for finite and infinite arrays of isotropic scatterers.

With the background laid out, we will develop an algorithm in which one can construct the 1D quasiperiodic lattice, the Fibonacci chain, in chapter 3. Then, by introducing variations to this method, we develop algorithms to produce two periodic approximations of the Fibonacci chain. The algorithms provided in this chapter provide essential steps and mathematical formulae that are built upon later, when developing the algorithms for more complicated 2D quasiperiodic structures. To our knowledge, there are no other well-documented and rigorous algorithms for the construction of quasiperiodic lattices via the projection method for mathematicians to apply.

In chapter 4 we consider 1D time-harmonic wave propagation through the previously constructed 1D lattices, using point scatterers on a 1D string. In developing

this theory we derive novel recursive formulae. The formulae are employed to construct comparisons between the three finite distributions of scatterers, and thus find suitable periodic lattices to approximate the Fibonacci chain. We derive a new formula in which one can find an effective wavenumber for a finite arbitrarily distributed array by modelling the array as a finite homogeneous section of string. The effective wavenumber of infinite periodic structures is also derived in a novel approach which can exploit prior knowledge of the wave propagation in a single finite period of the infinite structure. Applying this technique to the periodic lattice that represents the Fibonacci chain lattice enables the modelling of an infinite quasiperiodic lattice, which would otherwise not be possible.

Chapter 5 applies the 1D quasiperiodic lattice and its approximations to a 2D scenario. In this problem infinite circular cylinders with small radii are considered as scatterers in an infinite space. Assuming incoming time-harmonic plane waves in the plane perpendicular to the length of the cylinder allows this problem to be reduced to a 2D slice of the 3D set up, considering circular scatterers on a plane. In this chapter the specific scenario under consideration is an array finite in one direction and infinite in another. Consider an infinite single row of cylinders with periodic separation, then take a finite set of the rows, separated by spacings determined by the 1D Fibonacci chain. This arrangement of finite numbers of infinite periodic rows has also been referred to as "tube bundles" in the literature [55]. Considering this set up offers analysis involving the complications of 2D wave scattering, whilst keeping the lattice structure relatively simple with just one direction of quasiperiodicity. In this section we analyse the problem of one infinite periodic row from first principles, and then extend the recursive formulae from the 1D analysis into 2D, to be able to solve for a large number of rows with varying separation. As with the 1D analysis, once the recursive formulation has been derived, we are able to draw comparisons between the quasiperiodic and periodic structures. Analogously, effective properties of an infinite periodic structure with arbitrary period can be derived by exploiting the formulations derived for the finite period array.

Before it is possible to consider 2D wave propagation in a fully 2D quasiperiodic lattice we must develop analogous algorithms to those in chapter 3 in order to construct the 2D quasiperiodic lattices. We develop these algorithms in chapter 6, along with the

construction of the periodic average structure and approximant periodic lattices. We construct two 2D quasiperiodic lattices: the square Fibonacci lattice and the Penrose lattice. To construct the Penrose lattice we use the projection method from 5D, which is widely used in crystallography, but here we attempt to describe the method rigorously, and make the projection much more intuitive by using 4D space too.

In chapter 8 we determine the propagation properties of time-harmonic waves multiply scattered by a finite array of small circular cylinders distributed in a square Fibonacci lattice using the multipole method. We will draw comparisons between the scattering from this lattice and its approximations to determine an appropriate periodic lattice that can be used to model the square Fibonacci lattice. Results are given for the effective properties of this periodic lattice which models the effective properties of an infinite square Fibonacci lattice.

In chapter 9 we come to the main focus of our research: multiple wave scattering by the Penrose lattice. We again use the multipole method to determine the wave propagation through a finite array. As with the previous chapter, comparisons are made between the scattering from the Penrose lattice and its approximations to determine an appropriate periodic lattice that can be used to accurately model the Penrose lattice. Results are given for the effective properties of this periodic lattice which represents the effective properties of an infinite Penrose lattice.

In chapter 10 we summarise the achievements of this thesis, and discuss the future options for continued research in this area.

Chapter 2

Background

The work in this thesis combines two different areas of research: scalar wave propagation in heterogeneous media and quasiperiodic structures. Both topics are substantial in their content and existing literature, but the combination of the two is more limited. In this background chapter general overviews of both topics are given with a focus on the particular areas relating to the research presented in this thesis.

Providing a historical overview of wave propagation in random, periodic and quasiperiodic structures and a historical overview of quasiperiodic structures should aid the illustration of the motivation of the thesis. These overviews along with descriptions of some of the methods associated with multiple scattering theory provide the necessary tools to advance to the work of the thesis in which the worlds of wave theory and crystallography are combined.

2.1 Geometry

This section introduces the background to the quasiperiodic lattices investigated in this thesis. Details of the discovery, geometry and construction of the quasiperiodic structures and some related approximations are given.

2.1.1 Quasicrystals and the Penrose tiling

Quasiperiodic lattices are aperiodic but deterministic, where *deterministic* means that the lattice is generated by a well-defined formula, without randomness. A lattice with these characteristic therefore provides an intermediate structure between periodic and

random. Quasiperiodic structures are not just fictitious media that we consider merely due to these intermediate properties, they are also apparent in the atomic structures of some quite fascinating materials. Such structures exist in what are known as *quasicrystals*. Research in this area, considering associated properties and applications, is rapidly expanding. Thus, we are motivated by both the mathematical and physical aspects of quasiperiodicity.

We begin by reviewing the history and development of both quasicrystal and Penrose tilings; research for which happened in parallel and came together somewhat by chance.

The long standing definition of a *crystal* used to be a solid whose constituent atoms, molecules, or ions, are arranged in an ordered pattern in all three spatial directions. Importantly, these ordered patterns were defined to possess **only** two, three, four and six-fold rotational symmetries in their diffraction patterns, where *n-fold rotational symmetry* of an object means that a rotation of an angle $2\pi/n$ about a point (in 2D) does not alter the object. Figure 2.1 shows some examples of point lattices (left) and their diffraction patterns (right).

A *diffraction pattern* is a plot of the diffracted light intensity as a function of the scattering angle. It was thought that the only possibility of the ability to diffract in an ordered manner came from the existence of a large array of elements with periodic spacing due to Bragg diffraction. This ability can also be described as *long-range order*.

The definition stated that crystals have atomic structures with long-range periodic order that can be described by a single atom or atomic cluster that repeats itself at regular intervals.

One can determine the structure of the crystal from the diffraction pattern. More detail of diffraction theory can be found in [66], but we will discuss it briefly here. Denote the density of electrons in the crystal by the function $f(\mathbf{r})$, $\mathbf{r} \in \mathbb{R}^3$. If the atomic structure can be defined by some lattice Λ then

$$f(\mathbf{r}) = \sum_{\mathbf{l}\in\Lambda} \delta(\mathbf{r} - \mathbf{l}), \tag{2.1}$$

where $\delta(\mathbf{x})$ is the Dirac delta function. The Fourier transform of the density function

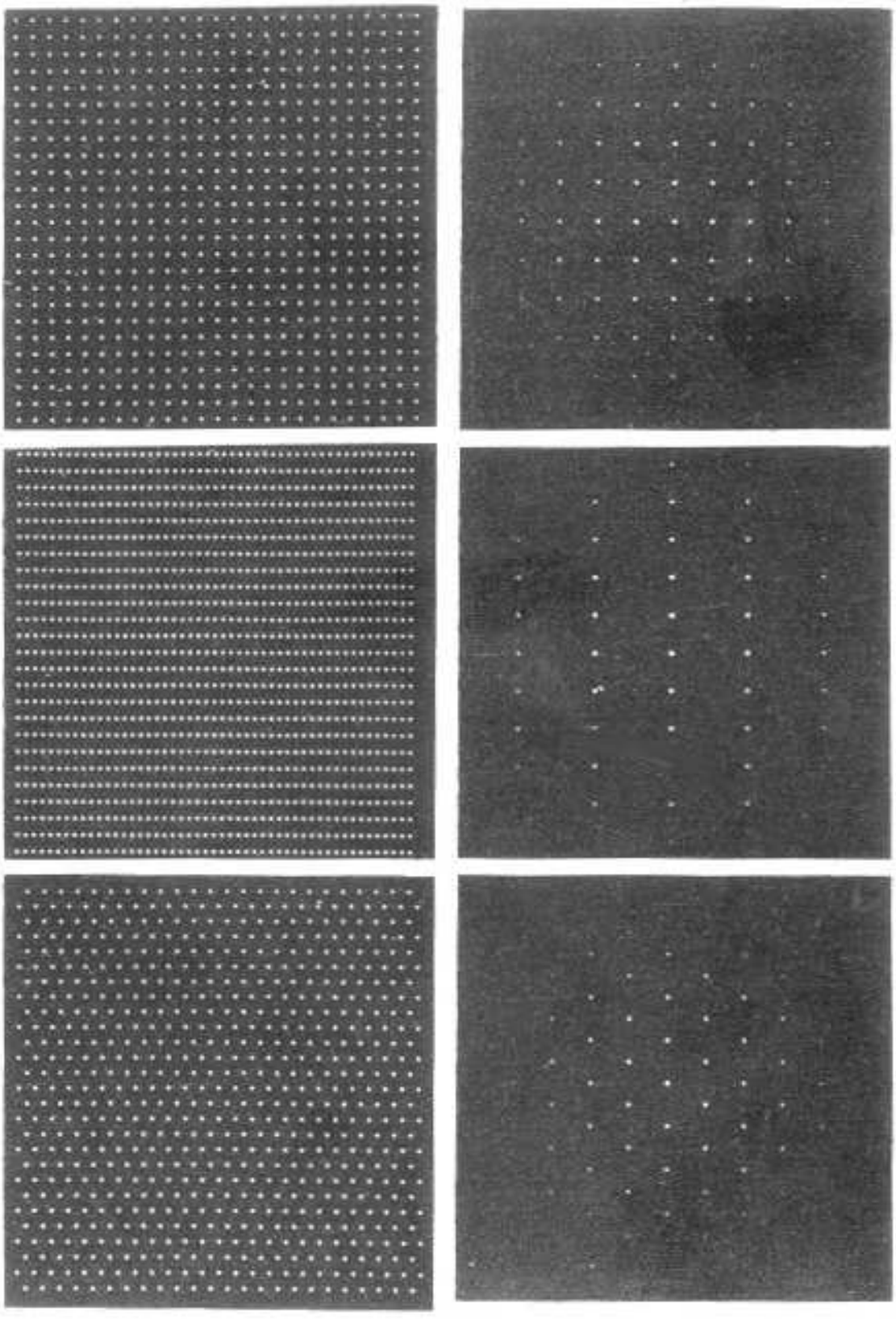

Figure 2.1: Three point lattices with square, rectangular and hexagonal arrangements (left) and their diffraction patterns (right). Image from [66].

is given by

$$F(\mathbf{q}) = \int_{-\infty}^{\infty} f(\mathbf{r}) e^{-2\pi i \mathbf{q}\cdot\mathbf{r}} d\mathbf{r}, \tag{2.2}$$

which is equal to zero except when $\mathbf{q} \in \Lambda^*$ the reciprocal lattice, defined such that

$$\mathbf{q}\cdot\mathbf{l} = 2\pi n, \quad \mathbf{q} \in \Lambda^*, \mathbf{l} \in \Lambda, n \in \mathbb{Z}. \tag{2.3}$$

Theorem 3.2 in [66] states that

$$\mathcal{F}\left(\sum_{\mathbf{l}\in\Lambda} \delta(\mathbf{r}-\mathbf{l})\right) = \sum_{\mathbf{l}^*\in\Lambda^*} \delta(\mathbf{q}-\mathbf{l}^*), \tag{2.4}$$

where $\mathcal{F}$ denotes the Fourier transform operator. This states that the diffraction pattern of a point lattice (inferred from the right of the equation) is the reciprocal point lattice (inferred from the left). Therefore, it is possible to use the data produced in an x-ray diffraction experiment along with inverse Fourier transforms to deduce the original atomic structure of the crystal.

The long standing definition of a *tiling* of n-dimensional (nD) space is an arrangement of a finite set of tiles that fill the space completely, with full tessellation. A *non-periodic tiling* is a tiling in which there is never translational symmetry in more than $(n-1)$ linearly independent directions. For example, a non-periodic tiling in 1D cannot have translation symmetry and a non-periodic tiling in 2D must not have translation symmetry in more than one direction. The tiles used to create such a tiling are *aperiodic tiles*. The tiles can only be classed as aperiodic if they **only** produce non-periodic tilings. Interest in non-periodic tilings began in the 1960's with Wang and Berger, [34]. Initially, the aim was to prove that such a set of tiles is possible, and then to decrease the number of tiles used. Berger's first set contained 20,426 tiles!

In the 1970s observations were made in the field of crystallography in which alloys produced diffraction patterns with orders of rotational symmetry other than two, three, four and six. Due to the long standing definition of crystals this work was disregarded.

Meanwhile, in 1974 Penrose managed to reduce the number of aperiodic tiles required to tile the 2D plane to just two, [62]. He found two sets of tiles, the fat and thin rhombi and the kite and dart, depicted in figures 2.2 and 2.3, respectively.
The tiles defined by Penrose must be decorated in a particular manner and placed to match these patterns accordingly, as depicted, so that they can only produce a non-periodic tiling. The tiling constructed is non-periodic but it exhibits a *five-fold*

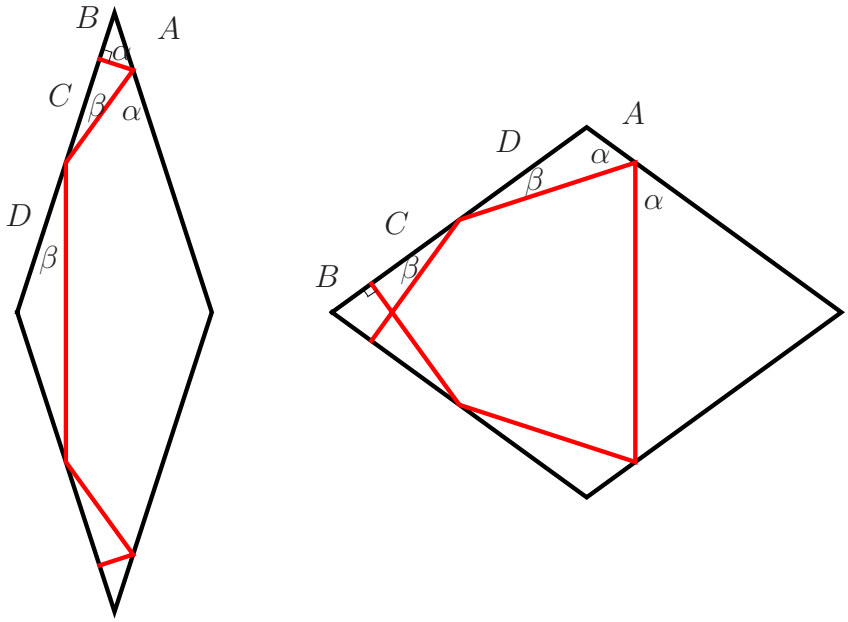

Figure 2.2: The rhomb tiles with the lines on that force the tiles together aperiodically and produce five sets of parallel lines called the Amman bars. Here, $A = \frac{1}{2}a_r \frac{\cos(2\pi/5)}{\cos(\pi/5)}$, $B = \frac{a_r}{2}\cos(2\pi/5)$, $C = a_r \sin^2(\pi/5)$, $D = \frac{a_r}{2}$, a_r is the edge length of the rhombi, $\alpha = \frac{3\pi}{10}$ and $\beta = \frac{\pi}{10}$.

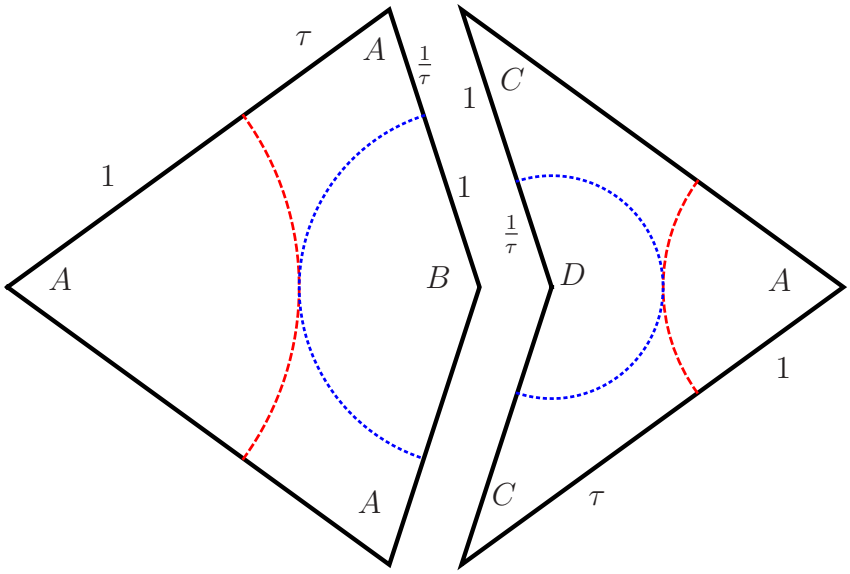

Figure 2.3: The kite and dart tiles, their angles, and one type of matching rule that can be used. Here $A = 2\pi/5$, $B = 4\pi/5$, $C = 2\pi/10$ and $D = 6\pi/5$.

rotational symmetry, and has many more interesting properties, details of which are given in [34]. Figure 2.4 depicts this five-fold rotational symmetry in a Penrose tiling made of the rhombic tiles.

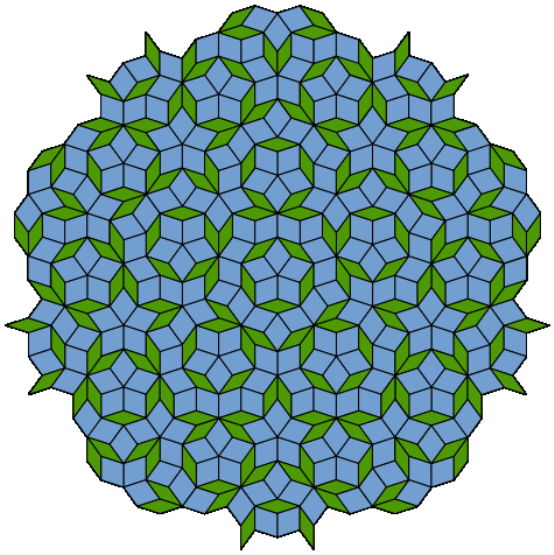

Figure 2.4: Penrose tiling with the two rhomb tiles. Image from [1].

The Penrose tiling is non-periodic and so contains no translational symmetry. However, at a distance there looks to be some order in the tiling and there are repeating patterns. This suggests some form of long-range order, in a different sense to the definition given earlier. In fact Grunbaum and Shephard [34] show that for some circular region $\mathcal{A}$, of diameter d, of a Penrose tiling, copies of $\mathcal{A}$ can be found within a region $p < \tau^5 d$, for $\tau = \frac{1+\sqrt{5}}{2}$ is the *golden ratio*. They state that this is an over estimation, and both Penrose and Ammann claim that the maximum distance p is actually $(\frac{1}{2} + \tau)d$. The fact that any finite patch $\mathcal{A}$ of tiling from the Penrose tiling appears infinitely many times in every Penrose tiling is known as the *Local Isomorphism Theorem*, and is also discussed in [34]. It reveals the "near" periodicity of such tilings.

In 1976 Ammann found a 3-D analogue to the Penrose Tiling that he thought could potentially model viruses which grow in a non-periodic way [67], but did not publish his work. (Further work has recently been conducted in this area with great success, see [78] and references within for further details).

There exist a few methods to construct the Penrose tiling that are more "mathematical" than merely matching the patterns on the tiles a mentioned above. De Bruijn's 1981 paper provides the tools needed [22]. Further approaches to the construction are introduced later in this background chapter.

Shechtman first observed quasicrystals in 1982, but this was received with disapproval and doubt from the scientific community. It was not until two years later that he published his findings, [68]. Shechtman found an Aluminium-Manganese (Al-Mn) alloy that was rapidly cooled after melting. The alloy produced a diffraction pattern that had five-fold rotational symmetry, as depicted in figure 2.5.

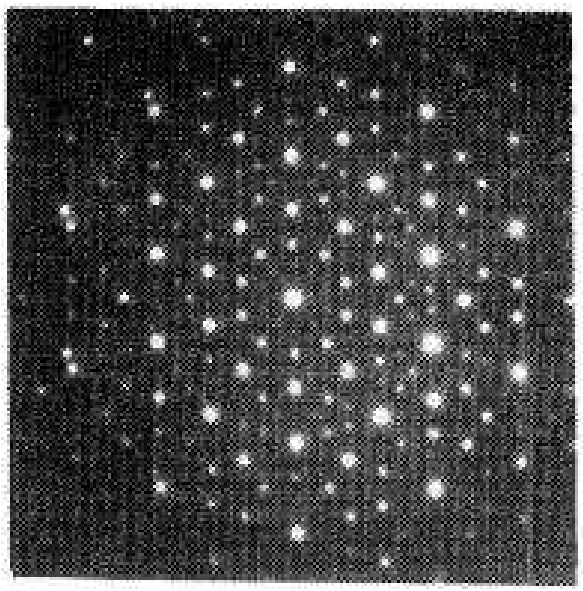

Figure 2.5: Electron diffraction pattern of an icosahedral Al-Mn quasicrystal. Image from [68].

The definition of the crystal along with an understanding of Bragg diffraction in ordered media did not allow for a five-fold rotation symmetry. Therefore, Shechtman's conjecture, *"we have thus a solid metallic phase with no translational order and with long-range orientational order"*, caused great controversy. He argued that the clear-cut diffraction pattern shows that there does exist long-range order in the solid, but due to this five-fold rotational symmetry it should not be periodic.

The quasicrystal reported by Shechtman was thermodynamically unstable, thus when heated it formed a regular crystal. This meant that any further studies of the structure were difficult. In 1987 the first stable quasicrystal was formed [77], opening the doors to research in this area. Eventually, once large numbers of stable quasicrystals could be produced for experimentation, people began to not only accept the concept of the quasicrystal, but to also see its potential applications.

In 1991 the International Union of Crystallography changed the definition of the

crystal. The definition is now separated in to two categories: those with *crystallographic* and *non-crystallographic* symmetries. The previous definition of the crystal where there exists translational symmetry within the crystal lies in the crystallographic category and quasicrystals lie in the non-crystallographic category.

Quasicrystals themselves have since evolved and are no longer restricted to just a five-fold rotational symmetry. There are quasicrystals that are quasiperiodic in just two of the three spatial directions called *polygonal* or *dihedral* quasicrystals. These have one periodic direction perpendicular to the quasiperiodic layers, and can have 8, 10 or 12-fold symmetry (octagonal, decagonal or dodecagonal respectively). There are also quasicrystals that are quasiperiodic in all three spatial directions. These have 5-fold symmetry and are called *icosahedral* quasicrystals.

By comparison of the diffraction pattern of quasicrystals with those of Penrose tilings, it was recognised how the two parallel discoveries of the quasicrystal and the Penrose tiling could be merged. The Penrose tiling became crucial in the development of quasicrystals, by representing a cluster of atoms in the quasicrystal by each Penrose rhomb. The vertices of tiles in the Penrose tiling, i.e. a Penrose lattice, can represent the atomic structure of one layer of a quasicrystal.

The non-periodic arrangement of the atomic structure in quasicrystals gives rise to many unusual properties, making it very different to conventional crystals. Jazbec's seminar [41] provides an instructive overview. One of the most useful properties of the quasicrystal is its hardness. This can be understood easily if we consider the difference between the quasiperiodic and periodic crystals. In periodic structures the atomic planes or layers can slide past one another when under strain. But in the quasiperiodic structures these planes do not exist and so analogous sliding is not possible. Other properties include low thermal conductivity, low electrical conductivity, reduced wetting, a low friction coefficient, high corrosion resistance, a ductile-brittle transition and superplasticity at high temperatures. Most of these properties are beneficial, but the brittle behaviour currently restricts the mechanical applications to coatings. Examples of applications are the coating on frying pans and other cookware, cylinder liners and piston coatings in motor-car engines, coatings on metallic parts for bone repair and prostheses, thermal screens in rocket motors and aero-engines turbines, hydrogen storage and a reflective layer within solar cells.

In 2009 the first natural quasicrystal was found [15] creating further interest and excitement in the field. Furthermore, in 2011, Shechtman's discovery was eventually rewarded and he was presented with a Nobel prize, [18].

With such a range of potential applications of quasicrystals and new interest in the area due to recent developments, we pose the question, *can analogous quasiperiodic composite structures on a slightly larger scale, often referred to as the mesoscale, also have interesting properties and applications?* For example, properties such as high hardness can be expected to still hold at a larger scale. With this motivation it would also be beneficial to understand the wave propagation through such structures.

There are various methods of mathematical construction of Penrose tilings. In this thesis the focus is on the *projection method*, which is discussed in sections 2.1.2 and 6. The *projection method* takes a selection of higher-dimensional lattice nodes and projects them to the dimension of space of interest. The projected nodes form the nodes of the quasiperiodic tiling, i.e. the vertices of the Penrose rhombi. For the Penrose lattices the projection is made from a 5D periodic lattice, due to the 5D reciprocal space, to a 2D plane. To produce other non-periodic tiling representations, one must consider different higher-dimensional spaces from which the projection is made. The dimension of this space reflects the rotational symmetry in the diffraction pattern of the quasicrystal. The least such projection dimension can be found using the Euler totient function $\phi(n)$ [66], where n is the order of the rotational symmetry. The Euler totient function is the number of integers less than and relatively prime to n, and be computed easily using the two properties

$$\phi(p^k) = p^{k-1}(p-1), \quad p \text{ prime}, \quad k \in \mathbb{Z} \tag{2.5}$$

$$\phi(n_1 n_2) = \phi(n_1)\phi(n_2), \quad n_1, n_2 \in \mathbb{Z}. \tag{2.6}$$

For example

$$\phi(8) = \phi(2^3) = 2^2(2-1) = 4. \tag{2.7}$$

Thus, the actual minimum dimension from which the Penrose tiling can be projected from is $\phi(5) = \phi(5^1) = 5^0(5-1) = 4$.

In this thesis the projection method for the Penrose tiling from 5D and 4D to 2D will be discussed as this is the pattern we are most interested in. However, the method and algorithm developed can be altered for other quasiperiodic lattices accordingly.

The projection method is rather complicated, and few full algorithms have been published ([82], [21]), so we begin by introducing the simpler 2D to 1D analogy, which we will use in the 1D wave propagation problems. After this foundation has been laid, it will be possible to discuss the projection method from five and 4D space.

2.1.2 Quasiperiodic lattices

In the previous section the concept of particular quasiperiodic lattices was introduced along with our interest in them due to their links with quasicrystals. The Penrose tiling gives the atomic positions of the first quasicrystal discovered [68] and is the 2D quasiperiodic lattice and quasicrystal most discussed. As mentioned in the previous section, the Penrose tiling can be constructed by projecting from a higher-dimensional space of order five. The 5D space is impossible to visualise and therefore the method can be difficult to apply. There is a lot of literature on the projection method, and great outlines described e.g. [66], but few exact algorithms have been published. A much easier projection to visualise is the 2D to 1D analogy of the Penrose tiling, also discussed in [66], which can define the 1D analogy, the Fibonacci chain. Let us discuss this 1D quasiperiodic lattice first to introduce the concept and notation.

The Fibonacci chain

The *Fibonacci chain* is a 1D aperiodic chain consisting of two different 'tiles'/lengthscales, L and S, or 'large' and 'small'. These lengths are related by the golden ratio τ by

$$L = \tau S, \tag{2.8}$$

where

$$\tau = \frac{1+\sqrt{5}}{2}. \tag{2.9}$$

There are three common ways in which the Fibonacci chain can be constructed. One of the simpler methods is called the *superposition method*. The superposition method follows on from the logic of Fibonacci numbers. The nth *Fibonacci number* is generated by summing the previous two Fibonacci numbers, i.e.

$$\mathrm{Fib}(n) = \mathrm{Fib}(n-1) + \mathrm{Fib}(n-2), \quad \text{for } \mathrm{Fib}(1) = \mathrm{Fib}(2) = 1. \tag{2.10}$$

The Fibonacci sequence is therefore of the form

$$1 \quad 1 \quad 2 \quad 3 \quad 5 \quad 8 \quad 13 \quad 21 \cdots . \tag{2.11}$$

The *Fibonacci chain* is generated in a similar manner. The nth Fibonacci chain is given by 'summing' the two previous Fibonacci chains together. Define the first chain which we will denote D_1 to contain an S spacing. Define the second chain D_2 to contain an L spacing. The third Fibonacci chain D_3 is obtained by appending the first chain to the end of the second, L and S. This is then repeated: D_4 is the sum of D_3 and D_2. Table 2.12 shows the Fibonacci chain pattern constructed in this manner.

n	D_n
1	S
2	L
3	LS
4	LSL
5	$LSLLS$
6	$LSLLSLSL$
7	$LSLLSLSLLSLLS$
8	$LSLLSLSLLSLLSLSLLSLSL$

(2.12)

A depiction of this Fibonacci chain is shown in figure 2.6 with regards to point masses on a string with separations between the masses determined by the Fibonacci chain.

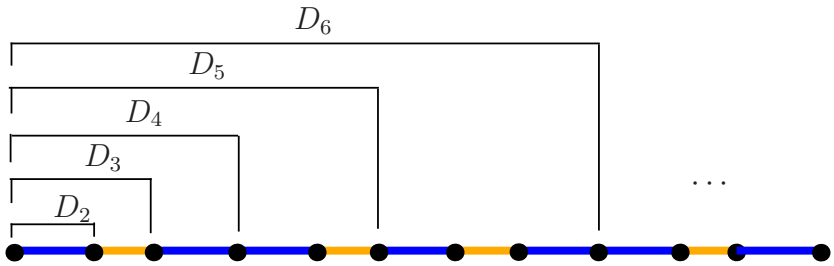

Figure 2.6: Example of a section of of the Fibonacci chain, with long L (blue) and short S (orange) spacings.

An alternative method of construction for the 1D Fibonacci chain is called the *substitution* method [34]. For the substitution method define D_1 to consist of one S

spacing, and apply the following substitutions on each recursion:

$$L \to LS, \quad S \to L. \tag{2.13}$$

Using this method the same Fibonacci chain described in table 2.12 is achieved.

The *projection method* is the final method available to construct the 1D Fibonacci chain. This is the most complicated, but is the method that extends to higher dimensions, and thus an extension of the construction algorithm will be possible to produce the Penrose tiling. This method works by first taking a square 2D lattice. A selection of lattice points is then taken which will be used in the projection. One approach to the selection of these lattice points is by taking a strip of the lattice at some specified irrational angle, and of a certain width, as depicted in figure 2.7 by the grey strip. Every point within this strip is included and projected down to a 1D line parallel to the strip boundaries to produce the Fibonacci chain.

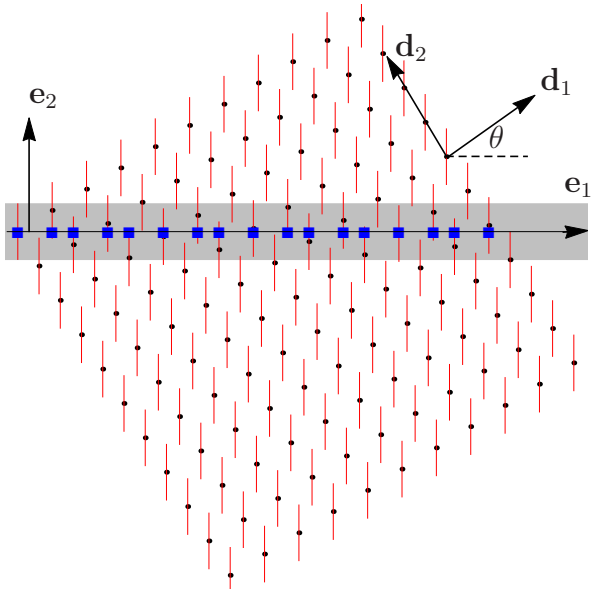

Figure 2.7: A depiction of the projection method from a 2D square lattice to the 1D Fibonacci chain using two alternative approaches to the selection of lattice nodes: via a strip (grey region); and via acceptance windows (red lines)

If the angle of the strip is altered to some rational angle, then it is not possible to achieve a quasiperiodic lattice, as the lattice will repeat itself. If the strip is too wide or too narrow, then it is not possible to achieve a fully quasiperiodic lattice of just two related lengths. This method is discussed in many books as part of an introduction to crystallography and the projection method, [66]. To construct the Fibonacci chain

the angle θ at which we must take the strip is

$$\tan\theta = \frac{1}{\tau}. \tag{2.14}$$

The height of the strip must be of a size that allows only one unit square of the lattice to lie within it. If we have one unit square which has two opposite diagonal lattice points laying on the two boundaries of the strip then we can only take one, i.e. we must have a '$<$' constraint on one boundary rather than a '$\leq$. A little trigonometry reveals that the height of this strip must be

$$h = \frac{\tau^2}{\sqrt{1+\tau^2}}, \tag{2.15}$$

when we have a unit square lattice. A derivation of the angle and the height of the strip can be seen in appendix A.1 and A.2, respectively.

An alternative method for the selection of N-dimensional (ND) lattice points for a d-dimensional (dD) quasiperiodic lattice is via *acceptance windows*. Acceptance windows are particular $(N-d)$D *polytopes* that are positioned on every ND lattice node. A polytope is a geometric object with flat sides that can exist in any number of dimensions. The ND lattice must be subtended from the dD space by the angle θ as depicted by the angle between $\mathbf{e}_1$ and $\mathbf{d}_1$ in figure 2.7. In the 2D to 1D projection the angle θ is given by equation (2.14). The selected lattice nodes are the nodes with an associated acceptance window that intersects the dD space. In the 2D to 1D projection the acceptance windows are derived to be lines, of length equal to the height of the strip just described, that are positioned on every 2D lattice node, as depicted by the red lines in figure 2.7. They are positioned in the same direction as the height of the strip. The dD space in this instance is the 1D line along the horizontal. It can be seen that the Fibonacci nodes (blue squares) are positioned where the acceptance windows intersect the horizontal line. This is the approach taken in this thesis, and is fully explained in section 3.1. It is mathematically easier than the strip to extend into higher dimensions.

We have developed an exact algorithm for the construction of the 1D Fibonacci chain using the projection method which is described in chapter 3.

In order to explain the extension to higher-dimensional projections for other quasiperiodic lattices, let us now define a few components of the 2D to 1D projection. Define

the 1D line subtended from the 2D lattice at an angle θ, the *parallel space*. This is the 1D line that the selected lattice points are projected to. Define the space perpendicular to this to be the *perpendicular space*.

The Penrose tiling

To construct 2D quasiperiodic lattices such as the Penrose tiling, an analogous projection method can be applied. In fact, the Penrose tiling is a 2D Fibonacci chain. For the Penrose tiling begin with a 5D unit hypercubic lattice. As mentioned in the previous section the minimal dimension from which the Penrose tiling can be projected from is actually 4D, however, in that instance a hypercubic lattice can no longer be used, a hyperrhombic lattice must be taken instead. Beginning with a 4D hyperrhombic lattice would complicate the extension of the 2D to 1D Fibonacci chain construction somewhat. However, using the minimum dimension of four has its advantages as it reduces the degrees of freedom of the entire problem by one, thus making the procedure a little easier and reduces the computation time. We will later discuss the projection from 4D, but as this is rarely used in practice, for this background introduction we shall stick to the commonly used 5D projection.

The *parallel space* in this projection is a 2D plane subtended from the 5D lattice by specific angles related to τ. The *perpendicular space* is a 3D *hyperplane* perpendicular to the parallel space. The selection of the 5D lattice nodes is made via a 5D "strip" or 3D acceptance windows. Using the strip method to select the lattice nodes to project results in a selection of the lattice nodes within the strip. Alternatively, using the acceptance windows method, one selects the nodes for which its associated acceptance window intersects the parallel space. The selected nodes in either method are the same and are then projected to the parallel space to give the 2D quasiperiodic Penrose lattice. As mentioned above, it is mathematically easier to apply the acceptance window method to determine the lattice nodes for selection. The derivation of the 3D acceptance windows will be given in chapter 6.

Alternative methods of construction for the 2D Penrose tiling exist. One example was given in section 2.1.1 (e.g. figure 2.2) whereby marked tiles could be placed together ensuring a continuation of the pattern. This is a more visual procedure which is harder to define mathematically.

Another example of a construction method for the Penrose tiling is via the *pentagrid method*. De Bruijn introduced the pentagrid method for constructing a Penrose rhombic tiling in 1981, [22]. In this method he defines five sets of parallel, equally spaced lines, each at an angle of $2\pi/5$ from each other. The five sets of lines are normal to the five vectors

$$\mathbf{d}_j = \begin{pmatrix} \cos(2\pi i/5) \\ \sin(2\pi i/5) \end{pmatrix}, \quad 1 \leq j \leq 5. \tag{2.16}$$

Every line in each set is then given an integer index. Examples in figures 2.8a and 2.8b depict the labelling of one set of lines and the full family of lines, respectively. The full family of lines is called the *pentagrid*.

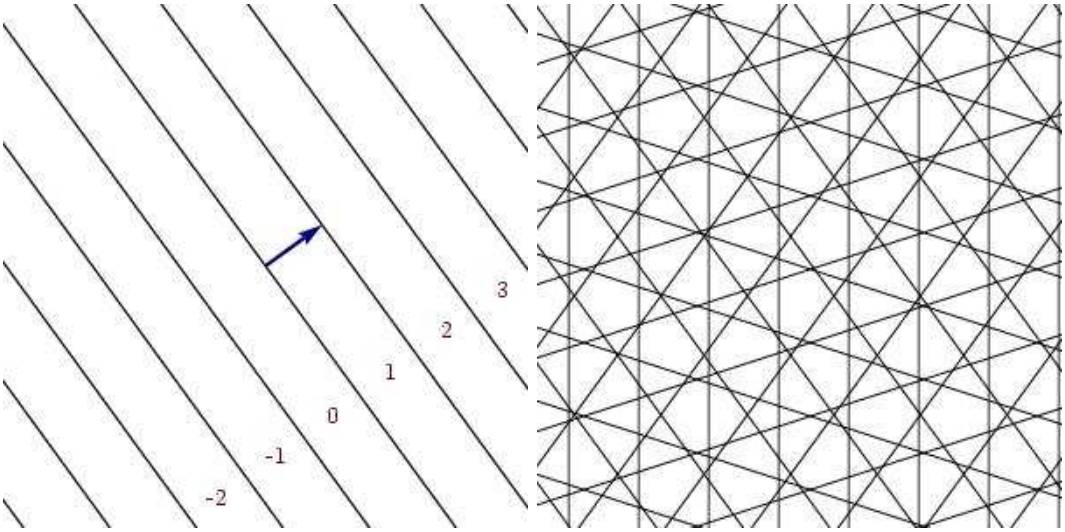

(a) One (of five) set of lines with labelling. (b) Family of all five set of lines.

Figure 2.8: Formation of the pentagrid for the construction of the Penrose tiling. Images from [8].

De Bruijn's description ensures that no more than two lines can intersect at any point by adding a shift γ_j on each set of lines $1 \leq j \leq 5$. He defines this shifted grid as a *regular* pentagrid. At each intersection of two lines there are four associated surrounding polygons formed by the lines. It is possible to define a 5-tuple of integers $(m_1, m_2, m_3, m_4, m_5)$ to each of these polygons that is determined by the integer index (figure 2.8a) of each of the five sets of lines surrounding the polygon. This 5-tuple is then used to define a lattice node of the Penrose tiling

$$\mathbf{x}_{\text{Pen}} = \sum_{j=1}^{5} m_j \mathbf{d}_j, \tag{2.17}$$

where the basis $\mathbf{d}_j$ is defined in equation (2.16). The computational difficulties in this method lie with determining the intersection points and the associated four sets of 5-tuples of integers.

Investigations of the pentagrid method have not been continued in this thesis because the method is only applicable to the 2D Penrose tiling. Although that is the main quasiperiodic structure of interest in this thesis, it would restrict further applications.

The pentagrid and the projection method are comparable in some ways. The pentagrid lines in the 2D plane correspond to hyperplanes in 5D space. The hyperplanes form shapes around the 5D lattice nodes in the form of the hypercubic Voronoi cell of the higher-dimensional lattice, which is what is used to define the acceptance windows in the projection method, [66]. The concept and formulae for the Voronoi cell for the Penrose tiling and its relation to acceptance windows are discussed in chapter 6.

2.1.3 Periodic average structures

The concept of a *periodic average structure (PAS)* for a quasiperiodic lattice was first discussed by Steurer and Haibach in 1999 [71]. Their aim was to find discrete periodic structures comparable in some way to the quasiperiodic structures. They hoped that the periodic structures could aid in the understanding of the geometry of quasicrystal to crystal transformations. The periodic structures would also enable the derivation of the physically most relevant Brillouin zones for the quasiperiodic structures.

The PAS is a periodic structure with period determined by the properties of the quasiperiodic structure in question. Steurer and Haibach [71] define a PAS for the 1D Fibonacci chain, 2D Penrose tiling and 3D Ammann tiling. The method used to derive such a lattice is based on a choice of a base set of reflections in the quasicrystal diffraction pattern which is defined in the reciprocal space of the lattice. By basing the structure of the periodic lattice on characteristics of the quasiperiodic structure, the PAS aims to capture the main essence of the properties of the quasiperiodicity.

The PAS defined for the 1D Fibonacci chain has a period which can be defined by the average spacing of the Fibonacci chain, $\bar{d}$. The average spacing is determined by the ratio of the length of the distribution over the number of spacings in the limit to

infinity, i.e.

$$\bar{d} = \lim_{N\to\infty} \frac{\mathrm{Fib}(N)S + \mathrm{Fib}(N+1)L}{\mathrm{Fib}(N) + \mathrm{Fib}(N+1)}. \tag{2.18}$$

Applying the relationship $L = \tau S$ gives

$$\bar{d} = \lim_{N\to\infty} \frac{S(1 + \tau\mathrm{Fib}(N+1)/\mathrm{Fib}(N))}{1 + \mathrm{Fib}(N+1)/\mathrm{Fib}(N)}. \tag{2.19}$$

In the limit $N \to \infty$, the ratio $\mathrm{Fib}(N+1)/\mathrm{Fib}(N)$ is well known to tend to τ the golden ratio, [34]. Thus the average spacing tends to

$$\bar{d} \to S\frac{1+\tau^2}{1+\tau} = (3-\tau)S, \tag{2.20}$$

using the well-known identity $\tau^2 = \tau + 1$.

For the 2D Penrose lattice the reciprocal lattice plane which contains the main reflections of the diffraction pattern is spanned by [71]

$$\bar{\mathbf{d}_1}^* = a^*\sqrt{3-\tau}\begin{pmatrix}\cos\pi/10\\ -\sin\pi/10\end{pmatrix}, \quad \bar{\mathbf{d}_2}^* = a^*\sqrt{3-\tau}\begin{pmatrix}0\\1\end{pmatrix}, \tag{2.21}$$

where a^* is the length of the higher-dimensional reciprocal base vectors and is related to the Penrose rhomb side length a_r and will be discussed further in chapter 6. In the work in this thesis we usually consider a unit higher-dimensional space and thus set $a^* = 1$. Using the formula for reciprocal lattice vectors (2.3) it can be shown that the PAS lattice basis vectors can be defined by

$$\bar{\mathbf{d}_1} = \frac{2}{\sqrt{5}a^*}\begin{pmatrix}1\\0\end{pmatrix}, \quad \bar{\mathbf{d}_2} = \frac{2}{\sqrt{5}a^*}\begin{pmatrix}\sin\pi/10\\ \cos\pi/10\end{pmatrix}, \tag{2.22}$$

One can see that the higher-dimensional approach is not necessary for the construction of the PAS, however, Steurer and Haibach choose to follow this route because it can allow further insight in to the meaning of PAS and quasicrystals. To create the PAS from the higher-dimensional approach one must project the higher-dimensional lattice down to the parallel plane. The derivation of these projections is described in sections 3.2 and 6.3.

The projection matrix used to project the higher-dimensional lattice nodes onto the PAS lattice nodes can also be applied to the acceptance windows in the higher-dimensional space. The boundaries of the projected acceptance windows give the maximum distance each quasiperiodic lattice node can lie from the nodes of the PAS.

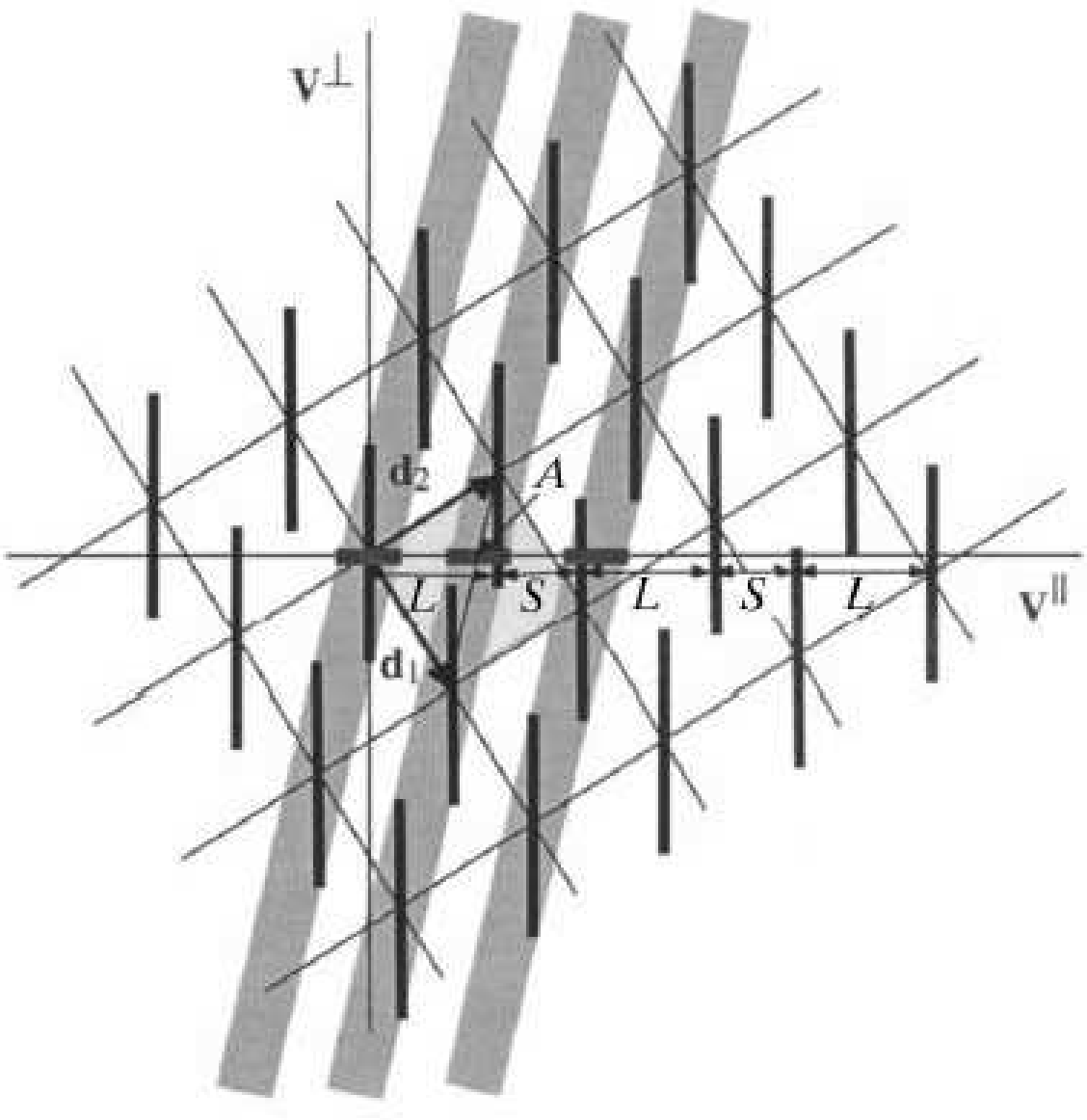

Figure 2.9: Projection of the 2D square lattice nodes and acceptance windows to the 1D PAS nodes and occupancy windows. Image from [71].

Define the projected acceptance window the *occupancy window*. Figure 2.9 shows an example of the projection of the acceptance windows for the 1D Fibonacci chain from the 2D square lattice taken from [71]. The vertical lines on each of the 2D lattice nodes denote the acceptance window. The horizontal thick black lines along the parallel space show the occupancy windows. The PAS nodes lie at the centre of the occupancy windows. The Fibonacci nodes are determined by the intersections of the acceptance windows with the parallel space/horizontal line.

The larger the area of the projected acceptance window compared to the unit cell of the PAS the further the quasiperiodic nodes can deviate from the PAS. If the

deviations are large then the two lattices are expected to be quite dissimilar. The 1D Fibonacci chain and its PAS are one-to-one, i.e. for every PAS node there is an associated Fibonacci chain node. However, the Penrose and Ammann tiling PASs are not one-to-one. This results in some PAS nodes with no associated quasiperiodic node nearby, and some with two neighbours!

There are some measurable quantities of the PAS in comparison to the quasiperiodic structure due to the projection of the acceptance windows. The quantities can help gauge whether or not the PAS is statistically "close" to the quasiperiodic structure or not. These quantities are the occupancy factor ρ_{occ} and the packing density ρ_{pac}. The *occupancy factor* is the fraction of the occupancy windows containing a quasiperiodic lattice node. For the one-to-one Fibonacci chain PAS this is obviously $\rho_{occ} = 1$. For the Penrose tiling the occupancy factor is shown [71] to be much lower $\rho_{occ} = 0.85$, therefore 15% of the projected acceptance windows are empty. When the windows are empty of quasiperiodic nodes the respective PAS nodes are classed as *defects*. The *packing density* is a measure of how much of the total parallel plane the projected atomic windows cover, obviously the larger the ρ_{pac} the further the quasiperiodic lattice node could lie from the PAS lattice node, and thus the less accurate the PAS is. The ideal PAS would have $\rho_{occ} = 1$ and $\rho_{pac} = 0$, the greater the deviation from this the worse the PAS is as an approximation to the quasiperiodic lattice. For the 1D Fibonacci chain $\rho_{pac} = \frac{1}{\sqrt{5}} = 0.447$ and for the 2D Penrose lattice $\rho_{pac} = \frac{3-\tau}{\tau} = 0.342$.

For the 1D PAS, there is a one-to-one relationship between the PAS and Fibonacci nodes, but a relatively high variance of quasiperiodic node to periodic. With the Penrose tiling, 15% of the PAS nodes are defects whilst there is a reasonable variance of the quasiperiodic to periodic node. These statistics suggest the PAS for a Penrose lattice may not be the most accurate of approximations. These stated measures are derived in [71].

Within Steurer and his colleagues' work they find some good PASs for other quasiperiodic structures, the 8-fold 2D quasiperiodic lattice for instance. In 2007 Steurer applied the concept of the PAS of quasiperiodic structures to phononics with a PhD student Sutter-Widmer [75]. Typically the study of scattering in quasicrystals is restrained to photonics due to the atomic spacing of the crystals and the wavelength

of light. Sutter-Widmer considers sound scattering through the quasiperiodic structures and how this compares to the scattering through their PASs. Some results from these investigations will be discussed in section 2.2.3.

In this thesis investigations of PAS lattices as approximations of quasiperiodic lattices are continued. It is of interest to investigate this PAS further from a more analytical approach, to see if improvements can be made, and to compare to other periodic approximations.

2.1.4 Approximants

An *approximant* to a quasiperiodic lattice is a periodic lattice that retains some of the quasiperiodicity of the original lattice within its unit cell. The approximant lattice can be derived by a slight alteration to the projection method used to construct the quasiperiodic lattices discussed in section 2.1.2.

After the publication of the discovery of quasicrystals [68] it was experimentally inaccessible to study the atomic structure of the then unstable quasicrystals. Investigations of alternative methods to understand this new phenomenon resulted in the work published by Elser and Henley [25], who proposed approximant structures for quasicrystals. Their aim was to find a structure closely related to that of the Al-Mn quasicrystal, which would provide a simpler model of the quasicrystal structure. The periodicity of the approximant structure agreed with the ideas of crystal growth via a replicating cell.

In the construction of the approximant via the projection method, τ is approximated by a rational number. The rational number chosen is the ratio of consecutive Fibonacci numbers,

$$\tau \approx \tau_n = \frac{\mathrm{Fib}(n+1)}{\mathrm{Fib}(n)}. \tag{2.23}$$

It is well known [34] that the ratio of consecutive Fibonacci numbers (2.23) tends to τ as $n \to \infty$. The n chosen in the approximation also determines the size of the periodic cell. The larger n the larger the size of the unit cell. As one would expect intuitively, as $n \to \infty$ the resemblance of the approximant to the quasiperiodic lattice improves.

The basics of the method for the construction of the approximant for the 1D Fibonacci chain are described as set out by Elser and Henley [25] to illustrate the theory. In the construction of the 1D quasiperiodic Fibonacci chain from a 2D unit

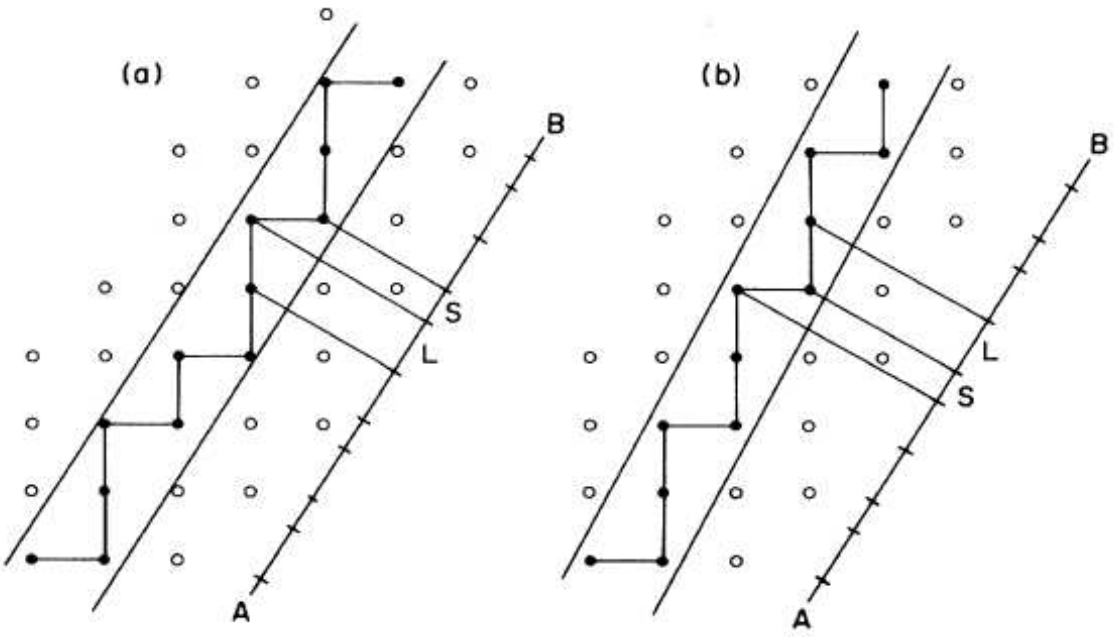

Figure 2.10: Comparison of the strip used in the projection method from 2D to 1D. (a) shows a strip with a gradient $m = \tau$ creating the Fibonacci chain lattice. (b) has a strip with gradient $m' = 2/1$ creating a periodic approximant of the Fibonacci chain. Image from [25].

square lattice as discussed in section 3.1, the perpendicular plane was positioned at an irrational angle $\theta + \pi/2$ from the 2D lattice, for θ defined in (2.14). For the approximant, take a rational approximation of this angle using $\tau \approx \tau_n$. The selection of 2D lattice nodes will vary slightly due to this change. Projecting the selection of 2D lattice nodes to the *same* parallel space as in the Fibonacci chain projection creates an approximant lattice. The L and S tiles continue to be the two tiles in the structure due to the continuation of the use of the parallel plane. However, the distribution of the tiles changes, due to the alteration of the perpendicular space. The rationality of its subtended angle forces a periodic arrangement of the tiles.

When using the strip approach to select the lattice nodes, the change in angle of the perpendicular plane relates to change in gradient of the entire strip. The parallel plane remains the same as with the quasiperiodic projection, and is no longer considered as the boundary of the strip. Figure 2.10 shows the difference in the two strips for the Fibonacci chain and the approximant with $\tau \approx \frac{2}{1}$. The formulation when using acceptance windows to select the lattice nodes will be discussed in detail in section 6.4.

The concept can be extended into higher dimensions using the same idea, but

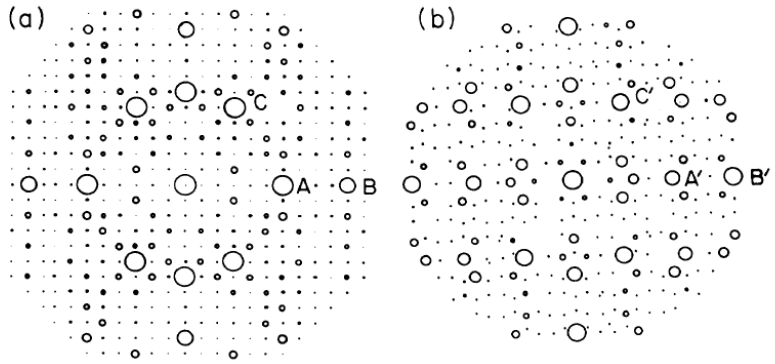

Figure 2.11: Diffraction Pattern for two 3D lattice structures, where the intensity is shown by the area of the circles. (a) is for an approximant of the 3D Penrose tiling, (b) is for the 3D Penrose tiling itself. Image from [25].

approximating τ in the multiple directions of the perpendicular plane. Elser and Henley [25] only discuss this extension in short for the 3D Penrose case.

The potential of this method as an accurate approximation of quasiperiodic lattices is portrayed in figure 2.11 taken from [25]. The diffraction patterns are shown for a slice of both the 3D Penrose tiling and an approximant. One can see how the approximant captures the same highest intensity peaks as the Penrose as well as other less intense characteristics..

With the progression of the theory behind the approximant, further work applied the concept of the approximant and papers become more detailed in regard to the exact construction. In 1988 Entin-Wohlman et al. [26] considered approximant lattices for the 2D Penrose tiling and relate the two using the concept of defects. They also begin by describing the 1D Fibonacci chain lattice approximant for ease. They show that each n-approximant has a unit cell of Fib$(n+1)$ L segments and Fib(n) S segments, so a total length containing Fib$(n+2)$ segments, for $\tau \approx \tau_n$. They also show that in 1D there is one defect per unit cell of the approximant. In 2D Entin-Wohlman et al. state that the minimal number of defects is one per unit cell, with explicit formulae

given dependent on the n chosen in the approximant. The method they mainly employ to extend into higher dimensions is the pentagrid method. The projection method is employed in this thesis, so their approach using the pentagrid is not discussed further here.

Lord et al. [49] and Subramaniam and Ramakrishnan [74] provide the work most influential to the research involving approximant structures in this thesis. Both papers employ the projection method to construct various quasiperiodic lattices and their approximations. The papers also give insight into the form of the periodic cell of the approximant. In the projection method they take the approach mentioned in 2.1.2 where the higher-dimensional hypercubic lattice is rotated through some oblique angles related to τ, with [74] deriving such rotation matrices. For a dD quasiperiodic lattice with N-fold rotational symmetry, they project from ND. The parallel space is dD spanned by $\mathbf{e}_i$, $1 \leq i \leq d$. The perpendicular space is $(N-d)$D spanned by $\mathbf{e}_i$, $d+1 \leq i \leq N$. In fact, both papers decompose the original rotation matrix of the higher-dimensional lattice R into two sub matrices: A, containing the components in the parallel space directions; and B, containing the components in the perpendicular space directions,

$$R = \begin{pmatrix} A \\ B \end{pmatrix}. \tag{2.24}$$

Thus A is a $d \times N$ matrix with column vectors $\mathbf{a}_i$ and B is a $(N-d) \times N$ matrix with column vectors $\mathbf{b}_i$, $1 \leq i \leq N$.

When taking approximations of τ in the construction of the approximant, apply only in the $(N-d)$D perpendicular space, i.e. the τ in the rows of B. Once the $N-d$ approximations of τ are defined, continue as before, projecting to the same parallel space. This results in a dD approximant lattice which consists of periodic unit cells which retain some quasiperiodicity and the same tiles as in the quasiperiodic lattice.

The periods of the approximant are determined by finding when the higher-dimensional lattice nodes lie on the parallel space, rather than when any acceptance window intersects the parallel space. Lattice nodes lie on the parallel space when there exists a linear combination of the $\mathbf{b}_i$ equal to zero,

$$n_1\mathbf{b}_1 + \cdots + n_N\mathbf{b}_N = \mathbf{0}, \quad n_i \in \mathbb{Z}. \tag{2.25}$$

The positions of these intersections on the parallel plane are

$$n_1\mathbf{a}_1 + \cdots + n_N\mathbf{a}_N, \tag{2.26}$$

and denote the vertices of the periodic cell of the approximant.

Linearly deforming the matrix B will allow the investigation of alternative periodic cell shapes and sizes. The linear deformation is possible since linear transformations of the perpendicular space do not affect the lattice produced in the parallel space, i.e. if T is a non-singular matrix then

$$n_1(T\mathbf{b}_1) + \cdots + n_N(T\mathbf{b}_N) \in T\mathbf{W}_N \tag{2.27}$$

if and only if

$$n_1\mathbf{b}_1 + \cdots + n_N\mathbf{b}_N \in \mathbf{W}_N, \tag{2.28}$$

where $\mathbf{W}_N$ is the acceptance window in the ND space. Papers [49] and [74] both investigate approximants for the Penrose tiling with periodic cells with basis vectors in two perpendicular directions and at an angle of $2\pi/5$ like a Penrose tile.

Although a lot of research was carried out with the approximant method at the time of the discovery of quasicrystals to grasp the complexities of the quasicrystalline structure, to our knowledge the structures have not been applied in many other contexts, and not at all in "phononics" or acoustics.

One application of the approximant structure in wave theory is in the work of Florescu et al. [29], where they use approximants to find photonic bandgaps of quasicrystals. This work is discussed further in section 2.2.3. Within this work the authors focus on orthorhombic approximants and define the dimensions of such dependent on the approximation of τ used. If $\tau \approx \tau_n = \frac{\mathrm{Fib}(n+1)}{\mathrm{Fib}(n)}$ the authors state that the unit cell has perpendicular side lengths of

$$L_x = 5\left(\mathrm{Fib}(n+1) + \mathrm{Fib}(n)(\tau - 1)\right), \tag{2.29}$$

$$L_y = \sqrt{3-\tau}\left(\mathrm{Fib}(n+1)\tau + \mathrm{Fib}(n)\right), \tag{2.30}$$

and

$$N = 10\mathrm{Fib}(n+1)(\mathrm{Fib}(n+1) + 2\mathrm{Fib}(n)) \tag{2.31}$$

is the number of vertices within one unit cell. Unfortunately, Florescu et al. give no derivation of these formulae and in chapter 9 it is shown that the periods of the approximant determined do not agree with the three quantities (2.29)-(2.31).

The concept of a repeating cell containing information about the lattice has been applied in wave propagation previously, but in application to random composites. Willoughby et al. [84], [83], define representative volume elements (RVEs), containing random distributions of scatterers, that can tessellate space to provide a model that agrees well with previous approximate approaches. In the instance of the approximant, there is the advantage of prior intuition for the period size and shape as a result of the approximation of the projection method.

2.2 Wave scattering

This section introduces the background to scalar wave propagation through distributions of scatterers. Details of some of the most influential works in the area are given. Methods for multiple scattering are discussed that will be applied to particular structures throughout the investigations of this thesis. All investigations in this thesis are for time-harmonic, or steady, waves and thus the time dependence $e^{-i\omega t}$ is assumed throughout, where ω is angular frequency and t is time.

2.2.1 Wave scattering by random media

Analysis of wave propagation in random media is difficult due to the non-deterministic scatterer positions. Therefore, analytic, numeric and experimental work continues as people strive to gain a better understanding of the effects of randomness. It is of paramount importance to achieve this understanding as wave scattering in random media is ubiquitous. Most materials contain some aspect of randomness in their structure, and even a manufactured periodic structure will contain some random perturbations due to error. The ability to accurately predict wave propagation through such structures will allow great advances in technology. For example, in non-destructive testing. Non-destructive testing requires an accurate model of the expected transmitted and reflected wave field for a material. If the received wave field differs from the expected then it is known that there is a fault in the material. Advances in the modelling of the scattering properties of the host material will improve the diagnosis of any faults within it.

Due to the non-deterministic nature of a random structure, little exact analysis of the wave propagation can be conducted. Instead, many approximations or averages must be applied. The approximations can be effective but the question arises, *how can one averaged wave field represent wave propagation through multiple different random configurations of scatterers?* Due to the high numbers of current investigations in the area we refer the reader to [31] for a multidisciplinary review of many approaches to 1D wave propagation in randomly layered materials. This reference will provide the interested reader with a broad introduction to the difficulties and solutions available for propagation through random structures.

In this chapter the focus is to provide an overview of the initial most influential work in the area. The chapter discusses the concepts of Foldy's averaging technique and Anderson localisation. These two approaches were the first highly-regarded investigations of the prediction of wave propagation through random media and motivate further exploration.

Foldy

The work of Foldy [30] is the first influential piece of research in the area of wave propagation in random media. The paper, written in 1945, investigates multiple scattering of waves by random distributions of isotropic scatterers, where isotropic scatterers are inclusions that scatter the incident waves equally in all directions. The method employed reduces the problem to a set of simultaneous linear algebraic equations. The set of equations involve complex integrations that are not possible to solve in general. Foldy introduces an alternative solution to the integrals through ensemble averaging and application of a closure condition. This section introduces the method and illustrates the theory for a 1D scattering problem.

Foldy begins by considering a steady-state scattering of waves of frequency ω, so that the value of the scalar wave function at the point $\mathbf{x}(x$ in 1D) at time t can be represented as $U(\mathbf{x})e^{-i\omega t}$. In the absence of scatterers, $U_0(\mathbf{x})$ will satisfy the wave equation $\nabla^2 U_0 + k_0 U_0 = 0$, where $k_0 = \frac{\omega}{c_0}$ and c_0 is the wave speed in the scatterer-free/host medium. The solution of the wave function $U(\mathbf{x})$ in the neighbourhood of the jth scatterer in 1D is of the form $A_j e^{ik_0|x-x_j|}$. Continuing with the 1D analogue of Foldy's work, define the external field acting on the jth scatterer as

$$U_j(x) = U(x) - A_j e^{ik_0|x-x_j|}. \tag{2.32}$$

Characterise the scattering properties of the scatterers by the relationship

$$A_j = g_j U_j(x_j), \tag{2.33}$$

where g_j an unknown scattering coefficient to be selected.

Define an incident wave $U_0(x)$, resulting in a wave function at x of the form

$$U(x) = U_0(x) + \sum_{j=1}^{N} A_j E(x, x_j), \tag{2.34}$$

where $E(x, x_j) = e^{ik_0|x-x_j|}$ in 1D. Combining equations (2.32) and (2.34) gives

$$U_n(x) = U_0(x) + \sum_{\substack{j=1 \\ j\neq n}}^{N} A_j E(x, x_j). \tag{2.35}$$

Substituting equation (2.33) in equations (2.34) and (2.35) results in *Foldy's fundamental equations for multiple scattering*,

$$U(x) = U_0(x) + \sum_{j=1}^{N} g_j U_j(x_j) E(x, x_j), \tag{2.36}$$

$$U_n(x_n) = U_0(x_n) + \sum_{\substack{j=1 \\ j\neq n}}^{N} g_j U_j(x_j) E(x_n, x_j). \tag{2.37}$$

Foldy proposes the following approach in order to find an expression for the configurational average of the field. The average of a physical quantity over the ensemble of configurations is called the *ensemble average* and is denoted by enclosing the quantity with angular brackets. For a function $f(x)$ the ensemble average is mathematically defined as

$$\langle f(x)\rangle = \int_L \cdots \int_L f(x; x_1, \ldots, x_N) p(x_1, \ldots, x_N) dx_1 \cdots dx_N, \tag{2.38}$$

where $p(x_1, \ldots, x_N)$ is the probability density function for the particular configuration (i.e. scatterers at locations $x_1, \ldots, x_N$) and L is the 1D line on which the scatterers are positioned. Introducing a subscript notation $\langle f\rangle_j$ indicates that the integral over the x_j is omitted. In the 1D set up described in this section, $\langle U_j(x_j)\rangle_j$ represents the external field acting on the jth scatterer averaged over all possible configurations of all of the other scatterers. All point masses are of the same mass and thus assumed to have the same scattering properties. Identical scattering properties means that $g_j = g$ in (2.33). A distribution of scatterers with uniform probability density function is also assumed. In 1D the uniform distribution relates to a length $0 \leq x \leq L$ in which the N scatterers lie with uniform likelihood. The probability density function for each single scatterer with a continuous uniform distribution over this interval is therefore $p(x_j) = \frac{1}{|L|}$ for $1 \leq j \leq N$. Taking the ensemble average of the field in equation (2.36), accounting for the stated assumptions, gives

$$\begin{aligned}\langle U(x)\rangle &= U_0(x) + \sum_{j=1}^{N} g \int_L \langle U_j(x_j)\rangle_j E(x, x_j) p(x_j) dx_j \\ &= U_0(x) + \frac{Ng}{|L|} \int_L \langle U_j(x_j)\rangle_j E(x, x_j) dx_j,\end{aligned} \tag{2.39}$$

where the integration over the j^{th} scatterer has been extracted. In order to evaluate $\langle U_j(x_j)\rangle_j$ it is necessary to go to higher order ensemble average equations. However, this yields unknown terms $\langle U_j(x_j)\rangle_{ij}$. Continuing, every extra order of ensemble average introduces an extra unknown. To overcome this problem Foldy introduced an approximation (now called the *Foldy closure condition*),

$$\langle U_j(x_j)\rangle_j = \langle U(x_j)\rangle. \tag{2.40}$$

The approximation (2.40) is the replacement of the external field acting on the jth scatterer averaged over all configurations of the other scatterers by the average field which would exist at the position of the jth scatterer when the scatterer is not present. Applying the closure condition to the equation (2.39) results in the following integral equation

$$\langle U(x)\rangle = U_0(x) + \frac{Ng}{|L|}\int_L \langle U(x_j)\rangle E(x, x_j)dx_j. \tag{2.41}$$

This equation can be manipulated with an application of the operator

$$\nabla^2 + k_0^2, \tag{2.42}$$

using the fact that $(\nabla^2 + k_0^2)E(x, x_j) = 2ik_0\delta(x - x_j)$. It is shown that

$$\begin{aligned}(\nabla^2 + k_0^2)\langle U(x)\rangle &= 0 + \frac{Ng}{|L|}\int_L \langle U(x_j)\rangle 2ik_0\delta(x - x_j)dx_j \\ &= \frac{Ng}{|L|}\langle U(x)\rangle 2ik_0.\end{aligned} \tag{2.43}$$

Let

$$k^2 = k_0^2 - \frac{2ik_0Ng}{|L|}, \tag{2.44}$$

so that (2.43) can be written as

$$(\nabla^2 + k^2)\langle U(x)\rangle = 0. \tag{2.45}$$

This suggests that the averaged field $\langle U(x)\rangle$ satisfies the wave equation in an averaged continuous medium with effective wavenumber k. Finding the average value of the wave function has been essentially reduced to solving a boundary value problem for the wave equation, the boundary conditions for which are implied by the integral equations themselves. In order to determine the form of the effective wavenumber in equation (2.44) associated with a random distribution of isotropic scatterers the form of the scattering coefficient g must be determined.

The 1D problem discussed in this chapter can be considered to be an infinite string with a distribution of point scatterers. With reference to [2], [60], [57], it can be shown that such a set up is governed by the equation,

$$\frac{\partial^2 U}{\partial x^2} + k_0^2 U(x) = -\frac{m\omega^2}{T} \sum_n \delta(x - x_n) U(x), \tag{2.46}$$

where m is the mass of each point scatterer, T is the string tension, $k_0 = \sqrt{\frac{\rho_0 \omega^2}{T}}$ is the wavenumber of the host string, and ρ_0 is the density of the host string. An alternative formulation of the wave field for a finite number of point scatterers with arbitrary distribution can be given by employing Green's functions for the host string. The 1D Green's function defined by the equation

$$\left(\frac{\partial^2}{\partial x^2} + k_0^2\right) G(|x - y|) = \delta(x - y) \tag{2.47}$$

is given by

$$G(|x - y|) = \frac{1}{2ik_0} e^{ik_0|x-y|}. \tag{2.48}$$

Combining the Green's function with equation (2.46) and using the sifting property of the delta function results in the following equations,

$$U(x) = U_0(x) - \frac{M\epsilon}{2i} \sum_{j=1}^{N} e^{ik_0|x-x_j|} U(x_j), \tag{2.49}$$

$$U(x_p)\left(1 + \frac{M\epsilon}{2i}\right) = U_0(x_p) - \frac{M\epsilon}{2i} \sum_{\substack{j=1 \\ j\neq p}}^{N} e^{ik_0|x_p-x_j|} U(x_j), \tag{2.50}$$

where $M = m/m_0 = m/(\rho_0 a)$, $\epsilon = ak_0$ and $a = L/N$ is the average spacing between the point scatterers. Comparison with equations (2.36) and (2.37) suggests that the scattering coefficient g in Foldy's work is of the form

$$g = -\frac{M\epsilon}{2i(1 + M\epsilon/2i)}. \tag{2.51}$$

Substitution into equation (2.44) for the wavenumber in Foldy's method gives

$$k^2 = k_0^2 + \frac{N}{|L|} \frac{M\epsilon}{2i(1 + M\epsilon/2i)} 2ik_0 \tag{2.52}$$

$$= k_0^2 + \frac{1}{a} \frac{M\epsilon}{1 + M\epsilon/2i} k_0 \tag{2.53}$$

$$= k_0^2 \left(1 + \frac{M}{1 + M\epsilon/2i}\right). \tag{2.54}$$

The effective wavenumber scaled on the host string wavenumber $\gamma = k/k_0$, is therefore defined by

$$\gamma^2 = \frac{k^2}{k_0^2} = 1 + \frac{M}{1 + M\epsilon/2i}. \tag{2.55}$$

In the low frequency limit, $\epsilon = ak_0 \ll 0$ (meaning the wavelengths are much longer than the distances between the scatterers), this can be expanded to give

$$\gamma^2 = 1 + M + i\frac{M^2}{2}\epsilon + \mathcal{O}(\epsilon^2), \tag{2.56}$$

or

$$\gamma = \sqrt{1 + M} + i\frac{M^2}{4\sqrt{1 + M}}\epsilon + \mathcal{O}(\epsilon^2). \tag{2.57}$$

Therefore, after following Foldy's assumptions and using the ensemble average and the closure condition, the resultant effective wavenumber is complex. A complex wavenumber relates to a continual attenuation of the wave as it travels through the random structure, despite the fact that energy is conserved. The concept of decay in the wave field due to randomness in a structure is, although physically contradictory, well believed. Further work that supports these ideas is that of Anderson.

The theory used in Foldy's work is applied to small isotropic scatterers. In this thesis the scatterers under consideration will be point scatterers on a string in 1D and small circular cylinders in 2D with Dirichlet (sound-soft) boundary conditions. Both of these scatterers behave as small isotropic scatterers in the same way as Foldy's scatterers. The work in 2D in this thesis can be extended to consider Neumann (sound-hard) boundary conditions which would represent anisotropic and thus different scatterers to those of Foldy [50].

Anderson

Anderson published a paper on the absence of diffusion in random lattices in 1958 [6]. The application under consideration in Anderson's work is the behaviour of electrons in random crystals, also considered in [7], [37] and [38]. The theory has since been applied to electromagnetic waves and acoustic waves [28], [5], [27], [80], [69].

Anderson's conclusion is that"*at sufficiently low densities* [of inclusion to host material], *transport does not take place; the exact wave functions are localised in a small region of space.*" In acoustics, transport is considered to be the propagation of the waves. Through studies of a random lattice with spins, electrons or other particles

at the nodes x_j with energy E_j and interaction V_{jk}, Anderson shows that transport ceases when

$$V_{jk} < \frac{1}{\mathbf{r}^3} \text{ for } \mathbf{r} \to \infty, \quad \text{and} \quad \bar{V} < V_c, \tag{2.58}$$

where$\mathbf{r}$ is distance, $\bar{V}$ is the average value of the interaction and V_c is a certain critical value. It is shown that the amplitude of the wave function around a node decreases rapidly with distance whilst the amplitude on the node remains finite.

In terms of acoustic wave propagation the theorem relates to the interference of coherent waves (in phase) after the multiple scattering from a random distribution of scatterers. The coherent scattering causes the transmission of the wave to decrease exponentially, and to completely halt for a critical amount of disorder. This is a behaviour which one would associate with incoherent wave (out of phase) scattering. In a 1D set up the transmission coefficient T of an acoustic wave through a random structure with localisation can be described by

$$|T| = \lim_{L\to\infty} e^{-\gamma L}, \tag{2.59}$$

where γ is known as the *Lyapunov exponent*, [80]. The inverse of the exponent γ^{-1} is equivalent to the maximum localisation length in 1D and defines the characteristic attenuation length of the random medium. The derivation of the exponent can be achieved using transfer matrices in random matrix theory. The use of transfer matrices is a common approach in many 1D wave propagation problems, thus making the theory of Anderson localisation highly applicable in 1D acoustics.

There exists a comparative difference in the effects of localisation in quantum mechanical and classical waves due to the governing equations for each [80]. Anderson's work in spin waves or other quantum mechanical waves are described by the Schrödinger equation rather than the Helmholtz equation (for acoustic or other classical waves). A comparison of the two equations leads to conclusions on the different localisation behaviours. The 1D Schrödinger equation is given by

$$\left(\frac{\partial^2}{\partial x^2} - E\right) u(x,\omega) = V(x)u(x,\omega). \tag{2.60}$$

The 1D wave equation is given by

$$\left(\frac{\partial^2}{\partial x^2} - \frac{1}{c^2(x)}\frac{\partial^2}{\partial t^2}\right) u(x,t) = 0. \tag{2.61}$$

To express (2.61) in a similar manner to the Schrödinger equation take the Fourier transform and decompose the velocity as

$$\frac{1}{c^2(x)} = \frac{1}{c_0^2}\left(1 - V(x)\right), \tag{2.62}$$

where c_0 is the velocity of the wave in the host medium, to give

$$\left(\frac{\partial^2}{\partial x^2} + k_0^2\right) u(x,\omega) = k_0^2 V(x) u(x,\omega). \tag{2.63}$$

Comparison of (2.63) with (2.60) highlights the dependence of the classical wave equation on k_0, that is not apparent in the Schrödinger equation. In the Schrödinger equation the potential provides a greater contribution to the system as the frequency decreases. However, for acoustics, the contribution of $V(x)$ decreases with frequency. A low contribution of $V(x)$ suggests that no localisation exists in the low frequency limit for acoustics. This is intuitive, as for low frequency the wavelength is much longer than the characteristic lengthscale in the disordered medium and hence the waves perceive the medium as an average homogenous medium. In the case of spin waves, the potential does not depend on the wavenumber but the energy of the system E. The potential $V(x)$ increases as E decreases. This implies that localisation is possible in all frequency ranges of quantum mechanical waves.

The conclusion of decay in the wave field raises the same questions, as with Foldy's hypothesis, inherent on the loss of energy in the system. These questions motivate the investigations of aperiodic structures in which the disorder is not completely random. The structures under consideration in this thesis have quasiperiodic distributions which are deterministic yet aperiodic. The deterministic nature allows the calculation of the effects of some disorder on the wave propagation without the use of simplifying assumptions or averaging.

2.2.2 Wave scattering by periodic media

Wave propagation in periodic media is generally more straightforward and easier to model than quasiperiodic or random media. This is because of the simplifications one can make due to the periodicity of the structure. For instance, when considering an infinite lattice with a periodically repeating unit cell, the scattering in the whole problem can be solved by restricting the geometry to just the unit cell, taking in

to consideration periodic boundary conditions. This section will discuss the work of Brillouin [17] and Bloch [16] which are both of paramount significance in the field. We refer the reader to [42] (appendix B in particular) for one example that includes an overview of waves in periodic media.

Work with periodicity is usually discussed in the form of periodic lattices due to photonic crystals and their periodic atomic lattices. The work in this thesis considers periodic and quasiperiodic structures with inclusions positioned on the lattice nodes, so this lattice notation will be used.

In general, define any position on the lattice with $\mathbf{r}$, and denote the period by $\mathbf{R}$. Define some periodic function on the lattice by $f(\mathbf{r})$ which must satisfy

$$f(\mathbf{r}) = f(\mathbf{r} + \mathbf{R}). \tag{2.64}$$

Consider the periodic function $f(\mathbf{r})$ to be composed of plane waves of varying wave vector. Take the Fourier transform $F(\mathbf{R}^*)$, and redefine as

$$f(\mathbf{r}) = \int F(\mathbf{R}^*) e^{i\mathbf{R}^*\cdot\mathbf{r}} d^3\mathbf{R}^*. \tag{2.65}$$

This gives

$$f(\mathbf{r} + \mathbf{R}) = \int F(\mathbf{R}^*) e^{i\mathbf{R}^*\cdot\mathbf{r}} e^{i\mathbf{R}^*\cdot\mathbf{R}} d^3\mathbf{R}^*. \tag{2.66}$$

Equations (2.65) and (2.66) can only satisfy (2.64) if

$$F(\mathbf{R}^*) = 0 \quad \text{or} \quad e^{i\mathbf{R}^*\cdot\mathbf{R}} = 1. \tag{2.67}$$

The former leads to trivial solutions, and hence the latter yields

$$\mathbf{R}^* \cdot \mathbf{R} = 2\pi n, \quad n \in \mathbb{Z}, \tag{2.68}$$

which defines the *reciprocal* lattice vectors $\mathbf{R}^*$.

The periodic function can now be defined as a sum of plane waves with periodic reciprocal lattice vector as the wave vector,

$$f(\mathbf{r}) = \sum_{\mathbf{R}^*} f(\mathbf{R}^*) e^{i\mathbf{R}^*\cdot\mathbf{r}}. \tag{2.69}$$

As one can see the direct lattice gives the periodicity of the medium, whilst the reciprocal lattice gives the periodicity of the waves propagating through the medium.

It is possible to formulate expressions for the reciprocal basis vectors in a straightforward manner. In 3D, let the direct lattice $\mathbf{R}$ be spanned by $\mathbf{d}_1$, $\mathbf{d}_2$ and $\mathbf{d}_3$, and the reciprocal lattice $\mathbf{R}^*$ by $\mathbf{d}_1^*$, $\mathbf{d}_2^*$ and $\mathbf{d}_3^*$. Then equation (2.68) becomes

$$(l_1\mathbf{d}_1 + l_2\mathbf{d}_2 + l_3\mathbf{d}_3) \cdot (m_1\mathbf{d}_1^* + m_2\mathbf{d}_2^* + m_3\mathbf{d}_3^*) = 2\pi n, \tag{2.70}$$

for $l_i, m_i, n \in \mathbb{Z}$ and $i = 1, 2, 3$, which can be satisfied if the reciprocal lattice basis vector $\mathbf{d}_i^*$ is defined such that

$$\mathbf{d}_i \cdot \mathbf{d}_j^* = 2\pi\delta_{ij}, \tag{2.71}$$

where δ_{ij} is the Kronecker delta.

Exploiting one of the qualities of the cross product

$$\mathbf{x} \cdot (\mathbf{x} \times \mathbf{y}) = 0 \quad \forall \mathbf{x}, \mathbf{y}, \tag{2.72}$$

allows the reciprocal lattice basis vectors to be expressed as

$$\mathbf{d}_1^* = \frac{2\pi\mathbf{d}_2 \times \mathbf{d}_3}{\mathbf{d}_1 \cdot (\mathbf{d}_2 \times \mathbf{d}_3)}, \quad \mathbf{d}_2^* = \frac{2\pi\mathbf{d}_3 \times \mathbf{d}_1}{\mathbf{d}_1 \cdot (\mathbf{d}_2 \times \mathbf{d}_3)}, \quad \mathbf{d}_3^* = \frac{2\pi\mathbf{d}_1 \times \mathbf{d}_2}{\mathbf{d}_1 \cdot (\mathbf{d}_2 \times \mathbf{d}_3)}, \tag{2.73}$$

or

$$\mathbf{D}^* = 2\pi(\mathbf{D}^T)^{-1}, \tag{2.74}$$

where $\mathbf{D}$ and $\mathbf{D}^*$ are 3×3 matrices with the respective basis vectors as columns.

With the defined reciprocal lattice vectors the entire problem can be reduced to one periodic cell. The expression for a plane wave satisfies

$$e^{i\mathbf{k}\cdot\mathbf{R}} = e^{i(\mathbf{k}+\mathbf{R}^*)\cdot\mathbf{R}}. \tag{2.75}$$

By the definition of the reciprocal lattice, both sides of the equation relate to the same mode. Thus the range of the wavenumber $\mathbf{k}$ can be restricted to a finite volume in the reciprocal space in which one part of the volume cannot be reached from the other by adding some linear commination in $\mathbf{R}^*$. The finite volume is called the first *Brillouin zone*. To construct the Brillouin zone around the origin of the reciprocal lattice for example, one must construct perpendicular bisectors of every reciprocal lattice vector from the origin. The intersection of all these bisectors encompass a volume that includes the origin point and determines the restircted zone.

The simplest example to illustrate the construction of a Brillouin zone in 2D is a square lattice. The direct lattice is spanned by $\mathbf{d}_1 = a\mathbf{e}_1$, $\mathbf{d}_2 = a\mathbf{e}_2$, therefore

the reciprocal lattice is spanned by $\mathbf{d}_1^* = \frac{2\pi}{a}\mathbf{e}_1$, $\mathbf{d}_2^* = \frac{2\pi}{a}\mathbf{e}_2$, which is square too. By taking the perpendicular bisectors of neighbouring lattice vectors it is shown that the Brillouin zone of a square lattice is a square itself, as depicted in figure 2.12.

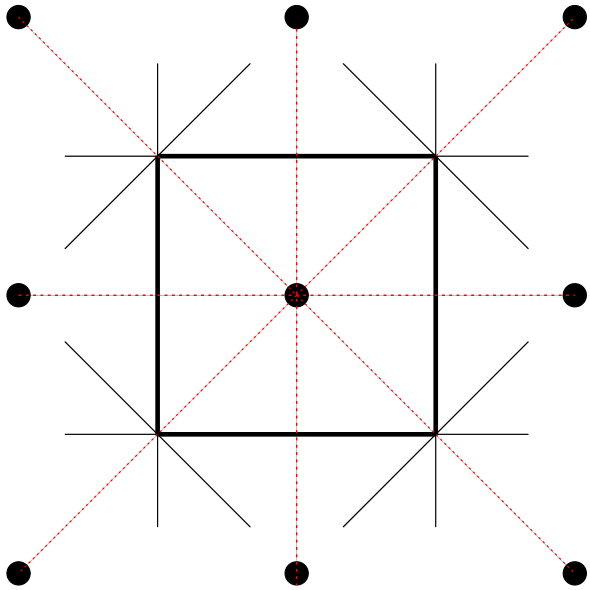

Figure 2.12: Construction of a Brillouin zone for a 2D square reciprocal lattice. Dashed lines (red) show the lines from the node to its neighbours, thin lines show the perpendicular bisectors, thick lines show the perimeter of the Brillouin zone, a square.

If there is rotational, mirror or inversion symmetry in the direct lattice then this is seen in the Brillouin zone too. The smallest region within the Brillouin zone for which the $\mathbf{k}$ are not related is called the *irreducible Brillouin zone*. The irreducible Brillouin zone for the square lattice can be seen in figure 2.13 in blue.

With this understanding of the periodicity in both the direct lattice spatially, and in the reciprocal lattice with the frequency, *Bloch's theorem* can be applied. The basic idea behind Bloch's theorem is that the wave propagation in each unit cell will be of the same form with an additional phase shift, thus one can solve the problem in a unit cell to get the solution for the infinite plane. For example, for acoustic problems governed by the scalar wave equation

$$\left(\nabla^2 + k^2\right) u(\mathbf{r}) = 0. \tag{2.76}$$

Periodicity within a structure with period $\mathbf{R}$ results in an expression for the field that satisfies

$$u(\mathbf{r} + \mathbf{R}) = u(\mathbf{r}) e^{i\boldsymbol{\gamma}\cdot\mathbf{R}}, \tag{2.77}$$

where $\boldsymbol{\gamma}$ is the Bloch wave vector and is restricted to the irreducible Brillouin zone.

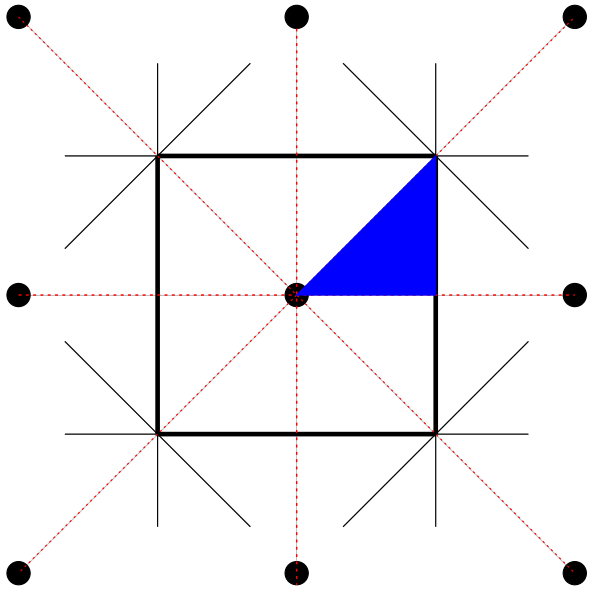

Figure 2.13: Construction of the irreducible Brillouin zone for a 2D square lattice. Dashed lines (red) show the lines from the node to its neighbours, thin lines show the perpendicular bisectors, thick lines show the perimeter of the Brillouin zone, blue area show the irreducible Brillouin zone.

The solution for the field $u(\mathbf{r})$ for all $\mathbf{r}$ is determined whilst only considering $\mathbf{r}$ in the reduced zone. How the solution is determined depends on the problem in hand. Bloch's theorem is applied to many scenarios within this thesis. We refer the reader to sections 2.3.2 and 2.4.4 for examples that can be discussed once further background has been given.

Section 2.3.2 discusses the derivation of the solution for an infinite periodic structure in 1D. The specific scenario is that of an infinite string with point scatterers that are periodically distributed. The field in each period is of the form (2.77) with left and right travelling waves related to other periodic cells by a phase shift.

Section 2.4.4 applies Bloch's theorem to a 2D doubly periodic distribution of circular cylinders with rectangular periodic cell. In chapter 7 the formulation is simplified by considering the small cylinder scenario, i.e. for $0 < ka \ll 1$. For this arrangement the problem can be reduced to a single equation in which the effective wavenumber can be determined in the particular domain of the reduced Brillouin zone.

2.2.3 Wave scattering by quasiperiodic media

In this section some of the existing literature regarding wave propagation in quasiperiodic media is discussed. Investigations vary in the type of waves, variety of quasiperiodic structure, method, motivation and application. A brief overview is given, with the main focus on work relating to that of this thesis.

After crystals with quasiperiodic atomic structures were discovered in 1984 (see section 2.1.1) the concept of wave propagation through particular quasiperiodic structures was initiated. Most preliminary investigations considered the propagation of light waves through such structures due to the dimensions of the crystals and the wavelength of light.

The first paper that aroused interest in the area was that of Kohmoto et al. in 1987 [44]. In the search for localised states analogous to Anderson localisation, this experimental investigation found interesting transmission properties of a 1D dielectric layered medium where the layers were determined by the Fibonacci chain.

Another experimental investigation, this time in acoustics, provided further inspiration. He and Maynard [36] considered a 2D Penrose lattice on which tuning forks were positioned in the centre of each rhombus as depicted in figure 2.14. The experiment relates to the 2D Schrödinger equation with a quasiperiodic potential. They observe band gaps with width related to the golden ratio τ.

Inspired by the results of Kohmoto et al. and He and Maynard, numerous other investigations to determine the band gaps of quasiperiodic media were conducted. Hattori et al. [35] experimentally explore the propagation of light waves through a 1D layered medium. Chan et al. [19] numerically determine the band gaps that arise due to dielectric rods positioned with a 2D octagonal tiling. Bayindir et al. [10], [11] perform experiments with dielectric rods positioned on the 2D Penrose tiling, extending their work to investigate waveguides due to line defects.

The progression of wave propagation in 1D quasiperiodic structures mainly incorporated layered materials and the use of techniques such as the transfer matrix method [81], [32], [43], [73], [20], [65]. These references cover a range of types of wave propagation, including elastic, light and sound.

Research involving wave propagation in 2D quasiperiodic structures mainly consists of scatterers positioned on the vertices of different quasiperiodic lattices. Some

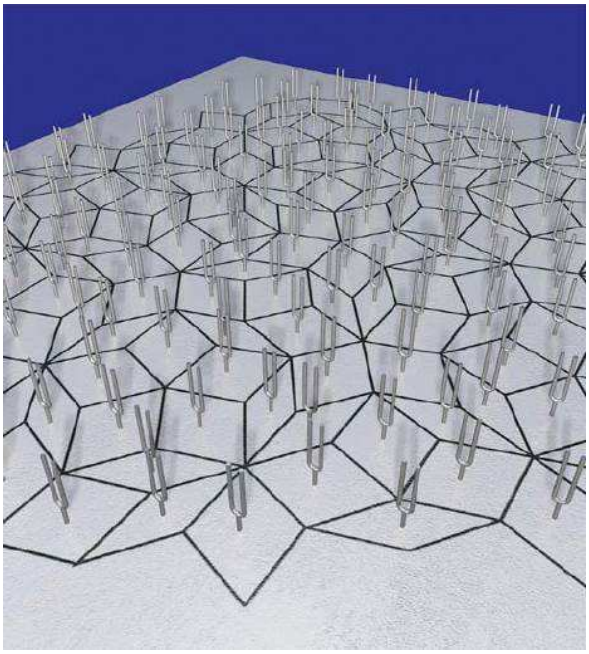

Figure 2.14: The set up for tunings forks with a Penrose lattice distribution. Image from [52].

examples of contributions are given in [46], [76], [75], [61], [29] and [56].

The work of Lai et al. [46] investigates acoustic propagation through a 2D quasiperiodic structure with 12-fold symmetry. The similarities of this investigation and that of this thesis is that the structure is a composite of aluminium cylinders in air and the authors use multiple scattering theory to solve the wave equation in 2D. The goal of their investigation was to predict the band gaps of infinite quasiperiodic structures numerically using a large but finite structure. In section 2.4 it is shown how to determine the solution for the scattered field with N arbitrary positioned small cylinders using the multipole method (a common method used in multiple scattering which will be discussed later). The computation involves numerically inverting an $N \times N$ matrix. For a large number of cylinders the matrix inversion can become computationally expensive and thus Lai et al. employ the sparse matrix canonical grid method (SPCGM). The SPCGM is applied to reduce computation by simplifying the calculations of the interactions between cylinders that have a large distance between them. The approach taken in their investigation could be utilised for future extensions of the work in this thesis.

Numerous investigations conducted by Steurer, his colleagues and his PhD student Sutter-Widmer [73], [76], [75] provide a great inspiration for the work in this thesis.

They consider the photonic and phononic band gap structures for a multitude of 1D and 2D quasiperiodic structures. Sutter-Widmer suggests that this work is of interest due to its "*(peculiar)*^{2} *nature*", the "squared" as a result of the peculiarities of both phononic crystals and quasicrystals! The mathematical method applied by these authors to solve the 2D wave equation is the finite difference time domain (FDTD) technique. The FDTD technique discretises the wave field in space and time and allows a numerical stepwise approximation of the propagation of the wave. It provides a flexible tool for the authors to compare the scattering of multiple quasiperiodic structures. The goal of these investigations was to determine the pseudo-Brillouin zones of the quasiperiodic structure as perturbation of the Brillouin zones of a periodic structure. The periodic structures they choose to analyse are periodic average structures (PAS), introduced in section 2.1.3. The period of the PAS is determined by the diffraction pattern (or Fourier transform, as discussed in section 2.1.1) of the quasiperiodic lattice.

Sutter-Widmer finds that the PAS defined for the 2D Penrose tiling does not provide an accurate representation of the Penrose lattice when circular cylinders are positioned on the lattice nodes. Figure 2.15 is taken from [73] and shows the differences in the two lattices and in the transmission in dB of the Penrose tiling (black) and its PAS (red) for a range of frequencies. It can be seen that the PAS is not capturing the same scattering properties as the Penrose tiling. In another paper however, Sutter-Widmer [75] shows that for the Penrose tiling, the resemblance between the scattering from the Penrose tiling and the PAS improves when the scatterer shape is changed to a star-shaped cylinder.

In this thesis we continue the investigation of the PAS lattice of circular cylinders as a periodic approximation of quasiperiodic lattices. We use the multipole method to compute the scattered field from the different structures and form further comparisons. Comparisons are also made between the quasiperiodic lattices and its approximant lattice (see section 2.1.4) as an alternative periodic approximation. To our knowledge, little research has been conducted in the field of wave propagation through approximant structures, and none to compare the quality of approximation between the PAS and the approximant.

In 2009, Florescu et al. [29] investigated the electromagnetic band gap structure of infinite periodic approximants. The authors compute the band gap structures for

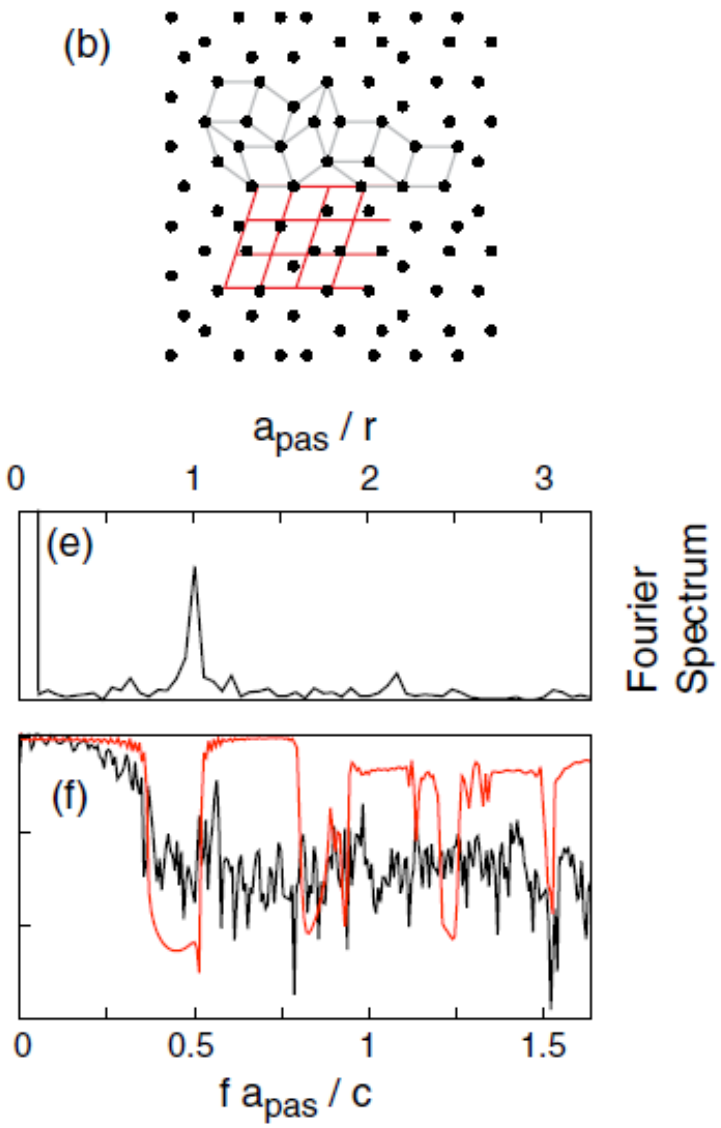

Figure 2.15: Section of Penrose tiling (black) and its rhombic PAS (red). The Fourier spectrum of the Penrose tiling. Transmission through the Penrose tiling (black) and its PAS (red). Image from [73].

infinite quasiperiodic structures using the plane-wave expansion (PWE) method. The PWE assumes periodicity which is not a feature of a quasiperiodic lattice. To overcome this hurdle Florescu et al. use sequences of increasingly accurate approximants to represent the quasiperiodic structure. The approximants contain the periodicity required whilst retaining information of the quasiperiodic lattice within the period. Florescu et al. see a convergence of the bandgaps for increasing size of approximant which suggests the approximants represent the fully quasiperiodic structure. They find that certain constructions of dielectric materials with quasiperiodic distributions give rise to reasonable sized band gaps. Although these band gaps are not as large as those

for standard periodic crystal structures, they find that some are highly isotropic,i.e. a stop band for the full irreducible Brillouin zone. These characteristics suggest that quasiperiodic materials may offer advantages over traditional periodic materials in applications. Florescu et al. offer examples of applications for example isotropic thermal radiation sources, where quasicrystals would provide more isotropic band gaps over periodic crystals.

The concept of an approximant as a periodic approximation of a quasiperiodic structure will be investigated in this thesis. The convergence of the bandgaps is considered as with Florescu et al. but finite lattices are also considered and direct comparisons of the scattered fields from approximant, PAS and quasiperiodic structures are formed.

2.3 One-dimensional wave scattering: point scatterers on a string

Within this thesis wave propagation through quasiperiodic arrays of scatterers in both 1D and 2D is considered. This section introduces the reader to the particular 1D scattering scenario under consideration: wave propagation along a 1D infinite string with point scatterers with particular distributions. Wave propagation is analysed in terms of the reflection and transmission of an incident wave from a finite distribution of scatterers. In the instance of an infinite number of scatterers with periodic distribution, the wave propagation is analysed in terms of *pass and stop bands*, i.e. frequency regimes in which waves can and cannot propagate.

For the formulation of the 1D problem consider a string of infinite extent in the x-direction, with density ρ and tension F. Along the 1D string distribute point scatterers of mass m. Assuming that there is no loading force on the string, the problem is governed by the homogeneous wave equation in 1D

$$\frac{\partial^2 y}{\partial x^2} = \frac{1}{c^2}\frac{\partial^2 y}{\partial t^2}, \tag{2.78}$$

where $c = \sqrt{\frac{F}{\rho}}$ is the wave velocity. See [33] for a derivation of the solution for harmonic waves, considering an initial time behaviour of the form $e^{-i\omega t}$,

$$y(x,t) = Ae^{-i(\omega t - kx)} + Be^{-i(\omega t + kx)}, \tag{2.79}$$

where the A and B are arbitrary constants symbolising the amplitudes of the right and left travelling waves, respectively, ω is the radial frequency of the wave, and k is the wavenumber of the wave.

Before proceeding, it is convenient to first non-dimensionalise on the wavenumber of the string by letting

$$X = kx, \tag{2.80}$$

and omitting time harmonic dependence, $y(x,t) = e^{-i\omega t}Y(X)$ for clarity. The solution (2.79) is now of the form

$$Y(X) = Ae^{iX} + Be^{-iX}. \tag{2.81}$$

2.3.1 One point scatterer

To illustrate how solutions for the wave propagation through arbitrary distributions of point scatterers in 1D are determined the method to analyse the wave scattering by one point scatterer positioned at the origin is initially discussed. This may seem trivial, but it is of great importance as it forms the basis of the analysis in 1D in this thesis. The results gained from the investigations in this section are the reflection and transmission coefficients across one discontinuity, R_1 and T_1 respectively. As the progression is made to scenarios with numerous scatterers with arbitrary positions, the reflection and transmission coefficients are determined recursively; thus, the results in this section are fundamental to the rest of the work in 1D.

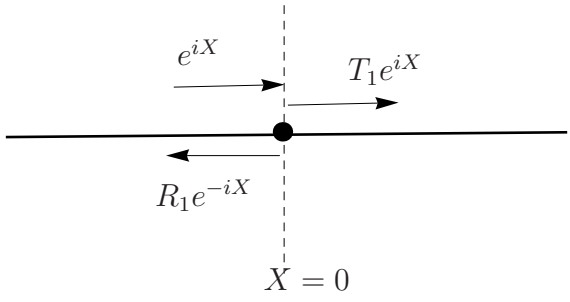

Figure 2.16: The set up for a single point scatterer on an infinite string.

Assume that a wave of unit amplitude is incident on the scatterer from the left, $u_{inc} = e^{iX}$. Use the form of the solution given in (2.81) to define the field to the left

and the right of the point scatterer at $X = 0$,

$$Y(X) = \begin{cases} e^{iX} + R_1 e^{-iX} & X \leq 0, \\ T_1 e^{iX} & X \geq 0, \end{cases} \tag{2.82}$$

i.e. to the left of the scatterer the wave is a composition of the incident and reflected wave, and to the right the transmitted. The boundary conditions on the scatterer at $X = 0$ are due to continuous displacement at the point scatterer, i.e.

$$e^{iX} + R_1 e^{-iX} = T_1 e^{iX}, \text{ at } X = 0, \tag{2.83}$$

and a change in slope due to the forces, i.e.

$$\frac{dY(X \to 0^+)}{dX} - \frac{dY(X \to 0^-)}{dX} = -\frac{m\omega^2}{Fk} Y(X = 0) \tag{2.84}$$

$$= -M\epsilon Y(X = 0), \tag{2.85}$$

where $\epsilon = kp$ and p are some arbitrary non-dimensional and dimensional lengthscales, respectively, $c = \frac{\omega}{k}$ and $M = \frac{m}{m_0} = \frac{m}{\rho p}$. Solving the simultaneous equations (2.83) and (2.85) with (2.82), one finds that the reflection and transmission coefficients due to a single point scatterer on a string are

$$R_1 = \frac{M\epsilon i}{2 - M\epsilon i}, \quad T_1 = \frac{2}{2 - M\epsilon i}. \tag{2.86}$$

The reflection and transmission coefficients R_1 and T_1 will be referred to throughout the recursive work for multiple point scatterers in section 4.

One point scatterer positioned away from the origin

For a point scatterer positioned at $X = A$ rather than the origin, then the formulation of the problem is altered slightly. In fact, the solutions (2.86) must be multiplied by a phase shift. The phase shift factor is due to the phase of the wave that is incident on the point scatterer. The derivation of this phase difference will now be discussed.

Define the scatterer location as $\bar{X} = A$. Thus in terms of the previous scatterer position $X = 0$, there is the relationship $X = \bar{X} - A$. The equations for the wave behaviour are now of the form

$$Y(\bar{X}) = \begin{cases} e^{i(\bar{X}-A)} + R_1 e^{-i(\bar{X}-A)} & \bar{X} \leq A, \\ T_1 e^{i(\bar{X}-A)} & \bar{X} \geq A. \end{cases} \tag{2.87}$$

To make future calculations simpler it is best to have the incoming wave of unit amplitude, therefore without loss of generality, multiply all in (2.87) by e^{iA} giving

$$Y(\bar{X}) = \begin{cases} e^{i\bar{X}} + R_1 e^{-i\bar{X}} e^{2iA} & \bar{X} \leq A, \\ T_1 e^{i\bar{X}} & \bar{X} \geq A. \end{cases} \tag{2.88}$$

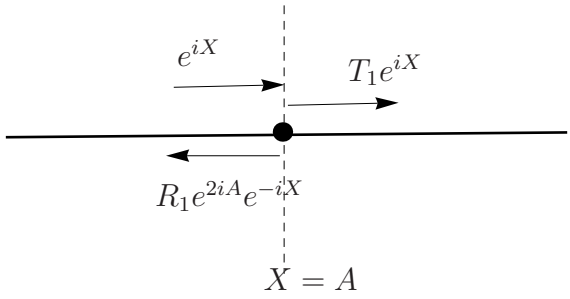

Figure 2.17: Modifications to the reflected and transmitted wave with a change in position of the scatterer from $X = 0$ to $X = A$.

Similarly, consider the case when the scatterer is at $\bar{X} = A$ but with an incident left-travelling wave. The wave field for a left-travelling wave incident on a scatterer at $X = 0$ is, by symmetry,

$$Y(X) = \begin{cases} T_1^o e^{-iX} & X \leq 0, \\ e^{-iX} + R_1^o e^{iX} & X \leq 0. \end{cases} \tag{2.89}$$

A superscript o notation has been used when the incident wave is coming from the opposite direction, i.e. a left-travelling incident wave.

Analogous to the right-propagating case above, for a scatterer at $\bar{X} = A$, the field can be expressed as

$$Y(\bar{X}) = \begin{cases} T_1^o e^{-i\bar{X}} & \bar{X} \leq A, \\ e^{-i\bar{X}} + R_1^o e^{i\bar{X}} e^{-2iA} & \bar{X} \leq A. \end{cases} \tag{2.90}$$

The two scenarios of a scatterer at $X = A$ and a right or left travelling incoming wave are depicted in figures 2.17 and 2.18, respectively.

It can be seen, by comparison of the transmission and reflection coefficients determined in (2.82) and (2.89) for a point scatterer at $X = 0$ with those in (2.88) and (2.90) for a scatterer at $X = A$, that the transmission coefficient remains the same but the reflection coefficient must be multiplied by a phase factor $e^{\pm 2iA}$ for incident waves from the left and right respectively.

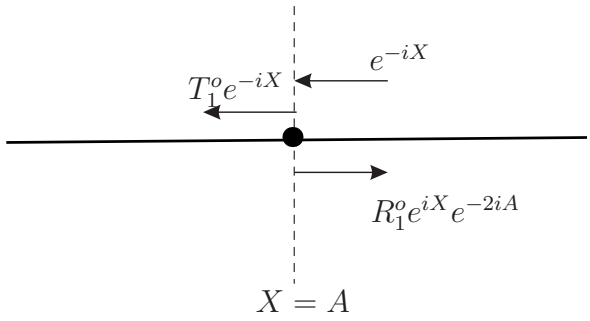

Figure 2.18: Modifications to the reflected and transmitted wave with a change in position of the scatterer and incident left travelling wave.

2.3.2 An infinite periodic array of point scatterers

The scenario of an infinite string with infinitely many point scatterers with a periodic distribution is of great interest in 1D problems. This is because, with such a geometry it is possible to employ Bloch's theorem, as mentioned in section 2.2.2, to find an effective wavenumber for the string and scatterers. The effective wavenumber can be used to determine the *pass* and *stop band* frequencies which depend on the periodic separation and mass of the point scatterers. Pass and stop band frequencies are the frequencies at which waves are propagating or attenuating, i.e. wave propagation can and cannot occur respectively. In 1D, when in a stop band, all the wave is reflected, i.e. $T = 0$. These effective properties of the string and scatterers are then used in many other geometries as a comparison.

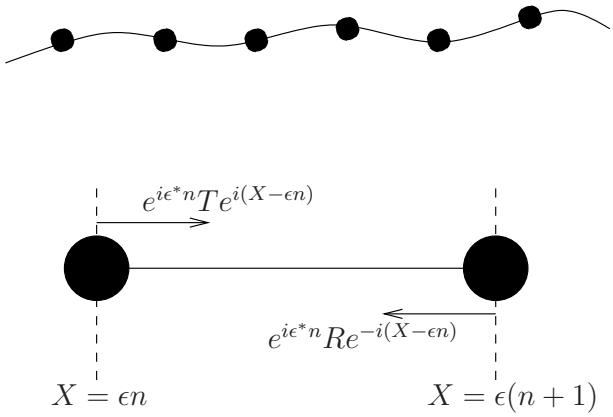

Figure 2.19: Structure of a string with infinitely many scatterers and a unit cell.

The approach applied in this section is an extension from [58] for layered media to point scatterers on a string. Consider an infinite string with point scatterers each of mass m placed a distance p from each other, with string density (mass/length) ρ

and tension F. Using the same non-dimensionalisation as in the one point scatterer problem, solutions can be posed for each periodic cell of the form

$$Y_n(X) = \begin{cases} u_{n-1}(X) & \epsilon(n-1) \leq X \leq \epsilon n, \\ u_n(X) & \epsilon n \leq X \leq \epsilon(n+1), \end{cases} \tag{2.91}$$

$$= \begin{cases} e^{i\epsilon^*(n-1)}(Re^{-i(X-\epsilon(n-1))} + Te^{i(X-\epsilon(n-1))}) & \epsilon(n-1) \leq X \leq \epsilon n, \\ e^{i\epsilon^* n}(Re^{-i(X-\epsilon n)} + Te^{i(X-\epsilon n)}) & \epsilon n \leq X \leq \epsilon(n+1), \end{cases} \tag{2.92}$$

where $\epsilon = kp$, and $\epsilon^* = k^*p$ are defined as the non-dimensional host and effective wavenumbers, respectively.

There are infinitely many boundary conditions of the same form as in the one point scatterer problem

$$u_{n-1}(\epsilon n) = u_n(\epsilon n), \tag{2.93}$$

$$\frac{\partial u_n(\epsilon n)}{\partial X} - \frac{\partial u_{n-1}(\epsilon n)}{\partial X} = -M\epsilon u_n(\epsilon n). \tag{2.94}$$

However, using the theories discussed in section 2.2.2, the general solution can be found by determining the solution in one unit cell, as depicted in figure 2.19. This gives the simultaneous equations

$$R(e^{-i(\epsilon^*+\epsilon)} - 1) = T(1 - e^{-i(\epsilon^*-\epsilon)}), \tag{2.95}$$

$$R(e^{-i(\epsilon^*+\epsilon)} - 1 - iM\epsilon) = T(e^{-i(\epsilon^*-\epsilon)} - 1 + iM\epsilon). \tag{2.96}$$

Upon solving for ϵ^* it is found that

$$\cos\epsilon^* = \cos\epsilon - \frac{M\epsilon\sin\epsilon}{2}. \tag{2.97}$$

The effective wavenumber in relation to the host string is $\frac{k^*}{k} = \frac{\epsilon^*}{\epsilon}$.

When there is an imaginary component in the effective wavenumber this results in decay in the wave, and thus the corresponding frequencies relate to a stop band. Therefore, plotting the real and imaginary components of the effective wavenumber will provide the pass and stop band frequencies. Figure 2.20 depicts this for an example with $M = 0.7$. The imaginary component of ϵ^* is zero except where the real component is constant. Consequently, the (blue solid) plot of the real component shows the propagating frequencies of the effective wavenumber and the (red dashed) plot of the

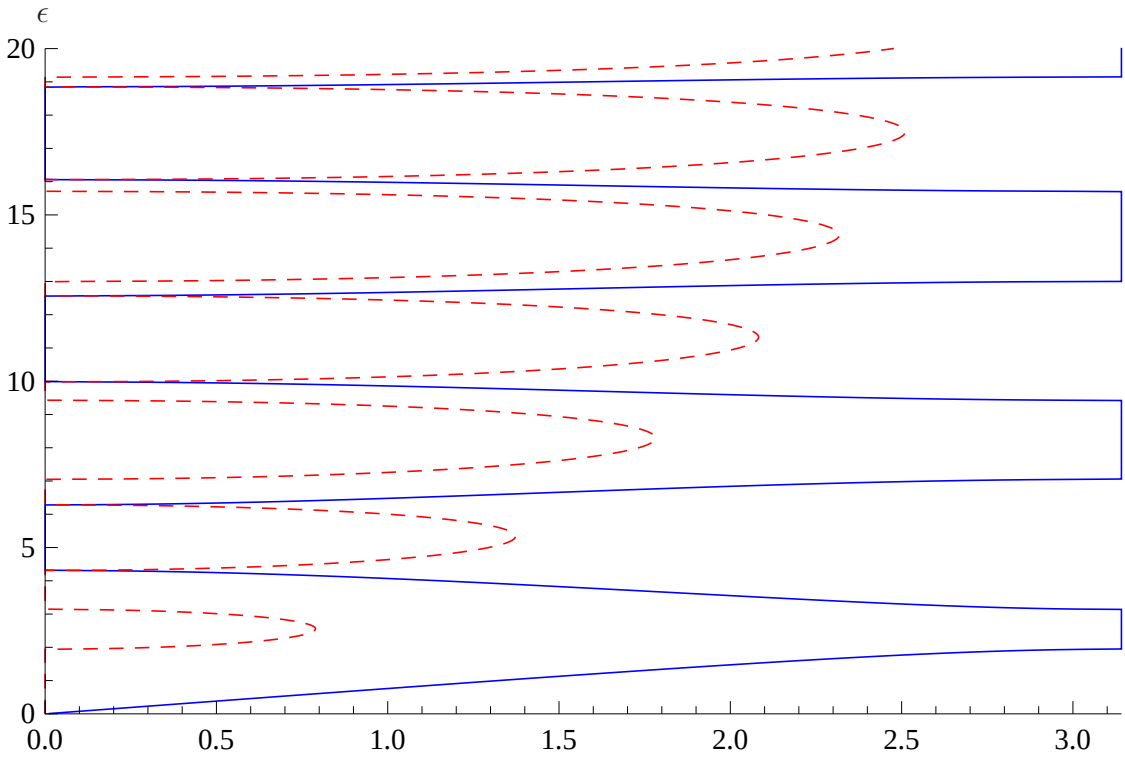

Figure 2.20: The magnitude of the real (blue solid) and imaginary (red dashed) components of ϵ^* for infinitely many periodic point scatterers with $M = 0.7$.

imaginary component depicts the stop bands. As one can also see from this figure, the size of the pass bands decrease as ϵ increases. The information gained with regards to the pass and stop bands for wave propagation through infinitely many periodic point scatterers can be used to draw comparisons with the finite case. Furthermore, it is possible to compare the propagation properties to non-periodic distributions of point scatterers. The comparison between the wave propagation through periodic structures as opposed to non-periodic structures facilitates the understanding of how introducing quasiperiodicity or randomness into a distribution of scatterers affects the stop and pass bands.

An extension of the method illustrated in this section is made in section 4.5, where point scatterers are distributed via the infinite periodic approximant. The approach remains the same as in this section, but the individual quasiperiodic periods add more complexity to the model.

2.4 Two-dimensional wave scattering: small cylinders in free space

This section introduces the reader to the particular 2D scattering scenario considered in this thesis: wave propagation through a medium composed of 2D circular scatterers in an acoustic region. The modelling of wave propagation in such a geometry is extensive in the literature and employs *multiple scattering theory*.

One method used in multiple scattering theory is the *multipole method*, which is especially effective for a finite array of circular scatterers. The multipole method solves for the displacement by summing the scattered waves from each obstacle, giving an exact solution as a system of simultaneous algebraic equations [50]. It is the 2D generalisation of the 1D multiple scattering system posed in (2.49) and (2.50). This section begins by considering cylinders with arbitrary radii a, but will be simplified by making an assumption of a small radii, i.e. $0 < ka \ll 1$, for reasons explained later. We will begin with analysis of the scattering from one cylinder to introduce notation and ideas, then extend to two and N cylinders.

2.4.1 One cylinder

Consider a circular cylinder of radius a positioned with its cross sectional circular centre at the origin in the (x, y) plane. An incident plane wave with angle of incidence α from the horizontal is of the form

$$u_{inc} = e^{ik(x\cos\alpha + y\sin\alpha)} = e^{ikr\cos(\theta-\alpha)}, \tag{2.98}$$

where (r, θ) are the plane polar coordinates, such that $x = r\cos\theta$ and $y = r\sin\theta$. The generating function for $J_n(z)$, the Bessel function of the first kind, is

$$e^{\frac{1}{2}z(t-t^{-1})} = \sum_{n=-\infty}^{\infty} t^n J_n(z). \tag{2.99}$$

Taking $t = ie^{i(\theta-\alpha)}$, one obtains the sum known as the *Jacobi expansion*, which can be used to re-express the incident field in (2.98) as

$$u_{inc} = e^{ikr\cos(\theta-\alpha)} = \sum_{n=-\infty}^{\infty} i^n J_n(kr)e^{in(\theta-\alpha)} = \sum_{n=0}^{\infty} \epsilon_n i^n J_n(kr)\cos n(\theta-\alpha), \tag{2.100}$$

where ϵ is the Neumann factor

$$\epsilon_n = \begin{cases} 1, & n = 0 \\ 2, & n \geq 1. \end{cases} \tag{2.101}$$

The 2D wave equation can rewritten in the time-independent form, omitting $e^{-i\omega t}$ for brevity, of the homogeneous Helmholtz equation

$$(\nabla^2 + k^2)u = 0, \tag{2.102}$$

which has separated solutions of the form

$$J_n(kr)e^{\pm in\theta}, \text{ and } Y_n(kr)e^{\pm in\theta}, \tag{2.103}$$

with $Y_n(kr)$ the Bessel function of the second kind. The Bessel functions can be combined as follows

$$\left(J_n(kr) + Y_n(kr)\right) e^{\pm in\theta} = H_n^{(1)}(kr)e^{\pm in\theta}, \tag{2.104}$$

where $H_n^{(1)}(kr)$ is the Hankel function of the first kind of order n. The expression in (2.104) satisfies the radiation condition at infinity (with the choice of time dependence) and is of a separable form similar to the incident wave. Therefore it can be used to pose a solution to the scattered field of the form

$$u_{sc} = \sum_{n=-\infty}^{\infty} i^n B_n H_n^{(1)}(kr)e^{in(\theta-\alpha)} = \sum_{n=0}^{\infty} \epsilon_n i^n B_n H_n^{(1)}(kr)\cos n(\theta - \alpha), \tag{2.105}$$

where the field is even about $\theta = \alpha$ and the coefficients B_n are determined by applying the boundary condition on the scatterer surface. The total field is now defined to be the sum of the incident and scattered fields

$$u(r, \theta) = u_{inc}(r, \theta) + u_{sc}(r, \theta). \tag{2.106}$$

Consider the cylinder to be 'sound-soft', i.e. Dirichlet boundary conditions on the radius of the cylinder,

$$u = 0 \text{ on } r = a. \tag{2.107}$$

Applying the boundary conditions to (2.106), it is found that

$$u = u_{inc} + u_{sc} = \sum_{n=0}^{\infty} \epsilon_n i^n \left[J_n(ka) + B_n H_n^{(1)}(ka)\right] \cos n(\theta - \alpha) = 0, \tag{2.108}$$

$$\Rightarrow B_n = -\frac{J_n(ka)}{H_n^{(1)}(ka)}. \tag{2.109}$$

So for $r \geq a$,

$$u(r,\theta) = \sum_{n=0}^{\infty} \epsilon_n i^n \left[J_n(kr) - \frac{J_n(ka)}{H_n^{(1)}(ka)} H_n^{(1)}(kr) \right] \cos n(\theta - \alpha). \tag{2.110}$$

If instead 'sound-hard' cylinders (Neumann boundary conditions) had been considered

$$\frac{\partial u}{\partial r} = 0 \text{ on } r = a, \tag{2.111}$$

then the coefficients would have been of the form

$$B_n = -\frac{J_n'(ka)}{H_n^{(1)'}(ka)}. \tag{2.112}$$

As mentioned in the introduction of this section, a simplification can be made by letting the radius a of these cylinders be small in comparison to the wavelength. Thus assume from now on that

$$0 < ka \ll 1. \tag{2.113}$$

This simplifies the expression for the field in (2.110) since the coefficients B_n will tend to some constant, as will be discussed now.

Referring to [4] (9.1.7-9.1.9), the limits for small arguments of the Bessel and Hankel functions are given by

$$J_n(ka) \sim \frac{(\frac{1}{2}ka)^n}{\Gamma(n+1)} = O((ka)^n), \tag{2.114}$$

$$H_0^{(1)}(ka) \sim 1 + \frac{2i}{\pi}\left(\gamma - \ln 2 + \ln(ka)\right) = O(\ln(ka)), \tag{2.115}$$

$$H_n^{(1)}(ka) \sim \frac{(\frac{1}{2}ka)^n}{\Gamma(n+1)} - i\frac{1}{\pi}\Gamma(n)\left(\frac{1}{2}z\right)^{-n} = O\left(\frac{1}{(ka)^n}\right), \quad n \neq 0, \tag{2.116}$$

where γ is Euler's constant and $\Gamma(n)$ is the gamma function. Substituting the limits into equation (2.109) gives, for small ka,

$$B_n \sim -\frac{J_n(ka)}{H_n^{(1)}(ka)} \sim -\frac{(ka)^n}{1/(ka)^n} = O((ka)^{2n}), \quad \text{for } n \neq 0, \tag{2.117}$$

$$B_0 \sim -\frac{J_0(ka)}{H_0^{(1)}(ka)} \sim -\frac{1}{1 + i\frac{2}{\pi}\left(\gamma - \ln 2 + \ln(ka)\right)} = O\left(\frac{1}{\ln(ka)}\right). \tag{2.118}$$

It can be seen that the term in equation (2.118) will be dominant in the limit $ka \to 0$, and thus

$$\sum_{n=-\infty}^{\infty} B_n \sim B_0 \sim -\frac{1}{1 + i\frac{2}{\pi}\left(\gamma - \ln 2 + \ln(ka)\right)}, \text{ as } ka \to 0. \tag{2.119}$$

Therefore, for a small cylinder radius, the scattered field in equation (2.105) has the asymptotic form

$$u_{sc} \sim -\frac{1}{1+\frac{2i}{\pi}\left(\gamma - \ln 2 + \ln(ka)\right)} H_0^{(1)}(kr), \quad ka \to 0. \tag{2.120}$$

This form of the scattered field in fact shows that the cylinder acts as a monopole source in this wave scattering problem. The expression for the scattered field from a small cylinder (2.120) will be used to extend this work to scenarios with N cylinders.

A comparison of equations (2.105) and (2.120) shows that the assumption of small scatterer radii simplifies the expression for the scattered field. An arbitrary sized cylinder has a scattered field involving an infinite sum over the order of the Hankel functions, whereas a small sound-soft cylinder produces a scattered field involving only a single Hankel function of order zero. The reduction of the infinite sum decreases computation time significantly. In this thesis, complexities are introduced through the distributions of the scatterers, therefore it is beneficial to make the single scattering problem as simple as possible. The case of an isotropic scatterer is also a realistic and relevant case, and is the discussion of the work by Foldy, as discussed in section 2.2.1. In future, once a better understanding of the quasiperiodic distributions has been formed, the work of this thesis can be extended to more general scatterer sizes and shapes.

One may notice at this point that the assumptions made are like those of Foldy [30], with a more thorough explanation behind the results. If sound-hard (Neumann) boundary conditions had been assumed, it can be shown via (2.112) that both the $n = 0$ and $n = 1$ order Hankel functions must be taken in the scattered field, at leading order. Thus, the cylinders would have acted as both monopole and dipole sources. This is something which Foldy does not mention.

2.4.2 Two cylinders

The approach to the calculation of the scattering from one cylinder is now extended to the problem with just two cylinders. This will allow an introduction of the ideas behind multiple scattering theory. Once the two cylinder problem has been fully explored, expressions can be formulated for the total field for a finite number of cylinders, with small radii.

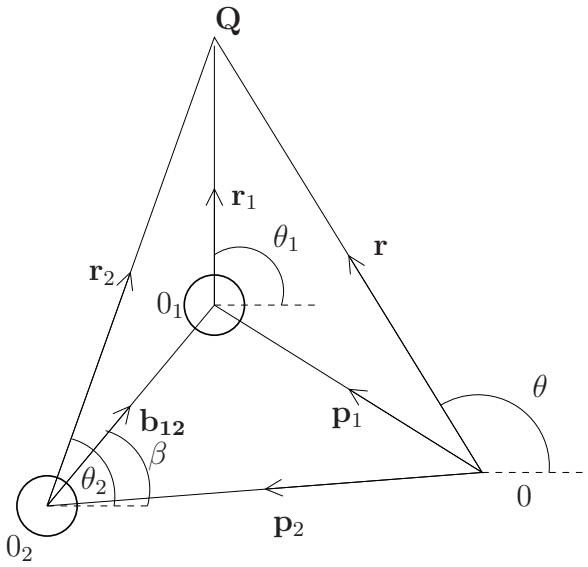

Figure 2.21: Set up of the two cylinders in which we want to consider wave scattering from.

In the case of one cylindrical scatterer of arbitrary radius, a solution was posed to the scattered field as in equation (2.105). For the case of two cylinders, a similar solution can be posed by expressing the scattered field as an infinite sum of multipoles at the centre of each circle.

$$u_{sc} = \sum_{n=-\infty}^{\infty} C_n^1 H_n^{(1)}(kr_1)e^{in(\theta_1-\alpha)} + \sum_{n=-\infty}^{\infty} C_n^2 H_n^{(1)}(kr_2)e^{in(\theta_2-\alpha)} \tag{2.121}$$

$$= \sum_{i=1}^{2} \sum_{n=-\infty}^{\infty} C_n^i H_n^{(1)}(kr_i)e^{in(\theta_i-\alpha)}, \tag{2.122}$$

where r_i, θ_i are the distance and angle of the ith cylinder from the observation point (local polar coordinates from the centre 0_i of each cylinder), and C_n^i are the unknown coefficients for each cylinder. See figure 2.21 for the configuration of this problem. In this figure, $\mathbf{Q}$ is the arbitrary observation point, and 0 is the origin.

The same small radius assumption is now employed as in the previous section, letting $ka \ll 1$. Equation (2.122) can be simplified using the reduction made previously for small radius in equation (2.120). The scattered field for two small cylinders can therefore be given simply by

$$u_{sc} \approx \sum_{i=1}^{2} C_i H_0^{(1)}(kr_i), \tag{2.123}$$

where $C_i = C_0^i$ for brevity. To find the C_i apply the boundary conditions on each

cylinder. Consider the sound-soft boundary conditions again,

$$u = 0, \text{ on } r_i = a, \tag{2.124}$$

where again the incident field is a plane wave and given by

$$u_{inc} = e^{ikr\cos(\theta-\alpha)}. \tag{2.125}$$

Since we are considering the situation $ka \ll 1$, when applying the boundary conditions at $r_j = a$ (i.e. $r = |\mathbf{p}_j| + a$) the incident wave takes the limit

$$u_{inc}(a) = e^{ik(|\mathbf{p}_j|+a)\cos(\theta-\alpha)} \to e^{ik(p_{jx}\cos\alpha + p_{jy}\sin\alpha)}, \text{ as } ka \to 0, \tag{2.126}$$

where $\mathbf{p}_j = (p_{jx}, p_{jy})$ is the location of the j^{th} cylinder. This limit can be used for u_{inc} when determining the C_i.

First, apply the boundary conditions at $r_1 = a$,

$$C_1 H_0^{(1)}(ka) + C_2 H_0^{(1)}(kr_2) = -u_{inc}(a) = -e^{ik(p_{1x}\cos\alpha + p_{1y}\sin\alpha)}. \tag{2.127}$$

Simplify further by rewriting r_2 as a function of r_1 and b_{12}, the distance between the two cylinders,

$$\begin{aligned} r_2 =& |\mathbf{r}_2| = |\mathbf{b_{12}} + \mathbf{r}_1| \\ &= \left[(b_{12}\cos\beta + r_1\cos\theta_1)^2 + (b_{12}\sin\beta + r_1\sin\theta_1)^2\right]^{1/2}, \end{aligned} \tag{2.128}$$

depicted figure 2.21. Considering kr_2 when $r_1 = a$ and letting $ka \to 0$,

$$kr_2 = k\left[(b_{12}\cos\beta + a\cos\theta_1)^2 + (b_{12}\sin\beta + a\sin\theta_1)^2\right]^{1/2} \to kb_{12}, \text{ as } ka \to 0. \tag{2.129}$$

An alternative derivation of this is shown in Appendix B.1 using Graf's addition theorem, for completeness.

By also considering the limit of $H_0^{(1)}(ka)$ for small ka, equation (2.127) becomes

$$C_1\left(1 + \frac{2i}{\pi}\left(\gamma - \ln 2 + \ln(ka)\right)\right) + C_2 H_0^{(1)}(kb_{12}) = -e^{ik(p_{1x}\cos\alpha + p_{1y}\sin\alpha)}. \tag{2.130}$$

Proceeding in the same way at the other boundary $r_2 = a$ gives the matrix equation

$$\begin{aligned} &\begin{pmatrix} 1 + \frac{2i}{\pi}\left(\gamma - \ln 2 + \ln(ka) + \frac{\pi}{2i}\right) & H_0^{(1)}(kb_{12}) \\ H_0^{(1)}(kb_{12}) & 1 + \frac{2i}{\pi}\left(\gamma - \ln 2 + \ln(ka) + \frac{\pi}{2i}\right) \end{pmatrix} \begin{pmatrix} C_1 \\ C_2 \end{pmatrix} \\ &= -\begin{pmatrix} e^{ik(p_{1x}\cos\alpha + p_{1y}\sin\alpha)} \\ e^{ik(p_{2x}\cos\alpha + p_{2y}\sin\alpha)} \end{pmatrix}. \end{aligned} \tag{2.131}$$

The matrix equation can easily be solved to determine the coefficients C_1 and C_2. The total field is then given by

$$u(r,\theta) \approx u_{inc}(r,\theta) + C_1 H_0^{(1)}(kr_1) + C_2 H_0^{(1)}(kr_2). \tag{2.132}$$

Note here that the limit used in equation (2.129) due to the small radii allows the simplification of the expression of the field at one boundary independently of r. If the small radii limit was not taken then it is no longer possible to do the same simple step. In this situation one must use Graf's addition theorem in order to express the field in a global coordinate system rather than two (or more for the finite case) local coordinate systems. Graf's addition theorem is applied in appendix B.1, which demonstrates this approach.

2.4.3 N cylinders

This section discusses the formulation of the wave field scattered by a finite distribution of small cylinders. Extensions of the concepts discussed for one and two cylinders in the previous two subsections are made.

Consider an incident wave of the form in equation (2.125). The scattered field extends to being a sum over the N cylinders,

$$u_{sc} \approx \sum_{i=1}^{N} C_i H_0^{(1)}(kr_i), \tag{2.133}$$

for small cylinder radii. Applying sound-soft boundary conditions on the cylinders. At $r_j = a$, for $j = 1, \ldots, N$ we find,

$$C_j H_0^{(1)}(ka) + \sum_{\substack{i=1 \\ i\neq j}}^{N} C_i H_0^{(1)}(kr_i) = -e^{ik(p_{jx}\cos\alpha + p_{jy}\sin\alpha)}, \tag{2.134}$$

$$\Rightarrow C_j \left(1 + \frac{2i}{\pi}\left(\gamma - \ln 2 + \ln(ka) + \frac{\pi}{2i}\right)\right) + \sum_{\substack{i=1 \\ i\neq j}}^{N} C_i H_0^{(1)}(kb_{ij}) = -e^{ik(p_{jx}\cos\alpha + p_{jy}\sin\alpha)} \tag{2.135}$$

where $\mathbf{p}_j = (p_{jx}, p_{jy})$ is the position of the j^{th} cylinder as before and b_{ij} is the distance between the ith and jth cylinders. Considering (2.135) for $j = 1, \ldots, N$ determines a matrix equation as an extension from two to N cylinders of the form

$$\mathbf{HC} = -\mathbf{E}, \tag{2.136}$$

where

$$\mathbf{H}_{ij} = \begin{cases} 1 + \frac{2i}{\pi}\left(\gamma - \ln 2 + \ln(ka)\right), & i = j, \\ H_0^{(1)}(kb_{ij}) = H_0^{(1)}(kb_{ji}), & i \neq j, \end{cases} \tag{2.137}$$

$$\mathbf{C} = \begin{pmatrix} C_1 \\ \vdots \\ C_N \end{pmatrix}, \quad \mathbf{E} = \begin{pmatrix} e^{ik(p_{1x}\cos\alpha + p_{1y}\sin\alpha)} \\ \vdots \\ e^{ik(p_{Nx}\cos\alpha + p_{Ny}\sin\alpha)} \end{pmatrix}. \tag{2.138}$$

The total field is again the sum of the incident and scattered fields,

$$u(r,\theta) \approx u_{inc}(r,\theta) + \sum_{i=1}^{N} C_i H_0^{(1)}(kr_i). \tag{2.139}$$

For a large (but finite) number of scatterers the matrix $\mathbf{H}$ can easily be inverted numerically to find the coefficients C_i.

The matrix equation (2.136) is applicable for arbitrary finite distributions of small circular cylinders and will be used in all future investigations of wave propagation in finite arrays of cylinders in this thesis.

2.4.4 An infinite doubly-periodic array of cylinders

Wave propagation in 2D doubly-periodic infinite arrays of cylinders can be analysed in a similar manner to the approach used in section 2.3.2 for 1D. Bloch's theorem is applied to reduce the problem to one period of the array, or one irreducible Brillouin zone, and frequencies for the propagating modes can be determined.

Define a rectangular lattice with period d in the x-direction and λd in the y-direction, as depicted in figure 2.22. Non-dimensionalise lengthscales with respect to the wavenumber of the host free space wavenumber k, determining the parameters

$$\eta = ak \ll 1, \qquad \text{cylinder radius,} \tag{2.140}$$

$$D = dk, \qquad \text{spacing lengthscale,} \tag{2.141}$$

$$\mathbf{p}_{st} = D(s, \lambda t), \qquad \text{location of } (s,t)^{\text{th}} \text{ cylinder,} \tag{2.142}$$

$$\theta_{st} = \arg(\mathbf{x} - \mathbf{p}_{st}), \qquad \text{angle of vector from } (s,t)^{\text{th}} \text{ cylinder to observation point.} \tag{2.143}$$

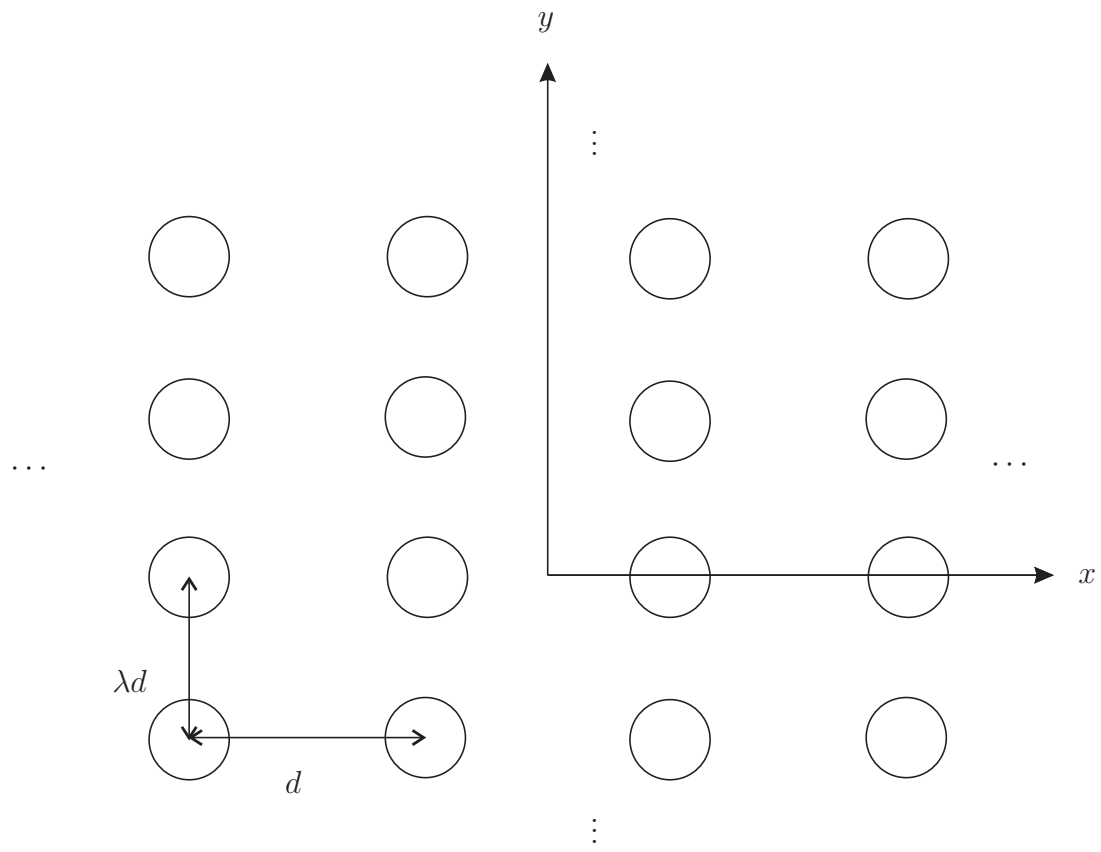

Figure 2.22: Set up of a doubly periodic array of circular cylinders.

For arbitrary sized circular cylinders, pose an eigensolution to the 2D Helmholtz equation in this set up of the form

$$u(\mathbf{x}) = \sum_{s=-\infty}^{\infty} \sum_{t=-\infty}^{\infty} \sum_{n=-\infty}^{\infty} C_n^{st} H_n^{(1)}(|\mathbf{x} - \mathbf{p}_{st}|) e^{in\theta_{st}}, \tag{2.144}$$

where the coefficients C_n^{st} are unknown. Due to the periodicity inherent in the geometry, Bloch's theorem can be applied to the unknown coefficients

$$C_n^{st} = C_n e^{i\gamma(s\cos\theta + \lambda t \sin\theta)}, \tag{2.145}$$

where $\gamma = |\boldsymbol{\gamma}| = |d\hat{\boldsymbol{\gamma}}|$, where $\boldsymbol{\gamma}$ and $\hat{\boldsymbol{\gamma}}$ are the non-dimensional and dimensional effective wavenumber, respectively.

As discussed in section 2.2.2 the effective wavenumber can be restricted to the frequencies within the irreducible Brillouin zone of the reciprocal space. Define the 2D direct lattice on which the circular scatterers lie by Λ. The lattice points $\mathbf{r}_{st} \in \Lambda$ are defined by

$$\mathbf{r}_{st} = sd\mathbf{e}_1 + t\lambda d\mathbf{e}_2. \tag{2.146}$$

Therefore the reciprocal lattice Λ^* contains reciprocal lattice points

$$\mathbf{r}^*_{st} = s\frac{2\pi}{d}\mathbf{e}_1 + t\frac{2\pi}{\lambda d}\mathbf{e}_2. \tag{2.147}$$

Restricting $\hat{\boldsymbol{\gamma}}$ to the triangular irreducible Brillouin zone of the reciprocal lattice (similar to that of figure 2.13), it is possible to represent the entire frequency space by

$$\hat{\boldsymbol{\gamma}}_{st} = \hat{\boldsymbol{\gamma}} + \mathbf{r}^*_{st}, \quad \text{or} \quad \boldsymbol{\gamma}_{st} = \boldsymbol{\gamma} + \mathbf{r}^*_{st} d. \tag{2.148}$$

The Bloch condition results in a simplification of the posed eigensolution of the form

$$u(\mathbf{x}) = \sum_{n=-\infty}^{\infty} C_n H_n^{(1)}(|\mathbf{x}|)e^{in\theta} \tag{2.149}$$

$$+ \sum_{s=-\infty}^{\infty} \sum_{\substack{t=-\infty \\ (s,t)\neq(0,0)}}^{\infty} \sum_{n=-\infty}^{\infty} C_n e^{i\gamma(s\cos\theta + \lambda t \sin\theta)} H_n^{(1)}(|\mathbf{x} - \mathbf{p}_{st}|)e^{in\theta_{st}}. \tag{2.150}$$

In this solution for the field in the 2D doubly-periodic array of scatterers there are three infinite sums inherent. Thus in this form, (2.150) is not computable exactly. The current main approaches to solving such a system are numerical, however some analytic approaches to determine a comparable computable expression have been made. Homogenisation is one technique, e.g. [59], that assumes $kd \ll 1$ and $a/d \ll 1$. Krynkin and McIver [45] [53] employ the method of matched asymptotic expansions to determine the field with restrictions $ka \ll 1$ and $a/d \ll 1$. Martin and Maurel [51] introduce integral representations of the Hankel function to reduce the system of equations with the assumptions $ka \ll 1$ and $k \simeq \gamma_{st}$. In this thesis we propose an alternative approach that only requires the small radius assumption $ka \ll 1$. This is discussed in detail in chapter 7.

Chapter 3

Construction algorithm for a one-dimensional quasiperiodic lattice and its periodic approximations

This chapter describes the *projection method* for the construction of a 1D quasiperiodic lattice known as a *Fibonacci chain*. The construction of two periodic lattices that approximate the quasiperiodicity within the Fibonacci chain is also discussed. Although numerous techniques for the construction of such lattices were discussed in section 2.1, this chapter concentrates on the method of projection from higher dimensions. The projection method is a rather complicated method to use in order to generate the 1D Fibonacci chain. However it is the ideal method for the construction of the approximant and to construct higher-dimensional quasiperiodic and approximant lattices. The projection method for the 2D Penrose lattice that is discussed in chapter 6 is difficult to visualise. By employing the projection method for the 1D analogue we introduce the reader to the method in a more manageable and intuitive way. The 2D to 1D projection method is described in full in this chapter, with numerous diagrams to assist the descriptions of the algorithms. When we extend to the projection from 5D and 4D to 2D in chapter 6 for the Penrose tiling, the method is analogous and so this chapter will provide the foundations required.

In the presentation of the background of the construction of quasiperiodic lattices

in section 2.1 it was shown that the projection method is a popular method. However, we have found that the literature does not provide a thorough explanation with enough of the required formulae for one to implement the method in a straightforward manner. Many of the references give only a brief discussion of the concept of the projection, or partially discuss the mathematics, or assume prior knowledge. The content of this chapter provides a stand-alone explanation of the method. The algorithm includes all relevant equations enabling mathematicians to apply this crystallographic method.

For a more experienced reader in this research area, a few differences in the approach used here to that in the literature may be noticed. The mathematical formulation of the projection differs from that in most references given in section 2.1, as it is based on the node positions in higher-dimensional space, rather than unit cells and their areas. The approach used to determine the selection of higher-dimensional lattice nodes for projection also differs from some of the literature. The definition of the acceptance windows is based upon a "decoration" of every lattice node with the window, whereas in the literature a common approach is to use a "strip". The two variations are equivalent in their outcomes but are mathematically different and are visualised differently. Figure 3.1 depicts both the acceptance windows (red lines) and the (grey) strip. The strip method is the one most applied in the literature, e.g. figure 2.7 taken from [39].

3.1 Fibonacci chain

The Fibonacci chain is a quasiperiodic structure in 1D that consists of two lengthscales L and S, where $L = \tau S$ and $\tau = \frac{1+\sqrt{5}}{2}$ is the golden mean. We introduced this structure in section 2.1.2 and briefly mentioned the three main construction methods: superposition, substitution and projection. In order to be able to extend the work from 1D structures to more complicated 2D quasiperiodic structures we will use the projection method. This method can be explained and visualised for the 1D chain which will make the extension to higher dimensions more straightforward.

In section 2.1.2 it was shown that the 1D quasiperiodic lattice can be created by projecting a 2D square lattice Λ to a 1D line. Only a selection $\mathcal{M}$ of the 2D lattice nodes Λ, which we denote by $\Lambda_{\mathcal{M}}$, should be projected. The selection of points $\mathbf{m} \in \mathcal{M}$,

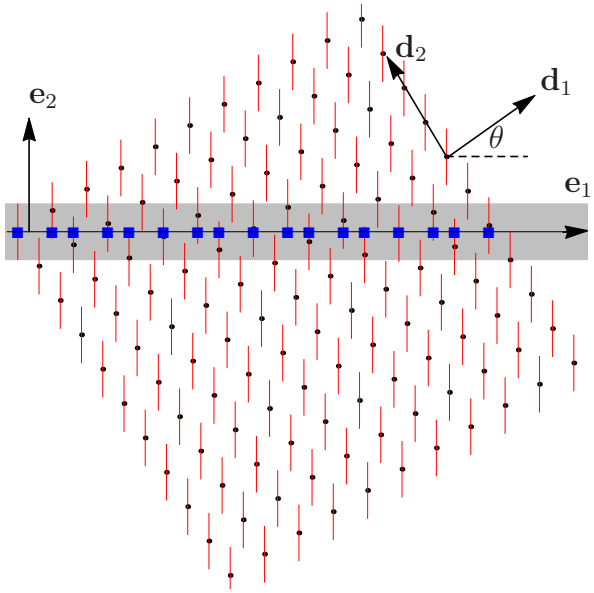

Figure 3.1: Depicting the projection method from a 2D square lattice to the 1D Fibonacci chain. We find the positions of the Fibonacci chain (blue squares along the horizonal) wherever we have an intersection of the acceptance windows (red lines) with the parallel space (horizontal line). Alternatively any 2D nodes that lie within the (grey) strip are projected to the parallel space.

where $\mathbf{m} = (m_1, m_2) \in \mathbb{Z}^2$, is determined via a set of acceptance windows which will be defined later in this section.

To construct the 1D Fibonacci chain it is necessary to project from a 2D square lattice to a 1D line. The 2D lattice must be rotated at some angle θ with respect to the 1D line. Define the 1D line to be the *parallel plane*, terminology which will translate to the higher-dimensional case. The 2D lattice nodes (black dots), parallel plane (black horizontal) and acceptance windows (red lines) are depicted in figure 3.1, generating the 1D Fibonacci chain (blue squares). To generate the Fibonacci chain, the 2D lattice must be inclined at an irrational angle θ from the parallel plane, where

$$\tan\theta = \frac{1}{\tau}. \tag{3.1}$$

Any other irrational angle would result in other aperiodic 1D lattices, but only this choice of θ results in the Fibonacci chain. One approach is to define the *parallel plane* to be the horizontal line spanned by $\mathbf{e}_1 = \begin{pmatrix} 1 & 0 \end{pmatrix}^T$ and then have the 2D square lattice rotated by θ in relation to the parallel plane. A square 2D unit lattice spanned by

$$\mathbf{d}_1 = \frac{1}{\sqrt{2+\tau}} \begin{pmatrix} 1 \\ -\tau \end{pmatrix}, \quad \mathbf{d}_2 = \frac{1}{\sqrt{2+\tau}} \begin{pmatrix} \tau \\ 1 \end{pmatrix}, \tag{3.2}$$

satisfies all of these constraints. Define the "plane" perpendicular to the parallel plane as the *perpendicular plane*. Again, in 2D these "planes" are in fact lines, but the terminology is defined with the extension to higher dimensions in mind. In this set up the *perpendicular plane* is the line spanned by $\mathbf{e}_2 = \begin{pmatrix} 0 & 1 \end{pmatrix}^T$.

The *acceptance window* used to determine the selection of 2D lattice nodes to be projected is a set of identical polytopes that are centred on each node. If the acceptance window intersects the parallel plane then that node is selected to be projected down to produce a Fibonacci node. The form of the polytope is determined by a projection of the so called "Voronoi cell" of the higher-dimensional lattice to the perpendicular space. The dimension of the polytope depends on the dimension of the perpendicular space. In the projection from 2D to 1D the *acceptance window* is a set of straight lines, of particular length, perpendicular to the parallel plane. We must define the Voronoi cell before we can formulate an expression for the acceptance window.

A *Voronoi cell* is the cell formed around a chosen lattice node by taking the perpendicular bisectors of every line from the the node to its neighbours in an analogous way to the Brillouin zone construction in section 2.2.2. The smallest such cell formed by the perpendicular bisectors is the Voronoi cell. The Voronoi cell associated with the unit square lattice case is very simple, as we show in figure 3.2, and is simply the unit square itself. The vertices of the unit square Voronoi cell associated with the

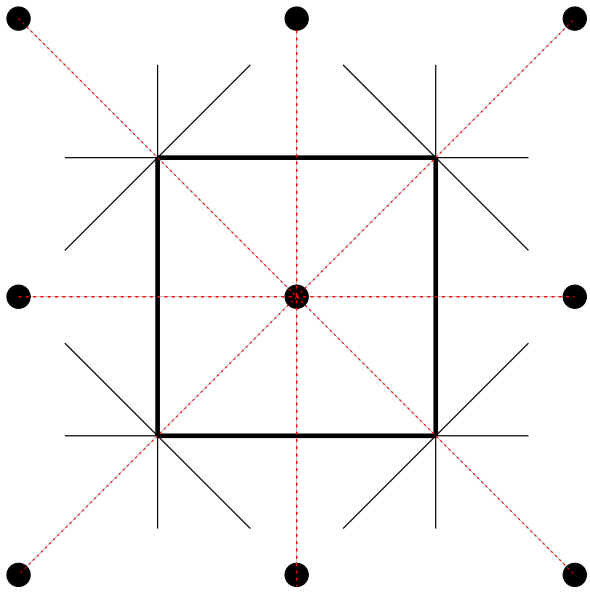

Figure 3.2: Construction of a Voronoi cell for a 2D square lattice. Dashed lines (red) show the lines from the node to its neighbours, thin lines show the perpendicular bisectors, thick lines show the Voronoi cell, a unit square.

lattice node at the origin can be defined by the position vectors

$$\mathbf{V}_2 = \sum_{i=1}^{2} n_i \mathbf{d}_i = \frac{1}{\sqrt{2+\tau}} \begin{pmatrix} n_1 + \tau n_2 \\ n_2 - \tau n_1 \end{pmatrix}, \tag{3.3}$$

where n_1, $n_2 \in \{-1/2, 1/2\}$.

To form the acceptance window the Voronoi cell is projected to the perpendicular space $\mathbf{e}_2$. The projected nodes are given by the $\mathbf{e}_2$ component of (3.3),

$$\mathbf{V}_2^{\perp} = \frac{1}{\sqrt{2+\tau}} \begin{pmatrix} 0 \\ n_2 - \tau n_1 \end{pmatrix}. \tag{3.4}$$

With the choice of n_1, $n_2 \in \{-1/2, 1/2\}$, this gives four points in a line. In general, the acceptance window associated with a higher-dimensional projection method is of the same dimension as the perpendicular space, and so is determined by the maximum area bounded by the projected Voronoi cell nodes. In the 2D to 1D projection method the projected Voronoi cell nodes are along one line, thus the "area" in this instance is the distance between the nodes. Two set of n_i give the maximum distance, $(n_1, n_2) = (-1/2, 1/2)$ and $(n_1, n_2) = (1/2, -1/2)$, i.e. $n_2 - \tau n_1 = \pm(1+\tau)/2$. These correspond to the lower and upper points respectively. Denote the acceptance window associated with the origin node in 2D by $\mathbf{W}_2$. The acceptance window for the origin 2D lattice node is given by

$$\mathbf{W}_2 = a\frac{1+\tau}{2\sqrt{2+\tau}}\mathbf{e}_2, \quad \text{for} \quad a \in (-1, 1]. \tag{3.5}$$

Note the open and closed intervals for a implying the window is exclusive and inclusive of the end points of the acceptance window, respectively. This is so that there is no overlapping of acceptance windows which would yield the inclusion of too many lattice nodes in $\Lambda_{\mathcal{M}}$.

The acceptance window defined in equation (3.5) is replicated on every 2D lattice node to give the full acceptance window of the 2D system which we call $\mathbf{A}_2$, and is defined as

$$\mathbf{A}_2 = \{m_1\mathbf{d}_1 + m_2\mathbf{d_2} + \mathbf{W}_2, \quad m_1, m_2 \in \mathbb{Z}\}. \tag{3.6}$$

The acceptance windows are depicted in figure 3.1 by the red lines. The grey strip shows the alternative method for the selection of nodes. It is a strip of equivalent height to the acceptance windows. We concentrate on the acceptance window method as it is mathematically easier to implement in higher dimensions.

The final stage of the projection method is to determine which acceptance windows intersect with the parallel space. The acceptance window is used to select its associated lattice node as a node to be projected if and only if the window intersects the parallel plane. That is if a node with position $m_1\mathbf{d}_1 + m_2\mathbf{d}_2$ has an associated acceptance window that intersects the parallel plane then $(m_1,\, m_2) \in \mathcal{M}$ and the lattice node is a part of the set

$$\Lambda_{\mathcal{M}} = m_1\mathbf{d}_1 + m_2\mathbf{d}_2, \quad (m_1, m_2) \in \mathcal{M}, \tag{3.7}$$

of selected lattice nodes for projection. To compute $\Lambda_{\mathcal{M}}$ determine the (m_1, m_2) for which the $\mathbf{e}_2$ component of $\mathbf{A}_2$ in equation (3.6) is zero, i.e. determine the (m_1, m_2) such that

$$\frac{1}{\sqrt{2+\tau}}\left(-\tau m_1 + m_2 + a\frac{1+\tau}{2}\right) = 0, \quad \text{for any} \quad a \in (-1, 1]. \tag{3.8}$$

This equation can be simplified to the following

$$-\frac{1+\tau}{2} < \tau m_1 - m_2 \leq \frac{1+\tau}{2}. \tag{3.9}$$

Once the set $\mathcal{M}$ of (m_1, m_2) that satisfy (3.9) has been determined it is possible to define the Fibonacci chain lattice points. Project the lattice points in $\Lambda_{\mathcal{M}}$ (3.7) to the parallel plane,

$$\mathbf{x}_{\text{Fib}} = \frac{1}{\sqrt{2+\tau}}\left(m_1 + \tau m_2\right)\mathbf{e}_1, \quad (m_1, m_2) \in \mathcal{M}, \tag{3.10}$$

Equation (3.10) gives the Fibonacci chain lattice positions along the parallel plane $\mathbf{e}_1$. The blue squares along the parallel plane in figure 3.1 depict a section of the Fibonacci chain lattice nodes.

In summary the projection method algorithm for the Fibonacci chain is as follows

- Construct a 2D square unit lattice subtended by the angle θ from the horizontal, defined in (3.2)
- Project a Voronoi cell to the perpendicular space to find the acceptance window associated with the origin node $\mathbf{W}_2$, defined in (3.5)
- Decorate every lattice node with the acceptance window to give the full set $\mathbf{A}_2$, defined in (3.6)

- Find the integer pairs $(m_1, m_2) \in \mathcal{M}$ which allow the intersection of $\mathbf{A}_2$ with the parallel plane to determine the selection of lattice nodes $\Lambda_{\mathcal{M}} = m_1\mathbf{d}_1 + m_2\mathbf{d}_2$ to be projected, defined in (3.9)

- Project this set of lattice nodes $\Lambda_{\mathcal{M}}$ to the parallel plane to determine the Fibonacci chain lattice nodes $\mathbf{x}_{\text{Fib}}$, (3.10).

This algorithm is inexpensive to run and large sections of the Fibonacci chain can be generated quickly.

We will later extend this method into higher dimensions in order to construct a 2D quasiperiodic lattice. It will no longer be possible to visualise every aspect of the algorithm; nevertheless, with the figures, definitions and step by step algorithm set out in this section, the extension is relatively straightforward.

3.2 Periodic average structure

The periodic average structure (PAS) is a periodic approximation of the quasiperiodic lattice with a period specifically chosen to represent its properties. As derived in section 2.1.3, in the 1D case the period $\bar{d}$ is chosen to be the average spacing of the Fibonacci chain and is given by

$$\bar{d} = (3 - \tau)S, \tag{3.11}$$

where S is the length of the small spacing in the Fibonacci chain. This lattice can be constructed simply with $\bar{\mathbf{d}} = \bar{d}\mathbf{e}_1$ as the basis vector of the 1D space. However, if we take advantage of the 2D space used in the higher-dimensional construction of the Fibonacci chain, we can gain further information that relates the PAS to the Fibonacci chain. This can aid in the understanding of how similar the two lattices are. The method was briefly discussed in section 2.1.3.

Consider a projection of the 2D square lattice nodes Λ defined earlier to the 1D PAS nodes $n\bar{\mathbf{d}}$, $n \in \mathbb{Z}$. The projection matrix chosen can also be used to project the acceptance windows $\mathbf{A}_2$, derived in the previous section (3.6). The projection of the acceptance windows results in discrete lengths in the 1D space around the PAS nodes which signify the maximum distance that the Fibonacci chain nodes can lie from the

PAS nodes. The smaller the area of this projected acceptance window, which we shall call the *occupancy window*, the more similar the lattices are.

Let us determine the projection matrix Π required to project the 2D lattice nodes to the 1D PAS. The projection matrix defined can then be applied to the acceptance windows. We wish to define a projection matrix Π such that

$$\Pi \cdot (m_1\mathbf{d}_1 + m_2\mathbf{d}_2) = n\bar{d}, \quad m_1, m_2, n \in \mathbb{Z}. \tag{3.12}$$

By the definition of the 2D square lattice we know that $\mathbf{d}_i \cdot \mathbf{d}_j = \delta_{ij}$, thus we can choose $\Pi = \alpha(\mathbf{d}_1 + \mathbf{d}_2)$, $\alpha \in \mathbb{R}$, and we require

$$\alpha(\mathbf{d}_1 + \mathbf{d}_2) \cdot (m_1\mathbf{d}_1 + m_2\mathbf{d}_2) = \alpha(m_1 + m_2). \tag{3.13}$$

If we allow $\alpha(m_1 + m_2) = n\bar{d}$ we achieve a one-to-one relationship between the PAS and Fibonacci lattice nodes. Hence, let $\alpha = \bar{d}$ and so the projection matrix, from (3.2) to (3.11) is

$$\Pi = \bar{d}(\mathbf{d}_1 + \mathbf{d}_2) \tag{3.14}$$

$$= \frac{S}{\sqrt{2+\tau}} \begin{pmatrix} (3-\tau)(1+\tau) \\ (3-\tau)(-\tau+1) \end{pmatrix} \tag{3.15}$$

$$= \frac{S}{\sqrt{2+\tau}} \begin{pmatrix} 3+2\tau-\tau^2 \\ -4\tau+3+\tau^2 \end{pmatrix} \tag{3.16}$$

$$= \frac{S}{\sqrt{2+\tau}} \begin{pmatrix} 2+\tau \\ 4-3\tau \end{pmatrix} \tag{3.17}$$

$$= S\sqrt{2+\tau} \begin{pmatrix} 1 \\ 3-2\tau \end{pmatrix}, \tag{3.18}$$

where we note the use of the identity $\tau^2 = \tau + 1$.

Applying the projection matrix Π to the acceptance window associated with the origin node defined in equation (3.5), gives us the occupancy window in the 1D parallel space, $\Pi \cdot \mathbf{W}_2 = O_1$, where

$$O_1 = a\left(\frac{1-\tau}{2}\right)S, \quad a \in (-1, 1], \tag{3.19}$$

which has length $S(\tau-1)$ and is directed along $\mathbf{e}_1$. This occupancy window is replicated on every PAS node for the full set.

Two measurements for the variation of the PAS compared to the quasiperiodic lattice nodes were discussed in section 2.1.3. The packing density is defined as the ratio of the occupancy window area per unit cell of the PAS. For the 1D PAS this is

$$\rho_{\text{pac}} = \frac{S(\tau - 1)}{S(3 - \tau)} = \frac{1}{\sqrt{5}} = 0.447. \tag{3.20}$$

The occupancy factor, which is defined as the fraction of the occupancy windows that contain a quasiperiodic lattice node, is $\rho_{\text{occ}} = 1$ since we could choose a one-to-one projection.

3.3 Approximant

The approximant is a periodic lattice with a finite period that contains some information of the quasiperiodic lattice it aims to represent. As discussed in section 3.1, the projection method is used to construct the approximant to quasiperiodic lattices. The method is the same except that τ is approximated by a chosen rational number, altering the projection slightly. We proceed by approximating τ by a rational number in the **perpendicular space component only**. By taking $\tau \approx \tau_n = \frac{\text{Fib}(n+1)}{\text{Fib}(n)}$, which converges to τ as $n \to \infty$, we slightly alter the acceptance windows within the projection and thus produce a modification of the quasiperiodic chain. The 2D lattice is skewed due to the approximation. Therefore the perpendicular space is subtended at a rational angle from the parallel plane rather than an irrational angle as with the quasiperiodic construction. The projection method with the rational angle yields a periodic lattice along the (original) parallel plane. The periodic cell thus contains a finite section of the quasiperiodic lattice. Since the parallel space and the components of the square lattice in this direction are kept the same (i.e. τ is not approximated in the $\mathbf{e}_1$ plane, see (3.21) below), then the lattice constructed consists of the same L and S spacings as the Fibonacci chain.

Define the approximant constructed with the approximation τ_n as the n-approximant. For the 1D n-approximant, the period is of length $\text{Fib}(n + 2)$. As one would expect intuitively, the larger the n chosen in the approximation of τ, the better the approximation and the better the accuracy of the periodic approximant. The limit of $n \to \infty$, the n-approximant describes the Fibonacci chain itself.

Begin by defining the approximant square lattice vectors, comparing to those used in the quasiperiodic projection (3.2),

$$\tilde{\mathbf{d}}_1 = \begin{pmatrix} \frac{1}{\sqrt{2+\tau}} \\ \frac{-\tau_n}{\sqrt{2+\tau_n}} \end{pmatrix}, \quad \tilde{\mathbf{d}}_2 = \begin{pmatrix} \frac{\tau}{\sqrt{2+\tau}} \\ \frac{1}{\sqrt{2+\tau_n}} \end{pmatrix}. \tag{3.21}$$

As noted above, we have only approximated τ in the $\mathbf{e}_2$ component of the basis vectors. This is to ensure an approximation is made, but that the resultant tiling still comprises the same shaped tiles as the quasiperiodic projection method. This was discussed in section 2.1.4 in particular with the matrix R in equation (2.24). The parallel and perpendicular spaces are still spanned by $\mathbf{e}_1$ and $\mathbf{e}_2$ respectively.

The next step is to define the lattice nodes of the approximant Voronoi cell. This is not the Voronoi cell of the approximant skewed 2D lattice but an approximant of the Voronoi cell of the square 2D lattice. That is, we consider a unit cell of the skewed 2D lattice. Taking the skewed unit cell rather than the Voronoi cell may seem to be a crude approximation of the original procedure carried out, but we believe it is in fact the correct approach to construct the approximant. Although analogous, it is easier to justify for the 5D to 2D projection in chapter 6 via the pentragrid description, and so will be discussed further there.

Comparison of the equation for the Voronoi cell nodes with the square lattice (3.3) with the approximation $\tau \approx \tau_n$ gives the approximant Voronoi nodes as

$$\sum_{i=1}^{2} n_i \tilde{\mathbf{d}}_i = \begin{pmatrix} \frac{n_1+\tau n_2}{\sqrt{2+\tau}} \\ \frac{n_2-n_1\tau_n}{\sqrt{2+\tau_n}} \end{pmatrix}, \tag{3.22}$$

where $n_i \in \{-1/2, 1/2\}$.

The acceptance window for the approximant $\tilde{\mathbf{W}}_2$, in comparison to (3.5), is given by

$$\tilde{\mathbf{W}}_2 = a\frac{1+\tau_n}{2\sqrt{2+\tau_n}}\mathbf{e}_2, \quad a \in (-1, 1]. \tag{3.23}$$

Decorating the lattice nodes with the acceptance window as with the quasiperiodic projection (3.6) we define the full acceptance window for the Fibonacci chain approximant

$$\tilde{\mathbf{A}}_2 = \left\{ \tilde{m}_1\tilde{\mathbf{d}}_1 + \tilde{m}_2\tilde{\mathbf{d}}_2 + \tilde{\mathbf{W}}_2, \quad (\tilde{m}_1, \tilde{m}_2) \in \mathbb{Z} \right\}, \tag{3.24}$$

as depicted in figure 3.3 by the red lines for varying n in the approximation of $\tau \approx \tau_n$. As before, to determine the selection of lattice nodes to be projected, i.e. $\tilde{\Lambda}_{\tilde{\mathcal{M}}}$, we

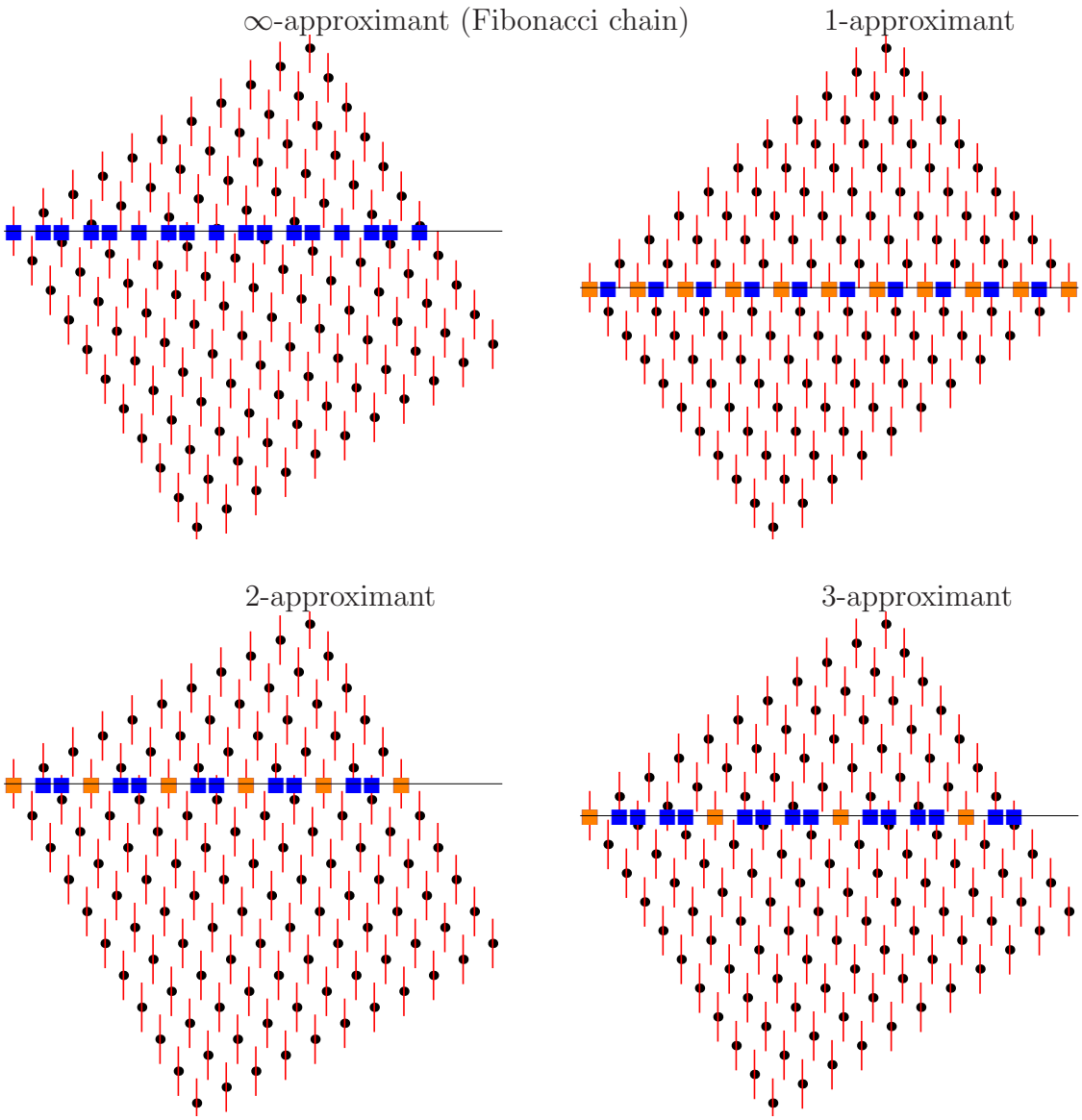

Figure 3.3: Depicting the projection method from the 2D square lattice to the 1D Fibonacci chain as compared with the approximant 2D lattice to varying approximants. We find the positions of the lattice nodes wherever we have an intersection of the acceptance windows (red lines) with the parallel space (horizontal). The lattice nodes are shown by the squares along the horizontal and the orange nodes depict the periods of the approximants.

must find the points at which the acceptance windows intersect the parallel space, or when the $\mathbf{e}_2$ component of equation (3.24) is equal to zero. The reduced intersection equation is

$$-\frac{1+\tau_n}{2} < \tilde{m}_1\tau_n - \tilde{m}_2 \leq \frac{1+\tau_n}{2}, \tag{3.25}$$

from which we are able to determine the allowable integer pairs $(\tilde{m}_1, \tilde{m}_2) \in \tilde{\mathcal{M}}$.

The lattice nodes along $\mathbf{e}_1$ can be found by projecting the lattice points in $\tilde{\Lambda}_{\tilde{\mathcal{M}}}$ to

the parallel plane, and are given by the same formulation as the quasiperiodic case, (3.10),

$$\mathbf{x}_{\text{approx}} = \frac{1}{\sqrt{2+\tau}}(\tilde{m}_1 + \tau\tilde{m}_2), \quad (\tilde{m}_1, \tilde{m}_2) \in \tilde{\mathcal{M}}. \tag{3.26}$$

The blue squares along the horizontal parallel plane in figure 3.3 show the projections of the lattice nodes $\tilde{\Lambda}_{\tilde{\mathcal{M}}}$ and the resulting finite sections of the approximant Fibonacci chain lattice nodes. Different approximations of τ are considered by increasing n. It can be seen how the period, depicted by the orange squares, increases for increasing n.

In summary the projection method algorithm for the Fibonacci chain approximant is as follows

- Construct a skewed 2D lattice with the approximation $\tau \approx \tau_n$ in the $\mathbf{e}_2$ component, defined in (3.21)
- Project an approximant Voronoi cell to the perpendicular space to find the acceptance window associated with the origin node $\tilde{\mathbf{W}}_2$, defined in (3.23)
- Decorate every lattice node with the acceptance window to give the full set $\tilde{\mathbf{A}}_2$, defined in (3.24)
- Find the integer pairs $(\tilde{m}_1, \tilde{m}_2) \in \tilde{\mathcal{M}}$ which allow the intersection of $\tilde{\mathbf{A}}_2$ with the parallel plane in order to determine the selection of the lattice nodes $\tilde{\Lambda}_{\tilde{\mathcal{M}}} = \tilde{m}_1\tilde{\mathbf{d}}_1 + \tilde{m}_2\tilde{\mathbf{d}}_2$ to be projected; these are defined in (3.25)
- Project this set of lattice nodes $\tilde{\Lambda}_{\tilde{\mathcal{M}}}$ to the parallel plane to determine the Fibonacci chain approximant lattice nodes $\mathbf{x}_{\text{approx}}$, defined in (3.26).

As with the construction of the 1D quasiperiodic lattice, the construction of the 1D approximant can be extended to higher dimensions using a similar algorithm. As such, these explanations of the construction of the 1D lattices will be important later.

3.4 Conclusions

In this chapter a rigorous algorithm for the construction of the 1D Fibonacci chain via the projection method has been derived. The algorithm and accompanying explanations and diagrams aim to provide a reader without a prior knowledge of quasiperiodic

structures, the projection method or crystallography with a tool to construct the Fibonacci lattice oneself. The algorithms to produce the PAS and the approximant for the Fibonacci chain were also thoroughly discussed.

The two periodic approximations of the 1D quasiperiodic lattice have different resemblances to the Fibonacci chain and are constructed in dissimilar ways. A comparison between the three lattices can be seen in the example in figure 3.4.

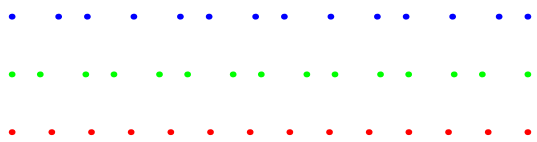

Figure 3.4: Fibonacci chain lattice vertices (blue), 1-approximant vertices (green) and PAS vertices (red).

Further comparisons between the three lattices will be drawn in the acoustic scattering properties of the lattices and is discussed in chapter 4.

Chapter 4

One-dimensional wave scattering by a Fibonacci chain structure

4.1 Problem statement

In section 2.3.1 the solution to the 1D scattering problem of wave propagation along a stretched string with a single point scatterer (a mass, or "bead") located at an arbitrary position was derived. These solutions can now be extended to the scenario of multiple point scatterers whose locations are determined by the 1D lattices as described in chapter 3. In this problem there are only two directions of propagation. Therefore, the scattering is expressed in terms of reflection and transmission of the incident wave by the scatterers.

Some preliminary details that will aid the construction of fast recursive formulae for the reflection and transmission coefficients for multiple point scatterers are first discussed, considering the multiple scattering of two point scatterers. The method applied for the two scatterer scenario can then be easily extended to cases with a finite number of point scatterers with an arbitrary (randomly generated or quasiperiodic) distribution. The main distribution of interest is the 1D Fibonacci chain. For this distribution a recursive formulation of the transmission and reflection coefficients is defined which allows an exponential increase in number of scatterers per recursion.

4.1.1 Two point scatterers

The multiple scattering from two point scatterers can be considered by decomposing into two sub-problems. Each of the sub-problems considers the scattering from a single scatterer, as solved in section 2.3.1. The two sub-problems must then be coupled to account for the effects on one another. The breakdown is depicted in the schematic in figure 4.1, along with how they are coupled.

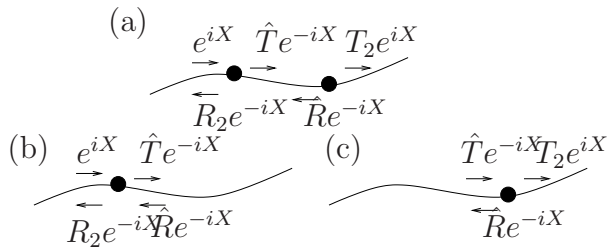

Figure 4.1: Decomposition of the two scatterer problem.

We wish to determine the reflection and transmission coefficients resulting from the scattering due to two point scatterers, R_2 and T_2, respectively. First consider problem (b) from figure 4.1 of a point scatterer at $X = 0$. The solution for R_2 is obtained by summing the resultant reflection due to the right travelling wave of unit amplitude (i.e. R_1e^{-iX}) and the transmission due to the left travelling wave of amplitude $\hat{R}$ (i.e. $\hat{R}T_1e^{-iX}$), to find that

$$R_2 = R_1 + T_1\hat{R}, \tag{4.1}$$

where R_1 and T_1 were derived in (2.86). Similarly, the amplitude of the transmission from the first scatterer is given by

$$\hat{T} = T_1 + R_1\hat{R}, \tag{4.2}$$

obtained by equating the transmission from the right travelling wave of unit amplitude and the reflection from the left travelling wave of amplitude $\hat{R}$.

The amplitude determined in equation (4.2) is the incoming wave in problem (c) from figure 4.1. Considering the phase shift due to the second point scatterer being at $X = A$ (A some arbitrary length) as discussed in section 2.3.1, we find that the reflection at the second scatterer is

$$\hat{R} = \hat{T}R_1e^{2iA} = (T_1 + R_1\hat{R})R_1e^{2iA}, \tag{4.3}$$

and the overall transmission through the two scatterers is

$$T_2 = (T_1 + R_1\hat{R})T_1. \tag{4.4}$$

Rearranging equation (4.3) gives

$$\hat{R} = \frac{T_1 R_1 e^{2iA}}{1 - R_1^2 e^{2iA}}. \tag{4.5}$$

Substitution into (4.1) and (4.4) and simplifying, it is found that the reflection and transmission coefficients for the scattering by two point scatterers with a separation A are

$$R_2 = R_1 + \frac{T_1^2 R_1 e^{2iA}}{1 - R_1^2 e^{2iA}}, \quad T_2 = \frac{T_1^2}{1 - R_1^2 e^{2iA}}. \tag{4.6}$$

This method can now be extended to a finite arbitrary number N of scatterers.

4.1.2 N point scatterers

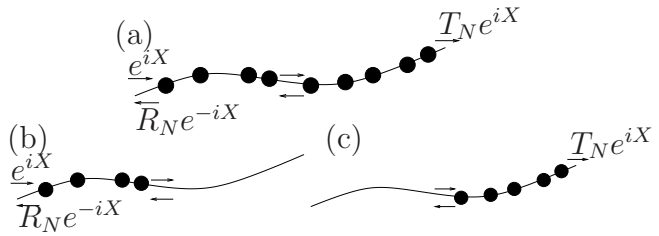

Figure 4.2: Decomposition of the N point scatterer problem.

The above method can be applied to arbitrary numbers and distributions of point scatterers, as depicted in figure 4.2. The figure illustrates how an arbitrary distribution of point scatterers can be decomposed into two smaller sub-problems. If the reflection and transmission of the two sub-problems, (b) and (c), are known, then it is possible to couple the two solutions to find the reflection and transmission associated with (a). A difficulty here is that the smaller problems will now have an incoming wave from the left (of any amplitude) and from the right, and are no longer positioned at the origin. This is where the distribution being non-periodic makes the problem slightly more involved; it is necessary to determine the reflection and transmission coefficients for both incoming right and left travelling waves. This was discussed in 2.3.1, and a superscript o notation is used to denote the 'opposite' problem, i.e. an incident left travelling wave. Changes in incoming amplitudes and phase shifts must also be taken into consideration.

With the solutions to the one point scatterer problem, (2.86), it has been shown how to apply these to the two point scatterers. This method can be extended to three scatterers and so on. It is therefore possible to find the N^{th} reflection and transmission coefficients R_N and T_N for large N remarkably quickly for a 1D distribution of point scatterers.

As in section 4.1.1, first consider the n scatterer problem in (b) with the first scatterer at $X = X_1 = 0$. This scatterer has an incident right travelling wave of unit amplitude and an incident left travelling wave to the n^{th} scatterer, due to the p scatterer problem, of unknown amplitude L. After finding expressions for the resultant left and right propagating waves of problem (a), consider the p scatterer problem in (c) with first scatterer at $X = X_{n+1}$. Working through as in section 4.1.1 one can simply show that the solutions for the $N = n + p$ point scatterer problem are

$$R_N = R_n + \frac{T_n^o T_n R_p e^{2iX_{n+1}}}{1 - R_n^o R_p e^{2iX_{n+1}}}, \tag{4.7}$$

$$T_N = \frac{T_n T_p}{1 - R_n^o R_p e^{2iX_{n+1}}}, \tag{4.8}$$

$$R_N^o = R_p^o e^{-2iX_{n+1}} + \frac{T_p^o T_p R_n^o}{1 - R_n^o R_p e^{2iX_{n+1}}}, \tag{4.9}$$

$$T_N^o = \frac{T_n^o T_p^o}{1 - R_n^o R_p e^{2iX_{n+1}}}, \tag{4.10}$$

where the superscript o denotes the 'opposite' problem, of an incoming left travelling wave. These formulae allow the computation of the reflection and transmission coefficients for arbitrarily positioned point scatterers, dependent on prior knowledge of a certain breakdown of the problem. These formulae are very general, and are applied later in section 4.3 for more a specific quasiperiodic geometry, which will allow the recursive formulae to be computed extremely rapidly for a large number of point scatterers.

4.2 Distributions of scatterers modelled as a homogeneous medium

For multiple scattering from a finite number of point scatterers on a string one can find an effective wavenumber for the wave passing through the length of scatterers

and string by comparison with a string which has a homogeneous *inclusion* section of some length of a different density to the *host* string as depicted in figure 4.3. For

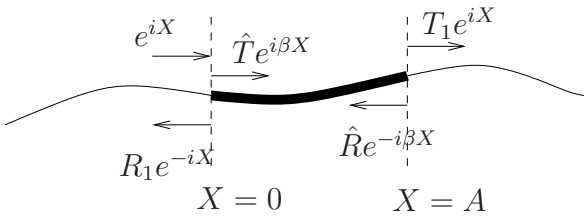

Figure 4.3: Infinite host string with inclusion of length A of different density.

this problem, consider an infinite string with density ρ_2 for $0 \leq x \leq a$ and density ρ_1 elsewhere. Non-dimensionalise the horizontal lengthscale by letting

$$X = k_1 x, \tag{4.11}$$

and so

$$k_2 x = \beta X, \tag{4.12}$$

$$\beta = \frac{k_2}{k_1}, \tag{4.13}$$

where k_1 and k_2 are the wavenumbers of the host and inclusion strings, respectively. The non-dimensionalised string displacement has the form

$$Y(X) = \begin{cases} Y_1(X) &= e^{iX} + R_1 e^{-iX} & X \leq 0 \\ Y_2(X) &= \hat{T}e^{i\beta X} + \hat{R}e^{-i\beta X} & 0 \leq X \leq A \\ Y_3(X) &= T_1 e^{iX} & A \leq X \end{cases} \tag{4.14}$$

where $A = k_1 a$.

At the points where the density changes, the string must have continuous displacement and slope, giving the boundary conditions

$$Y_1(0) = Y_2(0), \tag{4.15}$$

$$Y_1'(0) = Y_2'(0), \tag{4.16}$$

$$Y_2(A) = Y_3(A), \tag{4.17}$$

$$Y_2'(A) = Y_3'(A). \tag{4.18}$$

The dashed notation here denotes differentiation with respect to X. After some algebra

the boundary conditions lead to the simultaneous equations

$$1 + R_1 = \hat{T} + \hat{R}, \tag{4.19}$$

$$1 - R_1 = \beta\hat{T} - \beta\hat{R}, \tag{4.20}$$

$$\hat{T}e^{iA\beta} + \hat{R}e^{-iA\beta} = T_1 e^{iA}, \tag{4.21}$$

$$\beta\hat{T}e^{iA\beta} - \beta\hat{R}e^{-iA\beta} = T_1 e^{iA}, \tag{4.22}$$

which can be solved to give

$$R_1 = \frac{(1-\beta^2)(1-e^{2iA\beta})}{(1+\beta)^2 - (1-\beta)^2 e^{2iA\beta}}, \tag{4.23}$$

$$\hat{T} = \frac{2(1+\beta)}{(1+\beta)^2 - (1-\beta)^2 e^{2iA\beta}}, \tag{4.24}$$

$$\hat{R} = \frac{2(\beta-1)e^{2iA\beta}}{(1+\beta)^2 - (1-\beta)^2 e^{2iA\beta}}, \tag{4.25}$$

$$T_1 = \frac{4\beta e^{iA(\beta-1)}}{(1+\beta)^2 - (1-\beta)^2 e^{2iA\beta}}. \tag{4.26}$$

Figure 4.4 shows the computed results for the transmission and reflection from either

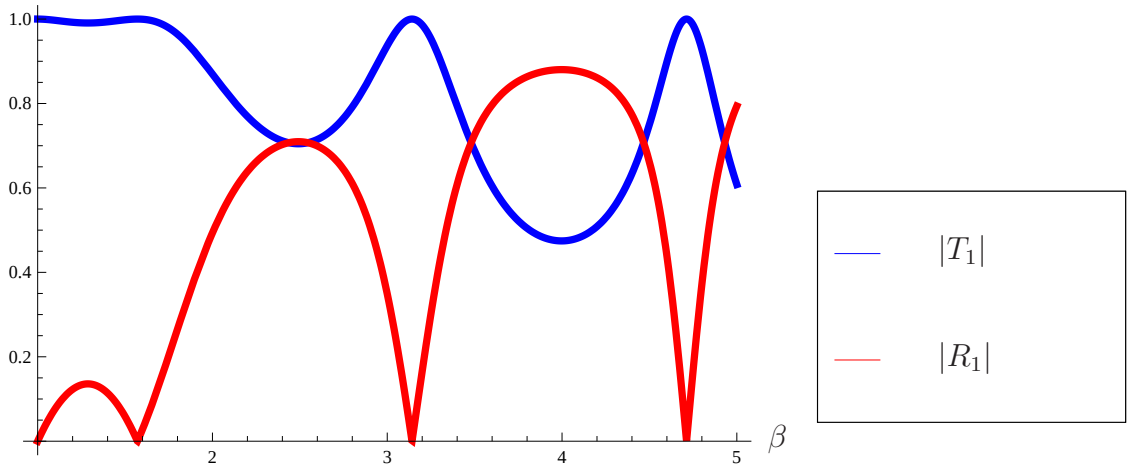

Figure 4.4: Transmission and reflection due to an inclusion of string of length $A = 2$.

end of the inclusion string for a particular parameter set.

The solutions for R and T from a finite point scatterer problem can be compared with equations (4.23) and (4.26) to determine the effective wavenumber β for the point scatterer problem and will now be discussed.

Equation (4.23) can be rearranged neatly to give β as a function of R_1. Firstly, rearrange to give

$$e^{2iA\beta} = \frac{R_1(1+\beta)^2 - (1-\beta^2)}{R_1(1-\beta)^2 - (1-\beta^2)}. \tag{4.27}$$

Then, assuming β is real (i.e. no attenuation in either string), it is known that

$$e^{2iA\beta}e^{2iA\bar{\beta}} = 1, \tag{4.28}$$

where $\bar{z}$ denotes the complex conjugate of z.

After a little algebra it can be shown that

$$\beta^2 = \frac{\Re(R_1) - |R_1|^2}{\Re(R_1) + |R_1|^2}. \tag{4.29}$$

It is also possible to determine the effective length of the homogeneous inclusion by finding the argument of equation (4.27),

$$A = \frac{1}{2\beta}\arg\left(\frac{R(1+\beta)^2 - (1-\beta^2)}{R(1-\beta)^2 - (1-\beta^2)}\right) + \frac{n\pi}{\beta} \tag{4.30}$$

since $e^{2iA\beta}$ has a period of $2n\pi$, $n \in \mathbb{Z}$.

Thus, by comparing two different 1D wave propagation problems, interesting equations for the effective properties of a finite point scatterer geometry have been determined, (4.29) and (4.30). Therefore, the computed reflection coefficient from an N-point scatterer problem can be applied to generate an effective wavenumber and an effective length for a homogeneous medium. Replacing the point scatterer distribution with this effective medium retains its reflection and transmission coefficients. We are now in the beneficial position of having a homogeneous material which can model a complicated aperiodic 1D structure. This formulae can be applied for any distribution of point scatterers without limitations.

4.3 Recursive formulation for wave scattering by point scatterers with a Fibonacci chain distribution

Understanding wave propagation in quasiperiodic media will aid in bridging the gap between theory in periodic and random media. In this chapter a 1D quasiperiodic lattice called the Fibonacci chain, as described in chapter 3, is investigated. In section 4.1.2 the formulation of the solutions for the reflection and transmission coefficients for a finite number of point scatterers was derived in a recursive manner. The recursive

methodology can be extended to consider a finite set of scatterers with a quasiperiodic distribution. The quasiperiodic Fibonacci chain allows simplifications of the formulae and thus solutions can be produced for large numbers (e.g. billions) of scatterers extremely rapidly. The simplifications made are due to the deterministic nature of the Fibonacci chain, and how it can be constructed using the superposition of the two previous chains. This deterministic property does not exist in fully random media, so although the recursive methodology can be applied, it will be computationally slower than that of the aperiodic Fibonacci chain.

With reference to figure 4.5, denote D_n as the nth distribution of the point scatterers via the Fibonacci chain. Thus D_1 and D_2 are distributions with one scatterer set at a distance S and L from the origin, respectively. D_3 is the superposition of D_1 to the end of D_2, i.e. two point scatterers positioned at $X = L$ and $X = L + S$. This continues, so the D_n is just a superposition of the D_{n-2} to the end of the D_{n-1}.

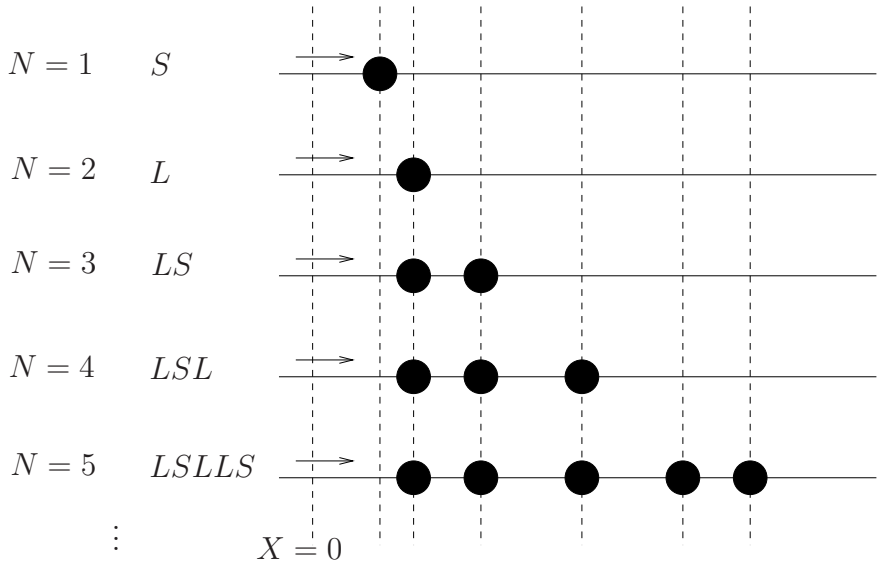

Figure 4.5: Fibonacci chain spacing of the point scatterers.

This chain can also be generated via alternative methods as described in chapter 3, but using the construction described above one can easily see how the D_n problem can be solved recursively using the solutions to the two previous problems.

As in section 4.1.2 it is necessary to formulate solutions for the opposite problems. The set up used here can be seen in figure 4.6. Let the D_1^o and D_2^o problems both be a scatterer at $X = 0$. Then the D_n^o problem is formed by bringing the D_{n-2}^o problem to the left of the D_{n-1}^o problem.

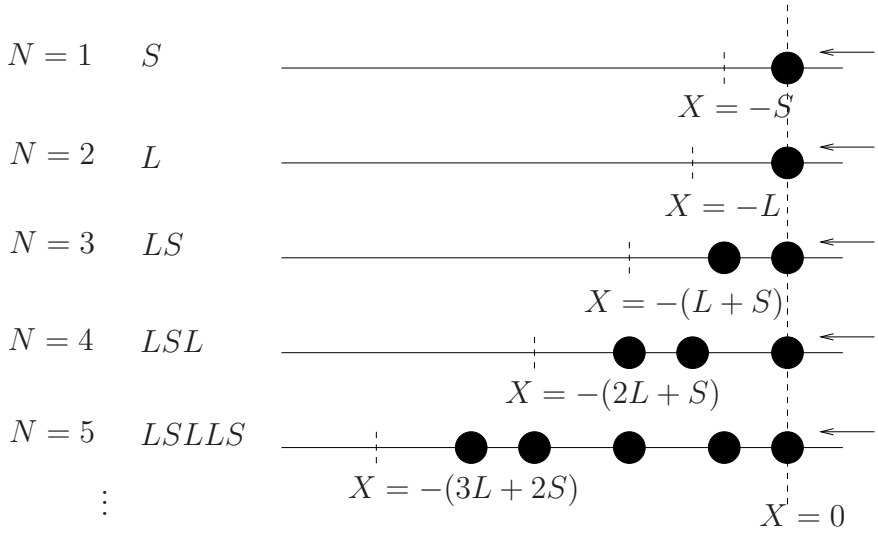

Figure 4.6: Spacing of the point scatterers for the opposite Fibonacci chain problem.

The D_1 and D_2 problems are simply one point scatterer problems, and from 2.3.1 it is known that the transmission and reflection coefficients are given by

$$\begin{aligned} T_1 &= T_2 = T_1^o = T_2^o = \frac{2}{2 - M\epsilon i}, \\ R_1 &= e^{2iS}\frac{M\epsilon i}{2 - M\epsilon i}, \\ R_2 &= e^{2iL}\frac{M\epsilon i}{2 - M\epsilon i}, \\ R_1^o &= R_2^o = \frac{M\epsilon i}{2 - M\epsilon i}, \end{aligned} \tag{4.31}$$

where $M = \frac{m}{m_0} = \frac{m}{\rho_0 \epsilon / k}$ and $\epsilon = (3 - \tau)S$ is the non-dimensional average spacing of the Fibonacci chain, as derived in section 2.1. The D_3 and D_3^o problems are just two point scatterer problems so can be solved as in section 4.1.1 giving

$$\begin{aligned} T_3 &= \frac{T_1 T_2}{1 - R_1 R_2^o}, \\ R_3 &= R_2 + \frac{R_1 T_2 T_2^o e^{2iL}}{1 - R_1 R_2^o} = R_2 + \frac{R_1 T_3 T_2^o e^{2iL}}{T_1}, \\ T_3^o &= \frac{T_1^o T_2^o}{1 - R_1 R_2^o}, \\ R_3^o &= R_1^o + \frac{T_1 R_2^o T_3^o e^{2iS}}{T_2^o}. \end{aligned} \tag{4.32}$$

Continuing for increasing N, decomposing the problem into sub-problems and using

the technique from section 4.1.2 it can be shown that

$$\begin{aligned} T_4 &= \frac{T_2 T_3}{1 - R_2 R_3^o}, \\ R_4 &= R_3 + \frac{R_2 T_4 T_3^o e^{2i(L+S)}}{T_2}, \\ T_4^o &= \frac{T_2^o T_3^o}{1 - R_2 R_3^o}, \\ R_4^o &= R_2^o + \frac{T_2 R_3^o T_4^o e^{2iL}}{T_3^o}, \end{aligned} \tag{4.33}$$

and

$$\begin{aligned} T_5 &= \frac{T_3 T_4}{1 - R_3 R_4^o}, \\ R_5 &= R_4 + \frac{R_3 T_5 T_4^o e^{2i(2L+S)}}{T_3}, \\ T_5^o &= \frac{T_3^o T_4^o}{1 - R_3 R_4^o}, \\ R_5^o &= R_3^o + \frac{T_3 R_4^o T_5^o e^{2i(L+S)}}{T_4^o}. \end{aligned} \tag{4.34}$$

It is possible to see a pattern forming, from $N \geq 3$.

Taking equations (4.31) as the initial formulae, the following relation is obtained for $N \geq 3$,

$$T_N = \tfrac{T_{N-2} T_{N-1}}{1 - R_{N-2} R_{N-1}^o}, \tag{4.35}$$

$$T_N^o = \tfrac{T_{N-2}^o T_{N-1}^o}{1 - R_{N-2} R_{N-1}^o}, \tag{4.36}$$

$$R_N = R_{N-1} + \tfrac{R_{N-2} T_N T_{N-1}^o e^{2i(q(N-1))S}}{T_{N-2}}, \tag{4.37}$$

$$R_N^o = R_{N-2}^o + \tfrac{T_{N-2} R_{N-1}^o T_N^o e^{2i(q(N-2))S}}{T_{N-1}^o}, \tag{4.38}$$

where

$$q(N)S = (\mathrm{Fib}(N-1)\tau + \mathrm{Fib}(N-2))S \tag{4.39}$$

is the end point of the Nth distribution for $N \geq 3$. This formulae for the reflection and transmission coefficients can be proved by induction and is accomplished in appendix A.3.

The recursive method can be applied to any distribution of scatterers. It has been applied to the Fibonacci distribution in this section, due to the aims of this thesis, but also due to its speed in calculating the solutions for large distributions. One benefit of this quasiperiodic distribution is that the number of scatterers in each

system grows exponentially on each recursion; one can calculate the reflection and transmission coefficients for a distribution containing Fib(N) point scatterers with only N recursions. Nevertheless, for other distributions this method can be applied. For example, a distribution with fully random spacings. Because of the non-deterministic nature of a random lattice only one scatterer can be added on each recursion. This example is illustrated in appendix C.2. The method can also be applied to variations in the masses M of the point scatterers or in the density of the string. Quasiperiodic and random variation in the mass of point scatterers is discussed briefly in appendix C.3 and C.4.

4.4 Comparison of wave scattering by a Fibonacci chain structure and its periodic approximations

In this section the transmission properties associated with the quasiperiodic Fibonacci chain are compared to those associated with two periodic structures: the periodic average structure (PAS) and the approximant, described in sections 3.2 and 3.3. The goal is to determine the periodic structure that best represents the propagation properties of the Fibonacci chain. A representative periodic structure may therefore be justifiable as a model of a complicated quasiperiodic structure. It will then be possible to apply the analytical tools discussed in section 2.3.2 to determine effective properties of an infinite periodic structure that could represent an infinite quasiperiodic structure.

Figure 4.7 shows the transmission coefficient for wave propagation through 21 point scatterers distributed according to the three methods above, Fibonacci chain (blue solid), PAS (red dashed) and approximant (green dotted), plotted as functions of increasing mass M. Note here that this is for 21 point scatterers, i.e. Fib(8), and *not* Fib(21).

The approximant structure used here is the lowest approximation, $\tau \approx \tau_1 = \frac{\text{Fib}(2)}{\text{Fib}(1)} = \frac{1}{1} = 1$. It can be seen that for small M the three different distributions have similar transmission properties, i.e. they all allow most of the wave to be transmitted. This is intuitive as for lower masses the scattering from the point masses is weak and hence its modification to the propagating wave is weak.

One can see that for point scatterers of mass $M \gtrsim 1.4$ the PAS transmission

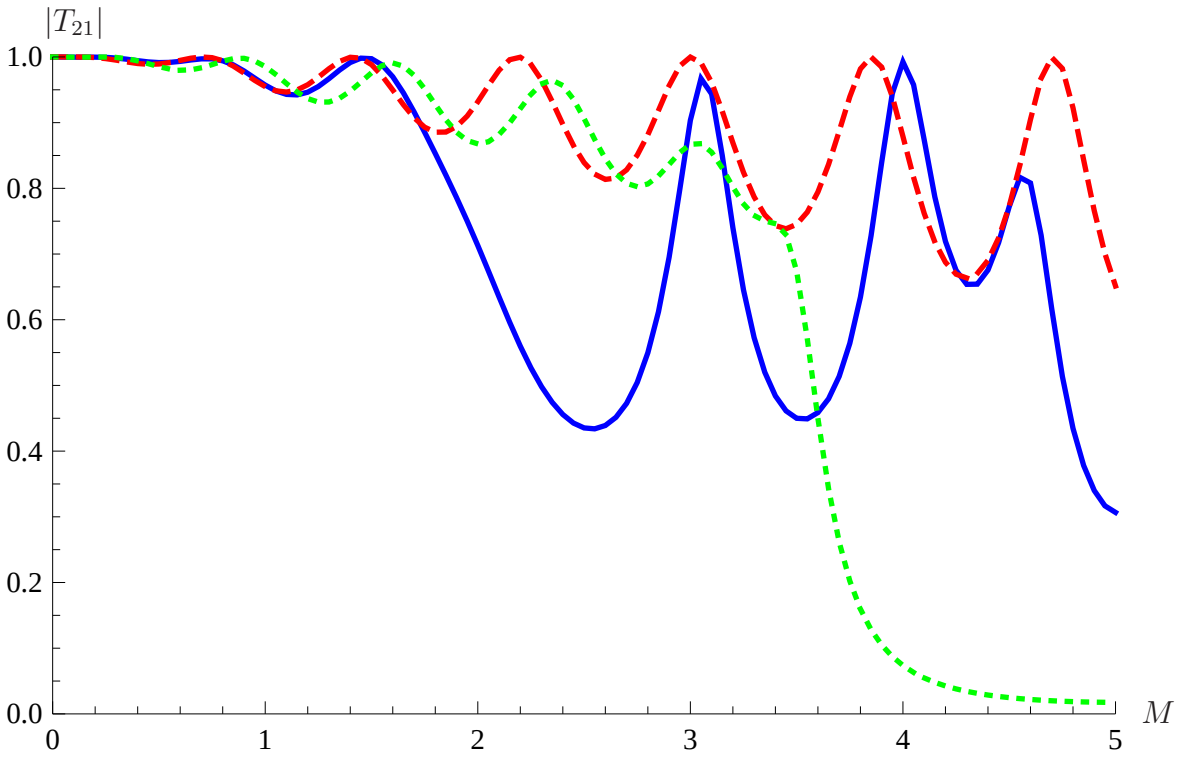

Figure 4.7: Comparison of the transmission through 21 point scatterers (i.e. Fib(8)) with Fibonacci chain (blue solid), period average structure (red dashed) and approximant (green dotted) distributions, for increasing mass of the point scatterers. The approximant used here is $\tau \approx \tau_1 = \frac{1}{1} = 1$.

deviates significantly from the Fibonacci transmission for the majority of scatterers, except a range around $4.2 < M < 4.7$, all depending on the required tolerance of the model. This suggests that this approximation is only appropriate as a representation of the Fibonacci chain for particular ranges of mass of the point scatterers, for 21 scatterers.

For the 1-approximant it is seen that as the mass of the point scatterers increases the similarities between the transmission of the approximant and the Fibonacci chain decrease. Thus, such a basic approximant is not a good model of the Fibonacci chain for larger mass size. One could expect such results when using such an approximation of τ; the golden ratio is $\tau = 1.61803398875\ldots$, which is not well represented by this chosen approximation ($\tau = 1$)!

Figure 4.8 shows how the transmission properties of the approximant change as the approximation of τ is improved. The approximant modelled here uses $\tau \approx \tau_3 = \frac{\text{Fib}(4)}{\text{Fib}(3)} = \frac{3}{2}$, which is much closer to τ than the previous approximant. The size of the periodic cell of the approximant is increased to $\text{Fib}(5) = 5$ spacings, thus the unit cell

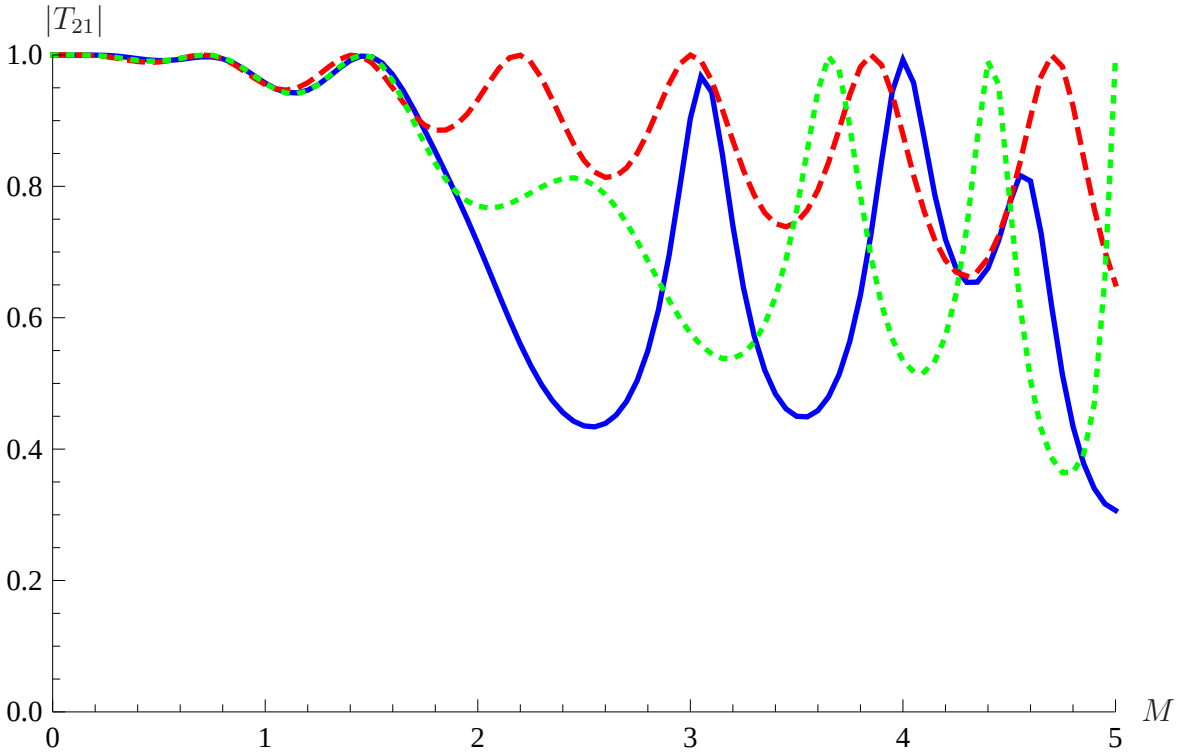

Figure 4.8: Comparison of the transmission through 21 point scatterers with Fibonacci chain (blue solid), period average structure (red dashed) and approximant (green dotted) distribution, for increasing mass of the point scatterers. The approximant used here is $\tau \approx \tau_3 = \frac{3}{2}$.

of the approximant which is acting as a representative volume element (RVE, discussed in [83], [84]) of the Fibonacci chain captures the quasiperiodicity better. In figure 4.8 there is a slight improvement in capturing the transmission properties of the Fibonacci chain with the improvement of the approximant.

We can continue to improve the approximation of τ in the approximant construction and see how the transmission properties compare. Although, obviously there is a limit to finding the best RVE without having an exact quasiperiodic chain for the number of scatterers under consideration! That is, in the examples so far, distributions of only 21 point scatterers have been considered, thus the RVE is required to be of a smaller size than 21 (i.e. less that Fib(8)).

In figure 4.9 the approximation of $\tau \approx \tau_4 = \frac{\text{Fib}(5)}{\text{Fib}(4)} = \frac{5}{3}$ has been used, and there is a significant improvement in agreement. For a period of just $\text{Fib}(6) = 8$ point scatterers, the transmission properties of the Fibonacci chain are being captured within a wider range of point mass sizes.

To reiterate this finding, figure 4.10 shows how the transmission coefficients vary for

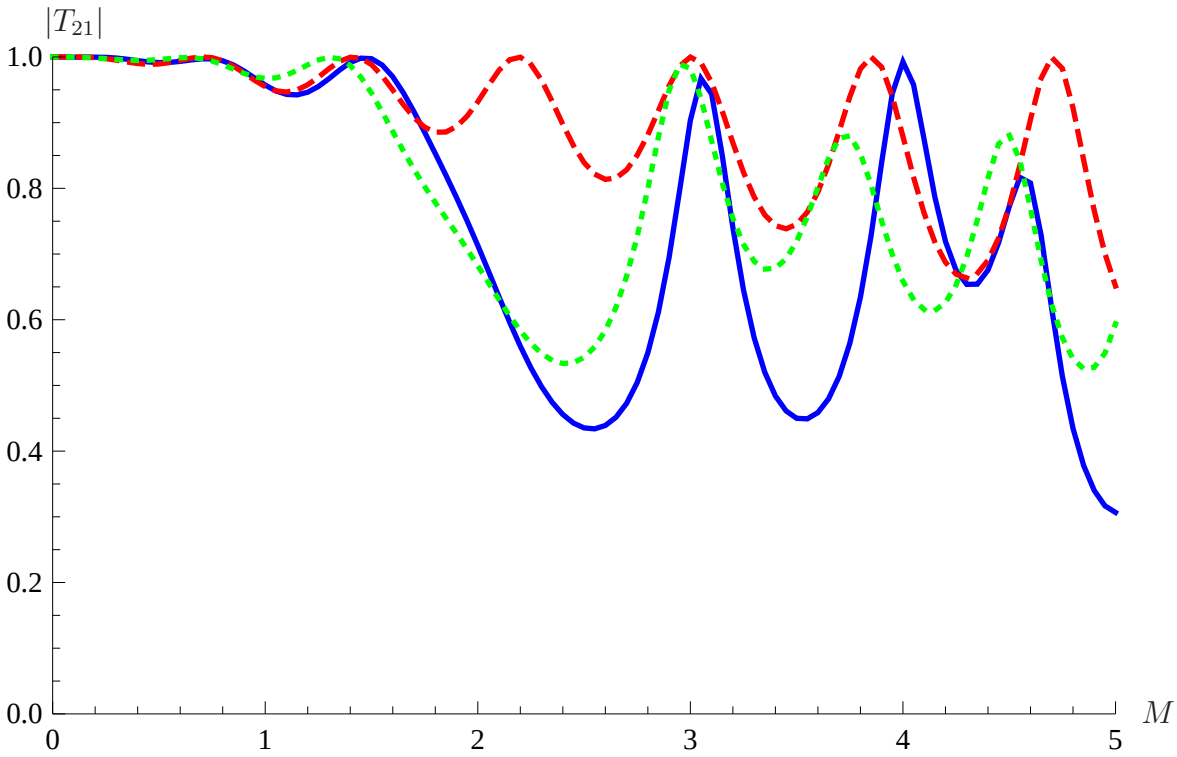

Figure 4.9: Comparison of the transmission through 21 point scatterers with Fibonacci chain (blue solid), period average structure (red dashed) and approximant (green dotted) distribution, for increasing mass of the point scatterers. The approximant used here is $\tau \approx \tau_4 = \frac{5}{3}$.

the three different distributions with a particular mass $M = 2.3$ and increasing number of scatterers. The choice of M is arbitrary but has been selected so that it is large enough to avoid the initial range of masses where there is accurate agreement between all distributions. This choice of M demonstrates the potential of the approximant, however it must be noted that this is just one example. It can be seen that for a periodic cell of length Fib(6) = 8 spacings, the approximant provides an accurate RVE for as many as 60 scatterers. The PAS continues to allow almost full transmission as the number of scatterers in the array is increased, whereas the Fibonacci chain and the approximant distributions offer a gradual loss in transmission.

It is plain to see from this section that for an appropriate choice of period of the approximant in relation to the sample size, the approximant provides a much better periodic representation of the quasiperiodic Fibonacci chain than the PAS. By capturing an essence of the quasiperiodicity within the periodic cell of the approximant we are able to "mimic" the scattering properties of a fully quasiperiodic distribution in 1D exceptionally well. Thus, the question we now wish to answer is how to determine

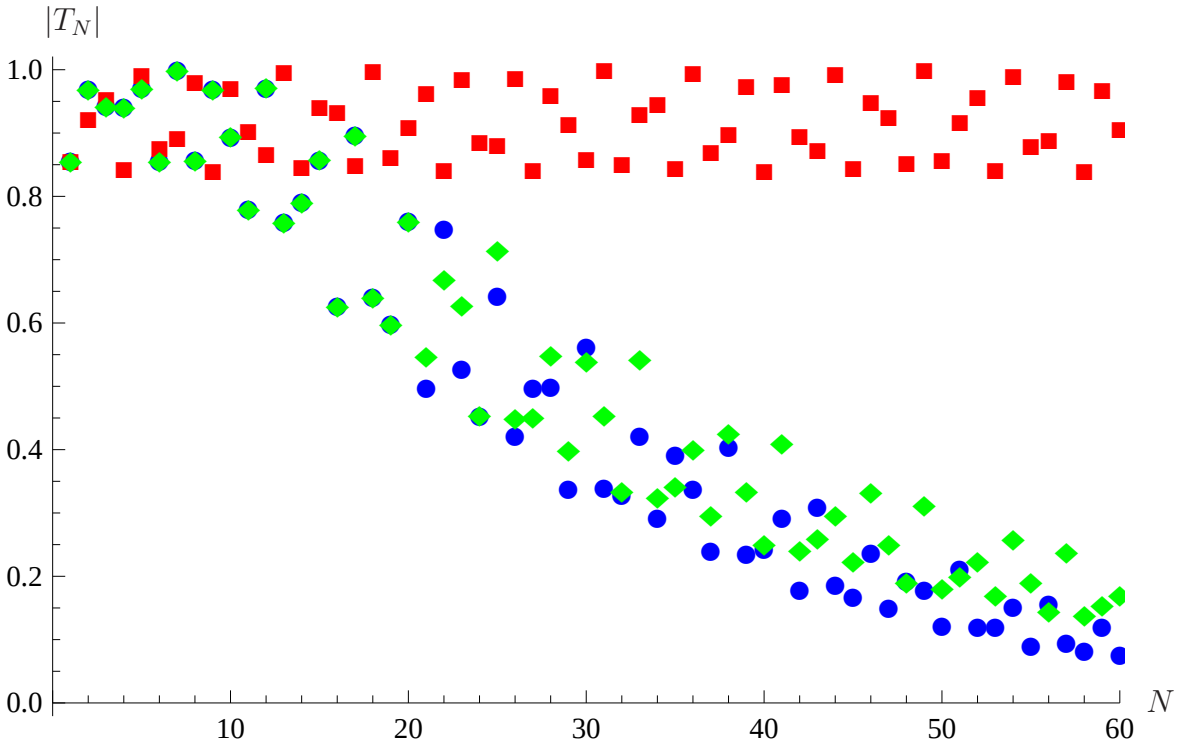

Figure 4.10: Comparison of the transmission through point scatterers of mass $M = 2.3$ with Fibonacci chain (blue circle), period average structure (red square) and approximant (green diamond) distribution, for increasing number of point scatterers. The approximant used here is $\tau \approx \tau_4 = \frac{5}{3}$.

the RVE needed to model various lengths of Fibonacci chain for certain parameters? Or, what is the smallest approximant cell size, or simplest rational approximation of τ that can be used?

Figure 4.11 shows how the transmission coefficients vary for other lengths of point scatterer distributions, continuing with the 4-approximant, $\tau \approx \tau_4$. Distributions of Fib(7), Fib(8), Fib(9) and Fib(10) scatterers are considered, and the approximant unit cell contains Fib(6) scatterers.

For Fib(7) scatterers the approximant gives exactly the same transmission coefficient as the Fibonacci chain. This is actually due to the distributions being identical in this length, even though the period of the approximant is less.

The approximant always provides the best match to the quasiperiodic distribution at the origin as discussed in section 3. So as the number of scatterers is increased, more mismatches between the two lattices are expected, and thus more discrepancies in the transmission. We can see that for a chain with Fib(9) and Fib(10) scatterers, the approximant manages to capture the Fibonacci chain scattering properties remarkably

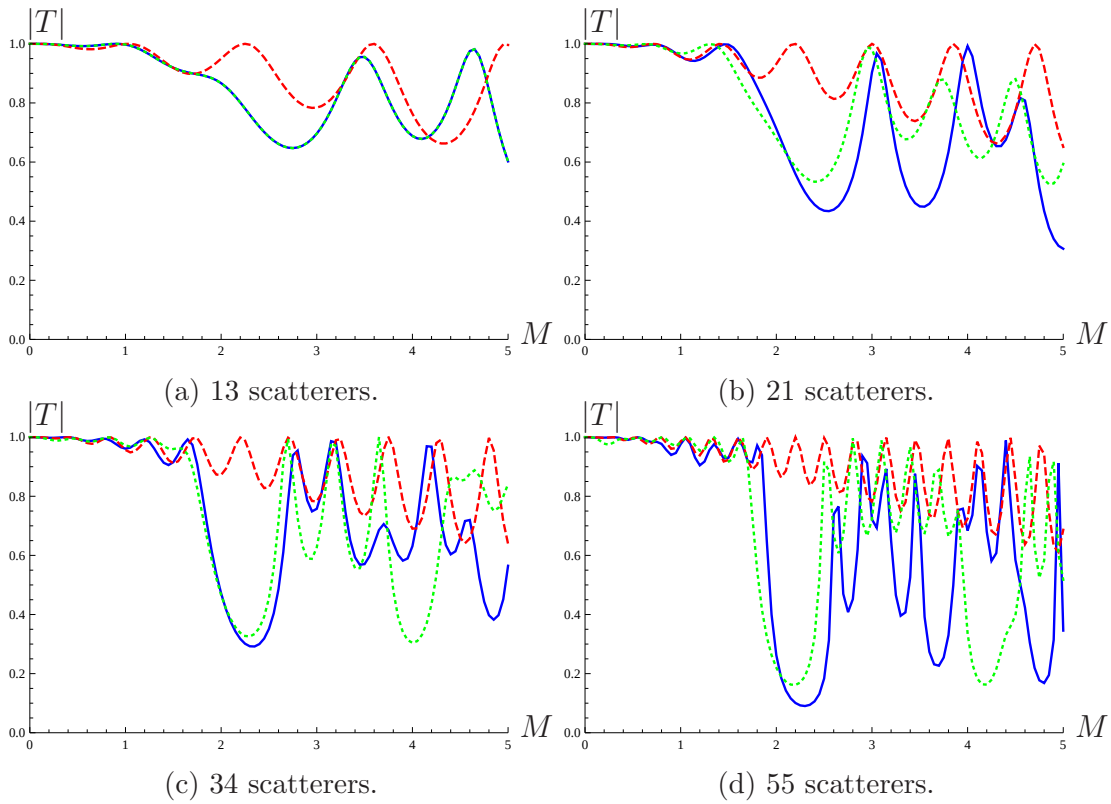

(a) 13 scatterers. (b) 21 scatterers.

(c) 34 scatterers. (d) 55 scatterers.

Figure 4.11: Comparison of the transmission through increasing Fibonacci numbers of point scatterers with Fibonacci chain (blue solid), period average structure (red dashed) and approximant (green dotted) distribution, for increasing mass of the point scatterers. The approximant used here is $\tau \approx \tau_4 = \frac{5}{3}$.

well until a critical mass M^*. This suggests that an n-approximant of with Fib$(n+2)$ scatterers could be an appropriate RVE for a Fibonacci chain distribution of Fib$(n+6)$ scatterers. However, to capture the scattering properties for larger masses a chain with Fib$(n+4)$ scatterers would be well represented.

To test this hypothesis, refer to figure 4.12 where we illustrate the transmission of the three different lattices for increasing total lengths of distributions again, but now with an improved approximant of $\tau \approx \tau_5 = \frac{\text{Fib}(6)}{\text{Fib}(5)} = \frac{8}{5}$. As before, it can be seen that the scattering properties of the Fibonacci chain are mimicked with the approximant for the mass range $0 \leq M \leq 5$ and for total lengths of Fib$(5+4)$. For lengths greater than this it is seen that general characteristics of the Fibonacci transmission such as the drops in transmission through the approximant are captured, but the higher transmission behaviour for larger M is not.

Increasing the accuracy of the approximation of τ further to $n = 6$ i.e. $\tau \approx \tau_6 = \frac{\text{Fib}(7)}{\text{Fib}(6)} = \frac{13}{8}$, giving an approximant periodic cell with Fib$(8) = 21$ scatterers, it can

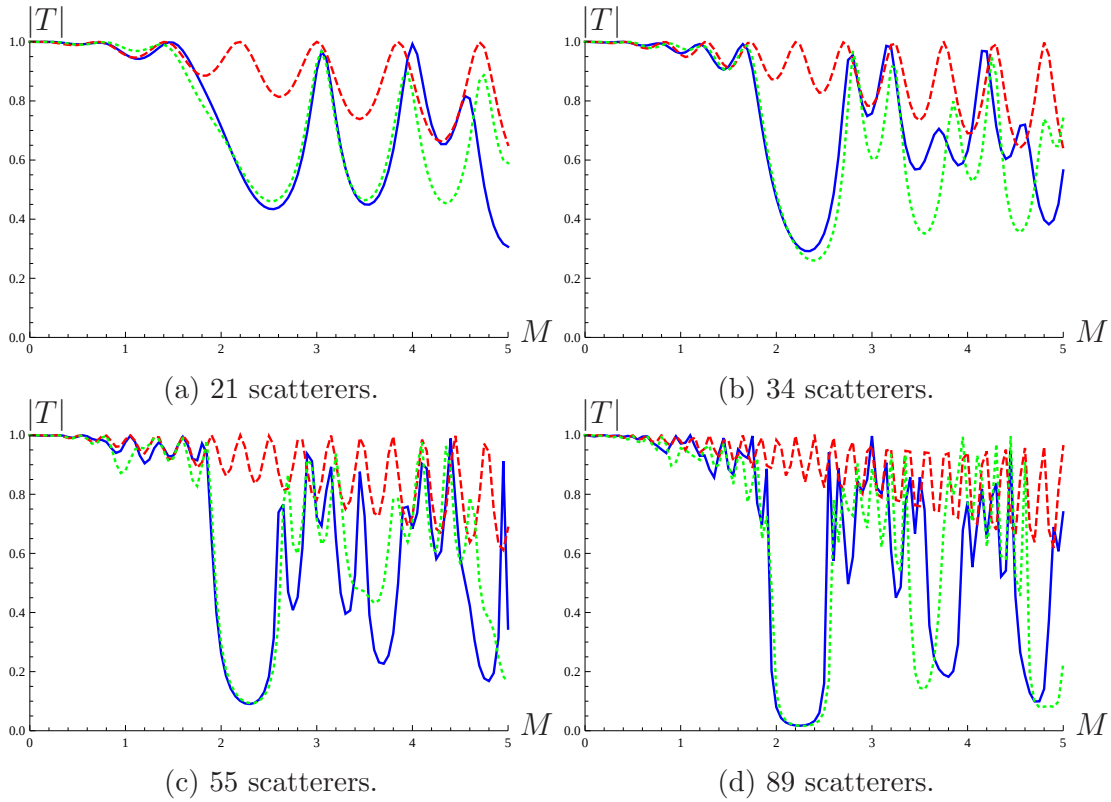

(a) 21 scatterers. (b) 34 scatterers.

(c) 55 scatterers. (d) 89 scatterers.

Figure 4.12: Comparison of the transmission through increasing Fibonacci numbers of point scatterers with Fibonacci chain (blue solid), period average structure (red dashed) and approximant (green dotted) distribution, for increasing mass of the point scatterers. The approximant used here is $\tau \approx \tau_5 = \frac{8}{5}$.

be seen that again a Fibonacci distribution of Fib$(n+4)$ =Fib$(10) = 55$ scatterers is very accurately modelled by the approximant, see figure 4.13. What is remarkable about this approximant however is that as the number of scatterers is increased, as before there are discrepancies between the high transmission properties, but now the approximant has almost identical "near" stop bands to the Fibonacci distribution! The capability of mimicking the low transmission coefficients was mentioned for the previous approximant, but has been reinforced here. Figure 4.14 shows the stop band replication for a chain of length Fib$(15) = 610$ as an example. For a chain with so many more scatterers than the approximant periodic cell, to be able to capture such properties suggests that an excellent RVE has been obtained.

It can be understood that the approximant becomes less accurate as a model for the Fibonacci chain as the number of scatterers is increased since the approximant is most accurate near the origin of the x-position of the scatterers, due to the projection method applied in the previous chapter. At the origin the quasiperiodicity of the

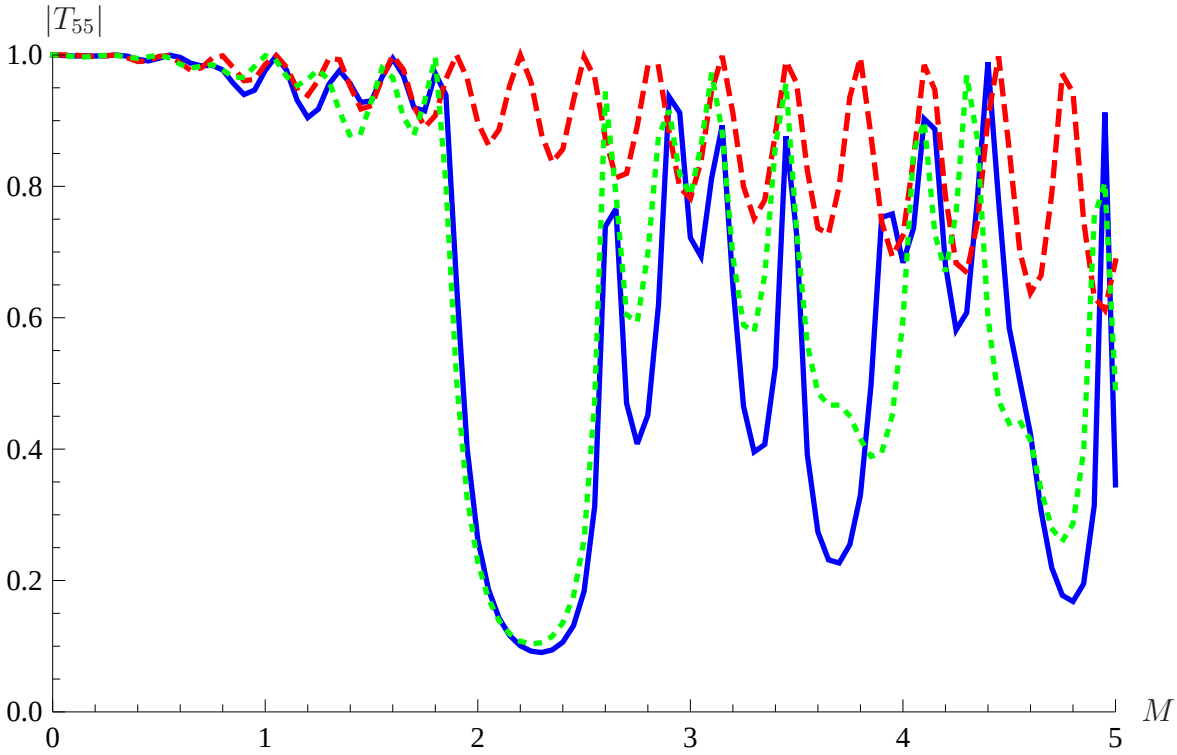

Figure 4.13: Comparison of the transmission through 55 point scatterers with Fibonacci chain (blue solid), period average structure (red dashed) and approximant (green dotted) distribution, for increasing mass of the point scatterers. The approximant used here is $\tau \approx \tau_6 = \frac{13}{8}$.

approximant unit cell matches with the quasiperiodicity of the Fibonacci chain, but further from the origin more discrepancies are expected. Therefore one unit cell of the approximant should mimic the scattering properties of the Fibonacci chain more accurately nearer the origin. The accuracy of the approximant unit cell compared to an equivalent length of Fibonacci chain can be gauged by taking an average of the transmission amplitude over various Fibonacci chain sections with one approximant unit cell length.

Define the transmission coefficient from a distribution of point scatterers with the Fibonacci chain within an approximant unit cell at the origin $\mathcal{T}_0$, a translation of one cell along $\mathcal{T}_1$, and so on, so that m translations of the unit cell away from the origin gives us the transmission for a length of Fibonacci chain within a unit cell called $\mathcal{T}_m$. The average amplitude can then be given by

$$\bar{T} = \frac{\sum_{m=m_{min}}^{m_{max}} \mathcal{T}_m}{m_{max} - m_{min} + 1}. \tag{4.40}$$

Figure 4.15 depicts comparisons of the average transmission of the Fibonacci chain

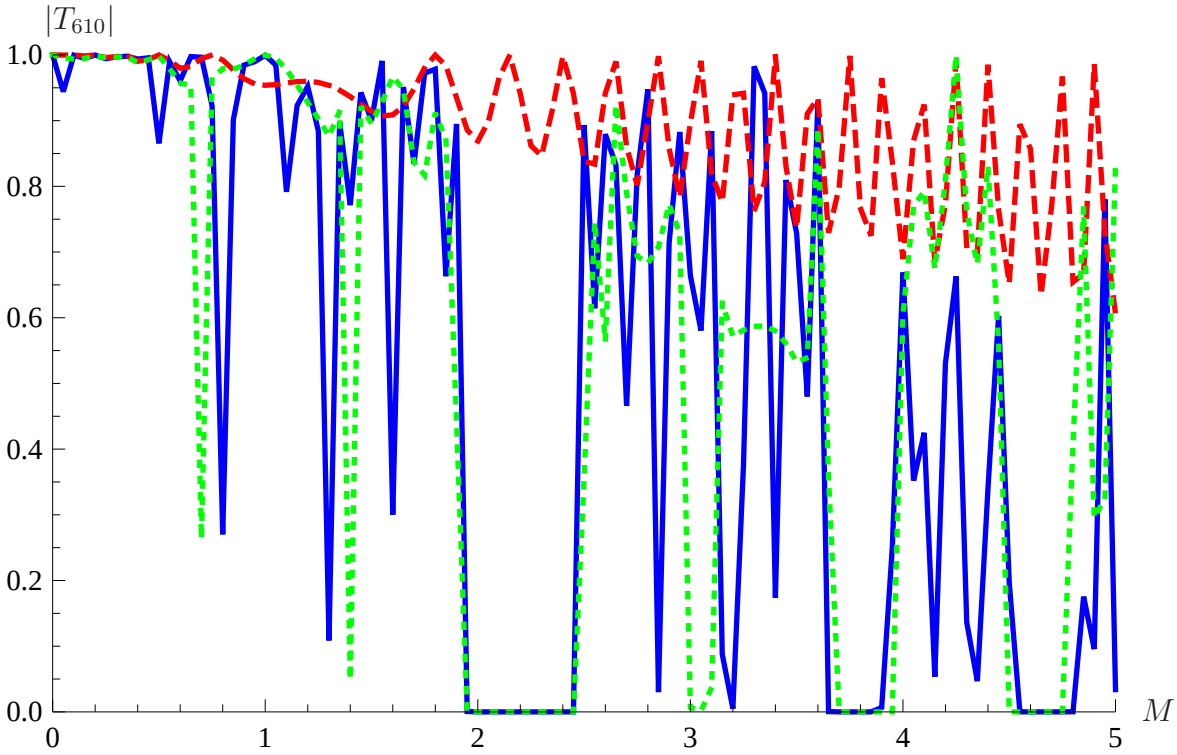

Figure 4.14: Comparison of the transmission through 610 point scatterers with Fibonacci chain (blue solid), period average structure (red dashed) and approximant (green dotted) distribution, for increasing mass of the point scatterers. The approximant used here is $\tau \approx \tau_6 = \frac{13}{8}$.

over three unit cells with the transmission for the approximant.

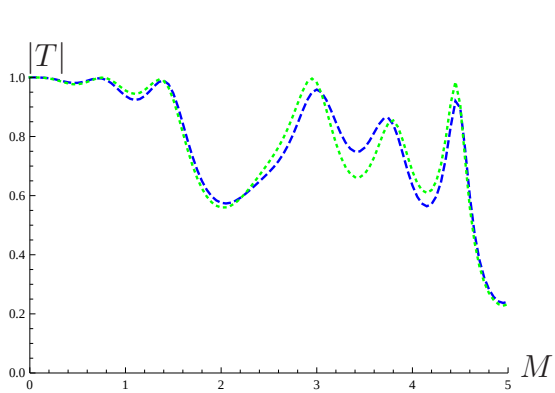

(a) Average taken over m for $0 \leq m \leq 2$.

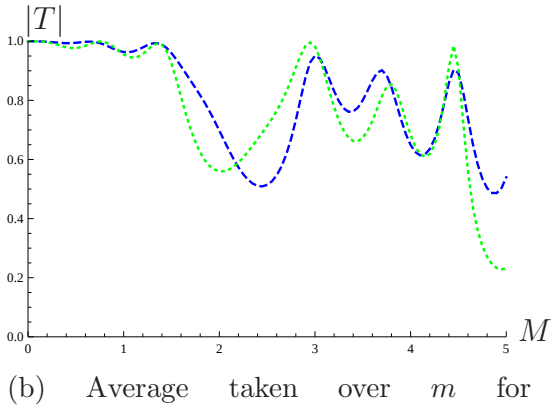

(b) Average taken over m for $26 \leq m \leq 28$.

Figure 4.15: Comparison of the average transmission through point scatterers with Fibonacci chain (blue dashed) and the transmission approximant (green dotted) distribution, for increasing mass M of the point scatterers, where the average over 3 varying cells of the Fibonacci chain has been taken. The approximant used here is $\tau \approx \frac{13}{8}$.

The left hand plot is for three cells from the origin, i.e. $0 \leq m \leq 2$, the right for three further away from the origin at $26 \leq m \leq 28$. We have averaged over three

cells as it was seen that the $n = 6$ approximant replicated the transmission of the Fibonacci chain well for a chain of 55 scatterers, three approximant unit cells contain 63 scatterers just over this length, so we expect good results for these.

The reason for the choice of the upper limit to be the 29th cell from the origin is that this gives is almost 610 point scatterers, which is the chain considered in figure 4.14 (in fact there are $29 \times \text{Fib}(8) = 29 \times 21 = 609$ scatterers). It can be seen, as expected, that closer to the origin the average transmission from the Fibonacci chain is better approximated by the approximant than further away. However, the approximation for $26 \leq m \leq 28$ should not be discounted as this still provides an excellent insight.

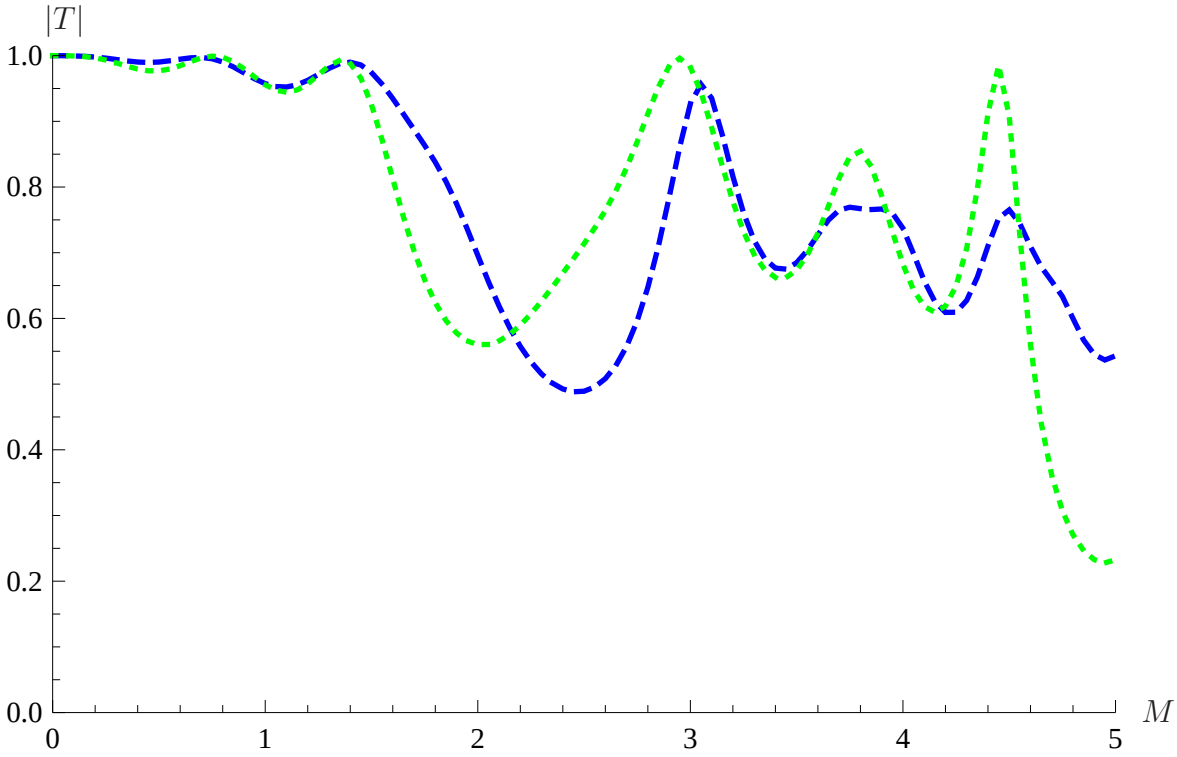

Figure 4.16: Comparison of the average transmission through point scatterers with Fibonacci chain (blue dashed) and the transmission approximant (green dotted) distribution, for increasing mass of the point scatterers, where the average over 29 varying cells of the Fibonacci chain for $0 \leq m \leq 28$ has been taken. The approximant used here is $\tau \approx \tau_6 = \frac{13}{8}$.

If the average over a larger number of unit cells is taken, a better average of the Fibonacci chain transmission will be achieved. Figure 4.16 depicts the average taken over 29 unit cells, with $0 \leq m \leq 28$. It is seen that the decrease in accuracy is not too great from the right hand plot in figure 4.15, suggesting that an average taken over just three cells manages to capture a good representation of the Fibonacci chain, and

thus it is not necessary to average over so many cells.

4.5 Wave scattering by an infinite approximant structure

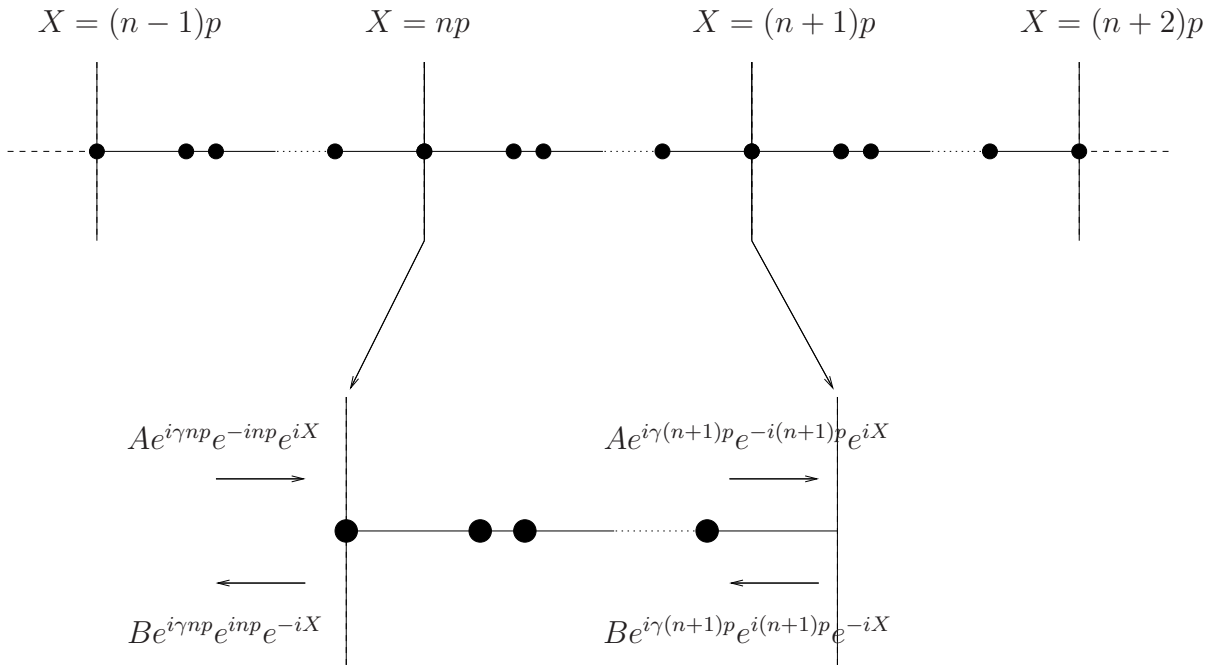

Figure 4.17: Infinite periodic lattice, with period of arbitrary approximant structure.

Now that it has been demonstrated that periodic structures in the form of an approximant provide good representations of the Fibonacci chain, consider the effective properties of such infinite periodic structures. As the quasiperiodic chain does not contain periodicity itself, Bloch wave analysis is not applicable. The infinite periodic approximant however should provide approximate effective properties of the infinite quasiperiodic chain which can be determined via Bloch wave analysis.

Although the computation of transmission and reflection coefficients for 1D quasiperiodic distributions of scatterers is rapid, the benefit of the computation of effective properties is that it provides simple formulae for overall properties of this, and other, quasiperiodic chains. The main motivation for this infinite periodic representation is for the extension into higher dimensions. Multiple scattering in 2D is much more complex than in 1D and thus more computationally intensive. The extension of the method used here into 2D will enable the rapid prediction of overall properties of a

2D quasiperiodic distribution of scatterers.

In figure 4.17 the breakdown of an infinite approximant lattice is depicted; one unit cell of the chosen approximant repeated infinitely many times. The figure also depicts the posed Bloch wave solution, in a manner similar to that of section 2.3.2, which is of the form,

$$u_n(X) = Ae^{i\gamma np}e^{-inp}e^{iX} + Be^{i\gamma np}e^{inp}e^{-iX}, \quad np - d < X \leq np, \tag{4.41}$$

$$u_{n+1}(X) = Ae^{i\gamma(n+1)p}e^{-i(n+1)p}e^{iX} + Be^{i\gamma(n+1)p}e^{i(n+1)p}e^{-iX}, \quad (n+1)p - d < X \leq (n+1)p, \tag{4.42}$$

where d is the distance between the last point scatterer in the cell and the end of the cell, i.e. the last scatterer in the $(n-1)$ cell and the first scatterer in the n cell.

This infinite periodic problem can be analysed with a different approach to that used in 2.3.2, by exploiting prior knowledge of the properties of the individual period. For instance, if there are m point scatterers within the periodic cell of length p_m then it is possible to formulate expressions for the transmission and reflection properties, T_m, R_m, T_m^o and R_m^o, using the recursive methods previously employed in this chapter. The outgoing Bloch wave solutions of the period can then be redefined as sums of the transmitted and reflected waves due to the two incident waves on the problem, analogously to 4.1.1. That is, the transmitted wave to the right of the cell is given by

$$Ae^{i\gamma(n+1)p_m}e^{-i(n+1)p_m} = Ae^{i\gamma np_m}e^{-inp_m}T_m + Be^{i\gamma(n+1)p_m}e^{i(n+1)p_m}R_m^o, \tag{4.43}$$

and the reflected wave to the left of the cell is given by

$$Be^{i\gamma np_m}e^{inp_m} = Ae^{i\gamma np_m}e^{-inp_m}R_m + Be^{i\gamma(n+1)p_m}e^{i(n+1)p_m}T_m^o. \tag{4.44}$$

Rearranging results in a matrix equation of the form

$$\mathbf{M}\begin{pmatrix} A \\ B \end{pmatrix} = \begin{pmatrix} T_m - e^{ip_m(\gamma-1)} & R_m^o e^{ip_m(\gamma+1)} \\ R_m & T_m^o e^{ip_m(\gamma+1)} - 1 \end{pmatrix}\begin{pmatrix} A \\ B \end{pmatrix} = \mathbf{0}. \tag{4.45}$$

Setting the determinant of $\mathbf{M}$ to zero,

$$\det(\mathbf{M}) = T_m T_m^o e^{ip_m(\gamma+1)} - T_m - T_m^o e^{2ip_m\gamma} + e^{ip_m(\gamma-1)} - R_m R_m^o e^{ip_m(\gamma+1)} \tag{4.46}$$

$$= -T_m^o e^{2ip_m\gamma} + \left(T_m T_m^o e^{ip_m} + e^{-ip_m} - R_m R_m^o e^{ip_m}\right)e^{i\gamma} - T_m \tag{4.47}$$

$$= 0, \tag{4.48}$$

gives an equation to solve for the unknown Bloch wave vector γ. This can be rearranged as

$$e^{ip_m\gamma} = \frac{1}{2T_m^o}\Bigg(T_m T_m^o e^{ip_m} + e^{-ip_m} - R_m R_m^o e^{ip_m} \pm \sqrt{(T_m T_m^o e^{ip_m} + e^{-ip_m} - R_m R_m^o e^{ip_m})^2 - 4T_m T_m^o}\Bigg) \tag{4.49}$$

$$= \pm\,\chi_m, \tag{4.50}$$

which leads to the result

$$\gamma_\pm = \frac{-i\log(\pm\chi_m)}{p_m}, \tag{4.51}$$

for which a choice of the positive or negative root must be made to determine the desired γ. Therefore it is possible to compute the effective wavenumber for an infinite periodic 1D lattice with periodic cell containing an arbitrary number and distribution of scatterers, with this simple equation (4.51). Exploiting prior knowledge of the microscale (the transmission and reflection coefficients for the periodic cell) has enabled a rapid computation of the effective properties on the macroscale. This approach enables solutions without the need to consider the two boundary conditions on each point scatterer within the period as in section 2.3.2 which would be computationally expensive for large cells. With this approach the number of simultaneous equations is always two, regardless of the period size!

For the n-approximant with the approximation $\tau \approx \tau_n = \frac{\mathrm{Fib}(n+1)}{\mathrm{Fib}(n)}$, there are $m = \mathrm{Fib}(n+2)$ point scatterers with a period of length

$$p_m = \mathrm{Fib}(n+1)L + \mathrm{Fib}(n)S, \tag{4.52}$$

and thus the calculations are straightforward.

Figure 4.18 depicts the imaginary component of the effective wavenumber γ for different approximant lattices as a function of the average spacing

$$\epsilon = \frac{\mathrm{Fib}(n+1)L + \mathrm{Fib}(n)S}{\mathrm{Fib}(n+2)}. \tag{4.53}$$

When there is an imaginary component of γ there is decay in the wave field and thus it is a stop band. In the diagram for the 6-approximant a numerical error occurs in the imaginary component, which can be neglected in this instance as it is only of interest to determine the frequencies of the stop bands and not the value of the imaginary

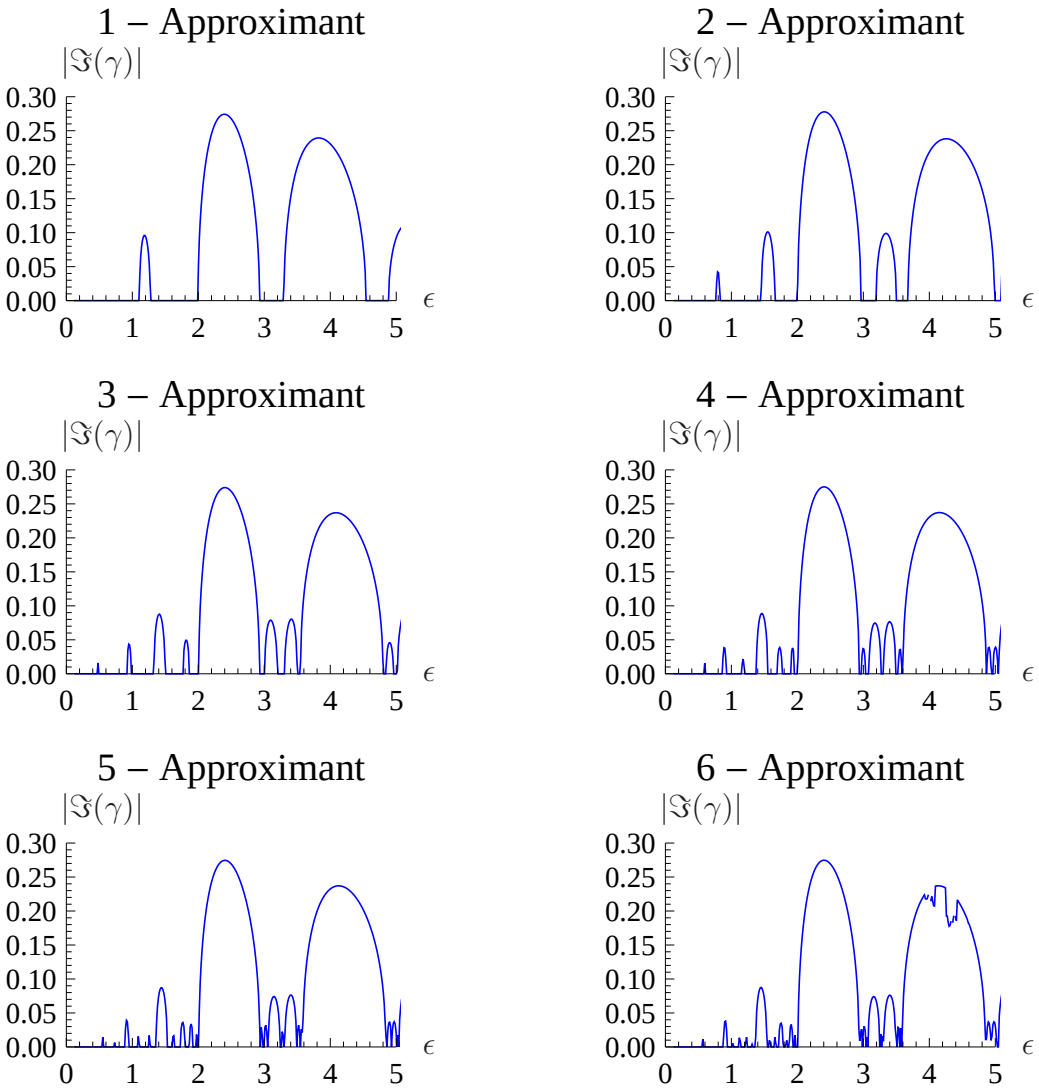

Figure 4.18: Comparison of the stop bands for varying infinite approximant lattices with $M = 0.7$.

component of γ. It is possible to see that the location of the stop bands converge as the accuracy of the approximant is increased. For example, figure 4.19 shows the position of the first stop band in terms of ϵ the average spacing as n is increased in the approximant, and rapid convergence can be seen. This implies that as n is increased and thus the resemblance of the approximant to the Fibonacci chain increases, accurate approximations of the effective properties of an infinite 1D quasiperiodic lattice are achieved. An approximant constructed with an approximation as low as $n = 6$ gives the converged position of the first stop band of the Fibonacci chain.

In 1D we have the benefit of being able to run computations for large numbers of scatterers rapidly. Therefore, it is possible to compare the band structure of the

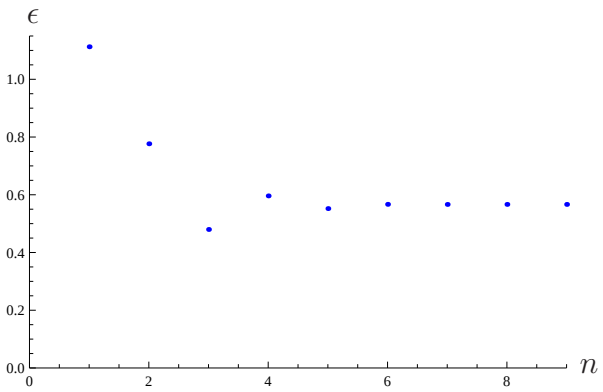

Figure 4.19: Comparison of the first stop band position for varying infinite approximant lattices with $M = 0.7$.

infinite approximant to a large Fibonacci chain. Figure 4.20 depicts the transmission coefficient for a Fibonacci distribution of Fib(55)=139583862445 scatterers for increasing ϵ, the non-dimensional average spacing scaled on the wavenumber. Excellent agreement with the infinite approximant results in figures 4.18 and 4.19 can be seen, further validating this approximation.

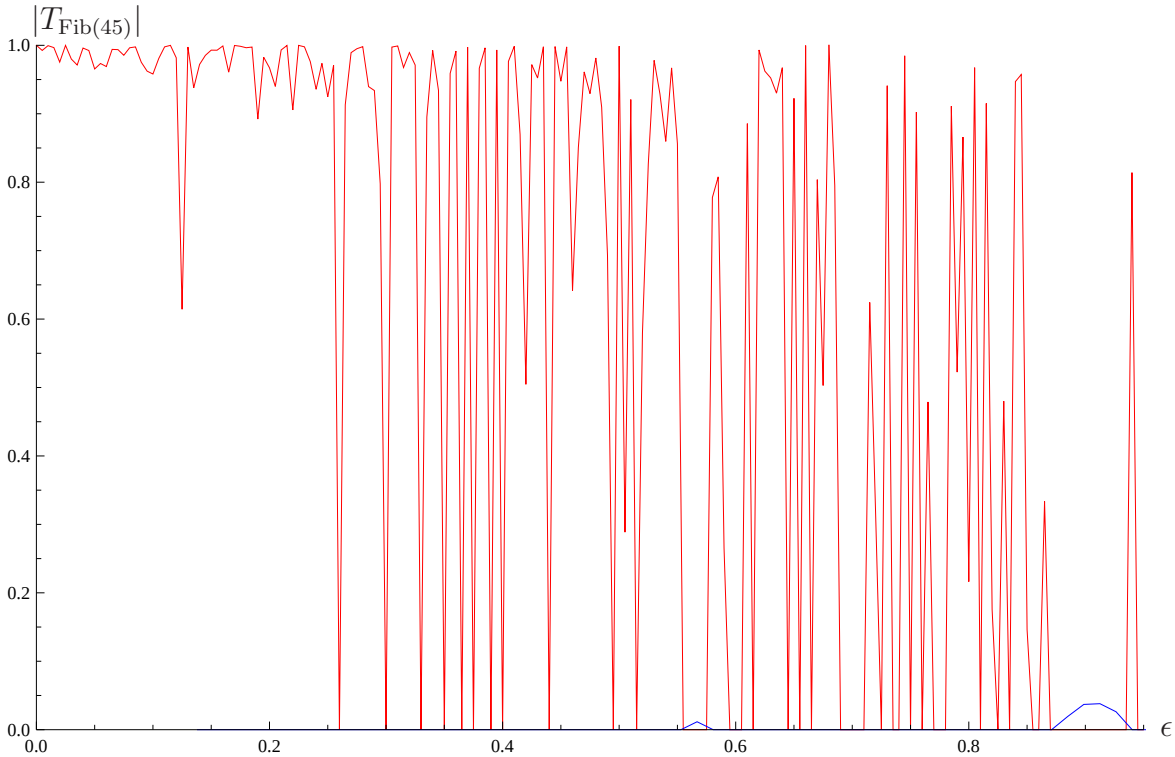

Figure 4.20: Transmission coefficient for a Fibonacci distribution of Fib(55) scatterers (red) compared to the infinite 6-approximant stop-band positions (blue), with $M = 0.7$.

4.6 Conclusions

This section has set out the motivation and ideas behind this thesis by considering a relatively simple 1D problem. Firstly, it was discussed how to solve the 1D wave scattering problem of waves along an infinite string with discrete point scatterers, i.e. masses or beads. Then fast recursive formulae were derived that determined the transmission and reflection of the wave propagation along arbitrary 1D point-scatterer distributions. With this methodology it is possible to formulate the transmission and reflection coefficients for different point scatterer distributions, allowing the comparison of the scattering properties of each.

1D wave propagation along infinite strings is well understood and discussed by Graff [33], for example. In this section we have extended his work to show how to analyse 1D wave propagation problems for point scatterers on strings with periodic, quasiperiodic and random distributions. The recursive formulation works by solving each scattering problem as the superposition of the solutions of two smaller sub-distributions. Working in such a way allows the formulation of results remarkably quickly, especially with the Fibonacci distribution whereby the number of point scatterers is increased by $\mathrm{Fib}(n)$ for the nth recursion. This means the distribution size is growing exponentially and it is possible to formulate the transmission properties for an extremely large number of point scatterers at great speed and efficiency.

With this new rapid formulation for the transmission and reflection coefficients it was shown how a comparison of a finite point scatterer distribution to a homogeneous inclusion of string of a different density can be drawn, and thus novel formulae for an effective wavenumber of a distribution of point scatterers was derived. This enabled the modelling of complicated distributions of point scatterers by a simple homogeneous string of particular density.

Comparisons of the transmission properties of the finite quasiperiodic Fibonacci distribution to periodic distributions were drawn. It was found that the periodic average structure, as described in section 3.2 only acts as a good approximation for relatively small values of mass $M = m/m_0$ of the point scatterers. Whereas, for approximants taken with an appropriate approximation of the golden ratio τ provide a much better model, even at larger M. The Fibonacci chain can be modelled well by

particular approximants, and thus we have determined a periodic distribution, which is easier to analyse.

It was shown that approximants determined by the approximation $\tau \approx \tau_n = \frac{\mathrm{Fib}(n+1)}{\mathrm{Fib}(n)}$ which have a unit cell containing $\mathrm{Fib}(n+2)$ point scatterers have capabilities of mimicking the full scattering properties of Fibonacci chain distributions of point scatterers with $\mathrm{Fib}(n+4)$ scatterers in total. Furthermore, "near" stop band properties were replicated for larger distributions than this, especially so with n as small as 6.

Rapid formulations were derived that determine the effective wavenumber of the infinite periodic approximant, exploiting knowledge of the transmission and reflection properties of the individual periods. This method can be applied to arbitrary repeating cells of any length and point scatterer distribution. It was shown that the position of the first cut off point converges as the accuracy of the approximant is increased, and thus an infinite Fibonacci chain lattice can be modelled with an approximant lattice. Again it was found that $n = 6$ gives an approximant which is a valid representation of the Fibonacci chain. These results were validated further by comparison to the transmission properties for a large Fibonacci distribution of scatterers.

In 1D it may seem redundant to find periodic models for the Fibonacci chain seeing as the recursive formulae for the Fibonacci chain works so fast, and thus it is easy and inexpensive to compute the scattering properties of extremely large quasiperiodic lattices. However, it has been demonstrated, in the 1D case, that the methodology of the construction of the periodic lattices, and their scattering properties, can be used effectively. This can now be extended into 2D or higher dimensions.

The work discussed in this chapter is easily extended to arbitrary distributions of point scatterers, and to other types of scatterers in 1D, some of this work is shown in appendix C. The formulae derived provide a novel insight into wave propagation through quasiperiodic media in 1D, and can be easily applied in many other situations.

Chapter 5

Two-dimensional wave scattering by a Fibonacci chain structure

The present section enables consideration of 1D quasiperiodicity within 2D multiple scattering. We consider infinite rows of small circular cylinders with all axes perpendicular to a 2D plane. Within each infinite row the scatterers are periodically separated, denoted the *in-row spacing*. The quasiperiodicity is introduced through the separation between each of the rows, denoted the *row spacing*.

5.1 Problem Statement

Consider an infinite row of circular cylinders distributed periodically along a line. We take propagation in the 2D plane perpendicular to the axes of the cylinders. Assume that the cylinders have small radii, as in section 2.4, allowing a simplification of the solution. We can then introduce quasiperiodic and random distributions by considering arrangements in which we have N infinite rows of periodically distributed cylinders, with quasiperiodic or random spacings between the rows. Similar problems have been considered before, with finite numbers of infinite periodic rows [13], [12], [55], [85]. However, none have considered the case of quasiperiodic distributions of rows. The previous works are designed to model rows of cylinders as tube bundles or ice floes. Tube bundles exist in devices such as heat exchange mechanisms in large industrial plants. The motivation for the understanding of wave propagation through such structures is for non-destructive testing of the device.

In this section the method applied will be discussed from first principles, without reference to these papers, as the notation and methods vary. Working in this way will allow the extension of the recursive method used in the 1D problems in chapter 4 to 2D.

5.1.1 One row

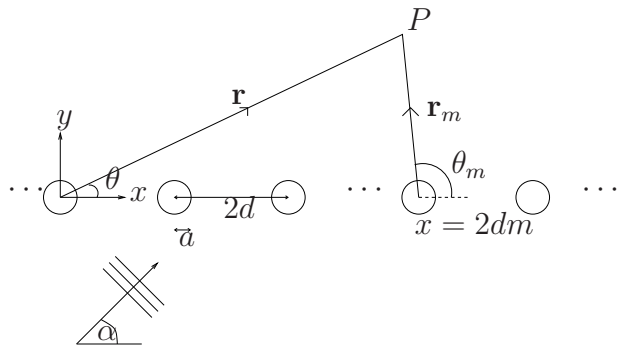

Figure 5.1: Set up for an infinite periodic row of cylinders with incident wave.

Begin by analysing the wave scattering properties for one row with an incident plane wave as depicted in figure 5.1. This problem has been considered by many before and is classed as a diffraction grating problem due to the effects of the periodic row on the scattered field. The first to investigate the scattering properties of the infinite periodic row of cylinders was Twersky, [79]. Many investigations followed in an attempt to evaluate the resultant infinite sum in the expression of the scattered field. One example is Linton's efficient evaluation [48] using integral representations and the Poisson summation formula. In this section we investigate the scattering from small cylinders and can therefore simplify the expression of the scattered field. We will discuss the method from first principles, due to this difference. It is desired to find the transmitted and reflected waves from this row so that it is possible to work recursively using the same method as in 1D, in chapter 4.

Consider an infinite row of small cylinders of radii a along a horizontal line with in-row spacing $2d$. Assume an incident field in the form of a plane wave of incident angle α, $u_{inc}(r,\theta) = e^{ikr\cos(\theta-\alpha)}$. Note that the following analysis is also applicable with an incident field in the form of a superposition of plane waves with different angles of incidence, and will be discussed later when considering multiple rows. The total field, which is a sum of the incident and scattered fields from the infinite number

of small circular cylindrical scatterers, is of the form

$$u(r,\theta) = u_{inc}(r,\theta) + \sum_{m=-\infty}^{\infty} b_m H_0^{(1)}(kr_m), \tag{5.1}$$

where

$$r_m = \left[(x-2dm)^2 + y^2\right]^{1/2}, \tag{5.2}$$

due to the horizontal arrangement, and b_m are the unknown coefficients.

Due to the periodicity in the x-direction of the forcing and the geometry, it is possible to employ Bloch's theorem to apply a periodicity condition to the coefficients b_m. Assume that

$$b_m = e^{2imkd\cos\alpha} B, \tag{5.3}$$

where k is the wavenumber. Substitution of the Bloch condition into equation (5.1) gives

$$u(r,\theta) = u_{inc}(r,\theta) + Be^{2itkd\cos\alpha} H_0^{(1)}(kr_t) + B\sum_{\substack{m=-\infty \\ m\neq t}}^{\infty} e^{2imkd\cos\alpha} H_0^{(1)}(kr_m). \tag{5.4}$$

Applying the sound-soft boundary condition on the t^{th} cylinder, as in section 2.4.3, gives

$$0 = u_{inc}(r=2dt,\theta=0) + Be^{2itkd\cos\alpha} C + B\sum_{\substack{m=-\infty \\ m\neq t}}^{\infty} e^{2imkd\cos\alpha} H_0^{(1)}(k2d|t-m|), \tag{5.5}$$

where C is the complex expansion of $H_0^{(1)}(ka)$ for $ka \to 0$, given by

$$C = \frac{2i}{\pi}\left(\gamma - \ln 2 + \ln(ka) + \frac{\pi}{2i}\right). \tag{5.6}$$

After some algebra and letting $m - t = n$, the unknown B is determined as

$$B = \frac{-u_{inc}(2dt,0)e^{-2itkd\cos\alpha}}{C + S_0^+(2kd,\cos\alpha) + S_0^-(2kd,\cos\alpha)}, \tag{5.7}$$

where $S_0^{\pm}$ are forms of Schlömilch series given by

$$S_0^{\pm}(2kd,\cos\alpha) = \sum_{n=1}^{\infty} e^{\pm 2ikdn\cos\alpha} H_0^{(1)}(2kdn). \tag{5.8}$$

For a single incident plane wave with angle of incidence α, the incident field can be written $u_{inc} = e^{ikr\cos(\theta-\alpha)}$. Therefore, in this instance, B can simplified to

$$B = \frac{-1}{C + S_0^+(2kd,\cos\alpha) + S_0^-(2kd,\cos\alpha)}. \tag{5.9}$$

In the form (5.8) $S_0^{\pm}$ can be solved via truncation of the infinite sum or by using ideas of Linton [48] to improve the convergence. Instead, evaluate these sums by expressing $H_0^{(1)}(2kdn)$ in integral form, [4] (9.1.25), and using contour integration.

$$S_0^+(2kd, \cos\alpha) = \sum_{n=1}^{\infty} e^{2ikdn\cos\alpha} H_0^{(1)}(2kdn) \tag{5.10}$$

$$= \sum_{n=1}^{\infty} e^{2ikdn\cos\alpha} \frac{1}{\pi i} \int_{-\infty}^{\infty+\pi i} e^{2kdn\sinh t} dt. \tag{5.11}$$

Introduce a convergence parameter in the sum, i.e.

$$S_0^+(2kd, \cos\alpha) = \sum_{n=1}^{\infty} e^{2ikdn\cos\alpha} \frac{1}{\pi i} \int_{-\infty}^{\infty+\pi i} e^{2kdn\sinh t} dt e^{-\epsilon n}, \tag{5.12}$$

where $|\epsilon| \ll 1$. The convergence parameter allows for an assumption of the convergence of the sum, and thus the possibility of interchanging the summation and integration. It can then be shown that

$$S_0^+(2kd, \cos\alpha) = \frac{1}{\pi i} \int_{-\infty}^{\infty+\pi i} \sum_{n=1}^{\infty} e^{2kdn(i\cos\alpha+\sinh t)-\epsilon n} dt, \tag{5.13}$$

and evaluating the sum gives

$$S_0^+(2kd, \cos\alpha) = \frac{1}{\pi i} \int_{-\infty}^{\infty+\pi i} \frac{e^{2ikd\cos\alpha+2kd\sinh t-\epsilon}}{1 - e^{2ikd\cos\alpha+2kd\sinh t-\epsilon}} dt. \tag{5.14}$$

In order to evaluate this integral we must find the poles and ensure that the contour does not pass through any. The poles of the integrand are when

$$1 - e^{2ikd\cos\alpha+2kd\sinh t-\epsilon} = 0. \tag{5.15}$$

That is,

$$e^{2in\pi} = e^{2ikd\cos\alpha+2kd\sinh t-\epsilon} \quad \Rightarrow \quad n\pi i = ikd\cos\alpha + kd\sinh t - \epsilon/2 \tag{5.16}$$

$$\Rightarrow \sinh t = \frac{(n\pi - kd\cos\alpha)i + \epsilon/2}{kd}. \tag{5.17}$$

See appendix B.2 for the full analysis of the pole positions.

Deform the contour of integration slightly from the step function to avoid the poles on the imaginary axis, figure 5.2 shows an example of the contour (red) and the poles (blue) for some specific choice parameters. The contour may have to be altered depending on the incident angle, wavenumber and separation used. Here note the

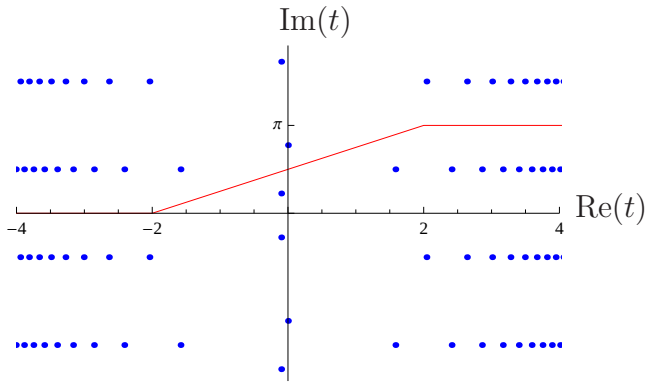

Figure 5.2: Plot of the contour of integration for S_0^+, and the poles. The parameters used here are $\alpha = \pi/4$, $k = 2$ and $2d = 1$.

contour of integration is from $-\infty$ to $\infty + \pi i$, so the contour in figure 5.2 must be followed from left to right.

To evaluate S_0^-, follow the same method. It is found that

$$S_0^-(2kd, \cos\alpha) = \frac{1}{\pi i}\int_{-\infty}^{\infty+\pi i} \frac{e^{-2ikd\cos\alpha + 2kd\sinh t - \epsilon}}{1 - e^{-2ikd\cos\alpha + 2kd\sinh t - \epsilon}} dt, \tag{5.18}$$

and the positions of the poles are given by

$$\sinh t = \frac{(n\pi + kd\cos\alpha)i}{kd} + \epsilon. \tag{5.19}$$

As long as it is ensured that the contours do not intersect any poles, the integrals can be evaluated rapidly by simply performing some numerical integration on Mathematica. Again, see appendix B.2 for the full analysis of the pole positions.

Now that the exact solution for the coefficient B has been found, the equation for the total field, (5.1), must be solved. It is now of the form

$$u(r,\theta) = u_{inc}(r,\theta) + B\sum_{m=-\infty}^{\infty} e^{2imkd\cos\alpha} H_0^{(1)}(kr_m), \tag{5.20}$$

where r_m is given by equation (5.2), B is given by equation (5.7), and $S_0^{\pm}$ are given by numerically integrating equations (5.14) and (5.18). The difficulty left to face is evaluating the infinite sum on the right hand side,

$$\sum_{m=-\infty}^{\infty} e^{2imkd\cos\alpha} H_0^{(1)}(kr_m). \tag{5.21}$$

This is much more difficult to simplify as the argument has multidirectional dependence r_m, not just x dependence as before.

Begin by writing $H_0^{(1)}(kr_m)$ in integral form, with x and y explicit, [3] (Appendix A),

$$H_0^{(1)}(kr) = \frac{1}{\pi i}\int_{-\infty}^{\infty} e^{-k\gamma(s)|y|+iksx}\frac{ds}{\gamma(s)}, \tag{5.22}$$

where $\gamma(s) = \sqrt{s^2-1}$, and s is some arbitrary integration variable. We must evaluate for argument kr_m rather than kr, so take the x and y length components of r_m, i.e.

$$H_0^{(1)}(kr_m) = \frac{1}{\pi i}\int_{-\infty}^{\infty} e^{-k\gamma(s)|y|+iks(x-2dm)}\frac{ds}{\gamma(s)}. \tag{5.23}$$

Apply the substitution

$$s = \cosh(t), \quad x = r\cos(\theta), \quad y = r\sin(\theta), \tag{5.24}$$

thus

$$ds = \sinh(t)dt \tag{5.25}$$

and

$$\gamma = -\sinh(t). \tag{5.26}$$

Equation (5.26) was chosen in order to ensure that $\gamma(s=0) = -i$ as required. For further details on the branch-cuts of γ and the contour path taken to avoid the branch-cuts see [3].

The limits of integration are now from $\infty + \pi i$ to $-\infty$. Now, when substituting in to the exponent, care must be taken with the $|y|$ term. The arrangement of scatterers is symmetric about the x-axis, and since the scatterers are isotropic, the scattered field will be symmetric about the x-axis too, i.e.

$$u_{sc}(r,\theta) = u_{sc}(r, 2\pi-\theta). \tag{5.27}$$

so it is possible to limit the range of r and θ to

$$r > 0, \quad 0 \le \theta < \pi, \tag{5.28}$$

and thus

$$|y| = |r\sin\theta| = r\sin\theta. \tag{5.29}$$

If it is required to calculate the field below the array, equation (5.27) should be applied.

After substitution the exponent becomes

$$\begin{aligned}
-k\gamma(s)|y| + iks(x-2dm) =& k\sinh(t)r\sin(\theta) + ik\cosh(t)r\cos(\theta) \\
& - ik\cosh(t)2dm && (5.30)\\
=& kr(-i\sinh(t)\sinh(i\theta) + i\cosh(t)\cosh(i\theta)) \\
& - 2ikdm\cosh(t) && (5.31)\\
=& kri\cosh(i\theta - t) - 2ikdm\cosh(t) && (5.32)\\
=& kr\sinh(i\theta - t + i\pi/2) - 2ikdm\cosh(t). && (5.33)
\end{aligned}$$

Substitution into equation 5.23 gives

$$H_0^{(1)}(kr_m) = -\frac{1}{\pi i}\int_{\infty+\pi i}^{-\infty} e^{kr\sinh(i\theta - t + i\pi/2) - 2ikdm\cosh(t)}dt. \tag{5.34}$$

To simplify this, use the substitution

$$t - i\theta - i\pi/2 = u - i\pi. \tag{5.35}$$

After some algebra the exponent (5.33) now becomes,

$$\begin{aligned}
& kr\sinh(i\theta - t + i\pi/2) - 2ikdm\cosh(t) && (5.36)\\
&= -kr\sinh(u - i\pi) - 2ikdm\cosh(u - i\pi/2 + i\theta) && (5.37)\\
&= -kr\left(-i\cosh(u)\sin(\pi) + \sinh(u)\cos(\pi)\right) \\
&\quad - 2ikdm\left(-i\sinh(u + i\theta)\sin(\pi/2) + \cosh(u + i\theta)\cos(\pi/2)\right) && (5.38)\\
&= kr\sinh(u) - 2kdm\sinh(u + i\theta). && (5.39)
\end{aligned}$$

Therefore the integral representation of the Hankel function can now be expressed by

$$\begin{aligned}
H_0^{(1)}(kr_m) &= -\frac{1}{\pi i}\int_{\infty+3i\pi/2-i\theta}^{-\infty+i\pi/2-i\theta} e^{kr\sinh(u) - 2kdm\sinh(u+i\theta)}du && (5.40)\\
&= \frac{1}{\pi i}\int_{-\infty+i\pi/2-i\theta}^{\infty+3i\pi/2-i\theta} e^{kr\sinh(u) - 2kdm\sinh(u+i\theta)}du. && (5.41)
\end{aligned}$$

To ensure that this integral exists it is necessary to check the integrand does not diverge at the extremes of our limits of integration. It can be easily checked that the $e^{kr\sinh(u)}$ term decays, but the $e^{-2kdm\sinh(u+i\theta)}$ term decays only if we define

$$\cosh u = -\sqrt{1 + \sinh^2 u}. \tag{5.42}$$

Now that $H_0^{(1)}(kr_m)$ is expressed in a compact form, return to evaluating the infinite sum (5.21).

Begin by introducing a convergence parameter in the sum, i.e.

$$\sum_{m=-\infty}^{\infty} e^{2imkd\cos\alpha} H_0^{(1)}(kr_m) e^{-\epsilon|m|}, \tag{5.43}$$

so that it is possible to later make some assumptions about the convergence of the sum, and thus the possibility of interchanging the summation and integration. Using the integral form for $H_0^{(1)}(kr_m)$ defined in (5.41), it can be shown that

$$\begin{aligned}
&\sum_{m=-\infty}^{\infty} e^{2imkd\cos\alpha} H_0^{(1)}(kr_m) e^{-\epsilon|m|} \\
&= \sum_{m=-\infty}^{\infty} e^{2imkd\cos\alpha} \frac{1}{\pi i} \int_{-\infty+i\pi/2-i\theta}^{\infty+3i\pi/2-i\theta} e^{kr\sinh(u)-2kdm\sinh(u+i\theta)} e^{-\epsilon|m|} du && (5.44)\\
&= \frac{1}{\pi i} \int_{-\infty+i\pi/2-i\theta}^{\infty+3i\pi/2-i\theta} e^{kr\sinh(u)} \sum_{m=-\infty}^{\infty} e^{2imkd\cos\alpha} e^{-2kdm\sinh(u+i\theta)} e^{-\epsilon|m|} du && (5.45)\\
&= \frac{1}{\pi i} \int_{-\infty+i\pi/2-i\theta}^{\infty+3i\pi/2-i\theta} e^{kr\sinh(u)} \left\{ \sum_{m=0}^{\infty} e^{(2kd(i\cos\alpha-\sinh(u+i\theta))-\epsilon)m} \right. \\
&\qquad \left. + \sum_{m=1}^{\infty} e^{(-2kd(i\cos\alpha-\sinh(u+i\theta))-\epsilon)m} \right\} du. && (5.46)
\end{aligned}$$

Reducing the sums gives,

$$\begin{aligned}
&\sum_{m=-\infty}^{\infty} e^{2imkd\cos\alpha} H_0^{(1)}(kr_m) e^{-\epsilon|m|} \\
&= \frac{1}{\pi i} \int_{-\infty+i\pi/2-i\theta}^{\infty+3i\pi/2-i\theta} e^{kr\sinh(u)} \left\{ \frac{1}{1-e^{2kd(i\cos\alpha-\sinh(u+i\theta))-\epsilon}} \right. && (5.47)\\
&\qquad \left. + \frac{e^{-2kd(i\cos\alpha-\sinh(u+i\theta))-\epsilon}}{1-e^{-2kd(i\cos\alpha-\sinh(u+i\theta))-\epsilon}} \right\} du && (5.48)\\
&= \frac{1}{\pi i} \left(I_1 + I_2 \right), && (5.49)
\end{aligned}$$

where

$$I_1 = \int_{-\infty+i\pi/2-i\theta}^{\infty+3i\pi/2-i\theta} e^{kr\sinh(u)} \frac{1}{1-e^{2kd(i\cos\alpha-\sinh(u+i\theta))-\epsilon}} du \tag{5.50}$$

and

$$I_2 = \int_{-\infty+i\pi/2-i\theta}^{\infty+3i\pi/2-i\theta} e^{kr\sinh(u)} \frac{e^{-2kd(i\cos\alpha-\sinh(u+i\theta))-\epsilon}}{1-e^{-2kd(i\cos\alpha-\sinh(u+i\theta))-\epsilon}} du. \tag{5.51}$$

Remembering that we are only considering small ϵ , if $\epsilon = 0$ then $I_1 = -I_2$ and thus the two integrals cancel out. Therefore in order to find the solution to (5.49), we must

consider the sum of the residues of the two integrals only. The pole positions must be found as for $S_0^{\pm}$.

For I_1 the poles are given by

$$\sinh(u+i\theta) = \left(\cos\alpha - \frac{n\pi}{kd}\right) i - \frac{\epsilon}{kd}, \tag{5.52}$$

which is similar to the equations we get for $S_0^{\pm}$ in appendix B.2, except here

$$\sinh(u+i\theta) = \sinh(v) = Ai - \epsilon. \tag{5.53}$$

In comparison to equation (B.6), here we are subtracting ϵ and A is defined by

$$A = \cos\alpha - \frac{n\pi}{kd}. \tag{5.54}$$

With these slight differences, follow an analogous method to that of appendix B.2, to find that for **case 1** ($|A| < 1$ and taking the top of the $\pm$ or $\mp$) the poles are given by

$$v \approx -\epsilon + (A + 2m\pi)\, i, \tag{5.55}$$

i.e. a finite number of poles to the left of the imaginary axis. For **case 2** ($|A| < 1$ and taking the bottom of the $\pm$ or $\mp$)

$$v \approx \epsilon + ((2m+1)\pi - A)\, i, \tag{5.56}$$

a finite number of poles to the right of the imaginary axis. But $v \approx \epsilon + m\pi i$ and $v \approx \epsilon + (2m+1)\pi i$ for $A = 0$. For **case 3(a)** ($A > 1$ and taking the top of the $\pm$ or $\mp$) it is found that

$$v \approx \ln[2A] + \left(\frac{\pi}{2} + 2m\pi + \frac{\epsilon}{A}\right) i, \tag{5.57}$$

just above the line $i\pi/2 + 2m\pi i$ to $i\pi/2 + 2m\pi i + \infty$. **Case 3(b)** ($A < -1$ and taking the top of the $\pm$ or $\mp$) gives, for $A = -\bar{A}$,

$$v \approx \ln\left[2\bar{A}\right] + \left(\frac{3\pi}{2} + 2m\pi - \frac{\epsilon}{\bar{A}}\right) i, \tag{5.58}$$

just below the line $3i\pi/2 + 2m\pi i$ to $3i\pi/2 + 2m\pi i + \infty$. **Case 4(a)** ($A > 1$ and taking the bottom of the $\pm$ or $\mp$) gives

$$v \approx -\ln[2A] + \left(\frac{\pi}{2} + 2m\pi - \frac{\epsilon}{A}\right) i, \tag{5.59}$$

just below the line $i\pi/2+2m\pi i$ to $i\pi/2+2m\pi i-\infty$. **Case 4(b)** ($A<-1$ and taking the bottom of the $\pm$ or $\mp$) gives

$$v \approx -\ln\left[2\bar{A}\right] + \left(-\frac{\pi}{2} + 2m\pi + \frac{\epsilon}{\bar{A}}\right) i, \tag{5.60}$$

just above the line $-i\pi/2+2m\pi i$ to $-i\pi/2+2m\pi i-\infty$.

The approach to finding the poles for I_2 is very similar as for I_1. The poles of I_2 are given by the expression

$$\sinh(v) = \sinh(u+i\theta) = \left(\cos\alpha + \frac{n\pi}{kd}\right) i + \epsilon = Ai + \epsilon, \tag{5.61}$$

which is the same formulation as for $S_0^{\pm}$ in appendix B.2 but with a different definition for A.

Figures 5.3 and 5.4 show the positions of the poles for I_1 and I_2 respectively, showing that it is possible to deform the contour path for I_1 up and to the left slightly, and down and to the right for I_2 without crossing any of the poles. Re-express I_2 as

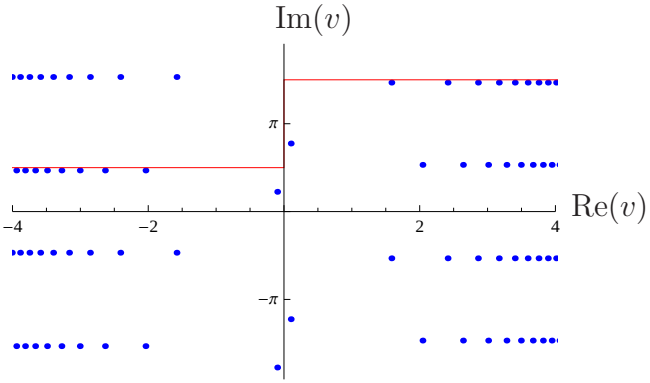

Figure 5.3: Plot of the contour of integration for I_1, and the poles. The parameters used here are $\alpha=\pi/4$, $k=2$, $2d=1$ and $\epsilon=0.1$.

$$I_2 = -\int_{\infty+3i\pi/2-i\theta}^{-\infty+i\pi/2-i\theta} e^{kr\sinh(u)} \frac{e^{-2kd(i\cos\alpha-\sinh(u+i\theta))-\epsilon}}{1-e^{-2kd(i\cos\alpha-\sinh(u+i\theta))-\epsilon}} du. \tag{5.62}$$

Sum the two integrals together and form a closed loop with the contour paths, letting $\epsilon\to 0$. See figure 5.5 to depict this. Close the loop at $\pm\infty$ which is justifiable since the residues become negligible at these point, this will be discussed further in section 5.1.1. Now I_1+I_2 can be found simply using Cauchy's residue theorem

$$I_1 + I_2 = -2\pi i \times \sum \text{Residues}, \tag{5.63}$$

and so

$$u(r,\theta) = u_{inc}(r,\theta) - 2B\sum \text{Residues}, \tag{5.64}$$

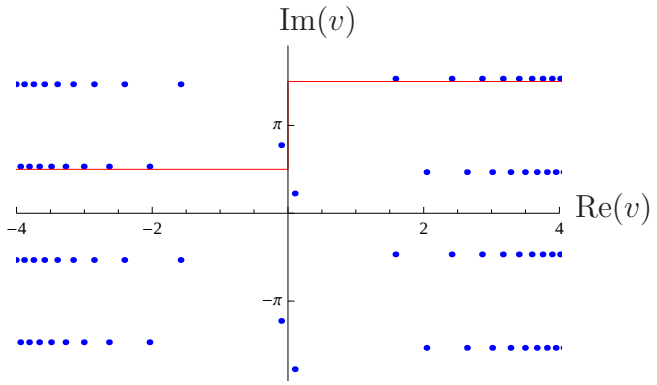

Figure 5.4: Plot of the contour of integration for I_2, and the poles. The parameters used here are $\alpha = \pi/4$, $k = 2$, $2d = 1$ and $\epsilon = 0.1$.

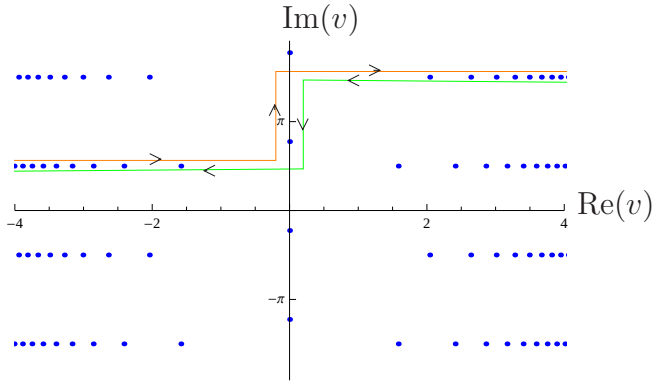

Figure 5.5: Plot of the contour of integration for $I_1 + I_2$, and the poles. The parameters used here are $\alpha = \pi/4$, $k = 2$, $2d = 1$.

where the family of residues arise from the poles within the contour shown in figure 5.5.

Convergence of the Sums of Residues

It is well known that if a function f can be expressed as a quotient of two functions

$$f(z) = \frac{g(z)}{h(z)}, \tag{5.65}$$

with $h(c) = 0$, and $h'(c) \neq 0$, for simple poles at c, then the residue at these points c, are given by

$$Res(f, c) = \frac{g(c)}{h'(c)}. \tag{5.66}$$

Inspection of the equation for I_1, (5.50), shows for $f_1(u)$, the integrand of I_1, that

$$g_1(u) = e^{kr \sinh u}, \tag{5.67}$$

$$h_1(u) = 1 - e^{2kd(i\cos\alpha - \sinh(u+i\theta))}, \tag{5.68}$$

$$h_1'(u) = 2kd \cosh(u + i\theta) e^{2kd(i\cos\alpha - \sinh(u+i\theta))}. \tag{5.69}$$

Since the exponential in equation (5.69) is equal to 1 at the poles u_n,

$$Res(f_1, u_n) = \frac{e^{kr\sinh u_n}}{2kd\cosh(u_n + i\theta)}. \tag{5.70}$$

Similarly, the residues for I_2 are given by

$$Res(f_2, u_n) = \frac{e^{kr\sinh u_n}}{2kd\cosh(u_n + i\theta)}. \tag{5.71}$$

To prove the convergence of the sums, consider the general equation for the residues given by

$$\sinh v_n = Ai, \tag{5.72}$$

for $A = \cos\alpha + \frac{n\pi}{kd}$. First evaluate the numerator of the residue,

$$\begin{aligned} \sinh u_n &= \sinh(v_n - i\theta) && (5.73)\\ &= \sinh v_n \cosh(-i\theta) + \cosh v_n \sinh(-i\theta) && (5.74)\\ &= Ai\cos\theta - i\cosh v_n \sin\theta. && (5.75) \end{aligned}$$

Using the definition of $\cosh v_n$ derived earlier in equation (5.42) this becomes

$$\begin{aligned} \sinh u_n &= i(A\cos\theta + \sqrt{1-A^2}\sin\theta) && (5.76)\\ &= Ai\cos\theta - \sqrt{A^2-1}\sin\theta. && (5.77) \end{aligned}$$

Thus the numerator can be rewritten as

$$e^{kr\sinh u_n} = e^{ikrA\cos\theta}e^{-kr\sqrt{A^2-1}\sin\theta}, \tag{5.78}$$

which includes an oscillatory term and a decaying term for $|A| \to \infty$ and $0 < \sin\theta < 1$, and the denominator is

$$2kd\cosh(u_n + i\theta) = 2kd\cosh v_n = -2kdi\sqrt{A^2-1}. \tag{5.79}$$

Therefore

$$Res(f_1, u_n) = Res(f_2, u_n) = \frac{e^{ikrA\cos\theta}e^{-kr\sqrt{A^2-1}\sin\theta}}{-2kdi\sqrt{A^2-1}}, \tag{5.80}$$

which is converging at an exponential rate. This justifies our ability to close the loop of $I_1 + I_2$ at $\pm\infty$, as the residues will be negligible for large $|A|$.

What we find in fact is that the only residues that contribute significantly to this infinite sum are the ones for which

$$|A| = \left|\cos\alpha + \frac{n\pi}{kd}\right| < 1. \tag{5.81}$$

These residues represent the propagating modes of the scattering. For $|A| > 1$, the modes are evanescent, they decay rapidly, and will thus will have no effect on the field at a sufficient distance away from the array. Due to the exponential decay, this distance does not have to be great. As can be seen in figure 5.6, the evanescent modes give almost no contribution to the scattered field at a distance just above $r = 1$ away from the array (with $k = 5$).

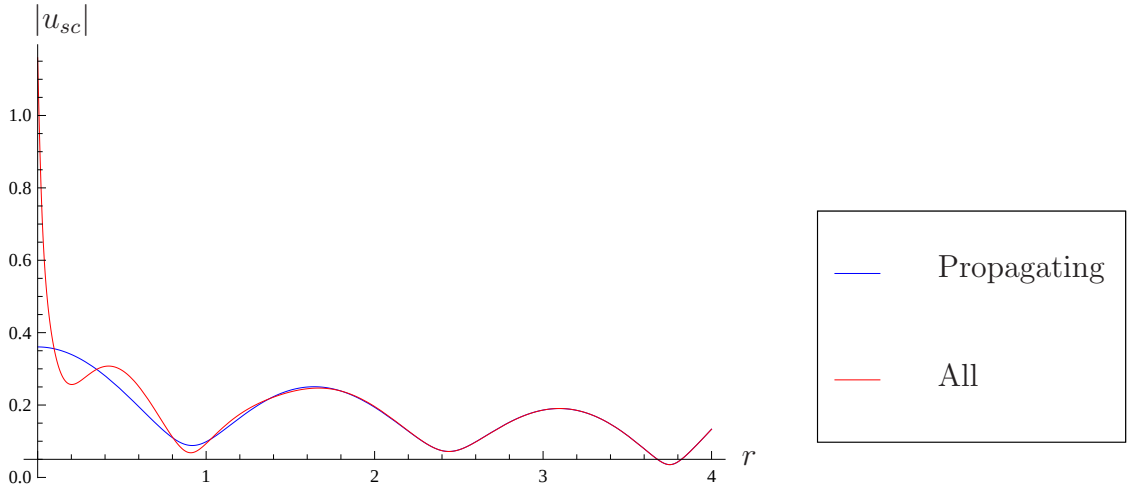

Figure 5.6: Scattered field for an infinite periodic array with $k = 5$, $a = 0.001$, $d = 1$, $\alpha = \pi/4$ and $\theta = \pi/4$. The blue curve shows the scattered field when we only consider the propagating plane waves for which $|A| < 1$, the red curve is the scattered field when taking into consideration the evanescent modes too.

Because the evanescent modes decay so quickly it is justifiable to represent the field as a sum of propagating plane waves, when "far" from the row. With these finite sums, it is possible to express the field in terms of transmission and reflection. The transmission will include the propagating modes through the row. The reflected field will include the propagating modes directed back from the row. With this it will be possible to extend this work to multiple rows.

Reflection and transmission

It has been demonstrated that the reflection and transmission coefficients from an infinite row of periodically spaced small circular cylinders can be approximated as

finite sums of propagating modes. Each of these modes represents a propagating plane wave travelling at a particular angle from the horizontal. The angles at which these propagating waves travel can be recovered from the "wave-like" term of the residues, (5.78):

$$\begin{aligned} e^{kr\sinh u_m} &= e^{ikr(A_m\cos\theta + i\sqrt{A_m^2-1}\sin\theta)} \\ &= e^{ikr(\cos\psi_m\cos\theta+\sin\psi_m\sin\theta)} \\ &= e^{ikr\cos(\theta-\psi_m)}, \end{aligned} \tag{5.82}$$

where

$$|A_m| = |\cos\psi_m| = \left|\cos\alpha + \frac{m\pi}{kd}\right| < 1, \quad m \in \mathbb{Z}. \tag{5.83}$$

This is now of the form of a plane wave propagating at an angle $0 < \psi_m < \pi$ from the horizontal, giving the transmitted scattering angles. Since the row is symmetric about $y = 0$, the reflected scattering angles are given by $2\pi - \psi_m$, where the angle is defined to always be taken clockwise from the x-axis, to the direction of travel. Express plane waves travelling in the negative y-direction by

$$e^{ikr\cos(\theta-(2\pi-\alpha))} = e^{ikr\cos(\theta+\alpha)}. \tag{5.84}$$

There exist a finite number of m that satisfy (5.83). Define the smallest such m by m_- and the largest by m_+ so that $m \in \mathbf{m} = \{m_-, \ldots, m_+\}$, and the number of transmitted (and reflected) is given by the number of elements in $\mathbf{m}$. In previous sections r and θ were restricted such that $r > 0$ and $0 < \theta < \pi$, so the equation for the total field (5.64) was valid above the array, i.e. the transmitted field,

$$u(r,\theta) = u_{inc}(r,\theta) + u_{sc}(r,\theta) \tag{5.85}$$

$$= u_{inc}(r,\theta) - 2B\sum \text{Residues} \tag{5.86}$$

$$= u_{inc}(r,\theta) + 2B\sum_{m=m_-}^{m_+} \frac{e^{ikr\cos(\theta-\psi_m)}}{2kdi\sqrt{A_m^2-1}}, \tag{5.87}$$

using the equation for the residues (5.80), equation (5.82), and rewriting A as A_m to show that it is a function of m. The form of B was given in equation (5.9) for an incident plane wave.

It is possible to associate α, the angle of incidence of the plane wave, with A_0, and

say $\alpha = \psi_0$, allowing a simplification to equation (5.87),

$$u(r,\theta) = \sum_{m=m_-}^{m_+} \left(\delta_{0m} + \frac{B}{kdi\sqrt{A_m^2 - 1}} \right) e^{ikr\cos(\theta - \psi_m)}. \tag{5.88}$$

From this expression extract the form of the transmission coefficients to be

$$t_m = \delta_{0m} + \frac{B}{kdi\sqrt{A_m^2 - 1}}, \tag{5.89}$$

for each of the propagating angles ψ_m.

A more general expression can be given for the transmission coefficients with an incident field comprising of a sum of plane waves. Any choice of number and angle of incidence of the plane waves can be chosen. However, in the following we restrict the analysis to consider an incident field which is a superposition of plane waves propagating at a set of angles determined by (5.83) for any arbitrary ψ_0. That is, define the incident wave to be of the form

$$u_{inc}(r,\theta) = \sum_{n=m_-}^{m_+} C_n e^{ikr\cos(\theta - \psi_n)}, \tag{5.90}$$

then the total field is just a sum of all the total fields for each incident angle. That is,

$$u(r,\theta) = \sum_{n=m_-}^{m_+} C_n \left(e^{ikr\cos(\theta-\psi_n)} + B_n \sum_{m=-\infty}^{\infty} e^{2imkd\cos\psi_n} H_0^{(1)}(kr_m) \right), \tag{5.91}$$

where B is now written as B_n as it depends on the incident angle ψ_n,

$$B_n = \frac{-1}{C + S_0^+(2kd, \cos\psi_n) + S_0^-(2kd, \cos\psi_n)}. \tag{5.92}$$

The total field can be rewritten as for one scattering angle,

$$u(r,\theta) = \sum_{n=m_-}^{m_+} C_n \left(e^{ikr\cos(\theta-\psi_n)} + \frac{B_n}{kd} \sum_{m=m_-}^{m_+} \frac{e^{ikr\cos(\theta-\psi_m)}}{\sqrt{1 - A_m^2}} \right), \tag{5.93}$$

where we note that each incident angle ψ_n for $n \in \mathbf{m} = \{m_-, \ldots, m_+\}$ scatters plane waves at each ψ_m for $m \in \mathbf{m}$, see appendix B.3 for the proof of this. Therefore, the transmission coefficients for multiple incident plane waves are given by

$$t_m = C_m + \sum_{n=m_-}^{m_+} \frac{C_n B_n}{kd\sqrt{1 - \cos^2\psi_m}}, \tag{5.94}$$

and the reflection coefficients are

$$r_m = \sum_{n=m_-}^{m_+} \frac{C_n B_n}{kd\sqrt{1 - \cos^2\psi_m}}. \tag{5.95}$$

It is also possible to write these reflection and transmission coefficients in terms of matrices, which will make computations easier when extending to work with larger numbers of rows. For instance, let

$$\mathbf{t} = \left(t_{m_-} \cdots t_{m_+} \right), \tag{5.96}$$

then

$$\mathbf{t} = \begin{pmatrix} C_{m_-} & \cdots & C_{m_+} \end{pmatrix} \left(\mathbf{I_M} + \frac{1}{kd} \begin{pmatrix} \frac{B_{m_-}}{\sqrt{1-\cos\psi_{m_-}}} & \cdots & \frac{B_{m_-}}{\sqrt{1-\cos\psi_{m_+}}} \\ \vdots & \ddots & \vdots \\ \frac{B_{m_+}}{\sqrt{1-\cos\psi_{m_-}}} & \cdots & \frac{B_{m_+}}{\sqrt{1-\cos\psi_{m_+}}} \end{pmatrix} \right) \tag{5.97}$$

$$= \mathbf{C} \left(\mathbf{I_M} + \boldsymbol{\gamma} \right), \tag{5.98}$$

where M is the number of scattering/incident angles and $\mathbf{I_M}$ is the $M \times M$ identity matrix. Similarly, the reflection coefficient vector can be expressed as

$$\mathbf{r} = \mathbf{C}\boldsymbol{\gamma}. \tag{5.99}$$

With these transmission and reflection coefficients it is now possible to extend the method and notation developed for one array, to multiple arrays.

5.2 Recursive formulation for wave scattering by infinite rows of scatterers with a Fibonacci chain distribution

With the solutions for the reflection and transmission for the single row it is possible to solve for the interaction between N rows via a composition of these solutions, as in 1D in section 4. We want to extend the work we did in 1D with the Fibonacci chain into 2D. This can be achieved by introducing a variation in row spacings between the infinite rows of cylinders, which is determined via the Fibonacci chain, as in figure 5.7. With the T and R found in section 5.1.1, the method will not differ from that used in 1D.

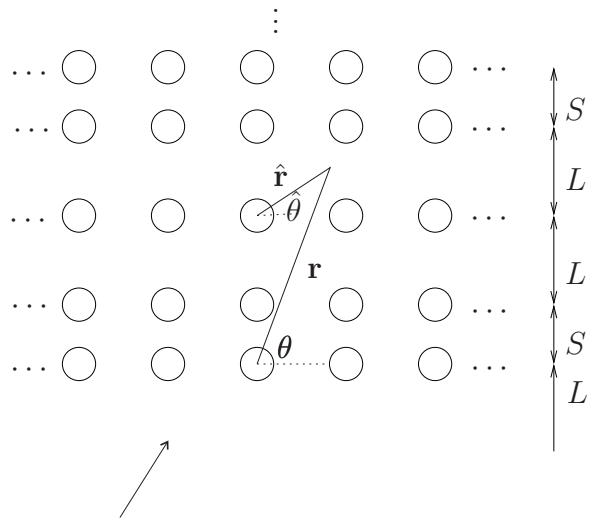

Figure 5.7: Set up for N infinite periodic rows of cylinders with separations determined via the Fibonacci chain, with incident wave of some form.

5.2.1 Phase difference

The work in the previous section was for a row along the horizontal at $y = 0$. This section will require the consideration of rows along various y positions. For Fibonacci chain separations between the rows, the y positions of the rows will be given by

$$y = q(N)S = (\mathrm{Fib}(N-1)\tau + \mathrm{Fib}(N-2))\, S, \tag{5.100}$$

as in the 1D case.

The calculations for one row must be adapted, to an arbitrary position. Previously the field was determined in terms of r and θ, the observation point, in relation to the origin. Now, define new parameters $\hat{r}$ and $\hat{\theta}$, which give the same observation point but in relation to an array along $y = q(N)S$ for arbitrary N, i.e.

$$\hat{r}\cos\hat{\theta} = r\cos\theta \tag{5.101}$$

$$\hat{r}\sin\hat{\theta} = r\sin\theta - q(N)S, \tag{5.102}$$

as depicted in figure 5.7. The solution must be determined for a row at $y = q(N)S$ in terms of $\hat{r}$ and $\hat{\theta}$.

It is possible to rewrite plane waves as functions of $\hat{r}$ and $\hat{\theta}$, as plane waves as functions of r and θ. Define a plane wave travelling in the positive y-direction at angle α by p_T and in the negative y-direction by p_R. Therefore

$$p_T(\hat{r},\hat{\theta}) = e^{ik\hat{r}\cos(\hat{\theta}-\alpha)}, \tag{5.103}$$

then upon expanding, it is found that

$$p_T(\hat{r},\hat{\theta}) = e^{ik\hat{r}(\cos\hat{\theta}\cos\alpha+\sin\hat{\theta}\sin\alpha)} \tag{5.104}$$

$$= e^{ikr(\cos\theta\cos\alpha+\sin\theta\sin\alpha)}e^{-ikq(N)S\sin\alpha} \tag{5.105}$$

$$= e^{-ikq(N)S\sin\alpha}p_T(r,\theta). \tag{5.106}$$

Similarly,

$$p_R(\hat{r},\hat{\theta}) = e^{ik\hat{r}\cos(\hat{\theta}+\alpha)} = e^{ikq(N)S\sin\alpha}p_R(r,\theta). \tag{5.107}$$

Equations (5.106) and (5.107) show that plane waves incident at any line $y = q(N)S$ can be expressed as just a phase shift multiplied by the form of plane waves incident at the line $y = 0$. Therefore it is very easy to make an adjustment, involving a phase shift, to the work in the previous section.

As an example, assume a sum of plane waves incident from below on an array at $y = L$ of the form

$$u_{inc}(r,\theta) = \sum_{m=m_-}^{m_+} C_m e^{ikr\cos(\theta-\psi_m)}, \tag{5.108}$$

where $m \in \mathbf{m} = \{m_-,\ldots,m_=\}$ are the integers that satisfy equation (5.83) for some arbitrary ψ_0. The incident wave that the array will see, in terms of $\hat{r}$ and $\hat{\theta}$, is

$$u_{inc}(r,\theta) = \sum_{m=m_-}^{m_+} C_m e^{ikL\sin\psi_m}e^{ik\hat{r}\cos(\hat{\theta}-\psi_m)}. \tag{5.109}$$

Therefore, the total field will be of the form, similar to equation (5.93),

$$u(r,\theta) = \sum_{n=m_-}^{m_+} C_n e^{ikL\sin\psi_n}\left(e^{ik\hat{r}\cos(\hat{\theta}-\psi_n)} + \frac{B_n}{kd}\sum_{m=m_-}^{m_+}\frac{e^{ik\hat{r}\cos(\hat{\theta}-\psi_m)}}{\sqrt{1-A_m^2}}\right). \tag{5.110}$$

Rewriting in terms of the original coordinate system, it is found that

$$u(r,\theta) = \sum_{n=m_-}^{m_+} C_n\left(e^{ikr\cos(\theta-\psi_n)} + \frac{e^{ikL\sin\psi_n}B_n}{kd}\sum_{m=m_-}^{m_+}\frac{e^{-ikL\sin\psi_m}e^{ikr\cos(\theta-\psi_m)}}{\sqrt{1-A_m^2}}\right). \tag{5.111}$$

Thus the transmission and reflection coefficients for an array along $y = L$ are given by

$$t_m = C_m + \frac{\sum_{n=m_-}^{m_+} C_nB_ne^{ikL(\sin\psi_n-\sin\psi_m)}}{kd\sqrt{1-\cos^2\psi_m}}, \tag{5.112}$$

$$r_m = \frac{\sum_{n=m_-}^{m_+} C_nB_ne^{ikL(\sin\psi_n-\sin\psi_m)}}{kd\sqrt{1-\cos^2\psi_m}}, \tag{5.113}$$

or in matrix form

$$\mathbf{t}(L) = \mathbf{C}\left(\mathbf{I_M} + \mathbf{\Gamma_T}(L)\right), \tag{5.114}$$

$$\mathbf{r}(L) = \mathbf{C}\mathbf{\Gamma_R}(L), \tag{5.115}$$

where

$$\mathbf{\Gamma_T}(L) = \frac{1}{kd}\begin{pmatrix} \frac{e^{ikL(\sin\psi_{m_-} - \sin\psi_{m_-})}B_{m_-}}{\sqrt{1-\cos^2\psi_{m_-}}} & \cdots & \frac{e^{ikL(\sin\psi_{m_-} - \sin\psi_{m_+})}B_{m_-}}{\sqrt{1-\cos^2\psi_{m_+}}} \\ \vdots & \ddots & \vdots \\ \frac{e^{ikL(\sin\psi_{m_+} - \sin\psi_{m_-})}B_{m_+}}{\sqrt{1-\cos^2\psi_{m_-}}} & \cdots & \frac{e^{ikL(\sin\psi_{m_+} - \sin\psi_{m_+})}B_{m_+}}{\sqrt{1-\cos^2\psi_{m_+}}} \end{pmatrix}, \tag{5.116}$$

and

$$\mathbf{\Gamma_R}(L) = \frac{1}{kd}\begin{pmatrix} \frac{e^{ikL(\sin\psi_{m_-} + \sin\psi_{m_-})}B_{m_-}}{\sqrt{1-\cos^2\psi_{m_-}}} & \cdots & \frac{e^{ikL(\sin\psi_{m_-} + \sin\psi_{m_+})}B_{m_-}}{\sqrt{1-\cos^2\psi_{m_+}}} \\ \vdots & \ddots & \vdots \\ \frac{e^{ikL(\sin\psi_{m_+} + \sin\psi_{m_-})}B_{m_+}}{\sqrt{1-\cos^2\psi_{m_-}}} & \cdots & \frac{e^{ikL(\sin\psi_{m_+} + \sin\psi_{m_+})}B_{m_+}}{\sqrt{1-\cos^2\psi_{m_+}}} \end{pmatrix}, \tag{5.117}$$

using ideas from equations (5.106) and (5.107).

Also, it is useful to note at this point that the case for an incoming wave from above,

$$u_{inc}(r,\theta) = \sum_{m=m_-}^{m_+} C_m e^{ikr\cos(\theta+\psi_m)} = \sum_{m=m_-}^{m_+} C_m e^{-ikd\sin\psi_m} u_{inc}(\hat{r},\hat{\theta}). \tag{5.118}$$

In a similar manner to that discussed earlier, equation (5.118) gives the transmission below the row of the form

$$\mathbf{t^o}(L) = \mathbf{C}\left(\mathbf{I_M} + \mathbf{\Gamma_{To}}(L)\right), \tag{5.119}$$

$$\mathbf{r^o}(L) = \mathbf{C}\mathbf{\Gamma_{Ro}}(L), \tag{5.120}$$

where

$$\mathbf{\Gamma_{To}}(L) = \frac{1}{kd}\begin{pmatrix} \frac{e^{ikL(-\sin\psi_{m_-} + \sin\psi_{m_-})}B_{m_-}}{\sqrt{1-\cos^2\psi_{m_-}}} & \cdots & \frac{e^{ikL(-\sin\psi_{m_-} + \sin\psi_{m_+})}B_{m_-}}{\sqrt{1-\cos^2\psi_{m_+}}} \\ \vdots & \ddots & \vdots \\ \frac{e^{ikL(-\sin\psi_{m_+} + \sin\psi_{m_-})}B_{m_+}}{\sqrt{1-\cos^2\psi_{m_-}}} & \cdots & \frac{e^{ikL(-\sin\psi_{m_+} + \sin\psi_{m_+})}B_{m_+}}{\sqrt{1-\cos^2\psi_{m_+}}} \end{pmatrix}, \tag{5.121}$$

and

$$\mathbf{\Gamma_{Ro}}(L) = \frac{1}{kd}\begin{pmatrix} \frac{e^{ikL(-\sin\psi_{m_-} - \sin\psi_{m_-})}B_{m_-}}{\sqrt{1-\cos^2\psi_{m_-}}} & \cdots & \frac{e^{ikL(-\sin\psi_{m_-} - \sin\psi_{m_+})}B_{m_-}}{\sqrt{1-\cos^2\psi_{m_+}}} \\ \vdots & \ddots & \vdots \\ \frac{e^{ikL(-\sin\psi_{m_+} - \sin\psi_{m_-})}B_{m_+}}{\sqrt{1-\cos^2\psi_{m_-}}} & \cdots & \frac{e^{ikL(-\sin\psi_{m_+} - \sin\psi_{m_+})}B_{m_+}}{\sqrt{1-\cos^2\psi_{m_+}}} \end{pmatrix}. \tag{5.122}$$

In this section we have derived equations for the reflection and transmission of an incident field of a sum of plane waves by a horizontal row of periodic cylinders along a line arbitrarily positioned along the y-axis. These equations can be applied to recursively determine the solutions for the transmission and reflection for N infinite periodic arrays with row separations determined by the 1D Fibonacci chain.

Denote D_N as the Nth distribution of the rows, with Fib(N) rows in total. The end position of the Fib(N)th row, is at $y = q(N)S$ as defined in equation (5.100). As with the 1D recursive formulation in section 3.1, the recursive solution is built upon the solutions of the two previous scattering problems (consisting of $N-1$ and $N-2$ rows).

5.2.2 One infinite row

Begin with one infinite row, D_1, located at $y = S$. Note that S has to be large enough to comply with the wide spacing approximation. That is, for particular parameters k and d, S must be of a distance great enough to ensure that the evanescent modes have decayed.

The solutions for D_1 are just a phase shift multiplying the original one array problem solved in section 5.1.1. Define an incident wave of the form

$$u_{inc} = \sum_{m=m_-}^{m_+} C_m e^{ikr\cos(\theta-\psi_m)}, \tag{5.123}$$

where it is noted that for a single incident plane wave at angle $\alpha = \psi_0$,

$$C_m = \delta_{0m}, \tag{5.124}$$

the Kronecker delta function.

Using equation (5.114) it can be seen that the transmission coefficients are given by

$$\mathbf{T_1} = \mathbf{C}\mathbf{t_1}(S) \tag{5.125}$$

$$= \mathbf{C}\left(\mathbf{I_M} + \mathbf{\Gamma_T}(S)\right), \tag{5.126}$$

and the reflection coefficients by

$$\mathbf{R_1} = \mathbf{C}\mathbf{r_1}(S) \tag{5.127}$$

$$= \mathbf{C}\mathbf{\Gamma_R}(S). \tag{5.128}$$

The definitions of $\mathbf{\Gamma_T}(S)$ and $\mathbf{\Gamma_R}(S)$ are given in equations (5.116) and (5.117), respectively.

When considering the Fibonacci chain in 1D, it was necessary to also consider the opposite problem, in which there is an incident wave from the opposite direction, due to the non-periodicity of the Fibonacci chain. We must do this again in 2D, where the opposite problem will be an incident wave from above. The solution to the opposite problem will be denoted with a superscript o. Using equations (5.119) and (5.120), the opposite transmission and reflection coefficients for D_1 are

$$\mathbf{T_1^o} = \mathbf{C}\mathbf{t_1^o}(S) \tag{5.129}$$

$$= \mathbf{C}\left(\mathbf{I_M} + \mathbf{\Gamma_{To}}(S)\right), \tag{5.130}$$

$$\mathbf{R_1^o} = \mathbf{C}\mathbf{r_1^o}(S) \tag{5.131}$$

$$= \mathbf{C}\mathbf{\Gamma_{Ro}}(S). \tag{5.132}$$

5.2.3 Two infinite rows

The set up for D_2 is one array again, but positioned at $y = L = \tau S$. The solutions will be very similar, just with a difference in phase shift:

$$\mathbf{T_2} = \mathbf{C}\mathbf{t_2}(L) \tag{5.133}$$

$$= \mathbf{C}\left(\mathbf{I_M} + \mathbf{\Gamma_T}(L)\right), \tag{5.134}$$

$$\mathbf{R_2} = \mathbf{C}\mathbf{r_2}(L) \tag{5.135}$$

$$= \mathbf{C}\mathbf{\Gamma_R}(L), \tag{5.136}$$

$$\mathbf{T_2^o} = \mathbf{C}\mathbf{t_2^o}(L) \tag{5.137}$$

$$= \mathbf{C}\left(\mathbf{I_M} + \mathbf{\Gamma_{To}}(L)\right), \tag{5.138}$$

$$\mathbf{R_2^o} = \mathbf{C}\mathbf{r_2^o}(L) \tag{5.139}$$

$$= \mathbf{C}\mathbf{\Gamma_{Ro}}(L). \tag{5.140}$$

5.2.4 Three infinite rows

For the third set up D_3 there are two arrays. One array is positioned at $y = L$, like in D_2. The second is positioned along $y = L + S$, a distance S away from the first. This second array is as for D_1. Therefore, as in the 1D recursive formulation, it is

possible to express the solution to D_3 in terms of the two previous problems D_2 and D_1. This is much more complicated than the 1D case, due to the multiple scattering angles, the phase shift, and the change in coordinate systems, so we will explain this problem step by step.

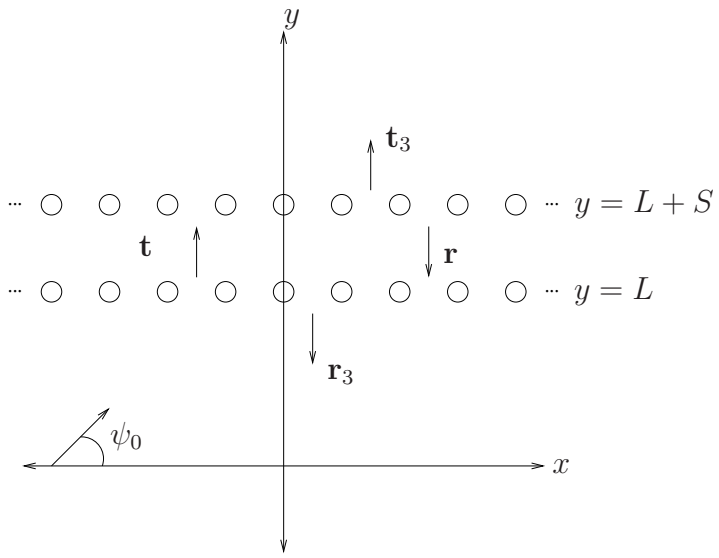

Figure 5.8: Set up for 2 infinite periodic rows of cylinders.

First, consider the D_2 case, but with the incoming plane wave as before and an incoming set of plane waves from above, as a result of the reflection from the second array. For the purpose of figure 5.8 we have depicted the superposition of plane waves travelling in each direction at each stage by the vectors of the amplitudes of each of the waves. For example, the plane waves travelling in the negative y-direction between the two rows, depicted as $\mathbf{r} = \begin{pmatrix} r_{m_-} & \dots & r_{m_+} \end{pmatrix}$, can be expressed by

$$\sum_{m=m_-}^{m_+} r_m e^{ikr\cos(\theta+\psi_m)}, \tag{5.141}$$

where the r_m are unknown. As a result, and from prior knowledge of the D_2 solutions, the reflection at the first array is a sum of the reflection of the original incident wave from below (of amplitudes given in the vector $\mathbf{C}$) and the transmission of the unknown waves from above, i.e.

$$\mathbf{r_3}(L) = \mathbf{C}\mathbf{r_2}(L) + \mathbf{r}\mathbf{t}_\mathbf{2}^\mathbf{o}(L), \tag{5.142}$$

and t is of the form

$$\mathbf{t} = \mathbf{C}\mathbf{t_2}(L) + \mathbf{r}\mathbf{r}_\mathbf{2}^\mathbf{o}(L). \tag{5.143}$$

Now consider the D_1 problem, but with an incident wave of amplitude $\mathbf{t}$ (5.143). It can be shown that $\mathbf{t_3}$ is of the form

$$\mathbf{t_3}(L) = \mathbf{t}\mathbf{t_1}(L+S) = (\mathbf{C}\mathbf{t_2}(L) + \mathbf{r}\mathbf{r_2^o}(L))\,\mathbf{t_1}(L+S), \tag{5.144}$$

and an alternative equation for $\mathbf{r}$ is also gained,

$$\mathbf{r} = \mathbf{t}\mathbf{r_1}(L+S) = (\mathbf{C}\mathbf{t_2}(L) + \mathbf{r}\mathbf{r_2^o}(L))\,\mathbf{r_1}(L+S). \tag{5.145}$$

Rearranging equation (5.145), we find that

$$\mathbf{r} = (\mathbf{C}\mathbf{t_2}(L)\mathbf{r_1}(L+S))\,(\mathbf{I}_M - \mathbf{r_2^o}(L)\mathbf{r_1}(L+S))^{-1}, \tag{5.146}$$

where $\mathbf{I}_M$ is the $M \times M$ identity matrix and M is the length of $\mathbf{m} = \{m_-, \ldots, m_+\}$. Therefore, by substituting in equations (5.144) and (5.142), it is found that

$$\begin{aligned}
\mathbf{T_3} &= \mathbf{C}\mathbf{t_3}(L) && (5.147)\\
&= \mathbf{C}\mathbf{t_2}(L)\left(\mathbf{I_M} + \mathbf{r_1}(L+S)\,(\mathbf{I_M} - \mathbf{r_2^o}(L)\mathbf{r_1}(L+S))^{-1}\,\mathbf{r_2^o}(L)\right)\mathbf{t_1}(L+S), && (5.148)\\
\mathbf{R_3} &= \mathbf{C}\mathbf{r_3}(L) && (5.149)\\
&= \mathbf{C}\left(\mathbf{r_2}(L) + \mathbf{t_2}(L)\mathbf{r_1}(L+S)\,(\mathbf{I_M} - \mathbf{r_2^o}(L)\mathbf{r_1}(L+S))^{-1}\,t_2^o(L)\right). && (5.150)
\end{aligned}$$

For the opposite problem, consider the same set up of the arrays but with an incoming wave from above. Working through in a similar manner the transmission and reflection coefficients are given by the expressions

$$\begin{aligned}
\mathbf{T_3^o} &= \mathbf{C}\mathbf{t_3^o}(L+S) && (5.151)\\
&= \mathbf{C}\mathbf{t_1^o}(L+S)\left(\mathbf{I_M} + \mathbf{r_2^o}(L)\,(\mathbf{I_M} - \mathbf{r_1}(L+S)\mathbf{r_2^o}(L))^{-1}\,\mathbf{r_1}(L+S)\right)\mathbf{t_2^o}(L), && (5.152)\\
\mathbf{R_3^o} &= \mathbf{C}\mathbf{r_3^o}(L+S) && (5.153)\\
&= \mathbf{C}\left(\mathbf{r_1^o}(L+S) + \mathbf{t_1^o}(L+S)\mathbf{r_2^o}(L)\,(\mathbf{I_M} - \mathbf{r_1}(L+S)\mathbf{r_2^o}(L))^{-1}\,\mathbf{t_1}(L+S)\right). && (5.154)
\end{aligned}$$

Note here that the position of the first array the incident waves see is taken as the argument of the transmission and reflection coefficients. Therefore, $\mathbf{t_3^o}$ and $\mathbf{r_3^o}$ depend on $(L+S)$ in this instance.

It is possible to continue in this way, by finding the unknown amplitude of the reflected wave between the two sets of rows, for any N.

5.2.5 N infinite rows

Working through for larger N and spotting the pattern, or by proving by induction as for 1D, it can be shown that the transmission and reflection for the D_N problem, $N \geq 4$, with Fib(N) rows of periodic cylinders can be given by

$$\begin{aligned}
\mathbf{T_N} =& \mathbf{C}\mathbf{t_N}(L) \\
=& \mathbf{C}\mathbf{t_{N-1}}(L)\Big(\mathbf{I_M}+ \\
& \mathbf{r_{N-2}}(L+q(N-1)S)\Big(\mathbf{I_M}-\mathbf{r^o_{N-1}}(q(N-1)S)\mathbf{r_{N-2}}(L+q(N-1)S)\Big)^{-1} \\
& \times \mathbf{r^o_{N-1}}(q(N-1)S)\Big)\mathbf{t_{N-2}}(L+q(N-1)S), \qquad (5.155)
\end{aligned}$$

$$\begin{aligned}
\mathbf{R_N} =& \mathbf{C}\mathbf{r_N}(L) \\
=& \mathbf{C}\Big(\mathbf{r_{N-1}}(L)+ \\
& \mathbf{t_{N-1}}(L)\mathbf{r_{N-2}}(L+q(N-1)S)\Big(\mathbf{I_M}-\mathbf{r^o_{N-1}}(q(N-1)S)\mathbf{r_{N-2}} \\
& \times (L+q(N-1)S)\Big)^{-1} t^o_{N-1}(q(N-1)S)\Big), \qquad (5.156)
\end{aligned}$$

$$\begin{aligned}
\mathbf{T^o_N} =& \mathbf{C}\mathbf{t^o_N}(q(N)S) \\
=& \mathbf{C}\mathbf{t^o_{N-2}}(q(N)S)\Big(\mathbf{I_M}+ \\
& \mathbf{r^o_{N-1}}(q(N-1)S)\Big(\mathbf{I_M}-\mathbf{r_{N-2}}(q(N-1)S+L)\mathbf{r^o_{N-1}}(q(N-1)S)\Big)^{-1} \\
& \times \mathbf{r_{N-2}}(q(N-1)S+L)\Big)\mathbf{t^o_{N-1}}(q(N-1)S), \qquad (5.157)
\end{aligned}$$

$$\begin{aligned}
\mathbf{R^o_N} =& \mathbf{C}\mathbf{r^o_N}(q(N)S) \\
=& \mathbf{C}\Big(\mathbf{r^o_{N-2}}(q(N)S)+ \\
& \mathbf{t^o_{N-2}}(q(N)S)\mathbf{r^o_{N-1}}(q(N-1)S)\Big(\mathbf{I_M}-\mathbf{r_{N-2}}(q(N-1)S+L) \\
& \times \mathbf{r^o_{N-1}}(q(N-1)S)\Big)^{-1}\mathbf{t_{N-2}}(q(N-1)S+L)\Big), \qquad (5.158)
\end{aligned}$$

where $q(N)$ is defined in (5.100). The proof by induction will not be discussed here as it is analogous to the 1D case. The general formulae in this form does not hold for $N = 3$ because of the initial position S in the D_1 problem. The general formulae for the N^{th} iteration is written in a form that assumes the first array is always at $y = L$ for D_N and the two previous scattering problems D_{N-1} and D_{N-2}, which is only the case for $N \geq 4$. The recursive formulae defined allow the computation of the transmission

and reflection coefficients for a large number of rows with quasiperiodic separations rather rapidly.

5.3 Comparison of wave scattering by a Fibonacci chain structure and its periodic approximations

In this section the scattered fields from multiple infinite-length rows of circular cylinders are compared. The spacings between the rows are determined by the Fibonacci chain and two periodic approximations, namely the PAS and approximant. A comparison is drawn between the amplitudes of the scattered propagating plane waves from each array.

For the results given in this section the parameters $k = 5$, $d = 0.5$ and $a = 0.001$ are chosen. The angle of incidence α and the number of rows n are varied. In order to comply with the wide spacing approximation between the rows the value $S = 2$ has been chosen for the small spacing of the Fibonacci chain. The wavenumber $k = 5$ was chosen so that the assumption $0 < ka \ll 1$ holds and so that the wavelength of the incident wave is less than the spacing between the rows. Having a wavelength smaller than the spacing ensures that the wave will be affected by the different spacings and thus will allow a fair comparison of the results between the three different distributions of rows.

Figure 5.9 shows the transmission coefficients for a set of up to twenty-one infinite rows with separations determined by the Fibonacci chain (blue), PAS (red) and 2-approximant (green). An incident angle of $\alpha = \pi/4$ was taken, resulting in the propagation of two plane waves between each row. The two modes of propagation in this case are $m = -1$ and $m = 0$, satisfying equation (5.83). The 2-approximant has a period of length $\mathrm{Fib}(4) = 3$, thus the first three rows in the 2-approximant and the Fibonacci distribution are identical. This is reflected in the transmission coefficients for $1 - 3$ rows. For greater numbers of rows, it can be seen that the transmission coefficients for both of the propagating modes through the 2-approximant distribution begin to deviate from those of the Fibonacci chain. The amplitudes of the transmission coefficients for the 2-approximant in general do reasonably well at approximating those of the Fibonacci chain, but the results diverge as the number of rows increases.

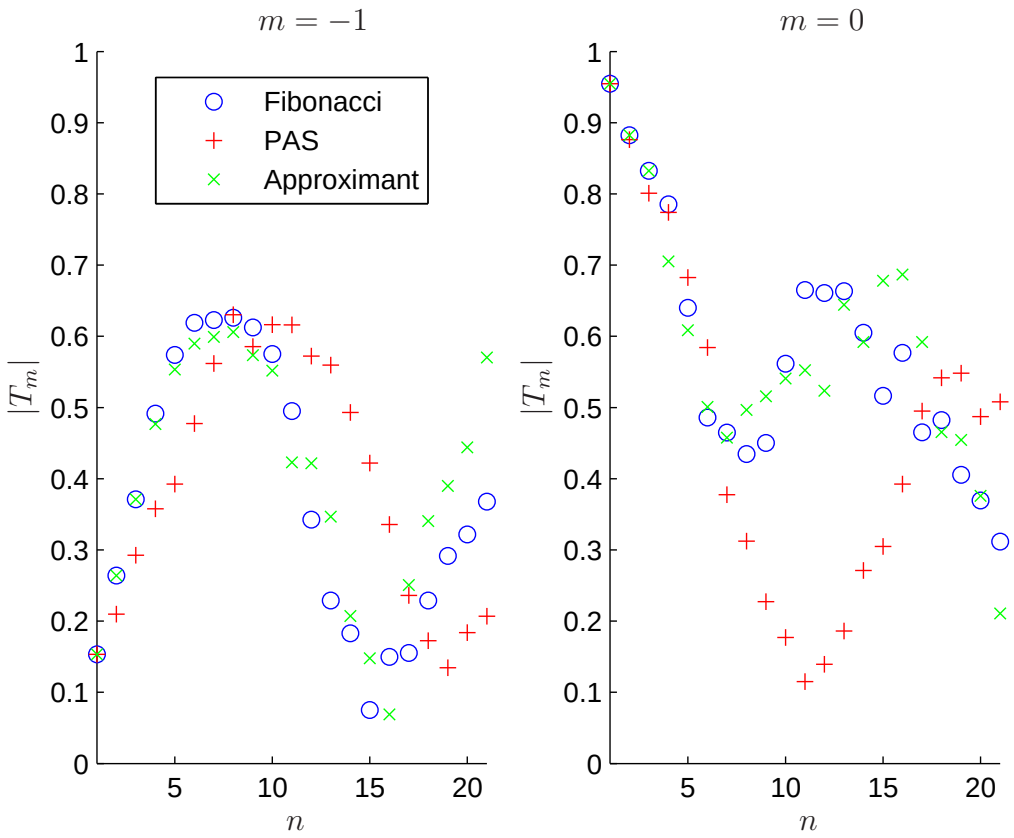

Figure 5.9: Transmission through n infinite-length periodic rows of cylinders with separation determined by the Fibonacci chain (blue), PAS (red) and 2-approximant (green), for a unit incident plane wave at angle $\alpha = \pi/4$ to the horizontal.

For rows with a distribution determined by the PAS the amplitudes again tend to deviate significantly from the amplitudes found for the Fibonacci chain distribution. For $8 - 16$ rows the difference is especially poor for the $m = 0$ mode. There are instances where the PAS does provide a better representation of the Fibonacci chain than the 2-approximant, e.g. for 17 rows, but this tends to be the exception.

Improving the accuracy of the approximation $\tau \approx \tau_n$ used in the construction of the approximant produces a distribution with a larger periodic cell containing a section of the Fibonacci chain. Although, it can be seen in figure 5.10 that the 3-approximant, using $\tau \approx \tau_3 = \text{Fib}(4)/\text{Fib}(3) = 3/2$, does not provide a much better representation of the Fibonacci chain than the 2-approximant. The accuracy of the $m = -1$ mode amplitude is increased for larger n compared to the 2-approximant, but is reduced for the $m = 0$ mode.

Increasing n to 4 in the approximant, the positions of the first twenty-one rows in

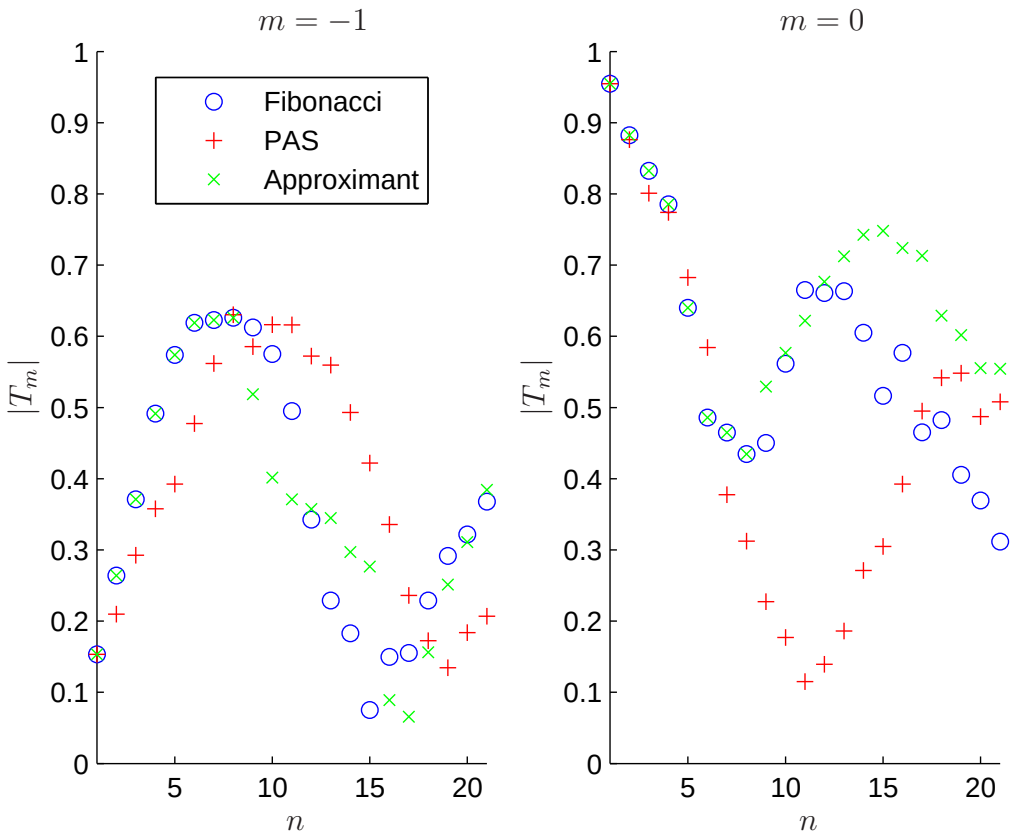

Figure 5.10: Transmission through n infinite-length periodic rows of cylinders with separation determined by the Fibonacci chain (blue), PAS (red) and 3-approximant (green), for a unit incident plane wave at angle $\alpha = \pi/4$ to the horizontal.

the Fibonacci chain and the 4-approximant are identical and thus as are the transmission coefficients. This is the case even though the period length of the 4-approximant is Fib(6) = 8.

Instead consider sections of the three distributions within the approximant periodic cell size, analogous to section 4.4. For the 4-approximant with unit cell of length 8, consider multiple sections of the Fibonacci chain of length 8. The approximant will contain the same arrangement of rows independent of the selection, since it is periodic. However, the arrangement of the rows determined by the Fibonacci chain and the PAS will alter. To gauge whether or not the approximant provides a good representation of the Fibonacci chain in the 2D multiple scattering through rows of cylinders, the transmission properties of the approximant through one unit cell of the approximant are compared to the average transmission properties of the Fibonacci chain and the PAS for multiple different sections.

For the 4-approximant, ten different sections of the Fibonacci chain and the PAS of length eight are taken. The average properties are plotted in figure 5.11. It can

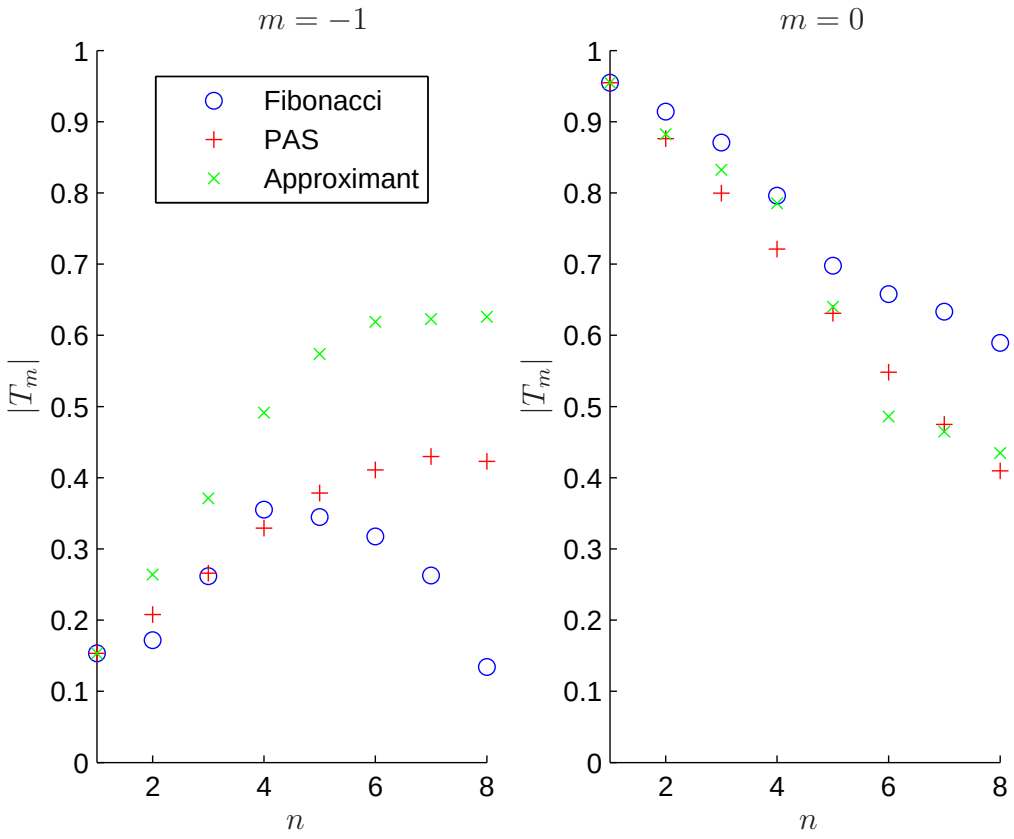

Figure 5.11: Average transmission through n infinite-length periodic rows of cylinders with separation determined by the Fibonacci chain (blue), PAS (red) and transmission through the 4-approximant (green), for a unit incident plane wave at angle $\alpha = \pi/4$ to the horizontal.

be seen that neither the amplitude of the transmission through the 4-approximant unit array nor the average amplitude of transmission through the PAS provide an accurate representation of the average transmission through the Fibonacci chain. For the $m = -1$ mode the PAS provides a very accurate representation for the first five rows, but thereafter does not, although it is closer than the 4-approximant. For the $m = 0$ mode the transmission through rows distributed with the 4-approximant and the average through the PAS distribution are very similar, and are not quite accurate with respect to the Fibonacci chain. The amplitude for $n = 8$ is of greatest interest as it is the transmission out of the end of the arrays. For both modes, neither the PAS or the 4-approximant estimate the transmission amplitude well.

The same procedure is carried out for the 5-approximant with a unit cell of length

Fib(7) = 13. Figure 5.12 shows the comparisons of the transmission coefficients for increasing number of arrays. In this instance it is seen that the PAS does not provide

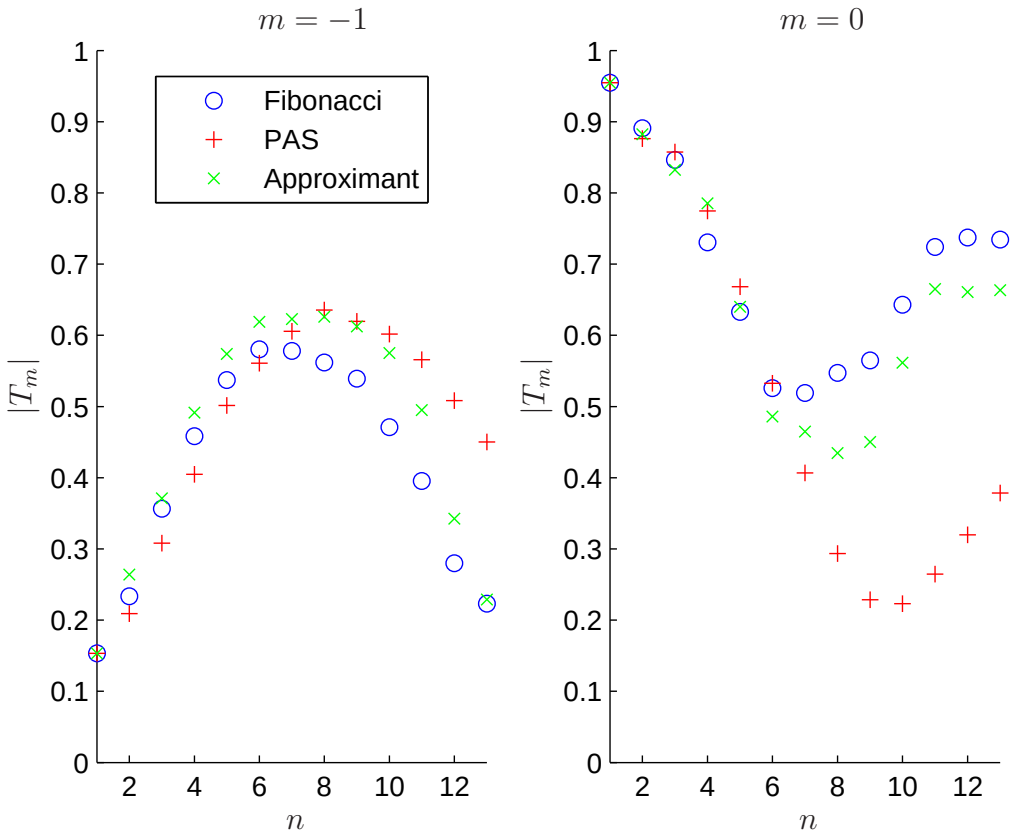

Figure 5.12: Average transmission through n infinite-length periodic rows of cylinders with separation determined by the Fibonacci chain (blue), PAS (red) and transmission through the 5-approximant (green), for a unit incident plane wave at angle $\alpha = \pi/4$ to the horizontal.

a good approximation of the Fibonacci chain. However, the amplitude of transmission through 13 rows of cylinders with a distribution determined by the 5-approximant are very similar to the average amplitude of transmission through the Fibonacci chain. For the $m = -1$ mode the amplitude of transmission for 13 rows is almost identical between the two cases.

In general this section has shown that the PAS can only provide a good representation of the Fibonacci chain in terms of the distribution of rows of cylinders for low numbers of rows. However, the approximant can provide a much better representation and for much larger numbers of rows. In particular the transmission through a 5-approximant periodic unit cell is very similar to that of the average transmission through multiple sections of the Fibonacci chain.

The examples given in this section were for a particular set of parameters and two propagating angles. Further work can be carried out to ensure the same behaviour is found for different parameters and more or less propagating modes. The accuracy of the n-approximant can be continued to be improved by increasing n; thus, for different parameter choices, higher n-approximants could be used.

Another example for the same parameter set but with $k = 3\pi$ is modelled. In this instance there are three propagating modes. Figure 5.13 shows that the 5-approximant still provides a good representation of the Fibonacci chain when there are more propagating modes. Comparing to the PAS, the 5-approximant provides a much better representation, especially for the $m = 0$ mode.

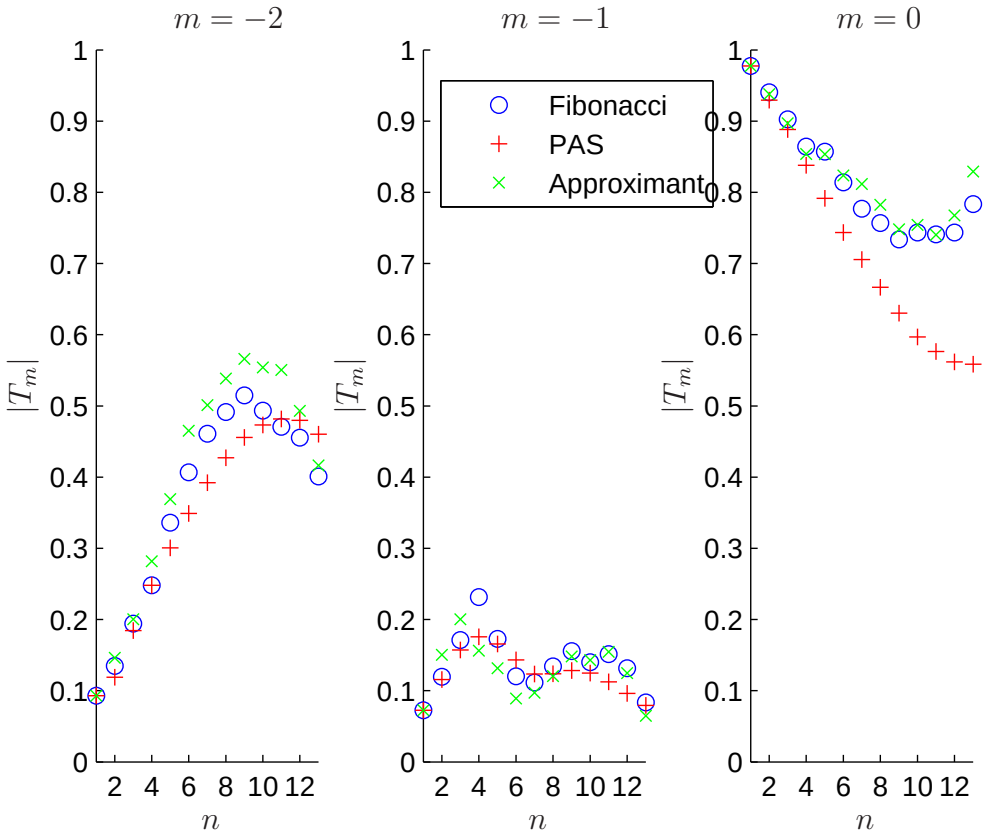

Figure 5.13: Average transmission through n infinite periodic rows of cylinders with separation determined by the Fibonacci chain (blue), PAS (red) and transmission through the 5-approximant (green), for an incident unit plane wave at angle $\alpha = \pi/4$ from the horizontal and $k = 3\pi$.

Having shown that the approximant can provide a good representation of the Fibonacci chain in terms of the distribution of tube bundles, the next step is to investigate the propagation of waves through an infinite periodic approximant. The effective

properties derived for the approximant can provide approximate effective properties of an infinite array of rows with a distribution determined by the Fibonacci chain.

5.4 Wave scattering by an infinite approximant structure

Wave propagation through an infinite number of rows can be calculated when there is periodicity inherent in the geometry, using ideas discussed in section 2.2.2. This section investigates the effective wave propagation through an infinite number of rows of cylinders with a periodic distribution. The formulations used here are similar to those used for the 1D periodic approximation in section 4.5. A combination of the previously resolved solutions for the transmission and reflection coefficients for a finite number of rows with Bloch's theorem allows a computation of the effective wavenumber of the infinite periodic array where each period contains the finite array of rows. For a scenario of an infinite number of rows with the same spacing D between each row, then the simple formulation of the transmission and reflection coefficients (5.126) and (5.128) for one row are used. For a scenario of an infinite approximant, where the period contains N quasiperiodically distributed rows, then the recursive formulation of the transmission and reflection coefficients (5.155) and (5.156) should be used. Similar work is discussed in [55], [24], [63] and [64] for the former case. This section discusses the formulation for the latter in full detail and continuing with the notation set out so far in this chapter. The theory discussed can be applied to any situation including the former case, or for a periodic cell of arbitrary distribution.

Consider an infinite periodic approximant array, whereby each row consists of an infinite number of small circular cylinders with periodic in-row separation (i.e. horizontal) $2d$ as with the previous work. The N-approximant has a periodic cell described in section 3.3 with a period of length $q(N)S = \mathrm{Fib}(N+1)L + \mathrm{Fib}(N)S$. An example of an approximant unit cell is given in figure 5.14. Assume a wide spacing between each row and thus propose a Bloch wave solution for the propagating modes $m_- \leq m \leq m_+$,

$$T_m e^{i\gamma_y q(N)Sn} = T_m e^{i\gamma_y q(N)S(n+1)}, \quad R_m e^{i\gamma_y q(N)Sn} = R_m e^{i\gamma_y q(N)S(n+1)}, \tag{5.159}$$

where γ_y is the Bloch wave vector in the y-direction. Without loss of generality consider

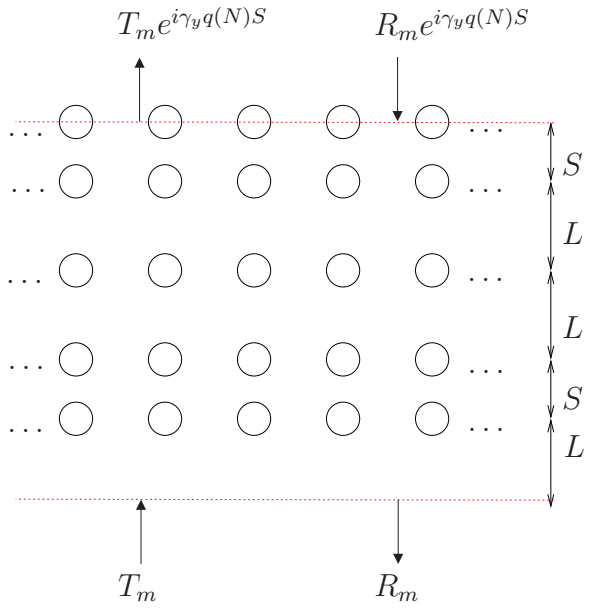

Figure 5.14: Single period of the approximant, with proposed Bloch wave solution.

the periodic cell at the origin and take $n = 0$. Expressing in matrix form the Bloch condition can be written

$$\mathbf{T} = \mathbf{TE}, \quad \mathbf{R} = \mathbf{RE}, \quad \text{for} \quad \mathbf{E} = e^{i\gamma_y q(N)S}\mathbf{I_M}. \tag{5.160}$$

Using the known solutions for transmission and reflection from the finite approximant cell it is possible to show that

$$\mathbf{TE} = \mathbf{T}t_N(L) + \mathbf{RE}r^o_N(q(N)S), \tag{5.161}$$

$$\mathbf{R} = \mathbf{T}r_N(L) + \mathbf{RE}t^o_N(q(N)S). \tag{5.162}$$

This can be rearranged to give the matrix equation

$$\begin{pmatrix}\mathbf{T} & \mathbf{R}\end{pmatrix}\begin{pmatrix}t_N(L) & -r_N(L)\\ \mathbf{0} & \mathbf{I_M}\end{pmatrix} = \begin{pmatrix}\mathbf{T} & \mathbf{R}\end{pmatrix}\mathbf{E}\begin{pmatrix}\mathbf{I_M} & \mathbf{0}\\ -r^o_N(q(N)S) & t^o_N(q(N)S)\end{pmatrix}. \tag{5.163}$$

Equation (5.163) can be re-expressed in the form $\mathbf{B} - \lambda_\mathbf{B}\mathbf{I} = \mathbf{0}$,

$$\begin{pmatrix}t_N(L) & -r_N(L)\\ \mathbf{0} & \mathbf{I_M}\end{pmatrix}\begin{pmatrix}\mathbf{I_M} & \mathbf{0}\\ -r^o_N(q(N)S) & t^o_N(q(N)S)\end{pmatrix}^{-1} - e^{i\gamma_y q(N)S}\mathbf{I} = \mathbf{0}, \tag{5.164}$$

and thus a solution for $e^{i\gamma_y q(N)S}$ can be determined by finding the eigenvalues $\boldsymbol{\lambda_B}$ of the matrix

$$\mathbf{B} = \begin{pmatrix}t_N(L) & -r_N(L)\\ \mathbf{0} & \mathbf{I_M}\end{pmatrix}\begin{pmatrix}\mathbf{I_M} & \mathbf{0}\\ -r^o_N(q(N)S) & t^o_N(q(N)S)\end{pmatrix}^{-1}. \tag{5.165}$$

Hence the effective wavenumbers for the N-approximant array of "tube bundles"/infinite-length rows are given by

$$\boldsymbol{\gamma}_y = \frac{\log \boldsymbol{\lambda}_{\mathbf{B}}}{iq(N)S}. \tag{5.166}$$

The eigenvalues can be computed numerically using Matlab or a similar package.

The similarity between the effective wavenumbers for an N-approximant distribution of infinite-length rows (5.166) and 1D point masses (4.51) can be seen. The difference is the computation of the eigenvalues in the 2D case which is more complicated due to the multi-dimensional matrix system.

It should be noticed that the dimension of the matrix $\mathbf{B}$ (5.165) depends on the number of propagating modes between each period. From the work with a finite number of rows of scatterers it is known that the scattering angles depend on the angle of incidence of the incoming plane wave (5.83). Using an approach suggested my Peter and Meylan [64], one can consider "incident" waves which propagate along the irreducible Brillouin zone edge of interest. That is, for an incident wave of the form

$$u_{inc} = e^{ikr\cos(\theta-\psi_0)}, \tag{5.167}$$

with k the host wavenumber, a Bloch condition was posed of the form

$$e^{im2dk\cos\psi_0}. \tag{5.168}$$

By setting

$$k\cos\psi_0 = \gamma_x, \tag{5.169}$$

the effective wavenumber in the x-direction, choices of ψ_0 can be made for particular γ_x on edges of the Brillouin zone. The irreducible Brillouin zone was discussed in section 2.2.2 and is depicted in figure 5.15, with node positions given by

$$0 = (0,0), \quad A = (\pi/(2d), 0), \quad B = (\pi/(2d), \pi/(q(N)S)), \tag{5.170}$$

for the rectangular unit cell in physical space.

We illustrate an example band diagram for the 2-approximant in figure 5.16. It can be seen that there is a full stop band for initial wavenumbers. This is a characteristic noted for small sound-soft scatterers and is discussed further in the next chapter. The approach employed here to find the band structure of the approximant can be

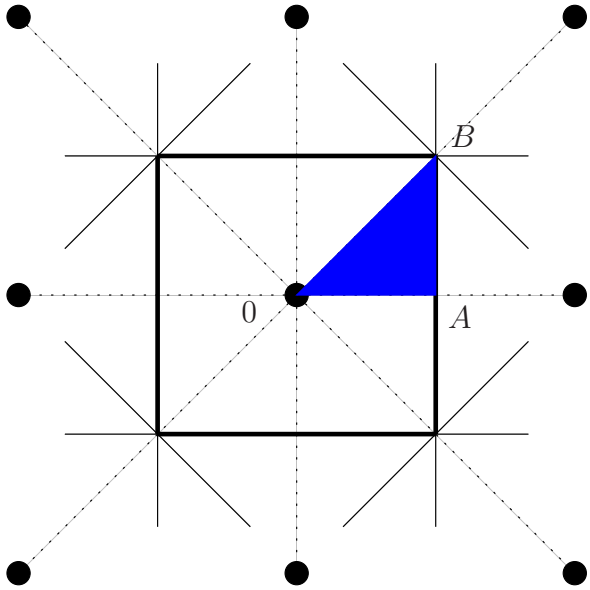

Figure 5.15: The irreducible Brillouin zone for a 2D square periodic lattice (blue shaded).

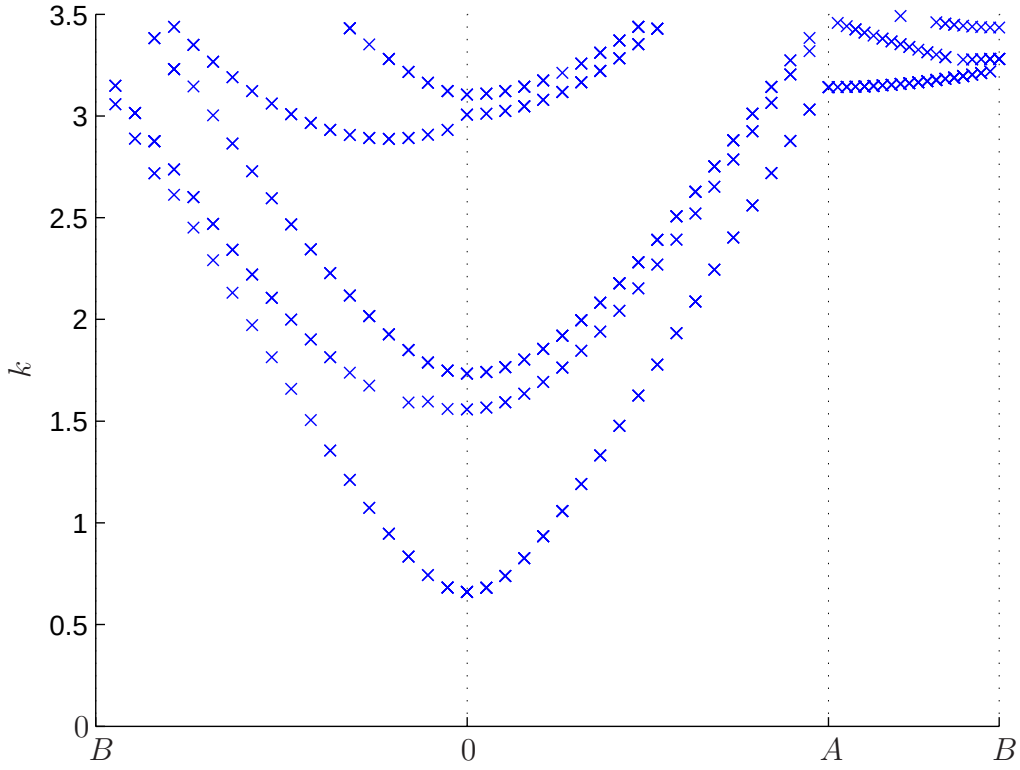

Figure 5.16: The full band diagram for a 2-approximant with $d = 1/2$, $L = 1$ and $a = 0.001$.

compared to the results achieved using an alternative method discussed in the next chapter for more general 2D periodic lattices.

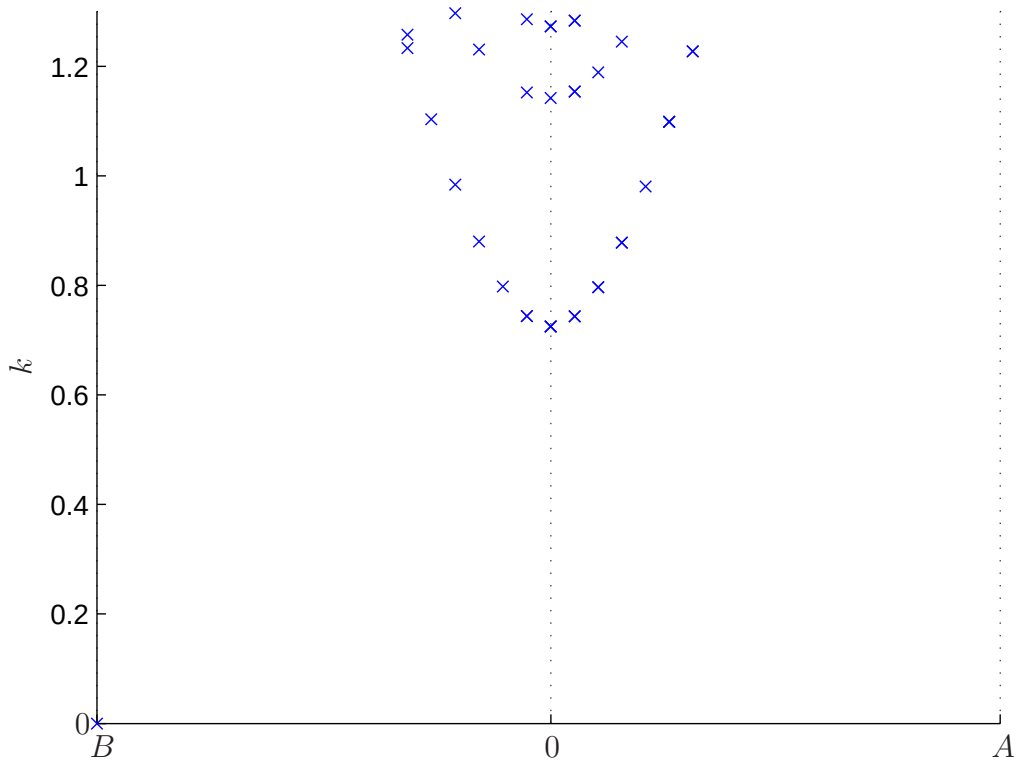

Figure 5.17: Partial band diagram for a 2-approximant with $d = 1/2$, $L = 1$ and $a = 0.001$.

To justify further the use of the approximant as a model for large or infinite arrays of rows with Fibonacci chain spacing we show the cut-on of the first mode for the 3-approximant in figure 5.17. It can be seen that for both approximants the cut-on wavenumber k_0 is similar, in fact $k_0 = 0.6609\ldots$ for the 2-approximant and $k_0 = 0.7248\ldots$ for the 3-approximant. The closeness in these results suggests that the approximant can predict the first mode of propagation for an infinite Fibonacci chain array of rows for low n in the n-approximant.

5.5 Conclusions

In this chapter we extended the methods applied in 1D to a 2D quasiperiodic array of scatterers with quasiperiodicity in one direction. It was shown how the transmission and reflection properties of finite arrays of infinite rows can be determined recursively, analogous to the 1D case. The analysis to derive the coefficients of the transmitted

and reflected plane waves from one row is similar to that of existing literature but is applied specifically to small scatterers, making a simplification in the expressions.

By comparing the amplitudes of the transmitted plane waves for arrays of rows with Fibonacci chain separations to arrays of rows with PAS and approximant separations it was demonstrated that the approximant can provide a much better representation of the Fibonacci chain than the PAS. For relatively low n in the n-approximant, the difference between the amplitudes related to the Fibonacci chain and the n-approximant were minimal. Since the approximant proved to be a good representation of the Fibonacci chain in the case of finite numbers of rows, we investigated Bloch-type waves and their properties in an infinite approximant array of rows. The analysis of the infinite problem involved an extension of the theory applied for the 1D infinite approximant in section 4.5 and the work of Peter and Meylan [64].

Chapter 6

Construction algorithm for two-dimensional quasiperiodic lattices and their periodic approximations

The construction methods for two different 2D quasiperiodic lattices are discussed in this chapter. The first lattice under consideration is called the *square Fibonacci lattice*. It is a 2D extension of the 1D Fibonacci chain discussed in chapter 3, and is depicted in figure 6.1. The second lattice under consideration is called the *Penrose lattice*. It is a more complicated lattice than the square Fibonacci lattice. The Penrose lattice incorporates 2D quasiperiodicity and has a resemblance to a 2D random distribution. To construct the Penrose lattice it is necessary to extend the 2D to 1D projection method, applied in chapter 3, to higher dimensions. The 2D Penrose lattice can be projected from a 5D or 4D space, both of which will be discussed in this chapter. As with the 1D case in chapter 3, the construction of two periodic approximations for each quasiperiodic lattice will be discussed.

6.1 Square Fibonacci lattice

The *square Fibonacci* (SF) lattice is a 2D quasiperiodic lattice, where the quasiperiodicity is apparent in just two orthogonal directions. The lattice nodes are determined

by the 1D Fibonacci chain in the two perpendicular directions. The two lengthscales L and S of the 1D Fibonacci chain relate to node separation in two directions in the 2D SF lattice. Figure 6.1 depicts the generation of the SF lattice. Lattice nodes are positioned at each intersection of the two perpendicular lines.

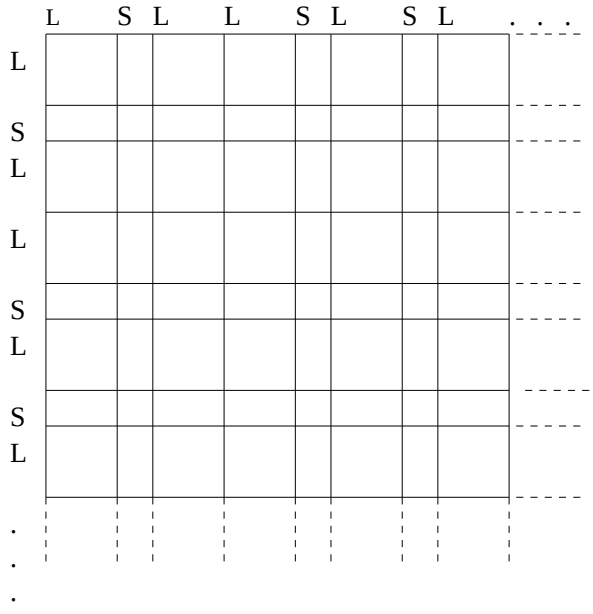

Figure 6.1: Set up of the square Fibonacci lattice.

In figure 6.1 it can be seen that the lattice contains three types of polygons: two squares of dimensions $L \times L$ and $S \times S$ and a rectangle of dimensions $L \times S$.

The SF lattice has been investigated before in [47]. Lifschitz studies the geometry and scalings of the lattice along with its diffraction pattern. He puts a case forward for future research in the area due to its relation to quasicrystals and photonic crystals. To our knowledge there has been no consideration of this lattice in acoustics before.

In (3.10) from section 3.1 the lattice positions of the Fibonacci chain were defined as

$$x^i = \frac{1}{\sqrt{2+\tau}}(m_1^i + \tau m_2^i), \quad \mathbf{m}^i = (m_1^i, m_2^i) \in \mathcal{M}, \tag{6.1}$$

where the superscript i notation has been introduced to denote the position of the ith lattice node. The set $\mathcal{M}$ is determined by following the algorithm in section 3.1 and satisfying the inequality (3.9), i.e.

$$-\frac{1+\tau}{2} < \tau m_1 - m_2 \leq \frac{1+\tau}{2}. \tag{6.2}$$

The lattice positions in the square Fibonacci (SF) lattice are therefore given by

$$\mathbf{x}_{\mathrm{SF}}^{m,n} = x^m \mathbf{e}_1 + x^n \mathbf{e_2}, \quad m, n \in \mathbb{Z}. \tag{6.3}$$

One aim of this thesis is to compare the SF lattice to the two periodic approximations, analogous to the 1D quasiperiodic structures in chapter 4. The periodic average structure and the approximant of the Fibonacci chain shall be considered. Again, the lattices are constructed by applying the 1D lattice in two perpendicular directions.

The PAS 1D nodes are given by

$$\mathbf{x}_{\mathrm{PAS}}^{m,n} = (3-\tau)S(m\mathbf{e}_1 + n\mathbf{e}_2), \tag{6.4}$$

where $(3-\tau)S$ is the average spacing of the Fibonacci chain, as derived in section 2.1.3.

In section 3.2 an occupancy window was defined for the PAS nodes, (3.19), of length $S(\tau-1)$. The occupancy window determined the distance that the Fibonacci lattice nodes could deviate from the PAS lattice nodes. The same occupancy window can be applied to the SF in two directions, resulting in a square occupancy window of edge length $S(\tau-1)$ centred at the PAS nodes. If the 2D occupancy window is defined by $\mathbf{O}_2 = (O_{2x}, O_{2y})$, then the x and y components of the occupancy window are given by

$$O_{2x} = O_{2y} = a\left(\frac{\tau-1}{2}\right)S, \quad a \in (-1, 1]. \tag{6.5}$$

Figure 6.2 shows how close an approximation the PAS is to the SF lattice. The resemblance suggests that solving this periodic scattering problem could give reasonably similar results to the multiple scattering from the SF lattice.

Figure 6.2: Square Fibonacci lattice vertices (blue), the PAS vertices (red) and the maximum range from the PAS vertices (red squares).

As with the 1D Fibonacci chain and its PAS, the 2D SF Fibonacci chain and its PAS are one-to-one; each PAS vertex has only one SF vertex associated with it. Therefore the occupancy factor is $\rho_{occ} = 1$. The packing density which measures the ratio of area of occupancy window to periodic cell is given by

$$\rho_{pac} = \frac{S^2(\tau-1)^2}{S^2(3-\tau)^2} = \frac{1}{5}. \tag{6.6}$$

A packing density as low as this along with a unit occupancy factor suggests that the PAS is a good representation of the SF lattice.

Using the concept of the PAS lattice and the occupancy windows defining the maximum distance that the SF nodes can lie from the PAS nodes, one can attempt to represent the SF lattice as a PAS lattice plus some random perturbation. The random perturbation can be restricted within the occupancy windows. For example, define a perturbation from the PAS lattice $\mathbf{x}^{m,n}_{\text{pPAS}}$ such that

$$\mathbf{x}^{m,n}_{\text{pPAS}} = \mathbf{r}^{m,n}_{\text{PAS}} + \boldsymbol{\epsilon}_{mn}, \quad \text{where } \boldsymbol{\epsilon}_{mn} = (\epsilon_m, \epsilon_n) \text{ and } \epsilon_m, \epsilon_n \in \mathcal{U}\left(-S\frac{\tau-1}{2}, S\frac{\tau-1}{2}\right), \tag{6.7}$$

where $\mathcal{U}[a,b]$ denotes a uniform distribution between a and b. One random generation is depicted in figure 6.3. It can be seen that in some instances the additional perturbation increases the accuracy of the approximation lattice node to the SF lattice nodes. However, due to the randomness of the perturbation, there are also instances

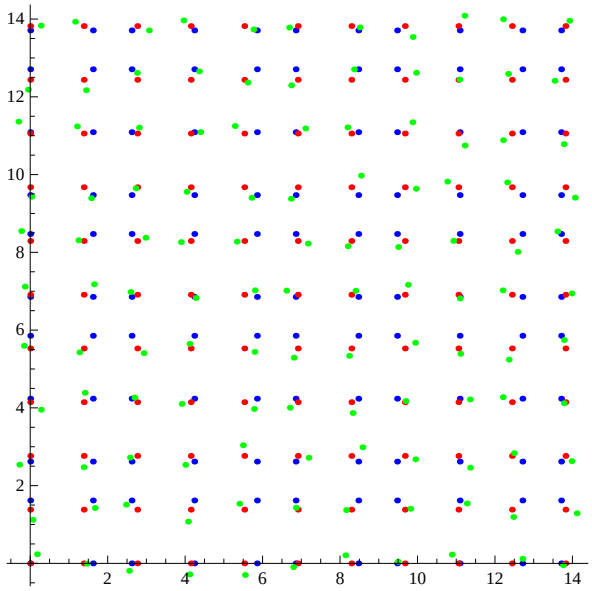

Figure 6.3: Square Fibonacci lattice vertices (blue), the PAS vertices (red) and the vertices that have been randomly perturbed from the PAS lattice (green).

where the perturbation is further away from the SF node than the PAS. If work was to continue in this approach it may be beneficial to consider the statistics of the PAS and the SF lattice distributions, and to reduce their differences. With more of an understanding of the occupancy window and distribution of SF nodes within them it could be possible to consider a different random distribution to the uniform distribution for the perturbation.

To construct the approximant lattice for the SF lattice again apply the 1D version in two perpendicular directions. In section 3.3 it was shown that the lattice nodes of the 1D approximant to the Fibonacci chain are given by the same equation (6.1). However the m_i will differ due to the difference in the algorithm. Denote the m_i for the approximant with a tilde, $\tilde{m}_i$. The inequality used to determine the $\tilde{m}_i$ for the approximant was shown to be

$$-\frac{1+\frac{\mathrm{Fib}(n+1)}{\mathrm{Fib}(n)}}{2} < \tilde{m}_1\frac{\mathrm{Fib}(n+1)}{\mathrm{Fib}(n)} - \tilde{m}_2 \leq \frac{1+\frac{\mathrm{Fib}(n+1)}{\mathrm{Fib}(n)}}{2}. \tag{6.8}$$

The set of lattice nodes for the approximant is similar to the SF lattice and is given by

$$\mathbf{x}^{m,n}_{\mathrm{approx}} = \tilde{x}^m\mathbf{e}_1 + \tilde{x}^n\mathbf{e_2}, \quad m,n \in \mathbb{Z}, \tag{6.9}$$

where

$$\tilde{x}^i = \frac{1}{\sqrt{2+\tau}}(\tilde{m}^i_1 + \tau\tilde{m}^i_2). \tag{6.10}$$

The two periodic approximations of the 2D SF lattice have similarities to the SF lattice, but in distinct ways. A comparison between the approximations, i.e. the approximant and the PAS, to the SF chain can be seen in figure 6.4. Near the origin the approximant and SF lattice nodes are in the same positions and thus the blue SF nodes cannot be seen.

6.2 The Penrose lattice

The *Penrose lattice* is a lattice that results from positioning lattice nodes on the vertices of the two tiles used in the 2D Penrose tiling. The Penrose lattice is the most famous quasiperiodic lattice discussed due to its links with quasicrystals and the Penrose tiling, two discoveries of paramount importance. The history of the Penrose tiling and quasicrystals was discussed in chapter 2.1. In this section, the construction

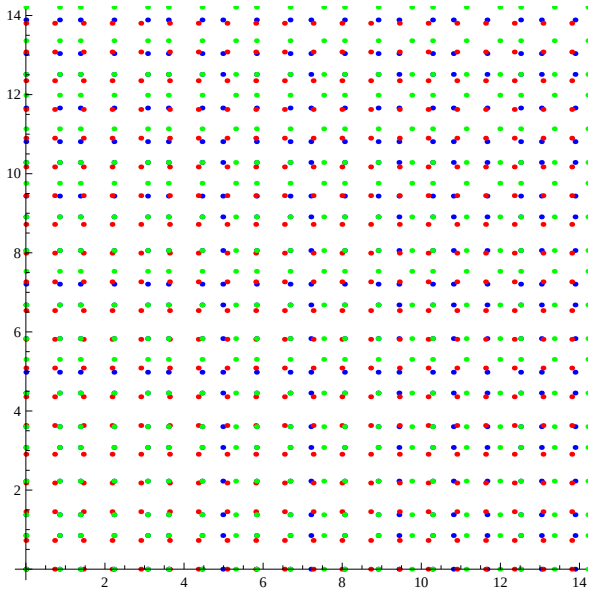

Figure 6.4: Square Fibonacci lattice vertices (blue), the associated PAS vertices (red) and the 2-approximant vertices (green).

of the Penrose tiling via the projection method is explained. As discussed in section 2.1, the Penrose tiling can be constructed by a projection from either 5D or 4D space. It is not possible to visualise the projection processes in these high dimensions, and so throughout this section the reader will be reminded of the analogous projection of the Fibonacci chain from 2D to 1D space discussed in section 3.1. Thus, the algorithms and figures given in section 3.1 should provide the basis needed to understand and apply the Penrose lattice projection.

The projection from 5D to 2D is analogous to the 2D to 1D projection as the unit cell is a hypercube, comparable to the square. As mentioned in the discussion of the background of the Penrose tiling, it is also possible to project from 4D space. However, the lattice in 4D is no longer hypercubic, it is hyperrhombic. This makes the extension more difficult, as determining the acceptance window via the Voronoi cell is much more complicated. Therefore in this chapter we begin with a 5D space in which we can determine the Voronoi cell and the acceptance window more simply. We choose to then project to the 4D space in order to reduce the dimensions and complexities inherent by one degree of freedom. We then use the 4D space and resultant projected acceptance windows, to project to 2D to construct the Penrose lattice.

The five-dimensional lattice

We begin with a 5D hypercubic lattice analogous to the 2D square lattice in section 3.1, and define the *parallel space* to be the 2D plane spanned by $\mathbf{e}_i$ for $i = 1, 2$. The *perpendicular space* is thus the 3D hyperspace spanned by $\mathbf{e}_i$ for $i = 1, 2, 3$. The hypercubic lattice must be rotated at some angle related to τ and the inherent 5-fold rotational symmetry of the Penrose lattice. The basis vectors

$$\mathbf{d}_i = \sqrt{\frac{2}{5}} \begin{pmatrix} \cos 2\pi i/5 \\ \sin 2\pi i/5 \\ \cos 4\pi i/5 \\ \sin 4\pi i/5 \\ 1/\sqrt{2} \end{pmatrix}, \quad i = 1, \ldots, 5, \tag{6.11}$$

for the 5D hypercubic lattice satisfy all requirements. This basis, or rotation with respect to the parallel plane, is used in all literature and references given in section 2.1. For further insight into the definition of the basis vectors see appendix B.4. The basis vectors relate to τ the golden ratio through the following identities

$$\cos 2\pi/5 = -\sigma/2, \qquad \sin 2\pi/5 = +\sqrt{1 - \cos^2 2\pi/5} = \tau\beta/2, \tag{6.12}$$

$$\cos 4\pi/5 = -\tau/2, \qquad \sin 4\pi/5 = +\sqrt{1 - \cos^2 4\pi/5} = \beta/2, \tag{6.13}$$

$$\cos 6\pi/5 = -\tau/2, \qquad \sin 6\pi/5 = -\sqrt{1 - \cos^2 6\pi/5} = -\beta/2, \tag{6.14}$$

$$\cos 8\pi/5 = -\sigma/2, \qquad \sin 8\pi/5 = -\sqrt{1 - \cos^2 8\pi/5} = -\tau\beta/2, \tag{6.15}$$

where

$$\sigma = \frac{1 - \sqrt{5}}{2} = 1 - \tau = -\frac{1}{\tau}, \tag{6.16}$$

$$\beta = \sqrt{3 - \tau}. \tag{6.17}$$

The set of 5D hypercubic lattice nodes, denoted by Λ_5, is therefore given by

$$\Lambda_5 = \left\{ \sum_{i=1}^{5} p_i \mathbf{d}_i \quad | \quad p_i \in \mathbb{Z} \right\}. \tag{6.18}$$

The next step in the algorithm for the projection method, as summarised at the end of section 3.1, is to determine the acceptance window in 5D. To do this it is first necessary to determine the Voronoi cell nodes in 5D, $\mathbf{V}_5$, [66]. The Voronoi cell of a

hypercubic lattice is a hypercube itself, analogous to the 2D square case discussed in chapter 3. The Voronoi hypercube in 5D has $2^5 = 32$ vertex points given by

$$\mathbf{V}_5 = \sum_{i=1}^{5} n_i \mathbf{d}_i, \quad \text{where } n_i \in \{-1/2, 1/2\}. \tag{6.19}$$

To define the acceptance window nodes project the Voronoi cell nodes to the perpendicular space, i.e. take the $\mathbf{e}_i$, $i = 1, 2, 3$, components of (6.19),

$$\mathbf{V}_5^{\perp} = \sqrt{\frac{2}{5}} \begin{pmatrix} 0 \\ 0 \\ \sum_{i=1}^{5} n_i \cos 4\pi i/5 \\ \sum_{i=1}^{5} n_i \sin 4\pi i/5 \\ 1/\sqrt{2} \sum_{i=1}^{5} n_i \end{pmatrix}. \tag{6.20}$$

The $\mathbf{e}_5$-component of these vectors can take six values,

$$\frac{1}{\sqrt{5}} \sum_{i=1}^{5} n_i \in \frac{1}{2\sqrt{5}} \{-5, -3, -1, 1, 3, 5\}. \tag{6.21}$$

The six values relate to the projection of the 5D hypercube vertices to six different parallel planes in the perpendicular space.

On inspection of the six sets of coordinates on the six planes of x_5, as shown in figure 6.5, it can be seen that the 5D hypercube points project to a 3D polyhedron, defined in (6.20), which contains regular 2D pentagons in four planes and single points in two planes. There are two planes with ten possible combinations of $\mathbf{n} = (n_1, \cdots, n_5)$. The ten nodes actually form one smaller pentagon inside a larger one. See figures 6.5 and 6.6 where this is illustrated to assist the reader. The four pentagons are all situated along a line between the two points in the other two planes, and are perpendicular to the line. For the cases where there are 10 nodes in the x_5-plane, and thus two pentagons, it is necessary to determine the nodes associated with the largest pentagon. The acceptance window is governed by the maximum area of the projected Voronoi cell, as with the 2D to 1D projection method.

Denote the 5-tuple of n_i that gives the largest area in the plane $x_5 = \frac{1}{\sqrt{5}} \frac{p}{2}$ by $\mathbf{n}_p$.

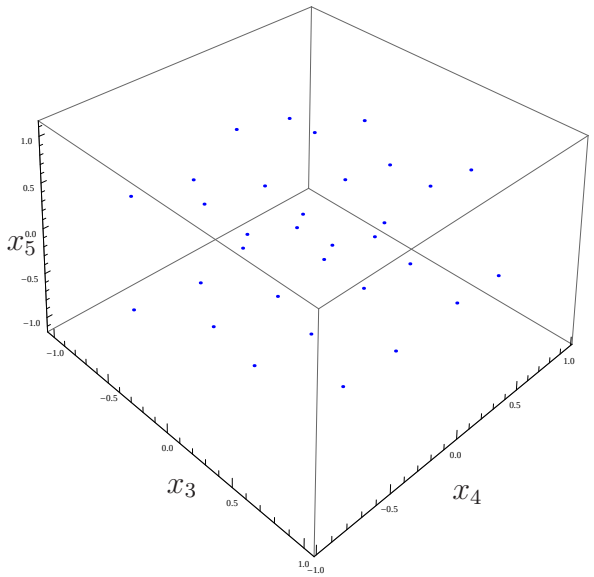

Figure 6.5: Voronoi cell nodes projected to the 3D perpendicular space.

It can be shown that the following 5-tuples can be determined for each plane

$$\mathbf{n}_{-5} = -\frac{1}{2}(1,1,1,1,1)\,, \tag{6.22}$$

$$\mathbf{n}_{-3} = -\frac{1}{2}\{1,1,1,1,-1\}\,, \tag{6.23}$$

$$\begin{aligned}\mathbf{n}_{-1} =& \frac{1}{2}\{(1,-1,1,-1,-1),(1,-1,-1,1,-1),(-1,1,-1,1,-1),\\ & (-1,1,-1,-1,1),(-1,-1,1,-1,1)\}\end{aligned} \tag{6.24}$$

$$\begin{aligned}\mathbf{n}_{1} =& \frac{1}{2}\{(-1,1,-1,1,1),(-1,1,1,-1,1),(1,-1,1,-1,1),(1,-1,1,1,-1),\\ & (1,1,-1,1,-1)\}\end{aligned} \tag{6.25}$$

$$\mathbf{n}_{3} = \frac{1}{2}\{1,1,1,1,-1\}\,, \tag{6.26}$$

$$\mathbf{n}_{5} = \frac{1}{2}(1,1,1,1,1)\,, \tag{6.27}$$

where the notation $\{a_1, \cdots, a_N\}$ denotes the set of N-tuples that contains all permutations of a_i, $1 \leq i \leq N$, for a_i a single element, e.g. $\{-1,1\} = \{(-1,1),(1,-1)\}$. The 5-tuples for $n_{\pm 1}$ contain the five of the ten combinations that result in the pentagon with the largest area.

The circumradii R_p of the four pentagons are

$$R_3 = R_{-3} = \sqrt{\frac{2}{5}}, \quad R_1 = R_{-1} = \sqrt{\frac{2}{5}}\tau. \tag{6.28}$$

At this point one can define the acceptance windows in 3D using the lattice nodes of the four pentagons and two points in the six different planes. However, it transpires

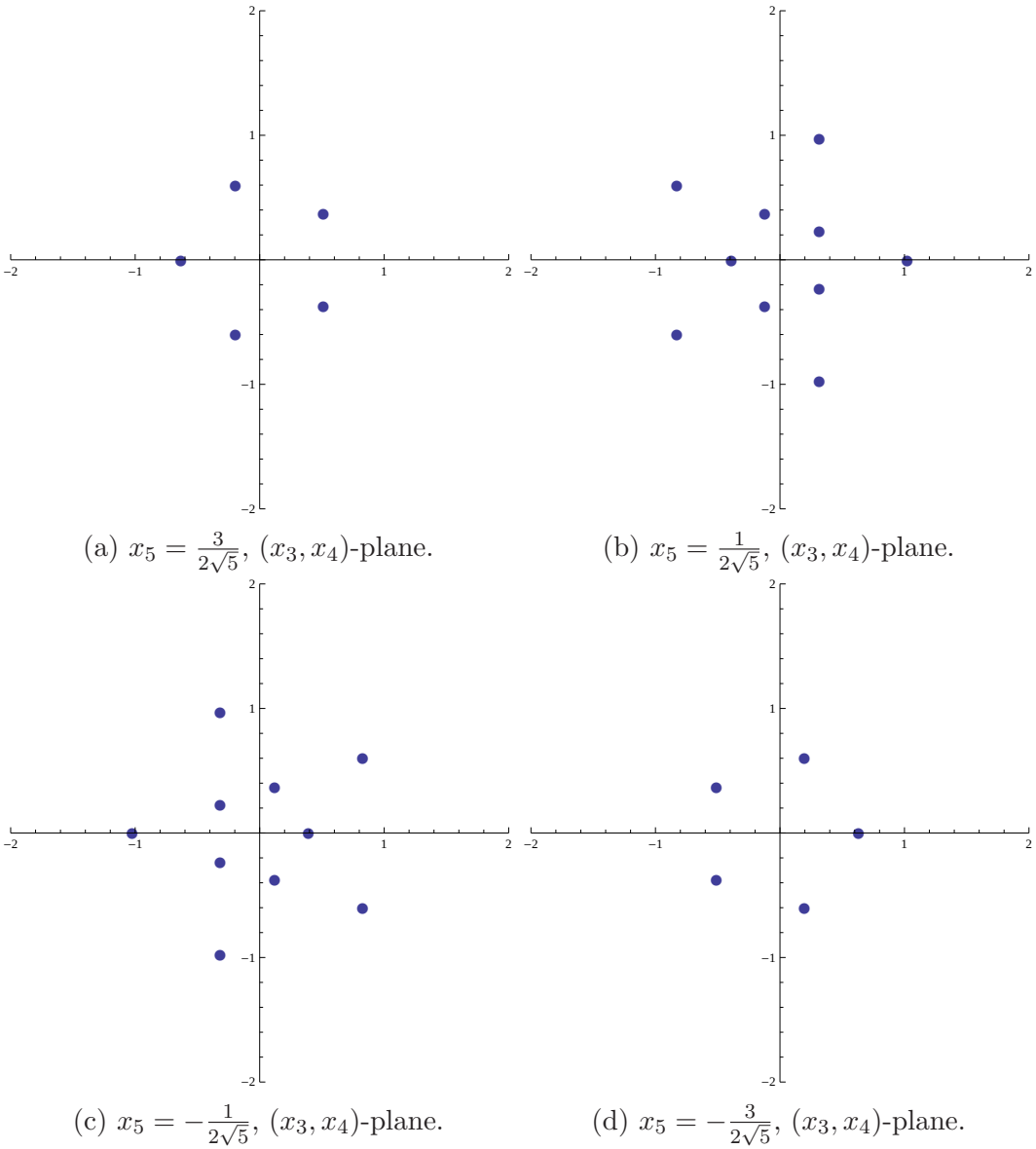

(a) $x_5 = \frac{3}{2\sqrt{5}}$, (x_3, x_4)-plane.

(b) $x_5 = \frac{1}{2\sqrt{5}}$, (x_3, x_4)-plane.

(c) $x_5 = -\frac{1}{2\sqrt{5}}$, (x_3, x_4)-plane.

(d) $x_5 = -\frac{3}{2\sqrt{5}}$, (x_3, x_4)-plane.

Figure 6.6: 2D cross sections of the projected 5D Voronoi cell to the 3D perpendicular space.

that we can simplify matters by projecting the 5D space into 4D and the 3D acceptance windows into 2D. The benefit of using this 4D lattice rather than the 5D is that four is the minimal dimension required to project to 2D space with 5-fold symmetry (determined by the Euler totient function as described in section 2.1.1), so we can disregard the extra unnecessary dimension. As previously mentioned, finding the Voronoi cell of this 4D lattice is not trivial, thus it is most efficient to project the 5D lattice to the 4D lattice, and thus project the acceptance window too. The reduction in dimension of the acceptance windows reduces the degrees of freedom when finding the intersections of acceptance windows with the parallel plane, making it computationally

less expensive in the long run.

The four-dimensional lattice

The basis vectors in 4D must retain the inherent 5-fold symmetry of the Penrose tiling. In appendix B.5 the derivation of particular basis vectors applicable to the projection of the Penrose tiling is given, i.e.

$$\mathbf{f}_i = \frac{2}{5}\begin{pmatrix} \cos 2\pi i/5 - 1 \\ \sin 2\pi i/5 \\ \cos 4\pi i/5 - 1 \\ \sin 4\pi i/5 \end{pmatrix}, \quad i = 1, \ldots, 5, \tag{6.29}$$

where it is noted that the basis vector $(f)_5 = \mathbf{0}$ is not required but is defined for ease of comparison with the five basis vectors of the 5D lattice. This set of basis vectors is also used in [71]. The resultant set of 4D lattice nodes is therefore given by the set Λ, where

$$\Lambda = \left\{ \sum_{i=1}^{4} p_i \mathbf{f}_i \quad | \quad p_i \in \mathbb{Z} \right\}. \tag{6.30}$$

The parallel plane is spanned by $\mathbf{e}_i$ for $i = 1, 2$ and the perpendicular plane by $\mathbf{e}_i$ for $i = 3, 4$.

The best way to proceed is to determine a projection matrix that takes the 5D lattice to the 4D lattice. To do this we define such a matrix Π that projects the 5D basis vectors to the 4D basis vectors, i.e.

$$\Pi \mathbf{d}_i = \mathbf{f}_i. \tag{6.31}$$

We begin by considering the projection of the sum of the basis vectors. It is known that

$$\sum_{i=1}^{5} \mathbf{d}_i = \sqrt{\frac{2}{5}} \begin{pmatrix} \sum_{i=1}^{5} \cos 2\pi i/5 \\ \sum_{i=1}^{5} \sin 2\pi i/5 \\ \sum_{i=1}^{5} \cos 4\pi i/5 \\ \sum_{i=1}^{5} \sin 4\pi i/5 \\ 5/\sqrt{2} \end{pmatrix} = \begin{pmatrix} 0 \\ 0 \\ 0 \\ 0 \\ \sqrt{5} \end{pmatrix} \tag{6.32}$$

and

$$\sum_{i=1}^{4}\mathbf{f}_i = \frac{2}{5}\begin{pmatrix} -4+\sum_{i=1}^{4}\cos 2\pi i/5 \\ \sum_{i=1}^{4}\sin 2\pi i/5 \\ -4+\sum_{i=1}^{4}\cos 4\pi i/5 \\ \sum_{i=1}^{4}\sin 4\pi i/5 \end{pmatrix} = -2\begin{pmatrix} 1 \\ 0 \\ 1 \\ 0 \end{pmatrix}. \tag{6.33}$$

So it is necessary to find a 4×5 matrix Π such that

$$\Pi\begin{pmatrix} 0 \\ 0 \\ 0 \\ 0 \\ \sqrt{5} \end{pmatrix} = -2\begin{pmatrix} 1 \\ 0 \\ 1 \\ 0 \end{pmatrix}. \tag{6.34}$$

Thus, the matrix Π requires the following components

$$\Pi_{15} = \Pi_{35} = -\frac{2}{\sqrt{5}} = -\sqrt{\frac{2}{5}}\sqrt{2}, \tag{6.35}$$

and we further choose

$$\Pi_{25} = \Pi_{45} = 0. \tag{6.36}$$

The remaining components can be chosen as $\sqrt{\frac{2}{5}}I_4$, where I_4 is the 4×4 identity matrix, so that all other points are mapped to the 4D part of themselves. The projection matrix can therefore be defined by

$$\Pi = \sqrt{\frac{2}{5}}\begin{pmatrix} 1 & 0 & 0 & 0 & -\sqrt{2} \\ 0 & 1 & 0 & 0 & 0 \\ 0 & 0 & 1 & 0 & -\sqrt{2} \\ 0 & 0 & 0 & 1 & 0 \end{pmatrix}. \tag{6.37}$$

It can be checked that this projection does indeed take the 5D to the 4D basis,

$$\Pi\mathbf{d}_i = \sqrt{\frac{2}{5}}\begin{pmatrix} 1 & 0 & 0 & 0 & -\sqrt{2} \\ 0 & 1 & 0 & 0 & 0 \\ 0 & 0 & 1 & 0 & -\sqrt{2} \\ 0 & 0 & 0 & 1 & 0 \end{pmatrix}\sqrt{\frac{2}{5}}\begin{pmatrix} \cos 2\pi i/5 \\ \sin 2\pi i/5 \\ \cos 4\pi i/5 \\ \sin 4\pi i/5 \\ 1/\sqrt{2} \end{pmatrix} = \frac{2}{5}\begin{pmatrix} \cos 2\pi i/5 - 1 \\ \sin 2\pi i/5 \\ \cos 4\pi i/5 - 1 \\ \sin 4\pi i/5 \end{pmatrix} = \mathbf{f}_i, \tag{6.38}$$

for $i = 1, \ldots, 4$, and $\Pi \mathbf{d}_5 = \mathbf{0}$.

The projection matrix Π defined in (6.37) can be applied to the acceptance window nodes in 5D, i.e. $\mathbf{V}_5^{\perp}$ in (6.20), to take them to 4D space.

$$\mathbf{V}_4^{\perp} = \Pi \mathbf{V}_5^{\perp} = \sqrt{\frac{2}{5}} \begin{pmatrix} 1 & 0 & 0 & 0 & -\sqrt{2} \\ 0 & 1 & 0 & 0 & 0 \\ 0 & 0 & 1 & 0 & -\sqrt{2} \\ 0 & 0 & 0 & 1 & 0 \end{pmatrix} \sqrt{\frac{2}{5}} \begin{pmatrix} 0 \\ 0 \\ \sum_{i=1}^{5} n_i \cos 4\pi i/5 \\ \sum_{i=1}^{5} n_i \sin 4\pi i/5 \\ \frac{1}{\sqrt{2}} \sum_{i=1}^{5} n_i \end{pmatrix} \tag{6.39}$$

$$= \frac{2}{5} \begin{pmatrix} -\sum_{i=1}^{5} n_i \\ 0 \\ \sum_{i=1}^{5} n_i \cos 4\pi i/5 - \sum_{i=1}^{5} n_i \\ \sum_{i=1}^{5} n_i \sin 4\pi i/5 \end{pmatrix}. \tag{6.40}$$

By comparison with the acceptance window nodes in 5D, namely $\mathbf{V}_5^{\perp}$ in equation (6.20), it can be seen that in the (x_3, x_4)-plane the same pentagons are produced with an additional shift in the x_3 direction, dependent on $p = 2\sum_{i=1}^{5} n_i$. The size of the pentagon has also been scaled by a factor of $\sqrt{\frac{2}{5}}$. That is, the circumradii of the pentagons in the 4D space r_p are given by

$$r_p = \sqrt{\frac{2}{5}} R_p. \tag{6.41}$$

The 5-tuples of n_i selected for each plane in the 5D case can be applied to the 4D projected Voronoi cell to determine the largest area, and thus the acceptance window.

The whole 5D Voronoi cell has now been projected to the 2D perpendicular plane in 4D space and therefore forms discrete 2D shapes. Figure 6.7 shows the nodes of the projection. In 5D the nodes $\mathbf{V}_5^{\perp}$ corresponded to a polyhedron that could be described in six planes. In 4D the nodes $\mathbf{V}_4^{\perp}$ correspond to six discrete polygons in the same (x_3, x_4)-plane. As in 5D, four of the polygons are regular pentagons, and the other two are single nodes at $(x_3, x_4) = (\pm 1, 0)$.

As in the 2D to 1D projection, it is now necessary to define acceptance windows $\mathbf{W}_4$ that describe the area within these pentagons. Due to the reflective symmetry of the pentagons in the x_3-axis, the geometry can be simplified to a half pentagon.

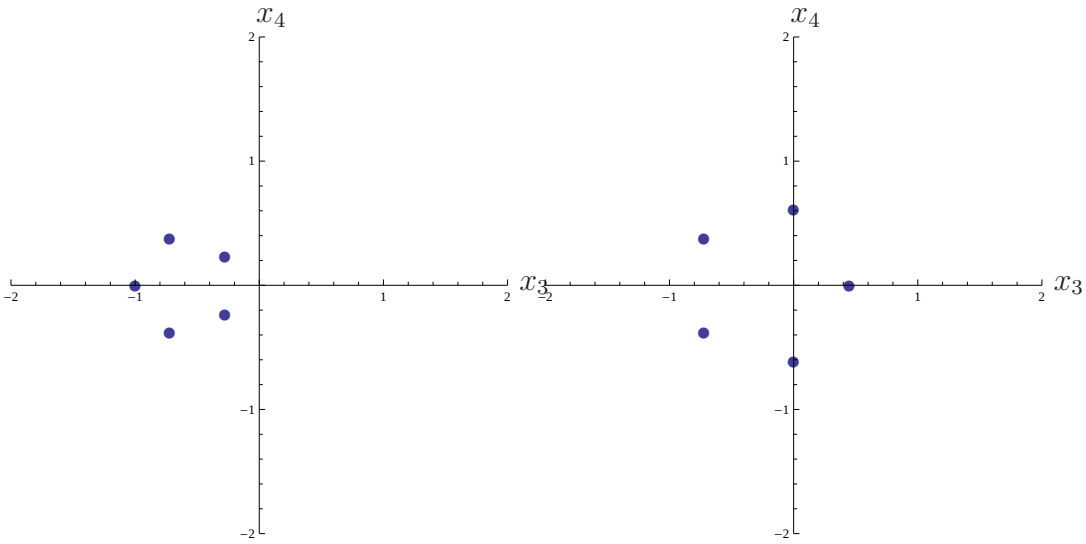

(a) Pentagon surface related to $p = 2\sum_{i=1}^{5} n_i = 3$.

(b) Pentagon surface related to $p = 2\sum_{i=1}^{5} n_i = 1$.

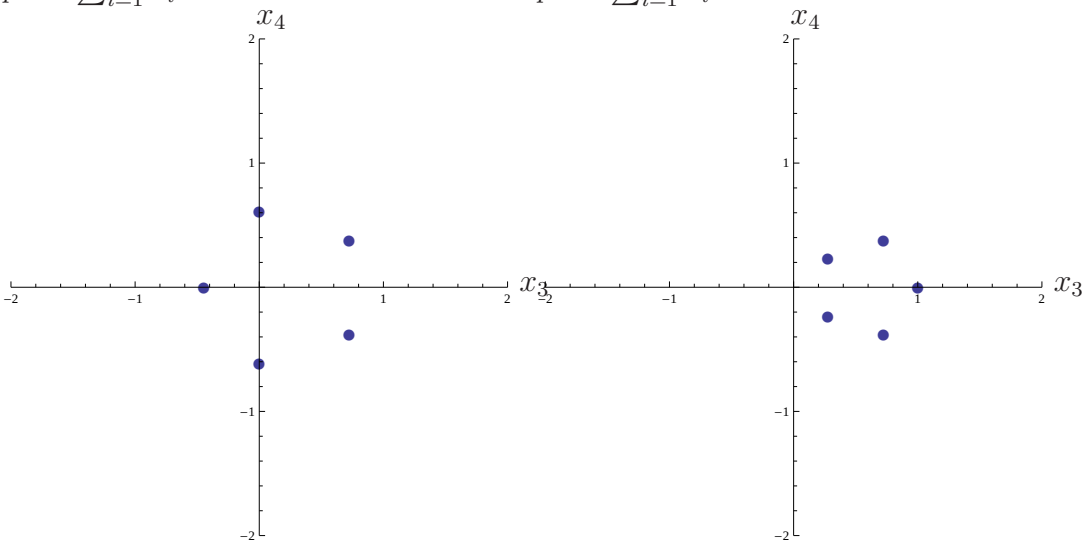

(c) Pentagon surface related to $p = 2\sum_{i=1}^{5} n_i = -1$.

(d) Pentagon surface related to $p = 2\sum_{i=1}^{5} n_i = -3$.

Figure 6.7: Projection of the 5D Voronoi cell to the 2D perpendicular space, i.e. the (x_3, x_4)-plane.

The area can be separated into two regions of x_3 which are bounded in the x_4-plane by the x_3-axis and the pentagon edge in each region. We denote these two regions by $j = 1, 2$. Figure 6.8 depicts this decomposition.

For each $p = 2\sum_{i=1}^{5} n_i$ an acceptance window $\mathbf{w}_4(p)$ should be defined so that

$$\mathbf{W}_4 = \bigcup_{p\in\{-5,-3,-1,1,3,5\}} \mathbf{w}_4(p). \tag{6.42}$$

It was shown earlier that on the planes relating to $p = \pm 5$ there exists a single node

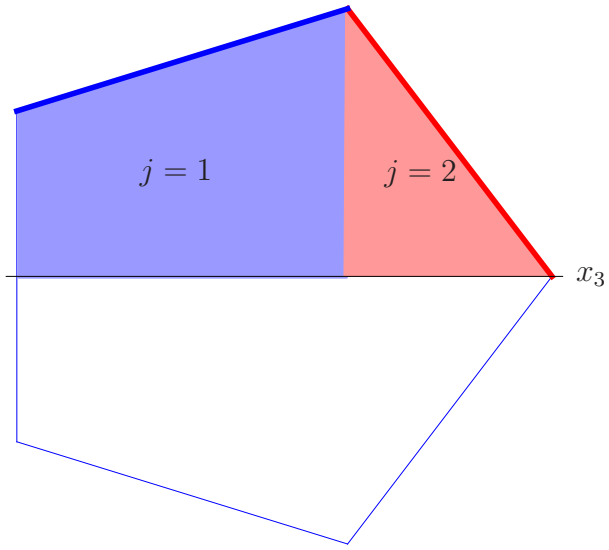

Figure 6.8: Pentagon in the (x_3, x_4)-plane. Required area for acceptance window definition is shaded. The shaded region is separated into two with different bounds in the x_4 plane.

of the acceptance window. Therefore,

$$\mathbf{w}_4(\pm 5) = \mp(\mathbf{e}_1 + \mathbf{e}_3), \tag{6.43}$$

since $\sum_{i=1}^{5} \cos 4\pi i/5 = \sum_{i=1}^{5} \sin 4\pi i/5 = 0$. In order to formulate expressions for the pentagonal shapes let us define the necessary vertex coordinates for the pentagons. From the vertex coordinates it is possible to define an equation for the lines that form the pentagon edges. Figure 6.9 shows the two possible arrangements of pentagons. The vertices defined by the letters A to F can be shown to have the (x_3, x_4) coordinates

$$A = (r_p \cos 4\pi/5 - p/5, r_p \sin 4\pi/5), \tag{6.44}$$

$$B = (r_p \cos 2\pi/5 - p/5, r_p \sin 2\pi/5), \tag{6.45}$$

$$C = (r_p - p/5, 0), \tag{6.46}$$

$$D = (-r_p - p/5, 0), \tag{6.47}$$

$$E = (-r_p \cos 2\pi/5 - p/5, r_p \sin 2\pi/5), \tag{6.48}$$

$$F = (-r_p \cos 4\pi/5 - p/5, r_p \sin 4\pi/5), \tag{6.49}$$

where r_p is the radius of the p pentagon, defined in equation (6.41).

Using the expression for a line through two points (x_1, y_1) and (x_2, y_2) in 2D space $y - y_1 = m(x - x_1)$ where $m = \frac{y_1 - y_2}{x_1 - x_2}$, expressions for the four lines AB, BC, DE and EF can be formulated. From the expressions for the pentagon edges, the area of

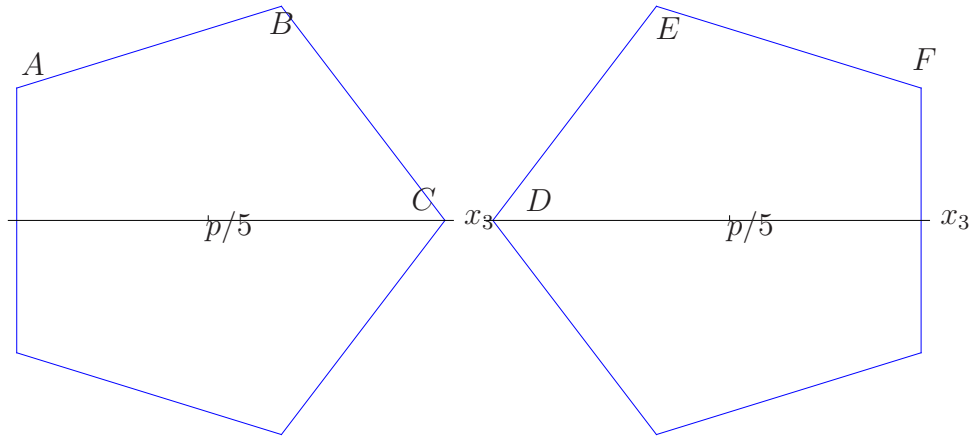

(a) Pentagon vertex coordinates, related to $p = 1, -3$.

(b) Pentagon vertex coordinates, related to $p = -1, 3$.

Figure 6.9: Vertex coordinates for the pentagonal acceptance windows in the (x_3, x_4) plane.

the pentagon can be defined. For a pentagon with orientation as in figure 6.9a the acceptance window can be defined as the union of the two regions $j = 1, 2$ (as shaded in figure 6.8), as

$$\mathbf{w}_4(p) = \bigcup_{j=1}^{2} \mathbf{w}_4(p)_j = \bigcup_{j=1}^{2} \begin{pmatrix} -p/5 \\ 0 \\ \mathbf{x}_3(p)_j \\ \mathbf{x}_4(p)_j \end{pmatrix}, \tag{6.50}$$

where for $p = 1, -3$,

$$\mathbf{x}_3(p)_1 \in [r_p \cos(4\pi/5) - p/5, r_p \cos(2\pi/5) - p/5], \tag{6.51}$$

$$|\mathbf{x}_4(p)_1| \leq \frac{\sin(2\pi/5) - \sin(4\pi/5)}{\cos(2\pi/5) - \cos(4\pi/5)}(\mathbf{x}_3(p)_1 - r_p \cos(4\pi/5) + p/5) + r_p \sin(4\pi/5), \tag{6.52}$$

$$\mathbf{x}_3(p)_2 \in [r_p \cos(2\pi/5) - p/5, -p/5 + r_p], \tag{6.53}$$

$$|\mathbf{x}_4(p)_2| \leq \frac{-\sin(2\pi/5)}{1 - \cos(2\pi/5)}(\mathbf{x}_3(p)_2 - r_p + p/5). \tag{6.54}$$

For pentagons of the opposite orientation, i.e. for $p = -1, 3$, we have

$$\mathbf{x}_3(p)_1 \in [-p/5 - r_p\cos(2\pi/5), -p/5 - r_p\cos(4\pi/5)], \tag{6.55}$$

$$|\mathbf{x}_4(p)_1| \leq -\frac{\sin(2\pi/5) - \sin(4\pi/5)}{\cos(2\pi/5) - \cos(4\pi/5)}(\mathbf{x}_3(p)_1 + r_p\cos(4\pi/5) + p/5) + r_p\sin(4\pi/5), \tag{6.56}$$

$$\mathbf{x}_3(p)_2 \in [-r_p - p/5, -p/5 - r_p\cos(2\pi/5)], \tag{6.57}$$

$$|\mathbf{x}_4(p)_2| \leq \frac{\sin(2\pi/5)}{1 - \cos(2\pi/5)}(\mathbf{x}_3(p)_2 + r_p + p/5). \tag{6.58}$$

The acceptance window defined in equation (6.42) is replicated on every lattice node to give us the full acceptance window of the 4D system $\mathbf{A}_4$.

$$\mathbf{A}_4 = \left\{ \sum_{i=1}^{4} m_i\mathbf{f}_i + \mathbf{W}_4, \quad m_i \in \mathbb{Z} \right\}. \tag{6.59}$$

We find that there is an overlap of the $\mathbf{w}_4(5)$ and $\mathbf{w}_4(-5)$ nodes when decorating every lattice node. Therefore it is only necessary to consider $p \in \{-3, -1, 1, 3, 5\}$ in $\mathbf{A}_4$, without loss of generality.

The final stage of the projection method is to determine which acceptance windows intersect the parallel space. That is, whenever the $\mathbf{e}_3$ and $\mathbf{e}_4$ components of $\mathbf{A}_4$ in equation (6.59) are zero,

$$\begin{pmatrix} \frac{2}{5}\sum_{i=1}^{4} m_i(\cos(4\pi i/5) - 1) + \mathbf{x}_3(p)_j \\ \frac{2}{5}\sum_{i=1}^{4} m_i\sin(4\pi i/5) + \mathbf{x}_4(p)_j \end{pmatrix} = \begin{pmatrix} 0 \\ 0 \end{pmatrix}, \quad p \in \{-3, -1, 1, 3, 5\}, \quad j = 1, 2. \tag{6.60}$$

This results in the choice of $\mathbf{m}_p = (m_1, m_2, m_3, m_4)$, determining the selection of 4D lattice nodes $\Lambda_{\mathbf{m}_p}$ for each value of p, such that

$$\frac{2}{5}\sum_{i=1}^{4} m_i(1 - \cos(4\pi i/5) + \epsilon) = \mathbf{x}_3(p)_j, \quad \text{and} \quad -\frac{2}{5}\sum_{i=1}^{4} m_i\sin(4\pi i/5) = \mathbf{x}_4(p)_j. \tag{6.61}$$

A small parameter $\epsilon \ll 1$ has been introduced in the $\mathbf{e}_3$ component. This is to address issues with the inequalities and duplication of points. In the projection of the Fibonacci chain in section 3.1 it was necessary to introduce differing inequalities (3.5), to avoid duplication of points. Due to the multiple dimensions in the acceptance window in this instance it is easier to introduce a small non-integer shift in the window.

By substituting equation (6.61) into equations for $\mathbf{x}_3(p)_j$ and $\mathbf{x}_4(p)_j$ for each $p \in \{-3, -1, 1, 3, 5\}$ and $j = 1, 2$ given in (6.51)-(6.58) we obtain the inequalities on the 4-tuple of integers $\mathbf{m}_p$ that yield intersection of the acceptance windows with the parallel

plane. The expression for the case $p = 5$ is given by

$$\begin{pmatrix} \frac{2}{5}\sum_{i=1}^{4} m_i(\cos(4\pi i/5) - 1) + \epsilon + 1 \\ \frac{2}{5}\sum_{i=1}^{4} m_i \sin(4\pi i/5) \end{pmatrix} = \begin{pmatrix} 0 \\ 0 \end{pmatrix}. \tag{6.62}$$

In the 2D to 1D projection method, the $\mathbf{m}$ that gave an intersection also determined which lattice nodes were to be projected to the parallel plane. In the 5D and 4D to 2D projection method the 5-tuple $\mathbf{m}$ will also denote which lattice nodes of the 5D hypercubic lattice should be selected to be projected. However, the $\mathbf{e}_1$ component of the 4D acceptance window includes some information from the 5D acceptance window and therefore must not be neglected. The information in the $\mathbf{e}_1$ component is related to the p defined by each pentagonal acceptance window and so it is necessary to treat the $\mathbf{m}_p$ for each p differently. The set $\mathbf{m} = \bigcup_{p\in\{-3,-1,1,3,5\}} \mathbf{m}_p$ gives the selection of lattice nodes required for the construction of the Penrose lattice, and the Penrose lattice nodes are given by

$$\mathbf{x}_{\text{Pen}} = \left(\frac{2}{5}\sum_{i=1}^{4} m_i(\cos 2\pi i/5 - 1) - \frac{p}{5}\right)\mathbf{e}_1 + \left(\frac{2}{5}\sum_{i=1}^{4} m_i \sin 2\pi i/5\right)\mathbf{e}_2, \tag{6.63}$$

for $m_i \in \mathbf{m}_p$ and $p \in \{-3, -1, 1, 3, 5\}$, where the $-\frac{p}{5}$ term in the $\mathbf{e}_1$ component is the contribution from the 5D space that must not be neglected.

An example of a section of the Penrose lattice determined using the given method is shown in figure 6.10. It can be seen how the nodes can be joined to give a representation of a section of Penrose tiling.

Using the algorithm described in this chapter and an initial unit hypercubic lattice, it is found that that the Penrose rhombi has an edge length of $a_r = \frac{2}{5}$. This disagrees with the expression given by Steurer and Haibach [71] by a factor of τ^2, due to scaling inherent in their method, which will be discussed in further detail in the proceeding section.

In summary, and analagous to the 2D to 1D projection in section 3.1, the projection method algorithm for the Penrose lattice is as follows

- Construct a 5D hypercubic unit lattice, suitably orientated as defined in (6.11)
- Project a Voronoi cell to the perpendicular space to find the acceptance window nodes $\mathbf{V}_5^{\perp}$, defined in (6.20)

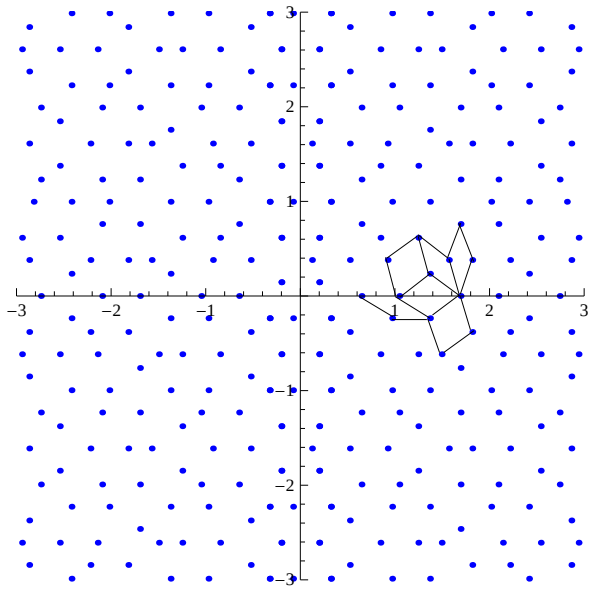

Figure 6.10: Penrose tiling vertices and an example of some of the tiles. This is in the $\mathbf{e}_1$, $\mathbf{e}_2$ plane.

- Apply a transformation matrix (6.37) to the 5D lattice and the 3D acceptance window to project to a 4D lattice (6.29) with 2D acceptance windows associated with the origin node, $\mathbf{W}_4$, defined in (6.42)
- Decorate every lattice node with the acceptance window to give the full set $\mathbf{A}_4$, defined in (6.59)
- Find the vectors $(m_1, m_2, m_3, m_4) \in \mathcal{M}$ which allow the intersection of $\mathbf{A}_4$ with the parallel plane, defined in (6.61)
- The intersection points on the parallel plane determine the Penrose lattice nodes $\mathbf{x}_{\text{Pen}}$, defined in (6.63).

6.3 Periodic average structure

The periodic average structure (PAS) is a periodic approximation of the quasiperiodic lattice with a period specifically chosen to represent its properties. In fact, as discussed in section 2.1.3, the method used to derive such a lattice is based on a choice of a base set of reflections in the Penrose lattice diffraction pattern which is defined in the reciprocal space of the lattice via the Fourier transform. The reciprocal lattice vectors spanning the plane containing the main reflections of the diffraction pattern

were defined in equation (2.21). This gave rise to a PAS basis defined by

$$\bar{\mathbf{d}}_1 = \frac{2}{\sqrt{5}a^*}\begin{pmatrix}1\\0\end{pmatrix}, \quad \bar{\mathbf{d}}_2 = \frac{2}{\sqrt{5}a^*}\begin{pmatrix}\sin\pi/10\\\cos\pi/10\end{pmatrix}, \tag{6.64}$$

where a^* is related the Penrose rhomb edge length a_r and will be discussed further below.

In section 3.2 the PAS for the 1D Fibonacci chain was introduced. It was shown that employing the higher-dimensional space, used in the construction of the Fibonacci chain, in the construction of the PAS provides further insight into the comparisons between the quasiperiodic lattice and its PAS. This comparison could be drawn through the lattice parameters of the quasiperiodic and periodic lattices and also through the occupancy window. The occupancy window is the projection of the acceptance window, and represents the maximum distance a quasiperiodic lattice node can lie from its associated PAS lattice node. The same concept can be applied to the Penrose lattice and its PAS, and will be discussed in this section.

It is necessary to project the 4D lattice nodes of the higher-dimensional space to the 2D lattice nodes of the PAS. There are infinitely many projections for this. One can also project the discrete 2D acceptance windows to the 2D plane spanned by $\mathbf{e}_1$ and $\mathbf{e}_2$ to determine the occupancy windows. We follow a projection used by Steurer and Haibach [71]. First project along the diagonal between the origin and $\sum_{i=1}^{4}\mathbf{f}_i$ of the 4D unit cell, so that the four pentagon centres project to the single origin of the cell. Then a projection can be performed that maps the 4D lattice points to the 2D lattice points. It can be shown that the projection

$$P = \frac{1}{a^*}\begin{pmatrix}1 & 0 & -1 & -\tau(3-\tau)^{1/2}\\0 & 1 & 0 & -\tau\end{pmatrix} \tag{6.65}$$

satisfies both these requirements. The projection matrix P gives $P(\sum_{i=1}^{4}\mathbf{f}_i) = \mathbf{0}$ and

the projection of the 4D basis vectors

$$P(\mathbf{f}_1) = \begin{pmatrix} 0 \\ 0 \end{pmatrix}, \tag{6.66}$$

$$P(\mathbf{f}_2) = \frac{2}{a^*\sqrt{5}} \begin{pmatrix} \sin \pi/10 \\ \cos \pi/10 \end{pmatrix} = \bar{\mathbf{d}}_2, \tag{6.67}$$

$$P(\mathbf{f}_3) = \frac{2}{a^*\sqrt{5}} \begin{pmatrix} -(1 + \sin \pi/10) \\ -\cos \pi/10 \end{pmatrix} = -(\bar{\mathbf{d}}_1 + \bar{\mathbf{d}}_2), \tag{6.68}$$

$$P(\mathbf{f}_4) = \frac{2}{a^*\sqrt{5}} \begin{pmatrix} 1 \\ 0 \end{pmatrix} = \bar{\mathbf{d}}_1. \tag{6.69}$$

The same projection matrix P (6.65) is now applied to the acceptance windows in the 4D space (6.59), analogous to the Fibonacci chain PAS in section 3.2. However, before this projection is applied we must consider whether or not this is the best projection for the current higher-dimensional space and acceptance windows. Steurer et al. [70], [72] discuss the scalings that can be applied to the acceptance window prior to projection to result in the optimal occupancy window and PAS for the Penrose tiling. They express the desire to achieve acceptance windows and higher-dimensional lattices that upon projection give occupancy windows and PAS nodes that are the most similar to the Penrose lattice. That is, a PAS with lattice parameters comparable to the Penrose rhomb edge length a_r, and occupancy windows that have occupancy factor ρ_{occ} as close to one and packing density ρ_{pac} as close to zero as possible (the occupancy factor and packing density were defined in the section 2.1.3). This is discussed in most detail for an octagonal structure in [70].

Applying the projection to the current acceptance window derived in the previous section, where $a^* = 1$, results in a PAS lattice given by (6.64) with basis vectors of length $|\bar{\mathbf{d}}_i| = 2/\sqrt{5}$ which is not similar to the edge length of the Penrose lattice $a_r = 2/5$. Instead apply a scaling to the acceptance window in perpendicular space. A scaling of the perpendicular space does not affect the lattice produced on the parallel space, apart from an inflation or deflation, as discussed by many [70], [49]. Applying a scaling of $1/\tau^2$ to the acceptance windows results in pentagonal acceptance windows encompassed by circles of radii

$$\lambda_1 = \lambda_4 = \frac{2}{5\tau^2}, \quad \lambda_2 = \lambda_3 = \frac{2}{5\tau}, \tag{6.70}$$

compared to equation (6.41). Having smaller acceptance windows in the 4D space results in a more dispersed selection of 4D lattice nodes to project, and thus an inflated Penrose lattice. In fact, in this instance the Penrose lattice is inflated by a factor τ^2 [70]. Therefore the Penrose rhombi now have edge lengths $a_r = 2\tau^2/5$, and so

$$a^* = \frac{2\tau^2}{5a_r}, \tag{6.71}$$

agreeing with [71]. This provides similar lattice parameters in the Penrose lattice and the PAS.

Applying the projection (6.65) to the scaled acceptance windows gives occupancy windows in the 2D plane with nodes

$$P\left(\frac{1}{\tau^2}\mathbf{V}_4^{\perp}\right) = \begin{pmatrix} 1 & 0 & -1 & -\tau(3-\tau)^{1/2} \\ 0 & 1 & 0 & -\tau \end{pmatrix} \frac{1}{\tau^2}\frac{2}{5} \begin{pmatrix} -\sum_{i=1}^5 n_i \\ 0 \\ \sum_{i=1}^5 n_i \cos 4\pi i/5 - \sum_{i=1}^5 n_i \\ \sum_{i=1}^5 n_i \sin 4\pi i/5 \end{pmatrix} \tag{6.72}$$

$$= \frac{2}{5\tau^2} \begin{pmatrix} -\sum_{i=1}^5 n_i \left(\cos 4\pi i/5 + \tau(3-\tau)^{1/2} \sin 4\pi i/5\right) \\ -\tau \sum_{i=1}^5 n_i \sin 4\pi i/5 \end{pmatrix}. \tag{6.73}$$

The occupancy windows are of the form of "stretched" pentagons centred at each of the PAS nodes. Figure 6.11 shows these shapes centred at the origin for example, and the ellipse shape which encloses them.

A comparison of the lattice nodes of the Penrose lattice (blue) and PAS (red) is shown in figure 6.12. In this figure we have superimposed a selection of the occupancy windows (red ellipses) to demonstrate the deviation of the Penrose nodes from the PAS. The occupancy windows have been represented by the largest ellipse in which the occupancy windows lie. It can be seen that some of the ellipses do not contain a (blue) Penrose node, and some contain two nodes. In fact, Steurer and Haibach [71] proved the proportion of these instances exactly. They showed that the frequency of singly occupied ellipses is 0.7236, of doubly occupied ellipses is 0.0652 and of unoccupied 0.2112. The packing density, relating the area of the unit cell of the PAS to the area of the occupancy window, is given by $\rho_{\text{pac}} = 0.447$.

By gaining a better understanding of the probability and distribution of the occupancy windows containing one, two or no Penrose nodes, and the distribution of

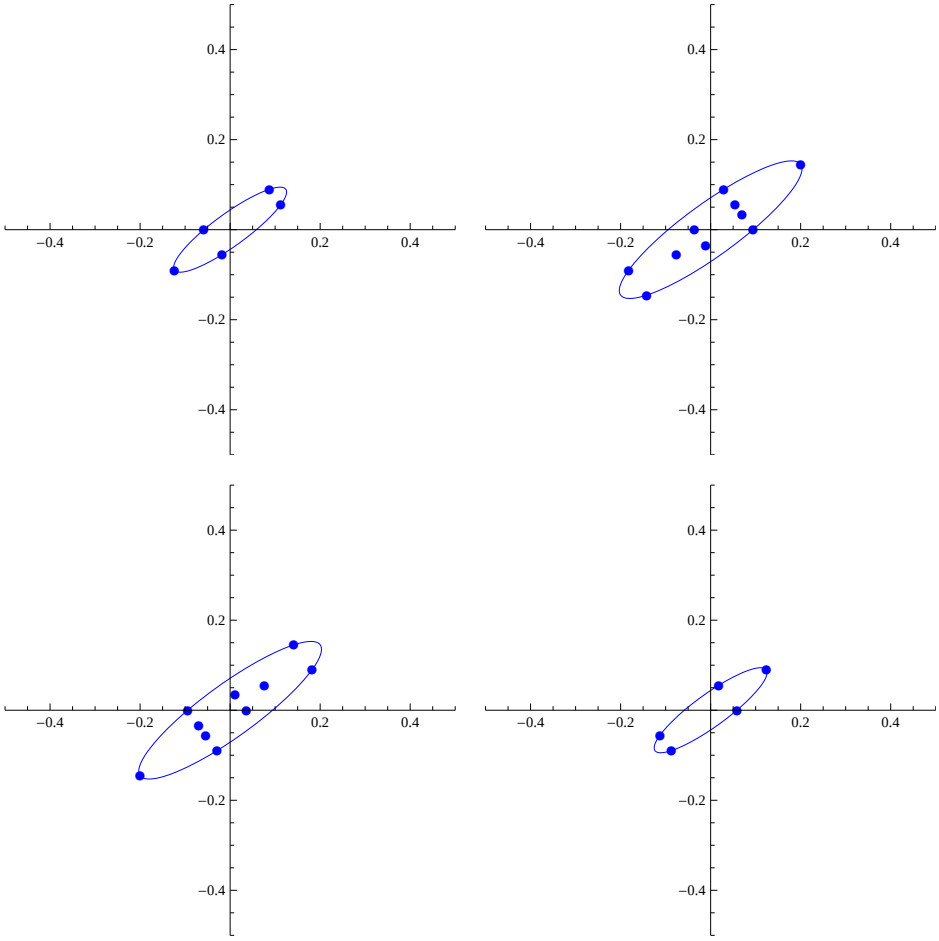

Figure 6.11: Vertices of the occupancy windows and the corresponding ellipse in which it lies, in the $\mathbf{e}_1$, $\mathbf{e}_2$ plane.

these nodes within the occupancy window, some interesting analysis of a perturbed PAS could be carried out in order to offer an alternative representation of the Penrose lattice.

6.4 Approximant

The approximant lattice for the Penrose tiling is a periodic lattice with a repeating unit cell that contains a section of quasiperiodicity from the Penrose tiling itself. The approximant was introduced in some detail in section 2.1.4 for both the Fibonacci chain and the Penrose tiling. The full formulae and algorithm for the construction of the Fibonacci chain approximant were given in section 3.3. In this chapter the method is applied to the 2D Penrose tiling when projecting from 4D space. The algorithm requires less computation than a similar algorithm determined by Lord et

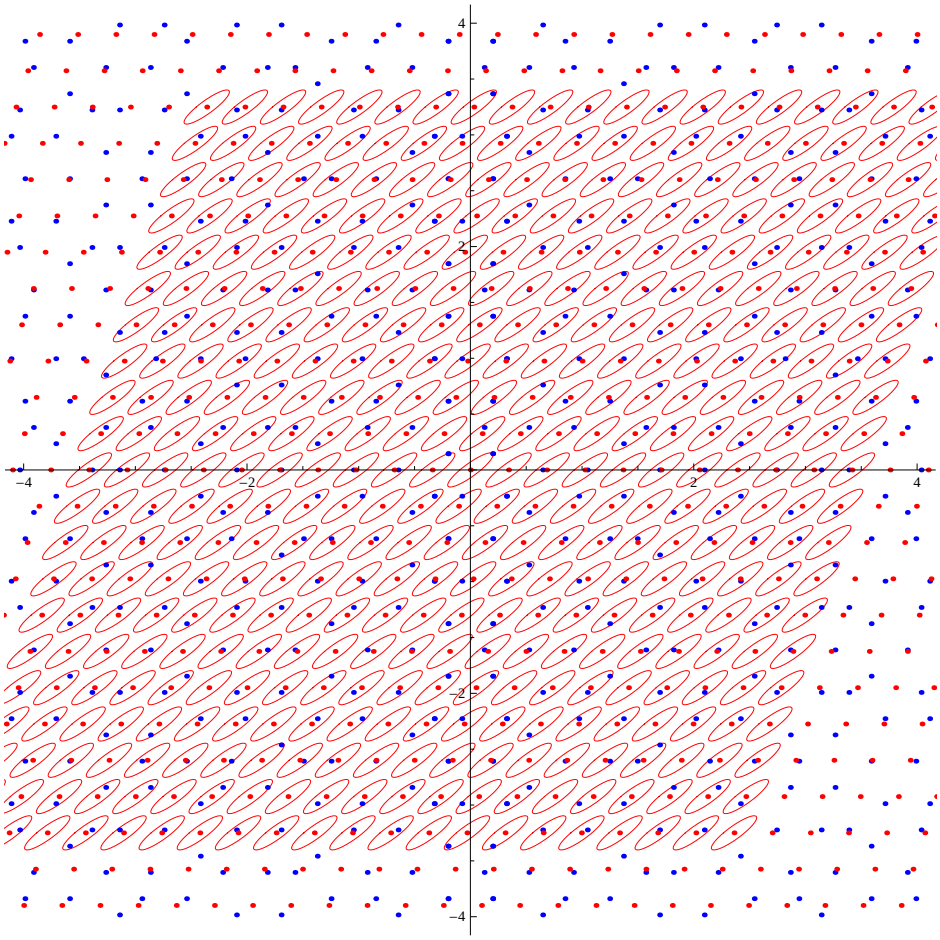

Figure 6.12: The Penrose tiling vertices (blue), the PAS vertices (red) and the range at which the Penrose vertices can lie from the PAS vertices (red ellipses).

al. [49] who choose to project from 5D and thus have a more complicated acceptance window. The algorithm for the construction of an approximant is described along with how the lattice differs from that of the Penrose tiling. The derivation of the unit cell of different approximants is also discussed.

Analogous to the Fibonacci chain approximant, the Penrose approximant is constructed by approximating τ in the perpendicular space components of the 4D space. This approximation is slightly more involved than with the 1D approximant as more than one approximation of τ can be made, i.e.

$$\tau \approx \tau_{N_i} = \frac{\text{Fib}(N_i + 1)}{\text{Fib}(N_i)}, \tag{6.74}$$

for $i = 1, 2$, the two dimensions of the perpendicular space.

Another complication is how the reciprocal of tau $\sigma = -\frac{1}{\tau}$ is approximated. We

specify two schemes of approximation, *scheme I*

$$\sigma_{N_i}^{I} = -\frac{1}{\tau} \approx -\frac{1}{\tau_{N_i}}, \tag{6.75}$$

and *scheme II*

$$\sigma_{N_i}^{II} = -\frac{1}{\tau} = 1 - \tau \approx 1 - \tau_{N_i}. \tag{6.76}$$

Denote the $(N_1, N_2)^{I/II}$-approximant as the approximant constructed with $\tau \approx \tau_{N_1}$ in the $\mathbf{e}_3$ component, $\tau \approx \tau_{N_2}$ in the $\mathbf{e}_4$ component and using scheme I/II. We note here that for increasing N_i, the two schemes converge. In fact, substitution of the approximation (6.74) into the two choices for σ, equations (6.75) and (6.76), gives

$$\sigma_{N_i}^{I} \approx -\frac{\mathrm{Fib}(N_i)}{\mathrm{Fib}(N_i)+1}, \tag{6.77}$$

and

$$\sigma_{N_i}^{II} \approx 1 - \frac{\mathrm{Fib}(N_i+1)}{\mathrm{Fib}(N_i)} = \frac{\mathrm{Fib}(N_i) - \mathrm{Fib}(N_i+1)}{\mathrm{Fib}(N_i)} = -\frac{\mathrm{Fib}(N_i-1)}{\mathrm{Fib}(N_i)}. \tag{6.78}$$

Therefore, the two approximations are related such that

$$\sigma_{N_i}^{I} = \sigma_{N_i-1}^{II}, \tag{6.79}$$

which converge to the same limit $-1/\tau$ for increasing N_i.

Approximating the perpendicular space components of the basis vectors for the Penrose tiling projection (6.29), using the identities (6.12)-(6.15), the approximations yield approximant basis vectors defined by

$$\tilde{\mathbf{f}}_1 = \frac{1}{5}\begin{pmatrix} 2(\cos 2\pi/5 - 1) \\ 2\sin 2\pi/5 \\ -\tau_{N_1} - 2 \\ \sqrt{3-\tau_{N_2}} \end{pmatrix}, \quad \tilde{\mathbf{f}}_2 = \frac{1}{5}\begin{pmatrix} 2(\cos 4\pi/5) - 1) \\ \sin 4\pi/5 \\ -\sigma_{N_1} - 2 \\ -\tau_{N_2}\sqrt{3-\tau_{N_2}} \end{pmatrix},$$
$$\tilde{\mathbf{f}}_3 = \frac{1}{5}\begin{pmatrix} 2(\cos 6\pi/5 - 1) \\ 2\sin 6\pi/5 \\ -\sigma_{N_1} - 2 \\ \tau_{N_2}\sqrt{3-\tau_{N_2}} \end{pmatrix}, \quad \tilde{\mathbf{f}}_4 = \frac{1}{5}\begin{pmatrix} 2(\cos 8\pi/5 - 1) \\ 2\sin 8\pi/5 \\ -\tau_{N_1} - 2 \\ -\sqrt{3-\tau_{N_2}} \end{pmatrix}. \tag{6.80}$$

The parallel space components are left exact, as with the 1D Fibonacci chain approximant, this ensures that the lattice produced still only consists of the thin and thick Penrose rhombi.

The next step is to define the lattice nodes of the approximant acceptance window. This is done by approximating the perpendicular space components of the nodes $\mathbf{V}_4^{\perp}$ (6.40), as

$$\tilde{\mathbf{V}}_4^{\perp} = \frac{1}{5}\begin{pmatrix} -2\sum_{i=1}^{5} n_i \\ 0 \\ -\tau_{N_1}(n_1+n_4) - \sigma_{N_1}(n_2+n_3) - 2\sum_{i=1}^{4} n_i \\ \sqrt{3-\tau_{N_2}}\left((n_1-n_4) + \tau_{N_2}(n_3-n_2)\right) \end{pmatrix}. \tag{6.81}$$

With the 1D analogy it was discussed that a unit cell of the skewed 2D lattice was taken rather than the Voronoi cell of the lattice in the procedure of defining the acceptance window, as it is for the quasiperiodic projection. We believe this is in fact the correct procedure, and that the term "Voronoi cell" is used in crystallography just because it happens that taking a unit cell around a lattice node in a square/hypercubic lattice is equivalent to a Voronoi cell. This hypothesis can be demonstrated when comparing the projection method to the pentagrid method, [66]. As described in the introduction in section 2.1.2, the five sets of lines in the pentagrid correspond to hyperplanes in the 5D space. The polygons formed by the lines in the pentagrid are used to determine the Penrose lattice points. These polygons relate to hypercubes around the nodes in 5D space, which are used to define the acceptance windows to then determine the Penrose lattice points. The approximation used in the perpendicular space in the projection method can equivalently be made in the pentagrid method via an approximation of the angles of three sets of the lines. This would cause changes in the shapes of the polygons formed in the pentagrid, which in turn relates to a different polytope around the nodes in 5D space. The polytope is a unit cell of the skewed higher-dimensional lattice. Therefore a unit cell of the skewed lattice should be taken around the lattice nodes, rather than the Voronoi cell, to be projected to the perpendicular space to define the acceptance windows.

Since the approximations of τ can be different in the two directions $(\mathbf{e}_3, \mathbf{e}_4)$, the acceptance windows no longer form regular pentagons in the (x_3, x_4)-plane. Instead the pentagons are irregular. Therefore the formulation of the area of acceptance windows is not a simple case of approximating τ in the set of inequalities defined for the area of pentagons in section 6.2, (6.51)-(6.58). However, the method for defining the area remains analogous.

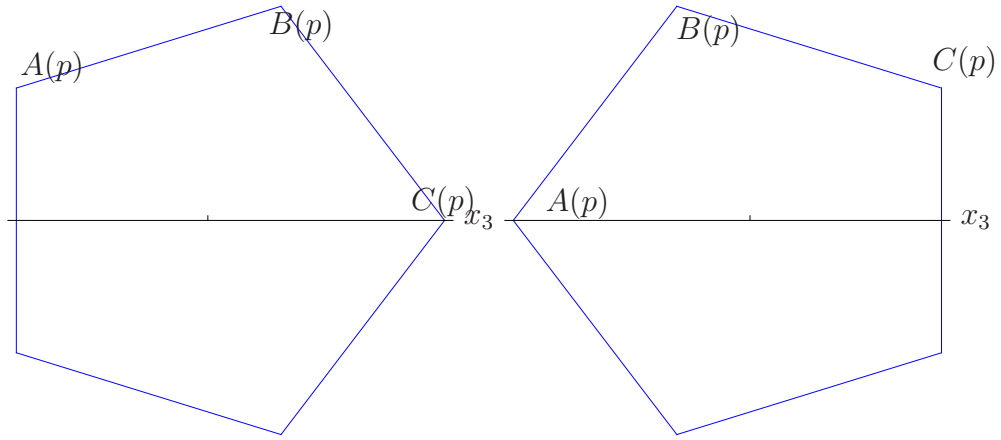

(a) Pentagon vertex coordinates, for $p = 1, -3$.

(b) Pentagon vertex coordinates, for $p = -1, 3$.

Figure 6.13: Vertex coordinates for the irregular pentagonal acceptance windows in the (x_3, x_4) plane.

The necessary vertices of the irregular pentagons for each $p \in \{-3, -1, 1, 3\}$ in the (x_3, x_4)-plane, as shown in figure 6.13, are given by

$$A(-3) = \frac{1}{5}\begin{pmatrix} 2+\sigma_{N_1} \\ \sqrt{3-\tau_{N_2}} \end{pmatrix}, \qquad B(-3) = \frac{1}{5}\begin{pmatrix} 2+\tau_{N_1} \\ \tau_{N_2}\sqrt{3-\tau_{N_2}} \end{pmatrix},$$
$$C(-3) = \frac{1}{5}\begin{pmatrix} 4+\tau_{N_1}+\sigma_{N_1} \\ 0 \end{pmatrix}, \tag{6.82}$$

$$A(-1) = \frac{1}{5}\begin{pmatrix} -\tau_{N_1}+\sigma_{N_1} \\ 0 \end{pmatrix}, \qquad B(-1) = \frac{1}{5}\begin{pmatrix} 0 \\ (\tau_{N_2}+1)\sqrt{3-\tau_{N_2}} \end{pmatrix},$$
$$C(-1) = \frac{1}{5}\begin{pmatrix} 2+\tau_{N_1} \\ \tau_{N_2}\sqrt{3-\tau_{N_2}} \end{pmatrix}, \tag{6.83}$$

$$A(1) = \frac{1}{5}\begin{pmatrix} -2-\tau_{N_1} \\ \tau_{N_2}\sqrt{3-\tau_{N_2}} \end{pmatrix}, \qquad B(1) = \frac{1}{5}\begin{pmatrix} 0 \\ (\tau_{N_2}+1)\sqrt{3-\tau_{N_2}} \end{pmatrix},$$
$$C(1) = \frac{1}{5}\begin{pmatrix} \tau_{N_1}-\sigma_{N_1} \\ 0 \end{pmatrix}, \tag{6.84}$$

$$A(3) = \frac{1}{5}\begin{pmatrix} -4-\tau_{N_1}-\sigma_{N_1} \\ 0 \end{pmatrix}, \qquad B(3) = \frac{1}{5}\begin{pmatrix} -2-\tau_{N_1} \\ \tau_{N_2}\sqrt{3-\tau_{N_2}} \end{pmatrix},$$
$$C(3) = \frac{1}{5}\begin{pmatrix} -2-\sigma_{N_1} \\ \sqrt{3-\tau_{N_2}} \end{pmatrix}. \tag{6.85}$$

The coordinates have been determined for each p using the set of $\mathbf{n} = (n_1, \cdots, n_5)$

determined in (6.22)-(6.27).

The areas of the acceptance windows are defined in the same manner as for the Penrose lattice (6.51)-(6.58), and are given by the inequalities

$$\tilde{\mathbf{x}}_3(p)_1 \in [A(p)_{x_3}, B(p)_{x_3}], \tag{6.86}$$

$$|\tilde{\mathbf{x}}_4(p)_1| \leq \frac{B(p)_{x_4} - A(p)_{x_4}}{B(p)_{x_3} - A(p)_{x_3}}(\tilde{\mathbf{x}}_3(p)_1 - B(p)_{x_3}) + B(p)_{x_4}, \tag{6.87}$$

$$\tilde{\mathbf{x}}_3(p)_2 \in [B(p)_{x_3}, C(p)_{x_3}], \tag{6.88}$$

$$|\tilde{\mathbf{x}}_4(p)_2| \leq \frac{C(p)_{x_4} - B(p)_{x_4}}{C(p)_{x_3} - B(p)_{x_3}}(\tilde{\mathbf{x}}_3(p)_1 - C(p)_{x_3}) + C(p)_{x_4}, \tag{6.89}$$

where the subscript x_3 and x_4 denote the x_3 and x_4 components of the polygon vertex coordinates, respectively.

The acceptance window for the approximant is defined as for the Penrose lattice (6.42); i.e.

$$\tilde{\mathbf{W}}_4 = \bigcup_{p\in\{-3,-1,1,3,5\}} \tilde{\mathbf{w}}_4(p), \tag{6.90}$$

where

$$\tilde{\mathbf{w}}_4(5) = -\begin{pmatrix} 1 \\ 0 \\ \frac{1}{5}(4 + \tau_{N_1} + \sigma_{N_1}) \\ 0 \end{pmatrix} \tag{6.91}$$

and

$$\tilde{\mathbf{w}}_4(p) = \bigcup_{j=1}^{2} \tilde{\mathbf{w}}_4(p)_j = \bigcup_{j=1}^{2} \begin{pmatrix} -p/5 \\ 0 \\ \tilde{\mathbf{x}}_3(p)_j \\ \tilde{\mathbf{x}}_4(p)_j \end{pmatrix}. \tag{6.92}$$

The acceptance window defined in equation (6.90) is replicated on every lattice node to give us the full acceptance window of the 4D system $\tilde{\mathbf{A}}_4$.

$$\tilde{\mathbf{A}}_4 = \left\{ \sum_{i=1}^{4} m_i \tilde{\mathbf{f}}_i + \tilde{\mathbf{W}}_4, \quad m_i \in \mathbb{Z} \right\}. \tag{6.93}$$

Analogous to the Penrose projection, it is now necessary to determine the points at which the acceptance windows intersect the parallel space (6.61),

$$\frac{1}{5}\left(2\sum_{i=1}^{4} \tilde{m}_i + \tau_{N_1}(\tilde{m}_1 + \tilde{m}_4) + \sigma_{N_1}(\tilde{m}_2 + \tilde{m}_3)\right) + \epsilon = \tilde{\mathbf{x}}_3(p)_j, \quad \text{and} \tag{6.94}$$

$$-\frac{1}{5}\sqrt{3 - \tau_{N_2}}\,((\tilde{m}_1 - \tilde{m}_4) - \tau_{N_2}(\tilde{m}_2 - \tilde{m}_3)) = \tilde{\mathbf{x}}_4(p)_j, \quad \tilde{m}_i \in \mathbb{Z}. \tag{6.95}$$

Substitution of equations (6.94) and (6.95) into equations (6.86)-(6.89) determines the required inequalities that must be solved to determine the 4-tuple of integers $\tilde{\mathbf{m}}_p$.

The Penrose approximant lattice nodes are therefore given by

$$\mathbf{x}_{\text{approx}} = \left(\frac{2}{5}\sum_{i=1}^{4}\tilde{m}_i(\cos 2\pi i/5 - 1) - \frac{p}{5}\right)\mathbf{e}_1 + \left(\frac{2}{5}\sum_{i=1}^{4}\tilde{m}_i \sin 2\pi i/5\right)\mathbf{e}_2, \qquad (6.96)$$

for $\tilde{\mathbf{m}}_p = (\tilde{m}_1, \ldots, \tilde{m}_4)$ and $p \in \{-3, -1, 1, 3, 5\}$.

In summary the algorithm for the projection method for the Penrose lattice approximant is as follows

- Construct a 4D lattice approximating the 4D hyperrhombohedral lattice that approximates τ in the perpendicular space, defined in (6.80)
- Approximate the perpendicular space components of the acceptance window nodes $\tilde{\mathbf{V}}_4{}^{\perp}$, defined in (6.81)
- Decorate every lattice node with the acceptance window to give the full set $\tilde{\mathbf{A}}_4$, defined in (6.93)
- Find the set of integers $\tilde{\mathbf{m}}_p = (\tilde{m}_1, \tilde{m}_2, \tilde{m}_3, \tilde{m}_4) \in \tilde{\mathcal{M}}$ which allows the intersection of $\tilde{\mathbf{A}}_4$ with the parallel plane, defined in (6.94)-(6.95)
- The intersection points on the parallel plane determine the Penrose approximant lattice nodes $\mathbf{x}_{\text{approx}}$, defined in (6.96).

In the background discussion of the approximant in section 2.1.4 it was shown how to determine the period of the approximant. The periods of the approximant are given when higher-dimensional lattice nodes lie on the parallel space. The nodes lie on the parallel space when the perpendicular space components of the node coordinates equal zero, i.e.

$$\begin{aligned} &2\sum_{j=1}^{4} q_j + \tau_{N_1}(q_1 + q_4) + \sigma_{N_1}(q_2 + q_3) = 0 \quad \text{and} \\ &\sqrt{3 - \tau_{N_2}}\,((q_1 - q_4) - \tau_{N_2}(q_2 - q_3)) = 0, \end{aligned} \qquad (6.97)$$

for $q_i \in \mathbb{Z}$. The set of 4-tuples $\mathbf{q} = (q_1, q_2, q_3, q_4)$ that satisfy (6.97) form a set $\mathcal{Q}$. The associated nodes of the periodic cell are given by the parallel space components of the

selected lattice nodes $\sum_{i=1}^{4} q_i \tilde{\mathbf{f}}_i \in \Lambda_{\mathcal{Q}}$, and

$$\mathbf{x}_{\text{period}} = \frac{2}{5} \begin{pmatrix} \sum_{i=1}^{4} q_i \left(\cos 2\pi i/5 - 1\right) \\ \sum_{i=1}^{4} q_i \sin 2\pi i/5 \end{pmatrix}. \tag{6.98}$$

The shape and size of the periodic cell depends on N_1, N_2 and the scheme used in the $(N_1, N_2)^{I/II}$-approximant. Altering the approximation or the scheme affects the equality (6.97) that must be solved, and thus alters the set $\mathcal{Q}$.

As mentioned in the background discussion of the approximant, the concept of choosing the periodic cell shape of the approximant has been investigated previously in [74] and [49]. For a 2D parallel space, two linear combinations of the parallel space basis vectors (parallel space components of the 4D basis vectors) can be selected to determine the periodic directions in the approximant. The same linear combination should then be applied to the perpendicular space components. However the linear combination of the perpendicular space basis vectors must be equal to zero (6.97). A linear transform can be applied to the perpendicular basis vectors to ensure that this equality is met. Applying linear transforms to the perpendicular space does not affect the lattice produced in the parallel space, making this method possible. An example of this procedure is discussed in some detail in [74] for an approximant with an orthorhombic unit cell from a 5D projection. It is shown that for the same approximant tiling multiple different periodic cells can be defined. For the work in this thesis the original perpendicular basis vectors will be kept. This is because we are mostly interested in the overall tiling produced rather than the period itself. For large regions of the tiling the period will become irrelevant. Thus we concentrate on the variations of the approximant tiling itself rather than specifying particular periods.

Figure 6.14 shows an example of a $(1, 2)^{I}$-approximant lattice (green) compared to the Penrose lattice (blue). The nodes of the period of the approximant are shown by purple crosses.

6.5 Conclusions

In this chapter we first extended the construction of the 1D Fibonacci chain and its approximations to create the 2D square Fibonacci lattice and approximations with ease. We also developed a rigorous algorithm for the construction of the 2D Penrose

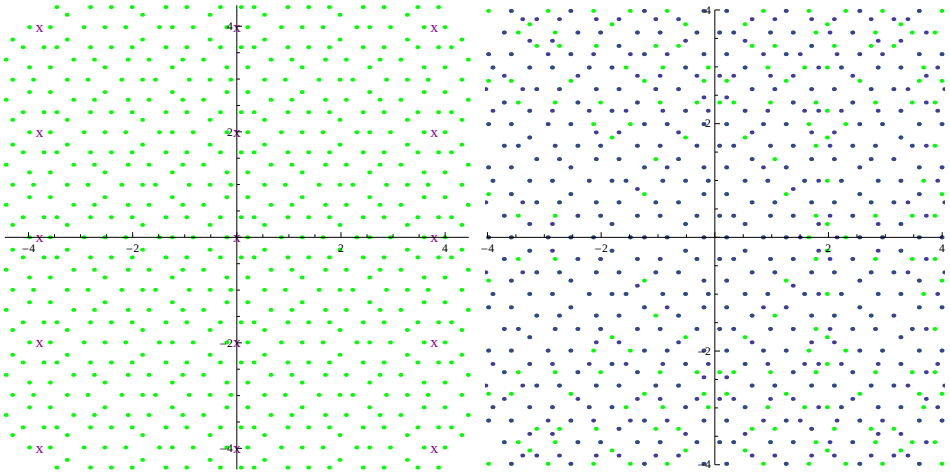

(a) $(1,2)^I$-approximant (green) and periodic cell nodes (purple).

(b) $(1,2)^I$-approximant (green) and Penrose lattice nodes (blue).

Figure 6.14: $(1,2)^I$-approximant lattice nodes compared to the Penrose lattice nodes.

lattice via the projection method. The algorithm and accompanying explanations and diagrams aim to provide a reader without a prior knowledge of quasiperiodic structures, the projection method or crystallography, with a tool to construct the Penrose lattice oneself. The algorithms to produce the PAS and the approximant for the Penrose lattice were also thoroughly discussed.

Comparisons between the quasiperiodic lattices and their approximations will be drawn by the acoustic scattering properties of the lattices and is discussed in chapters 8 and 9 for the square Fibonacci (SF) and Penrose lattices respectively.

Chapter 7

Wave scattering by two-dimensional infinite periodic arrays of scatterers

In this chapter the novel approach determining analytic expressions for the effective wave propagation through infinite periodic arrays of small circular cylinders is discussed. Initially, the scenario of a doubly-periodic rectangular lattice, as introduced in section 2.4.4, is considered. The approach taken differs from that exploited by others in the existing literature and lifts restrictions on the period lengthscales. With the techniques and notation provided in the doubly-periodic scenario, the extension is made to orthorhombic periodic lattices in which the periodic cell can contain multiple arbitrarily-positioned scatterers. The motivation for modelling such a periodic lattice is to enable the prediction of wave propagation through a 2D, infinite, periodic approximant array of small circular scatterers, analogous to the 1D approximant in section 4.5. The approximant lattices for the square Fibonacci and Penrose lattices were discussed previously in chapter 6.

7.1 Doubly-periodic lattice

To begin, we continue from the work introduced in section 2.4.4, for wave propagation in a doubly-periodic lattice, and the notation and parameters remain the same. The lattice is rectangular and has period d and λd in the x and y directions respectively,

referring to figure 7.1.

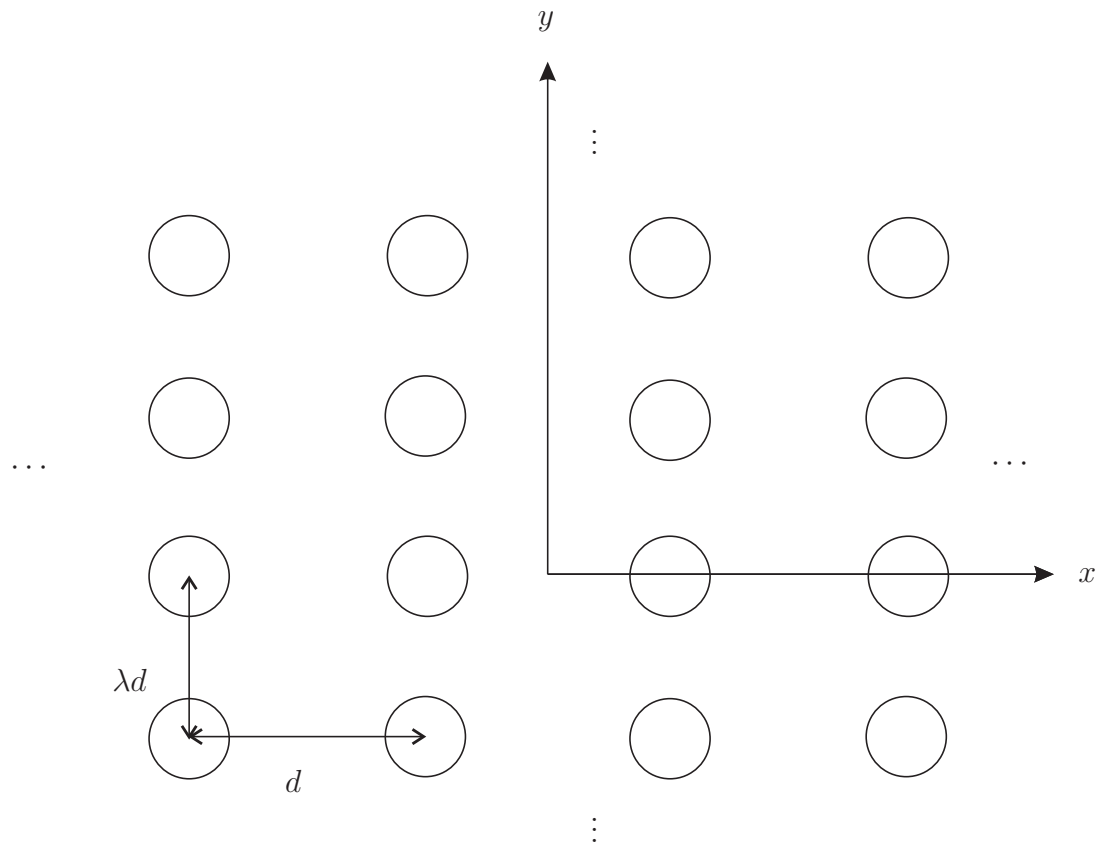

Figure 7.1: Set up of a doubly periodic array of circular cylinders.

For circular cylinders of arbitrary radius a, an eigensolution of the 2D Helmholtz equation can be posed of the form

$$u(\mathbf{x}) = \sum_{n=-\infty}^{\infty} C_n H_n^{(1)}(|\mathbf{x}|)e^{in\theta} \tag{7.1}$$

$$+ \sum_{s=-\infty}^{\infty} \sum_{\substack{t=-\infty \\ (s,t)\neq(0,0)}}^{\infty} \sum_{n=-\infty}^{\infty} C_n e^{i\gamma(s\cos\theta+\lambda t\sin\theta)} H_n^{(1)}(|\mathbf{x}-\mathbf{p}_{st}|)e^{in\theta_{st}}, \tag{7.2}$$

where $\mathbf{p}_{st} = D(s, \lambda t)$, $D = kd$ and $\gamma = |\boldsymbol{\gamma}|$ is the non-dimensional effective wavenumber scaled on the lengthscale d. Applying the restriction $0 < ka \ll 1$ for small cylinders, as with the work in section 2.4, yields a reduction in the infinite sum over all orders of the Hankel function. This assumption simplifies the expression in (7.2), at leading order in ka, to

$$u(\mathbf{x}) = CH_0^{(1)}(|\mathbf{x}|) + \sum_{s=-\infty}^{\infty} \sum_{\substack{t=-\infty \\ (s,t)\neq(0,0)}}^{\infty} Ce^{i\gamma(s\cos\theta+\lambda t\sin\theta)} H_0^{(1)}(|\mathbf{x}-\mathbf{p}_{st}|), \tag{7.3}$$

where C replaces the former coefficient C_0.

Apply sound-soft/Dirichlet boundary conditions on each of the cylinders. Take the $(0,0)^{th}$ cylinder at the origin, without loss of generality,

$$u(\eta) = 0 = H_0^{(1)}(\eta) + \sum_{s=-\infty}^{\infty} \sum_{\substack{t=-\infty \\ (s,t)\neq(0,0)}}^{\infty} e^{i\gamma(s\cos\theta+\lambda t\sin\theta)} H_0^{(1)}(|\mathbf{p}_{st}|), \tag{7.4}$$

by letting $\eta = ka \to 0$.

In section 5.1.1 the integral representation of the Hankel function was applied, where the x and y components of the argument are expressed independently. The same integral representation should be applied here,

$$H_0^{(1)}(|\mathbf{p}_{st}|) = H_0^{(1)}(D\sqrt{s^2+\lambda^2 t^2}) = -\frac{i}{\pi}\int_{-\infty}^{\infty} e^{-\beta(\alpha)|s|D+i\alpha D\lambda t}\frac{d\alpha}{\beta(\alpha)}, \tag{7.5}$$

for

$$\beta(\alpha) = \begin{cases} -i\sqrt{1-\alpha^2}, & |\alpha| \leq 1, \\ \sqrt{\alpha^2-1}, & |\alpha| > 1. \end{cases} \tag{7.6}$$

Substitution of the integral representation (7.5) into equation (7.4) results in

$$H_0^{(1)}(\eta) = \sum_{s=-\infty}^{\infty} \sum_{\substack{t=-\infty \\ (s,t)\neq(0,0)}}^{\infty} e^{i\gamma(s\cos\theta+\lambda t\sin\theta)} \frac{i}{\pi}\int_{-\infty}^{\infty} e^{-\beta(\alpha)|s|D+i\alpha D\lambda t}\frac{d\alpha}{\beta(\alpha)}. \tag{7.7}$$

Assuming convergence of the sum, this is equivalent to

$$H_0^{(1)}(\eta) = \frac{i}{\pi}\int_{-\infty}^{\infty} \frac{1}{\beta} \sum_{s=-\infty}^{\infty} \sum_{\substack{t=-\infty \\ (s,t)\neq(0,0)}}^{\infty} e^{i\gamma s\cos\theta} e^{i\gamma\lambda t\sin\theta} e^{-\beta(\alpha)|s|D} e^{i\alpha D\lambda t} d\alpha, \tag{7.8}$$

and decompose the sum as shown:

$$\begin{aligned} H_0^{(1)}(\eta) = \frac{i}{\pi}\int_{-\infty}^{\infty} \frac{1}{\beta}\Bigg\{ &-1 + \sum_{s=-\infty}^{\infty} e^{is\gamma\cos\theta-\beta D|s|} \\ &+ \sum_{\substack{t=-\infty \\ t\neq 0}}^{\infty} e^{i\lambda t\gamma\sin\theta+i\alpha D\lambda t} \sum_{s=-\infty}^{\infty} e^{is\gamma\cos\theta-\beta D|s|} \Bigg\} d\alpha. \end{aligned} \tag{7.9}$$

The infinite sum over s can expanded as follows

$$\sum_{s=-\infty}^{\infty} e^{is\gamma\cos\theta-\beta D|s|} = \sum_{s=-\infty}^{-1} e^{is\gamma\cos\theta-\beta D|s|} + \sum_{s=0}^{\infty} e^{is\gamma\cos\theta-\beta D|s|} \tag{7.10}$$

$$= \sum_{s=1}^{\infty} e^{-is\gamma\cos\theta-\beta Ds} + \sum_{s=0}^{\infty} e^{is\gamma\cos\theta-\beta Ds} \tag{7.11}$$

$$= \frac{e^{-i\gamma\cos\theta-\beta D}}{1-e^{-i\gamma\cos\theta-\beta D}} + \frac{1}{1-e^{i\gamma\cos\theta-\beta D}} \tag{7.12}$$

$$= \frac{e^{\beta D}-e^{-\beta D}}{e^{\beta D}+e^{-\beta D}-2\cos(\gamma\cos\theta)} \tag{7.13}$$

$$= \frac{\sinh(\beta D)}{\cosh(\beta D)-\cos(\gamma\cos\theta)}, \tag{7.14}$$

assuming convergence for all α on the integration contour. Substitution of the expansion (7.14) into equation (7.9) gives

$$\begin{aligned} H_0^{(1)}(\eta) =& \frac{i}{\pi}\int_{-\infty}^{\infty}\frac{1}{\beta}\Bigg\{-1+\frac{\sinh(\beta D)}{\cosh(\beta D)-\cos(\gamma\cos\theta)} \\ &+\sum_{\substack{t=-\infty\\ t\neq 0}}^{\infty} e^{i\lambda t\gamma\sin\theta+i\alpha D\lambda t}\frac{\sinh(\beta D)}{\cosh(\beta D)-\cos(\gamma\cos\theta)}\Bigg\}d\alpha \qquad (7.15)\\ =& \frac{i}{\pi}\int_{-\infty}^{\infty}\frac{1}{\beta}\left(\frac{\sinh(\beta D)}{\cosh(\beta D)-\cos(\gamma\cos\theta)}-1\right)d\alpha \\ &+\frac{i}{\pi}\sum_{\substack{t=-\infty\\ t\neq 0}}^{\infty} e^{i\lambda t\gamma\sin\theta}\int_{-\infty}^{\infty}\frac{e^{i\alpha D\lambda t}}{\beta}\frac{\sinh(\beta D)}{\cosh(\beta D)-\cos(\gamma\cos\theta)}d\alpha. \qquad (7.16)\end{aligned}$$

The first integral in equation (7.16) can be manipulated to ensure convergence,

$$\begin{aligned} &\frac{i}{\pi}\int_{-\infty}^{\infty}\frac{1}{\beta}\left(\frac{\sinh(\beta D)}{\cosh(\beta D)-\cos(\gamma\cos\theta)}-1\right)d\alpha \\ =&\frac{i}{\pi}\int_{-\infty}^{\infty}\frac{1}{\beta}\left(\frac{\sinh(\beta D)}{\cosh(\beta D)-\cos(\gamma\cos\theta)}-\frac{\sinh(\beta D)}{\cosh(\beta D)}+\frac{\sinh(\beta D)}{\cosh(\beta D)}-1\right)d\alpha \qquad (7.17)\\ =&\frac{i}{\pi}\int_{-\infty}^{\infty}\frac{1}{\beta}\left(\frac{\sinh(\beta D)}{\cosh(\beta D)-\cos(\gamma\cos\theta)}-\frac{\sinh(\beta D)}{\cosh(\beta D)}\right)d\alpha \\ &+\frac{i}{\pi}\int_{-\infty}^{\infty}\frac{1}{\beta}\left(\frac{\sinh(\beta D)}{\cosh(\beta D)}-1\right)d\alpha \qquad (7.18)\\ =&\frac{i}{\pi}\int_{-\infty}^{\infty}\frac{\sinh(\beta D)}{\beta\cosh(\beta D)}\left(\frac{\cos(\gamma\cos\theta)}{\cosh(\beta D)-\cos(\gamma\cos\theta)}\right)d\alpha-\frac{i}{\pi}\int_{-\infty}^{\infty}\frac{e^{-\beta D}}{\beta\cosh(\beta D)}d\alpha \qquad (7.19)\\ =&I_1(\gamma,\theta)+I_2. \qquad (7.20)\end{aligned}$$

Both $I_1(\gamma,\theta)$ and I_2 can be integrated numerically taking care to take the contour above the branch-point at $\alpha=-1$ and below the branch-point at $\alpha=1$, as depicted

in figure 7.2, where these are the branch-points of $\beta(\alpha)$. (Note, in fact, that I_1 does not contain any branch-cuts.) The integral $I_1(\gamma,\theta)$ has additional poles at

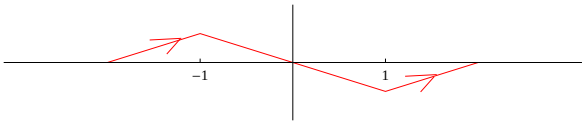

Figure 7.2: Deformation of contour for $I_1(\gamma,\theta)$ and I_2.

$$\cosh(\beta D)=\cos(\gamma\cos\theta) \quad \Rightarrow \quad \beta_m=\begin{cases} -\frac{i}{D}(\gamma\cos\theta+2m\pi), & m>-\frac{\gamma\cos\theta}{2\pi}, \\ \frac{i}{D}(\gamma\cos\theta+2m\pi), & m<-\frac{\gamma\cos\theta}{2\pi}, \end{cases} \tag{7.21}$$

$$\Rightarrow \alpha_m^{\pm}=\pm\sqrt{1+\beta_m^2}=\begin{cases} \pm\frac{1}{D}\sqrt{D^2-(\gamma\cos\theta+2m\pi)^2}, & (\gamma\cos\theta+2m\pi)^2<D^2, \\ \pm\frac{i}{D}\sqrt{(\gamma\cos\theta+2m\pi)^2-D^2}, & (\gamma\cos\theta+2m\pi)^2>D^2, \end{cases} \tag{7.22}$$

for $m\in\mathbb{Z}$, but these are also avoided by the above deformation.

The second integral in equation (7.16) requires some more thought, although the positions of the poles are the same as for $I_1(\gamma,\theta)$, (7.22). The integrand is branch-cut free and so can be evaluated using a "D-contour" and Jordan's Lemma. Whether or not the 'D' deformation is made in the positive or negative imaginary direction of the α-plane depends on the sign of t in the infinite sum. For $t\geq 0$ it is necessary to deform up and thus the positive poles α_m^+ must be accounted for. For $t<0$ it is necessary to deform down and thus the negative poles α_m^- must be accounted for. Applying the Cauchy residue theorem, as discussed in section 5.1.1, it is easily shown that

$$\int_{-\infty}^{\infty}\frac{e^{i\alpha D\lambda t}}{\beta}\frac{\sinh(\beta D)}{\cosh(\beta D)-\cos(\gamma\cos\theta)}d\alpha=\begin{cases} 2\pi i\sum_{m=-\infty}^{\infty}\frac{e^{i\alpha_m^+ D\lambda t}}{\alpha_m^+ D} & t\geq 0 \\ -2\pi i\sum_{m=-\infty}^{\infty}\frac{e^{i\alpha_m^- D\lambda t}}{\alpha_m^- D} & t<0 \end{cases} \tag{7.23}$$

$$=2\pi i\sum_{m=-\infty}^{\infty}\frac{e^{i\alpha_m^+ D\lambda|t|}}{\alpha_m^+ D}, \quad t\in\mathbb{Z}. \tag{7.24}$$

Therefore the second term in (7.16) can be expressed as

$$\frac{i}{\pi}\sum_{\substack{t=-\infty\\ t\neq 0}}^{\infty}e^{i\lambda t\gamma\sin\theta}\int_{-\infty}^{\infty}\frac{e^{i\alpha D\lambda t}}{\beta}\frac{\sinh(\beta D)}{\cosh(\beta D)-\cos(\gamma\cos\theta)}d\alpha$$

$$=-2\sum_{\substack{t=-\infty\\ t\neq 0}}^{\infty}e^{i\lambda t\gamma\sin\theta}\sum_{m=-\infty}^{\infty}\frac{e^{i\alpha_m^+ D\lambda|t|}}{\alpha_m^+ D} \tag{7.25}$$

$$=-2\sum_{m=-\infty}^{\infty}\frac{1}{\alpha_m^+ D}\left(\sum_{t=1}^{\infty}e^{i\lambda(\gamma\sin\theta+D\alpha_m^+)t}+\sum_{t=-\infty}^{-1}e^{i\lambda(\gamma\sin\theta-D\alpha_m^+)t}\right) \tag{7.26}$$

$$= -2 \sum_{m=-\infty}^{\infty} \frac{1}{\alpha_m^+ D} \left(\sum_{t=1}^{\infty} e^{i\lambda(\gamma \sin\theta + D\alpha_m^+)t} + \sum_{t=1}^{\infty} e^{-i\lambda(\gamma \sin\theta - D\alpha_m^+)t} \right) \tag{7.27}$$

$$= -2 \sum_{m=-\infty}^{\infty} \frac{1}{\alpha_m^+ D} \left(\frac{e^{i\lambda(\gamma \sin\theta + D\alpha_m^+)}}{1 - e^{i\lambda(\gamma \sin\theta + D\alpha_m^+)}} + \frac{e^{-i\lambda(\gamma \sin\theta - D\alpha_m^+)}}{1 - e^{-i\lambda(\gamma \sin\theta - D\alpha_m^+)}} \right) \tag{7.28}$$

$$= -2 \sum_{m=-\infty}^{\infty} \frac{1}{\alpha_m^+ D} \left(\frac{\cos(\lambda\gamma \sin\theta) - e^{iD\lambda\alpha_m^+}}{\cos(D\lambda\alpha_m^+) - \cos(\lambda\gamma \sin\theta)} \right) \tag{7.29}$$

$$= \Sigma_1(\gamma, \theta). \tag{7.30}$$

Since $\alpha_m^+ \sim im$ as $m \to \pm\infty$ the summand in Σ_1 tends to zero exponentially, and thus Σ_1 is rapidly convergent.

Substitution of equations (7.20) and (7.30) into equation (7.16) results in the following analytic expression for $\boldsymbol{\gamma}$,

$$H_0^{(1)}(\eta) = I_1(\gamma, \theta) + I_2 + \Sigma_1(\gamma, \theta). \tag{7.31}$$

The above expression can easily be computed for various parameters to determine γ given particular θ. The real $\boldsymbol{\gamma}$ which satisfy equation (7.31) represent the propagating effective wavenumbers for particular frequencies and periods in $D = kd$.

7.2 Approximant lattice

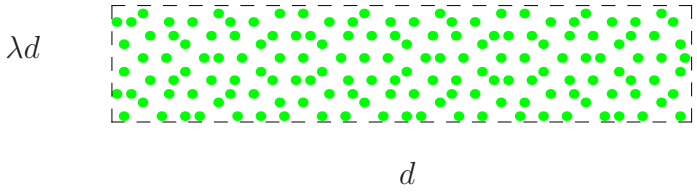

Figure 7.3: Periodic unit cell containing nodes of the $(2,2)^I$-approximant structure.

This section extends the approach taken to determine effective wave propagation properties for a doubly-periodic lattice, where each periodic cell contains a single scatterer, to an infinite, periodic structure where each cell contains N scatterers of arbitrary position. The theory is applied to the infinite, periodic approximant structure, but it is applicable to any distribution within the cell. The assumption of small radii, $ka \ll 1$, is still taken for mathematical convenience.

Figure 7.3 depicts an example of a unit cell of a $(2,2)^I$-approximant, discussed in detail in chapter 6. Define the non-dimensional period lengthscales D and λD in the x and y directions, as with the doubly-periodic scenario. The N scatterers in the periodic unit cell have non-dimensional locations $\mathbf{b}^j = k(x^j, y^j)$, $1 \leq j \leq N$, and thus the position of the j^{th} scatterer in the $(s,t)^{\text{th}}$ cell is given by

$$\mathbf{p}_{st}^j = \mathbf{p}_{st} + \mathbf{b}^j = D(s, \lambda t) + \mathbf{b}^j. \tag{7.32}$$

Pose an eigensolution to the 2D Helmholtz equation of a similar form to that of the doubly-periodic lattice (7.3), except that there exists an additional sum over the finite number of scatterers in the periodic cell,

$$u(\mathbf{x}) = \sum_{s=-\infty}^{\infty} \sum_{t=-\infty}^{\infty} \sum_{j=1}^{N} C_{st}^j H_0^{(1)}(|\mathbf{x} - \mathbf{p}_{st}^j|). \tag{7.33}$$

Apply an analogous Bloch condition to the unknown coefficients as with the doubly-periodic case (2.145)

$$C_{st}^j = C^j e^{i\gamma(s\cos\theta + \lambda t \sin\theta)}, \tag{7.34}$$

resulting in

$$\begin{aligned} u(\mathbf{x}) = &\sum_{s=-\infty}^{\infty} \sum_{t=-\infty}^{\infty} \sum_{j=1}^{N} C^j e^{i\gamma(s\cos\theta + \lambda t \sin\theta)} H_0^{(1)}(|\mathbf{x} - \mathbf{p}_{st}^j|) \qquad (7.35) \\ = &C^\ell \left(H_0^{(1)}(|\mathbf{x} - \mathbf{b}^\ell|) + \sum_{s=-\infty}^{\infty} \sum_{\substack{t=-\infty \\ (s,t)\neq(0,0)}}^{\infty} H_0^{(1)}(|\mathbf{x} - \mathbf{p}_{st}^\ell|) e^{i\gamma(s\cos\theta + \lambda t \sin\theta)} \right) \\ &+ \sum_{\substack{j=1 \\ j\neq\ell}}^{N} C^j \sum_{s=-\infty}^{\infty} \sum_{t=-\infty}^{\infty} H_0^{(1)}(|\mathbf{x} - \mathbf{p}_{st}^j|) e^{i\gamma(s\cos\theta + \lambda t \sin\theta)}. \qquad (7.36) \end{aligned}$$

With the solution posed in this form (7.36), apply the sound-soft boundary conditions on the ℓ^{th} cylinder in the $(0,0)^{\text{th}}$ periodic cell, i.e. at $\mathbf{x} = \mathbf{b}^\ell + \eta$,

$$\begin{aligned} 0 = &C^\ell \left(H_0^{(1)}(\eta) + \sum_{s=-\infty}^{\infty} \sum_{\substack{t=-\infty \\ (s,t)\neq(0,0)}}^{\infty} H_0^{(1)}(|\mathbf{p}_{st}|) e^{i\gamma(s\cos\theta + \lambda t \sin\theta)} \right) \\ &+ \sum_{\substack{j=1 \\ j\neq\ell}}^{N} C^j \sum_{s=-\infty}^{\infty} \sum_{t=-\infty}^{\infty} H_0^{(1)}(|\mathbf{b}^{j\ell} - \mathbf{p}_{st}|) e^{i\gamma(s\cos\theta + \lambda t \sin\theta)}, \end{aligned} \tag{7.37}$$

where $\mathbf{b}^{\ell j}$ is the non-dimensional separation between the ℓ^{th} and j^{th} scatterers,

$$\mathbf{b}^{\ell j} = \mathbf{b}^{\ell} - \mathbf{b}^{j} = k(x^{\ell} - x^{j}, y^{\ell} - y^{j}) = D(x^{\ell j}, y^{\ell j}), \tag{7.38}$$

$$\text{with} \quad x^{\ell j} = \frac{1}{d}(x^{\ell} - x^{j}), \quad y^{\ell j} = \frac{1}{\lambda d}(y^{\ell} - y^{j}), \tag{7.39}$$

and $\mathbf{p}_{st}$ is defined in equation (7.32) and only depends on the period (s, t). Note here that because of the scaling on $x^{\ell j}$ and $y^{\ell j}$,

$$-1 \leq x^{\ell j}, y^{\ell j} \leq 1. \tag{7.40}$$

In an analogous manner to the multipole method for a finite array of scatters in section 2.4.3, the boundary conditions can be applied to all the scatterers in the $(0, 0)^{\text{th}}$ cell $1 \leq j \leq N$, to determine a matrix equation of the form

$$\mathbf{HC} = \mathbf{0}, \tag{7.41}$$

where $\mathbf{C}$ is an $N \times 1$ vector containing the unknown coefficients C^j and the matrix $\mathbf{H}$ has components

$$\mathbf{H}_{\ell\ell} = H_0^{(1)}(\eta) + \sum_{s=-\infty}^{\infty} \sum_{\substack{t=-\infty \\ (s,t)\neq(0,0)}}^{\infty} H_0^{(1)}(|\mathbf{p}_{st}|) e^{i\gamma(s\cos\theta + \lambda t \sin\theta)}, \tag{7.42}$$

$$\mathbf{H}_{\ell j} = \sum_{s=-\infty}^{\infty} \sum_{t=-\infty}^{\infty} H_0^{(1)}(|\mathbf{b}^{\ell j} - \mathbf{p}_{st}|) e^{i\gamma(s\cos\theta + \lambda t \sin\theta)}, \quad \ell \neq j. \tag{7.43}$$

Note that the diagonal entries of the matrix $\mathbf{H}$ relate to the field on the ℓ^{th} scatterer in the $(0, 0)^{\text{th}}$ cell to the scattered field due to the ℓ^{th} scatterers in every other cell. This is exactly the same as the doubly-periodic case, and the equality between equations (7.4) and (7.42) can be seen. Therefore, using the procedure laid out in the previous section, it can be seen that

$$\mathbf{H}_{\ell\ell} = H_0^{(1)}(\eta) - I_1(\gamma, \theta) - I_2 - \Sigma_1(\gamma, \theta). \tag{7.44}$$

The off-diagonal entries of the matrix $\mathbf{H}$ relate to the field at the ℓ^{th} scatterer in each cell to all other scatterers in that cell. The approach to manipulate this expression (7.43) is an extension to that in the previous section 7.1 and will be discussed now.

Employ the integral representation of the Hankel function used previously (7.5) in the expression for the off-diagonal matrix entries $\mathbf{H}_{\ell j}$. The argument of the Hankel function in this expression is

$$|\mathbf{b}^{\ell j} - \mathbf{p}_{st}| = D\sqrt{(x^{\ell j} - s)^2 + \lambda^2 (y^{\ell j} - t)^2}, \tag{7.45}$$

and therefore

$$\mathbf{H}_{\ell j} = \sum_{s=-\infty}^{\infty}\sum_{t=-\infty}^{\infty}\left(-\frac{i}{\pi}\int_{-\infty}^{\infty}\frac{1}{\beta}e^{i\alpha D\lambda(t-y^{\ell j})-\beta D|s-x^{\ell j}|}d\alpha\right)e^{i\gamma(s\cos\theta+\lambda t\sin\theta)} \tag{7.46}$$

$$= -\frac{i}{\pi}\int_{-\infty}^{\infty}\frac{1}{\beta}\sum_{t=-\infty}^{\infty}e^{i\alpha D\lambda(t-y^{\ell j})}e^{i\lambda t\gamma\sin\theta}\sum_{s=-\infty}^{\infty}e^{is\gamma\cos\theta}e^{-\beta D|s-x^{\ell j}|}d\alpha. \tag{7.47}$$

The evaluation of the infinite sum over s is similar to that in equation (7.14), but the $-1 \leq x^{\ell j} \leq 1$ term must be taken into consideration. The sum can be represented as

$$\sum_{s=-\infty}^{\infty}e^{is\gamma\cos\theta}e^{-\beta D|s-x^{\ell j}|}$$

$$= \sum_{s=-\infty}^{-1}e^{is\gamma\cos\theta}e^{-\beta D|s-x^{\ell j}|} + e^{-\beta D|x^{\ell j}|} + \sum_{s=1}^{\infty}e^{is\gamma\cos\theta}e^{-\beta D|s-x^{\ell j}|} \tag{7.48}$$

$$= \sum_{s=1}^{\infty}e^{-(i\gamma\cos\theta+\beta D)s}e^{-\beta Dx^{\ell j}} + e^{-\beta D|x^{\ell j}|} + \sum_{s=1}^{\infty}e^{(i\gamma\cos\theta-\beta D)s}e^{\beta Dx^{\ell j}} \tag{7.49}$$

$$= \frac{e^{-i\gamma\cos\theta-\beta D}}{1-e^{-i\gamma\cos\theta-\beta D}}e^{-\beta Dx^{\ell j}} + e^{-\beta D|x^{\ell j}|} + \frac{e^{i\gamma\cos\theta-\beta D}}{1-e^{i\gamma\cos\theta-\beta D}}e^{\beta Dx^{\ell j}}. \tag{7.50}$$

For $x^{\ell j} > 0$ this can be simplified to

$$\sum_{s=-\infty}^{\infty}e^{is\gamma\cos\theta}e^{-\beta D|s-x^{\ell j}|} = \frac{1}{1-e^{-i\gamma\cos\theta-\beta D}}e^{-\beta Dx^{\ell j}} + \frac{e^{i\gamma\cos\theta-\beta D}}{1-e^{i\gamma\cos\theta-\beta D}}e^{\beta Dx^{\ell j}} \tag{7.51}$$

$$= \frac{1}{1-e^{-i\gamma\cos\theta-\beta D}}e^{-\beta Dx^{\ell j}} - \frac{1}{1-e^{-i\gamma\cos\theta+\beta D}}e^{\beta Dx^{\ell j}}. \tag{7.52}$$

Similarly, for $x^{\ell j} < 0$ the summation is simplified to

$$\sum_{s=-\infty}^{\infty}e^{is\gamma\cos\theta}e^{-\beta D|s-x^{\ell j}|} = \frac{e^{-i\gamma\cos\theta-\beta D}}{1-e^{-i\gamma\cos\theta-\beta D}}e^{-\beta Dx^{\ell j}} + \frac{1}{1-e^{i\gamma\cos\theta-\beta D}}e^{\beta Dx^{\ell j}} \tag{7.53}$$

$$= -\frac{1}{1-e^{i\gamma\cos\theta+\beta D}}e^{-\beta Dx^{\ell j}} + \frac{1}{1-e^{i\gamma\cos\theta-\beta D}}e^{\beta Dx^{\ell j}}. \tag{7.54}$$

Thus, for all $x^{\ell j}$ this can be expressed as

$$\sum_{s=-\infty}^{\infty}e^{is\gamma\cos\theta}e^{-\beta D|s-x^{\ell j}|} = \frac{e^{-\beta D|x^{\ell j}|}}{1-e^{-i\mathrm{sgn}(x^{\ell j})\gamma\cos\theta-\beta D}} - \frac{e^{\beta D|x^{\ell j}|}}{1-e^{-i\mathrm{sgn}(x^{\ell j})\gamma\cos\theta+\beta D}} \tag{7.55}$$

$$= \frac{\sinh(\beta D|x^{\ell j}|)e^{i\mathrm{sgn}(x^{\ell j})\gamma\cos\theta} + \sinh(\beta D(1-|x^{\ell j}|))}{\cosh(\beta D)-\cos(\gamma\cos\theta)}, \tag{7.56}$$

where

$$\mathrm{sgn}(x) = \begin{cases} -1 & x \leq 0 \\ 1 & x > 0 \end{cases} \tag{7.57}$$

Substitution of (7.56) into equation (7.47) results in the following modification

$$\mathbf{H}_{\ell j} = -\frac{i}{\pi}\int_{-\infty}^{\infty}\frac{1}{\beta}\sum_{t=-\infty}^{\infty} e^{i\alpha D\lambda(t-y^{\ell j})}e^{i\lambda t\gamma\sin\theta} \times\left(\frac{\sinh(\beta D|x^{\ell j}|)e^{i\mathrm{sgn}(x^{\ell j})\gamma\cos\theta}+\sinh(\beta D(1-|x^{\ell j}|))}{\cosh(\beta D)-\cos(\gamma\cos\theta)}\right)d\alpha. \tag{7.58}$$

Evaluation of the integral in (7.58) can be done in an analogous manner to the previous section, using a 'D-contour'. Comparing equation (7.58) to the analogous integral in the doubly-periodic problem (7.16), it can be seen that the positions of the poles $\alpha_m^{\pm}$ remain the same, and are given by (7.22).

For $t \geq 1$ and thus $t - y^{\ell j} \geq 0$, it is necessary to deform the D-contour up into the positive imaginary half-plane thus picking up the contribution from the positive poles α_m^+. For $t \leq -1$ and thus $t - y^{\ell j} \leq 0$, it is necessary to deform down and pick up contributions from the negative poles α_m^-. When $t = 0$, the direction of the deformation will depend on the sign of $y^{\ell j}$. That is, for $y^{\ell j} > 0$ deform down, and for $y^{\ell j} < 0$ deform up.

Applying the Cauchy residue theorem to (7.58) it can be shown that for $y^{\ell j} > 0$,

$$\mathbf{H}_{\ell j} = 2\sum_{m=-\infty}^{\infty}\left\{\frac{\sinh(\beta_m D|x^{\ell j}|)e^{i\mathrm{sgn}(x^{\ell j})\gamma\cos\theta}+\sinh(\beta_m D(1-|x^{\ell j}|))}{D\sinh(D\beta_m)}\right\} \times\left\{\sum_{t=1}^{\infty}\frac{1}{\alpha_m^+}e^{i\alpha_m^+ D\lambda(t-y^{\ell j})}e^{i\lambda t\gamma\sin\theta}-\sum_{t=-\infty}^{0}\frac{1}{\alpha_m^-}e^{i\alpha_m^- D\lambda(t-y^{\ell j})}e^{i\lambda t\gamma\sin\theta}\right\}. \tag{7.59}$$

The expression in the first braces can be simplified further using the definition of β_m in (7.21) as follows

$$\begin{aligned}
&\frac{\sinh(\beta_m D|x^{\ell j}|)e^{i\mathrm{sgn}(x^{\ell j})\gamma\cos\theta}+\sinh(\beta_m D(1-|x^{\ell j}|))}{D\sinh(D\beta_m)}\\
=&\frac{1}{D\sinh(D\beta_m)}\left\{\sinh(\beta_m D|x^{\ell j}|)\left(\cos(\gamma\cos\theta)+i\mathrm{sgn}(x^{\ell j})\sin(\gamma\cos\theta)\right)\right.\\
&\left.+\sinh(\beta_m D)\cosh(\beta_m D x^{\ell j})-\cosh(\beta_m D)\sinh(\beta_m D|x^{\ell j}|)\right\} &(7.60)\\
=&\frac{i\sinh(\beta_m D x^{\ell j})\sin(\gamma\cos\theta)+\sinh(\beta_m D)\cosh(\beta_m D x^{\ell j})}{D\sinh(\beta_m D)} &(7.61)\\
=&\frac{1}{D}\left(\frac{-i\sin(|\gamma\cos\theta+2m\pi|x^{\ell j})\sin(\gamma\cos\theta)}{-i\sin(|\gamma\cos\theta+2m\pi|)}i+\cos(|\gamma\cos\theta+2m\pi|x^{\ell j})\right) &(7.62)\\
=&\frac{e^{ix^{\ell j}|\gamma\cos\theta+2m\pi|}}{D}. &(7.63)
\end{aligned}$$

The summations over t in the final braces on the second line of equation (7.59) can be simplified as follows

$$\sum_{t=1}^{\infty} \frac{1}{\alpha_m^+} e^{i\alpha_m^+ D\lambda(t-y^{\ell j})} e^{i\lambda t\gamma \sin\theta} - \sum_{t=-\infty}^{0} \frac{1}{\alpha_m^-} e^{i\alpha_m^- D\lambda(t-y^{\ell j})} e^{i\lambda t\gamma \sin\theta} \tag{7.64}$$

$$= \frac{1}{\alpha_m^+} \left\{ \sum_{t=1}^{\infty} e^{i\alpha_m^+ D\lambda(t-y^{\ell j})} e^{i\lambda t\gamma \sin\theta} + \sum_{t=-\infty}^{0} e^{-i\alpha_m^+ D\lambda(t-y^{\ell j})} e^{i\lambda t\gamma \sin\theta} \right\} \tag{7.65}$$

$$= \frac{1}{\alpha_m^+} \left\{ \sum_{t=1}^{\infty} e^{-i\alpha_m^+ D\lambda y^{\ell j}} e^{i\lambda(\gamma \sin\theta + D\alpha_m^+)t} + \sum_{t=0}^{\infty} e^{i\alpha_m^+ D\lambda y^{\ell j}} e^{-i\lambda(\gamma \sin\theta - D\alpha_m^+)t} \right\} \tag{7.66}$$

$$= \frac{1}{\alpha_m^+} \left\{ e^{-i\alpha_m^+ D\lambda y^{\ell j}} \frac{e^{i\lambda(\gamma \sin\theta + D\alpha_m^+)}}{1 - e^{i\lambda(\gamma \sin\theta + D\alpha_m^+)}} + e^{i\alpha_m^+ D\lambda y^{\ell j}} \frac{1}{1 - e^{-i\lambda(\gamma \sin\theta - D\alpha_m^+)}} \right\} \tag{7.67}$$

$$= -\frac{i}{\alpha_m^+} \left\{ \frac{e^{i\lambda\gamma \sin\theta} \sin(D\lambda\alpha_m^+ y^{\ell j}) + \sin(D\lambda\alpha_m^+(1 - y^{\ell j}))}{\cos(D\lambda\alpha_m^+) - \cos(\lambda\gamma \sin\theta)} \right\}. \tag{7.68}$$

Substitution into equation (7.59) gives the off-diagonal matrix entries of the form, for $y^{\ell j} > 0$,

$$\mathbf{H}_{\ell j} = -2i \sum_{m=-\infty}^{\infty} \frac{e^{ix^{\ell j}|\gamma \cos\theta + 2m\pi|}}{D\alpha_m^+} \left(\frac{e^{i\lambda\gamma \sin\theta} \sin(D\lambda\alpha_m^+ y^{\ell j}) + \sin(D\lambda\alpha_m^+(1 - y^{\ell j}))}{\cos(D\lambda\alpha_m^+) - \cos(\lambda\gamma \sin\theta)} \right). \tag{7.69}$$

Analogously, it can be shown that for the case $y^{\ell j} < 0$,

$$\mathbf{H}_{\ell j} = 2i \sum_{m=-\infty}^{\infty} \frac{e^{ix^{\ell j}|\gamma \cos\theta + 2m\pi|}}{D\alpha_m^+} \left(\frac{e^{-i\lambda\gamma \sin\theta} \sin(D\lambda\alpha_m^+ y^{\ell j}) - \sin(D\lambda\alpha_m^+(1 + y^{\ell j}))}{\cos(D\lambda\alpha_m^+) - \cos(\lambda\gamma \sin\theta)} \right). \tag{7.70}$$

By comparing the equations for $\mathbf{H}_{\ell j}$ for $y^{\ell j} \leqslant 0$, (7.69) and (7.70), it is possible to define the off-diagonal matrix elements for all $y^{\ell j} \neq 0$,

$$\begin{aligned} \mathbf{H}_{\ell j} =& 2i \sum_{m=-\infty}^{\infty} \frac{e^{ix^{\ell j}|\gamma \cos\theta + 2m\pi|}}{D\alpha_m^+} \\ & \times \left(\frac{-\mathrm{sgn}(y^{\ell j}) e^{\mathrm{sgn}(y^{\ell j}) i\lambda\gamma \sin\theta} \sin(D\lambda\alpha_m^+ y^{\ell j}) - \sin(D\lambda\alpha_m^+(1 - |y^{\ell j}|))}{\cos(D\lambda\alpha_m^+) - \cos(\lambda\gamma \sin\theta)} \right) \end{aligned} \tag{7.71}$$

$$= \Sigma_2(\gamma, \theta). \tag{7.72}$$

The convergence of the sum is exponential for increasing $|m|$ and $y^{\ell j} \neq 0$. For cases when $y^{\ell j} = 0$, an alternative approach is best taken.

First, separate the $t = 0$ term in the infinite sum over t in equation (7.58) to give

$$\begin{aligned}
\mathbf{H}_{\ell j} =& -\frac{i}{\pi}\int_{-\infty}^{\infty}\frac{1}{\beta}\left(e^{-i\alpha D\lambda y^{\ell j}}+\sum_{\substack{t=-\infty\\ t\neq 0}}^{\infty}e^{i\alpha D\lambda(t-y^{\ell j})}e^{i\lambda t\gamma\sin\theta}\right)\\
&\times\left(\frac{\sinh(\beta D|x^{\ell j}|)e^{i\mathrm{sgn}(x^{\ell j})\gamma\cos\theta}+\sinh(\beta D(1-|x^{\ell j}|))}{\cosh(\beta D)-\cos(\gamma\cos\theta)}\right)d\alpha \qquad (7.73)\\
=& -\frac{i}{\pi}\int_{-\infty}^{\infty}\frac{e^{-i\alpha D\lambda y^{\ell j}}}{\beta}\left(\frac{\sinh(\beta D|x^{\ell j}|)e^{i\mathrm{sgn}(x^{\ell j})\gamma\cos\theta}+\sinh(\beta D(1-|x^{\ell j}|))}{\cosh(\beta D)-\cos(\gamma\cos\theta)}\right)d\alpha\\
&-\frac{i}{\pi}\int_{-\infty}^{\infty}\frac{1}{\beta}\sum_{\substack{t=-\infty\\ t\neq 0}}^{\infty}e^{i\alpha D\lambda(t-y^{\ell j})}e^{i\lambda t\gamma\sin\theta}\\
&\times\left(\frac{\sinh(\beta D|x^{\ell j}|)e^{i\mathrm{sgn}(x^{\ell j})\gamma\cos\theta}+\sinh(\beta D(1-|x^{\ell j}|))}{\cosh(\beta D)-\cos(\gamma\cos\theta)}\right)d\alpha \qquad (7.74)\\
=& I_3(\gamma,\theta)+\Sigma_3(\gamma,\theta). \qquad (7.75)
\end{aligned}$$

The first integral in (7.75), $I_3(\gamma,\theta)$, can be evaluated numerically avoiding the poles as shown previously, using a contour path similar to that depicted in 7.2. The second term $\Sigma_3(\gamma,\theta)$ can be evaluated using a "D-contour" as already discussed. Applying the Cauchy residue theorem to $\Sigma_3(\gamma,\theta)$ in (7.75) it can be shown that

$$\begin{aligned}
\Sigma_3(\gamma,\theta) =& -\frac{i}{\pi}\int_{-\infty}^{\infty}\frac{1}{\beta}\sum_{\substack{t=-\infty\\ t\neq 0}}^{\infty}e^{i\alpha D\lambda(t-y^{\ell j})}e^{i\lambda t\gamma\sin\theta}\\
&\times\left(\frac{\sinh(\beta D|x^{\ell j}|)e^{i\mathrm{sgn}(x^{\ell j})\gamma\cos\theta}+\sinh(\beta D(1-|x^{\ell j}|))}{\cosh(\beta D)-\cos(\gamma\cos\theta)}\right)d\alpha \qquad (7.76)\\
=& 2\sum_{m=-\infty}^{\infty}\left\{\frac{\sinh(\beta_m D|x^{\ell j}|)e^{i\mathrm{sgn}(x^{\ell j})\gamma\cos\theta}+\sinh(\beta_m D(1-|x^{\ell j}|))}{D\sinh(D\beta_m)}\right\}\\
&\times\left\{\sum_{t=1}^{\infty}\frac{1}{\alpha_m^{+}}e^{i\alpha_m^{+}D\lambda(t-y^{\ell j})}e^{i\lambda t\gamma\sin\theta}-\sum_{t=-\infty}^{-1}\frac{1}{\alpha_m^{-}}e^{i\alpha_m^{-}D\lambda(t-y^{\ell j})}e^{i\lambda t\gamma\sin\theta}\right\} \qquad (7.77)\\
=& 2\sum_{m=-\infty}^{\infty}\frac{e^{ix^{\ell j}|\gamma\cos\theta+2m\pi|}}{D}\\
&\times\left\{\sum_{t=1}^{\infty}\frac{1}{\alpha_m^{+}}e^{i\alpha_m^{+}D\lambda(t-y^{\ell j})}e^{i\lambda t\gamma\sin\theta}-\sum_{t=-\infty}^{-1}\frac{1}{\alpha_m^{-}}e^{i\alpha_m^{-}D\lambda(t-y^{\ell j})}e^{i\lambda t\gamma\sin\theta}\right\}. \qquad (7.78)
\end{aligned}$$

The summations over t in equation (7.78) can be simplified as follows

$$\sum_{t=1}^{\infty} \frac{1}{\alpha_m^+} e^{i\alpha_m^+ D\lambda(t-y^{\ell j})} e^{i\lambda t\gamma \sin\theta} - \sum_{t=-\infty}^{-1} \frac{1}{\alpha_m^-} e^{i\alpha_m^- D\lambda(t-y^{\ell j})} e^{i\lambda t\gamma \sin\theta} \tag{7.79}$$

$$= \frac{1}{\alpha_m^+} \left\{ \sum_{t=1}^{\infty} e^{i\alpha_m^+ D\lambda(t-y^{\ell j})} e^{i\lambda t\gamma \sin\theta} + \sum_{t=-\infty}^{-1} e^{-i\alpha_m^+ D\lambda(t-y^{\ell j})} e^{i\lambda t\gamma \sin\theta} \right\} \tag{7.80}$$

$$= \frac{1}{\alpha_m^+} \left\{ \sum_{t=1}^{\infty} e^{-i\alpha_m^+ D\lambda y^{\ell j}} e^{i\lambda(\gamma \sin\theta + D\alpha_m^+)t} + \sum_{t=1}^{\infty} e^{i\alpha_m^+ D\lambda y^{\ell j}} e^{-i\lambda(\gamma \sin\theta - D\alpha_m^+)t} \right\} \tag{7.81}$$

$$= \frac{1}{\alpha_m^+} \left\{ e^{-i\alpha_m^+ D\lambda y^{\ell j}} \frac{e^{i\lambda(\gamma \sin\theta + D\alpha_m^+)}}{1 - e^{i\lambda(\gamma \sin\theta + D\alpha_m^+)}} + e^{i\alpha_m^+ D\lambda y^{\ell j}} \frac{e^{-i\lambda(\gamma \sin\theta - D\alpha_m^+)}}{1 - e^{-i\lambda(\gamma \sin\theta - D\alpha_m^+)}} \right\} \tag{7.82}$$

$$= \frac{1}{\alpha_m^+} \left\{ \frac{\cos(\lambda\gamma \sin\theta - D\lambda\alpha_m^+ y^{\ell j}) - e^{iD\lambda\alpha_m^+} \cos(D\lambda\alpha_m^+ y^{\ell j})}{\cos(D\lambda\alpha_m^+) - \cos(\lambda\gamma \sin\theta)} \right\}. \tag{7.83}$$

Substitution into equation (7.78) gives an expression of the form,

$$\Sigma_3(\gamma, \theta) = 2 \sum_{m=-\infty}^{\infty} \frac{e^{ix^{\ell j}|\gamma \cos\theta + 2m\pi|}}{D\alpha_m^+} \left\{ \frac{\cos(\lambda\gamma \sin\theta - D\lambda\alpha_m^+ y^{\ell j}) - e^{iD\lambda\alpha_m^+} \cos(D\lambda\alpha_m^+ y^{\ell j})}{\cos(D\lambda\alpha_m^+) - \cos(\lambda\gamma \sin\theta)} \right\}. \tag{7.84}$$

The expression in (7.84) has been derived to enable evaluation of the off-diagonals for $y^{\ell j} = 0$. In fact this expression can be used for all $y^{\ell j}$, but is not applicable to the case $x^{\ell j} = 0$. Therefore, it is suggested that expression (7.72) should be applied for $y^{\ell j} \neq 0$ and all $x^{\ell j}$, and expression (7.75) should be applied for $y^{\ell j} = 0$ and $x^{\ell j} \neq 0$. In an instance $y^{\ell j} = x^{\ell j} = 0$ then $\ell = j$ and it is not necessary to calculate an off diagonal entry. Therefore, express (7.84) for $y^{\ell j} = 0$

$$\Sigma_3(\gamma, \theta) = 2 \sum_{m=-\infty}^{\infty} \frac{e^{ix^{\ell j}|\gamma \cos\theta + 2m\pi|}}{D\alpha_m^+} \left\{ \frac{\cos(\lambda\gamma \sin\theta) - e^{iD\lambda\alpha_m^+}}{\cos(D\lambda\alpha_m^+) - \cos(\lambda\gamma \sin\theta)} \right\}. \tag{7.85}$$

The convergence of the sum is exponential for increasing $|m|$, therefore it is possible to truncate at modest order in order to obtain an accurate evaluation. The combination of the truncated sum (7.85) and the numerically integrated $I_3(\gamma, \theta)$ provides the required off-diagonal matrix elements of $\mathbf{H}$ for instances when $y^{\ell j} = 0$.

The matrix equation (7.41) can be solved with the expressions derived for the matrix entries, (7.44) and (7.72) or (7.75). Effective wavenumbers $\boldsymbol{\gamma}$ can be determined for prescribed parameters by satisfying

$$\det\left(\mathbf{H}(\gamma, \theta)\right) = 0. \tag{7.86}$$

7.3 Conclusions

In this chapter novel analytic expressions to determine the effective properties of wave propagation through infinite doubly-periodic structures have been derived.

In section 7.1, a doubly-periodic lattice is considered, where there is one repeated lattice node. The expression for the effective wavenumber (7.31) involves easily computable integrals and a summation. In section 7.2, an infinite orthorhombic periodic structure is considered, where the periodic cell contains N arbitrarily positioned lattice nodes. The expression for the effective wavenumber (7.86) involves calculating the determinant of a matrix whose entries involve computable integrals and summations.

We demonstrate the methods applied in this chapter by calculating the full band structure for a square doubly-periodic lattice. The second method can be applied to this structure by positing four nodes in each period cell, i.e. nodes at $(0,0)$, $(0,1)$, $(1,0)$ and $(1,1)$, with a period $d = 2$ and $\lambda = 1$. Figure 7.5 depicts the band diagram for the irreducible Brillouin zone as depicted in figure 7.4 with node positions

$$0 = (0,0), \quad A = (\pi, 0), \quad B = (\pi, \pi). \tag{7.87}$$

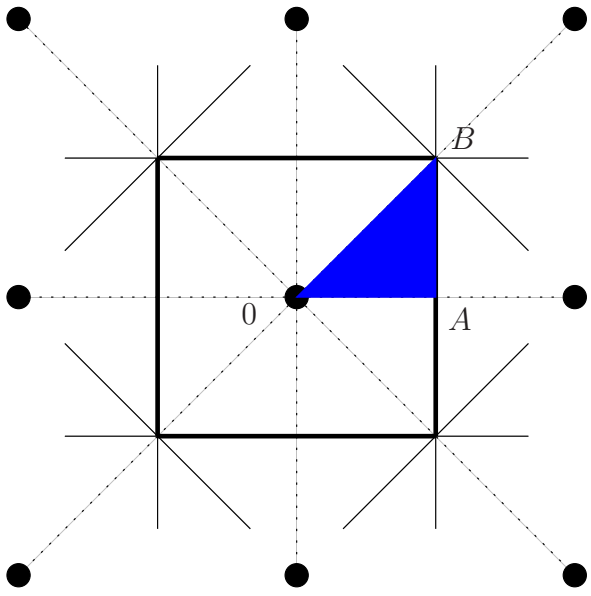

Figure 7.4: The irreducible Brillouin zone for a 2D square periodic lattice (blue shaded).

The calculations for figure 7.5 have been conducted with a small radius of $a = 0.05$, and period $d = 1$. It can be seen that there exists a complete band gap initially, which

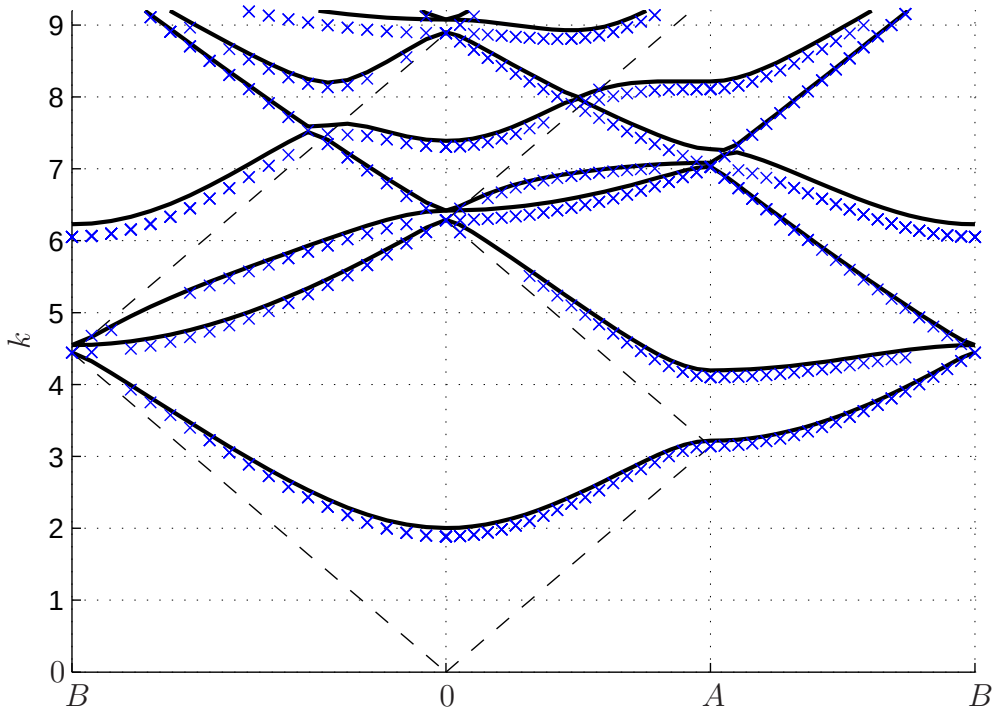

Figure 7.5: The full band diagram for a 2D square periodic lattice with $d = 1$ and $a = 0.05$. Solutions achieved using the method of this chapter (blue crosses) and the PWE (black solid line). The black dashed line shows the solution for a scatter-free medium.

is of reasonable size. This characteristic for doubly-periodic arrays of small, sound-soft, circular cylinders has been observed previously [45], and in a slightly different application of pinned thin elastic plates [54], and our results agree well. We have also validated the method outlined in this chapter by comparing to the results achieved using the numerical approximation of the problem via the plane wave expansion (PWE) method, shown by the solid lines in figure 7.5, [9]. Barnwell took particular limits of material parameters in his model that attempt to numerically model the small sound-soft scatterer regime. The accuracy of Barnwell's method can be improved by taking greater limits and including more plane waves in the computation. However, this becomes computationally very expensive. For the purpose of this thesis and validation of our results, we take the solutions achieved with the PWE and $101^2 = 10201$ plane waves to demonstrate the effectiveness of our method. Figure 7.5 also depicts the bands for a scatter-free region (dashed lines).

The approach employed restricts the set up to small $ka \ll 1$, but employs no other

assumptions. The theory for the approximant structure is actually applicable to any orthorhombic periodic structure with an arbitrary distribution of scatterers in the periodic cell. In this thesis, the dispersion relations are applied to approximant structures for the 2D square Fibonacci and Penrose lattices, in chapters 8 and 9 respectively.

Chapter 8

Two-dimensional wave scattering by a square Fibonacci structure

8.1 Problem statement

The analysis of 2D multiple scattering for small circular scatterers using the multipole method was discussed in section 2.4. Using this method each sound-soft scatterer, which was assumed to have small radius a such that $0 < ka \ll 1$, was shown to act as a monopole source. It is possible to calculate the total scattered field as a sum of these sources with unknown amplitudes dependent on the interactions of all the scatterers in the system. The amplitudes can be determined by applying the sound-soft boundary conditions to each scatterer in turn, resulting in a matrix equation of the form (2.136). The matrix contains information of the location of each scatterer in terms of every other scatterer.

The square Fibonacci (SF) lattice was introduced in chapter 6 as an extension of the 1D Fibonacci chain to two perpendicular directions. Two periodic lattices which will be used to compare to the SF lattice were also introduced; the periodic average structure (PAS) and the approximant. These were also simply constructed using the 1D PAS and approximant in two perpendicular directions.

Now that the scatterer positions for the three different lattices are known, they can be used along with the equations derived via the multipole method to compare the scattering properties of each. It was observed in 1D how the periodic lattices compared to the Fibonacci chain, now we wish to see if the same conclusions are drawn when

extending into 2D.

In 1D the acoustic wave scattering due to the inclusions was restricted to two directions. This made comparisons of the results relatively simple, as just the transmission could be analysed. In 2D the scattering is omnidirectional in the entire 2D plane. Therefore, a simple value such as a transmission coefficient can not be defined.

In order to compare the scattered fields between the three lattices in 2D we will analyse the scattered fields for varying positions in the 2D plane. Consider a polar coordinate system (r, θ), then it is possible to compare the fields for varying r and/or θ.

Figure 8.1a depicts the set up of an array of scatterers centred at the origin with the polar coordinates defined, where $r = |\mathbf{r}|$. Figures 8.1b and 8.1c depict two different observation (red) lines for analysis of the scattered field. The former is for a fixed angle and varying distance r. The latter is for a fixed distance r from the lattice and varying angle θ.

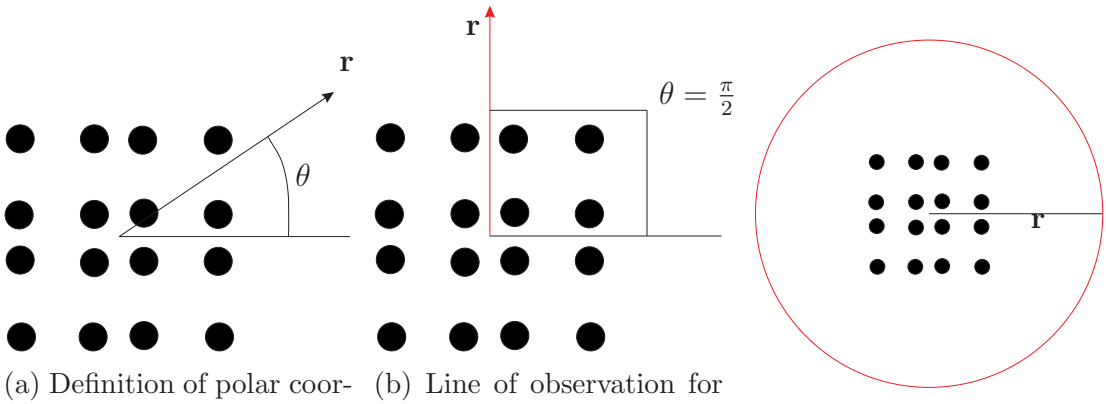

(a) Definition of polar coordinates with respect to the inclusions.

(b) Line of observation for specified $\theta = \frac{\pi}{2}$ and varying r.

(c) Line of observation for specified r and varying θ.

Figure 8.1: Array of inclusions centred at the origin with polar coordinates defined. Red lines depicts the observation lines for analysis of the scattered field.

Considering both the observation lines (red) in figure 8.1 for different distributions of scatterers and different frequencies of waves should allow a fair comparison to be drawn.

It is desired to see the effects of acoustic wave scattering of wavelengths that are small enough to "see" the scatterers and their distribution. Therefore the results computed are for a wavelength λ such that it is of similar scale to s and ℓ, where s and ℓ are the dimensional short and long spacings in the Fibonacci chain. Setting

$s = 1$ and $k = \frac{2\pi}{\lambda} = 5$ satisfies these restraints. The radii of the cylinders is set to $a = 0.001$, satisfying the small scatterer assumption $0 < ka \ll 1$. We arbitrarily choose an incident plane wave of unit amplitude propagating at an angle $\alpha = \pi/2$ from the horizontal.

8.2 Comparison of wave scattering by a square Fibonacci structure and its periodic approximations

In this section the acoustic scattering properties of the quasiperiodic SF chain are compared to those of its PAS and approximant. We want to find an appropriate periodic structure to mimic the propagation properties of the SF chain. By doing this, we will enable modelling of a complicated quasiperiodic structure by a periodic structure. We can then use the method applicable to infinite 2D periodic structures to find effective material properties that can represent an infinite 2D SF distribution of scatterers.

Figure 8.2 shows the lattice positions for 21×21 arrays of point masses with the three different distributions. Note here that this is for 21 point masses and not Fib(21). The approximant has been constructed with the $n = 1$-approximation, $\tau \approx \tau_1 = \frac{\text{Fib}(2)}{\text{Fib}(1)} = 1$. It can be seen that the approximant looks to give an inaccurate representation of the SF lattice, and does not occupy as much space as the SF and PAS lattices.

A comparison of the scattered field from the three different arrays can be seen in figures 8.3, 8.4 and 8.5. Figure 8.3 is a plot of the absolute value of the scattered field for at an observation point with $\theta = \pi/2$ and r increasing. It can be seen that outside the array ($r > W/2$ where W is the width of the approximant array) the scattered fields becomes less oscillatory. From this we can justify the analysis of the scattered fields to be taken at some r in the far field, and consider the effect of the angle of observation. We choose $r = 2W$ as an appropriate distance.

In figure 8.4 we have taken $r = 2W$ and considered the value of the scattered field for all θ. It can be seen that the scattering is predominantly in the same direction as the

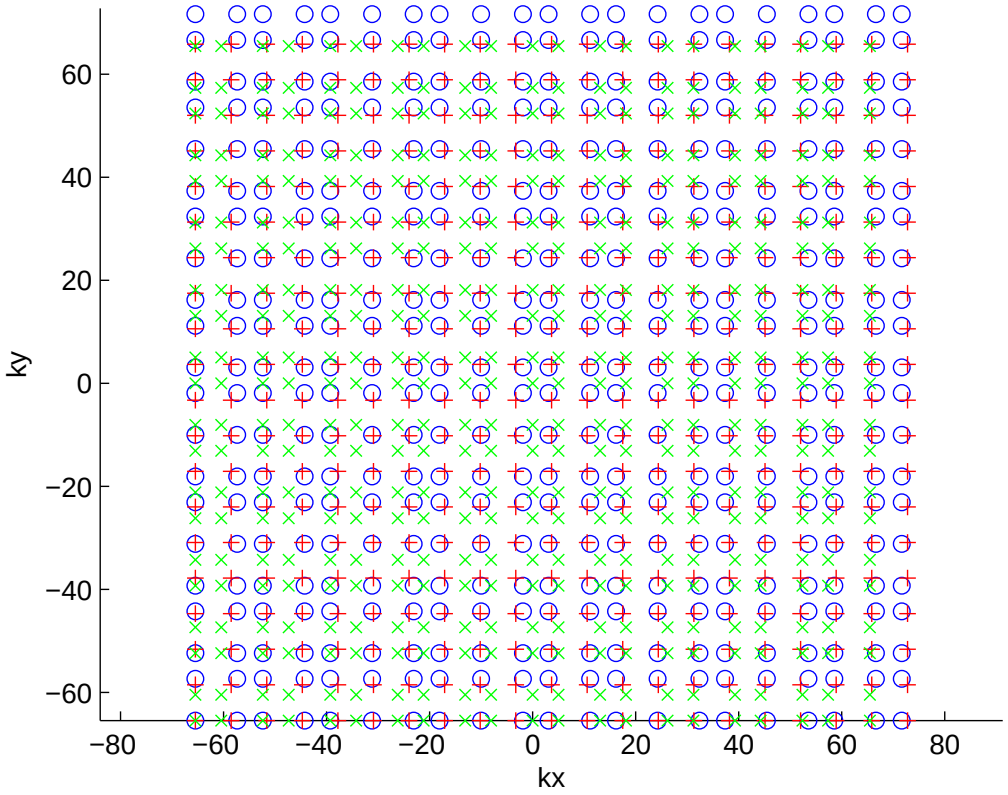

Figure 8.2: Lattice nodes for the SF (blue circle), PAS (red plus) and 1-approximant (green cross) lattices.

angle of incidence $\alpha = \pi/2$. In this figure the amplitude of the scattered field is plotted for all three lattices. Whilst this plot is interesting as it shows the scattering pattern from the arrays, it is difficult to compare the three scattered patterns. Therefore, in figure 8.5 a plot of the absolute error is given. Where we define the error as the difference between the amplitude of the scattered field from the SF lattice and the amplitudes from the two approximations. It can be seen in this figure that neither approximation provide a good representation of the scattering due to the SF lattice. The 1-approximant has slightly less error around the dominant angle $\pi/2$, but is still quite significant.

As in the 1D comparisons in section 4, we can improve the accuracy of the approximation of τ used in the approximant to attempt to improve the accuracy of the scattered field.

Consider the 3-approximant, i.e. $\tau \approx \tau_3 = \frac{\text{Fib}(4)}{\text{Fib}(3)} = \frac{3}{2}$. In 1D this proved to be a better approximation, see section 4.4. The lattice positions for the three lattices can

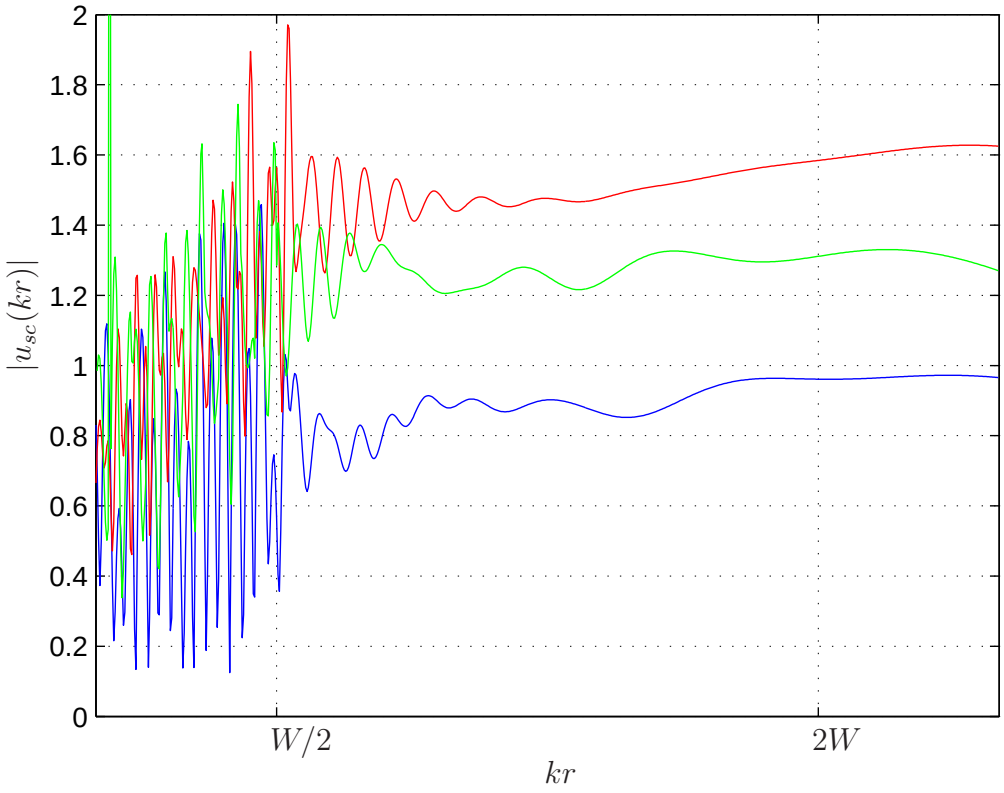

Figure 8.3: Scattered amplitude for $\theta = \frac{\pi}{2}$ and varying r for the SF (blue), PAS (red) and 1-approximant (green) 21×21 lattices.

be seen in figure 8.6. The improvement between the $n = 1$ and $n = 3$ approximant lattices compared to the SF can easily be seen.

Figure 8.7 shows the error is the approximation of the SF scattered amplitude at $r = 2W$ for the two different approximate lattices. The error in the PAS approximation is the same as the previous example as both the SF and PAS lattice are the same. The 3-approximant is showing to provide a much better representation, with very low error.

We can continue to increase the accuracy of the approximant to determine whether the approximant continues to provide a good representation of the SF. We can also consider arrays of varying sizes. For $n = 4$, i.e. $\tau \approx \tau_4 = \frac{\text{Fib}(5)}{\text{Fib}(4)} = \frac{5}{3}$, the scattered fields are calculated for arrays of 21×21, 34×34 and 55×55 scatterers. Figures 8.8 and 8.9 display the results for the 34×34 and 55×55 arrays. The lattice nodes positions for the 21×21 arrays of SF chain and 4-approximant are identical, and thus the scattered fields are too. For arrays with 34×34 scatterers, figure 8.8 demonstrates a similar

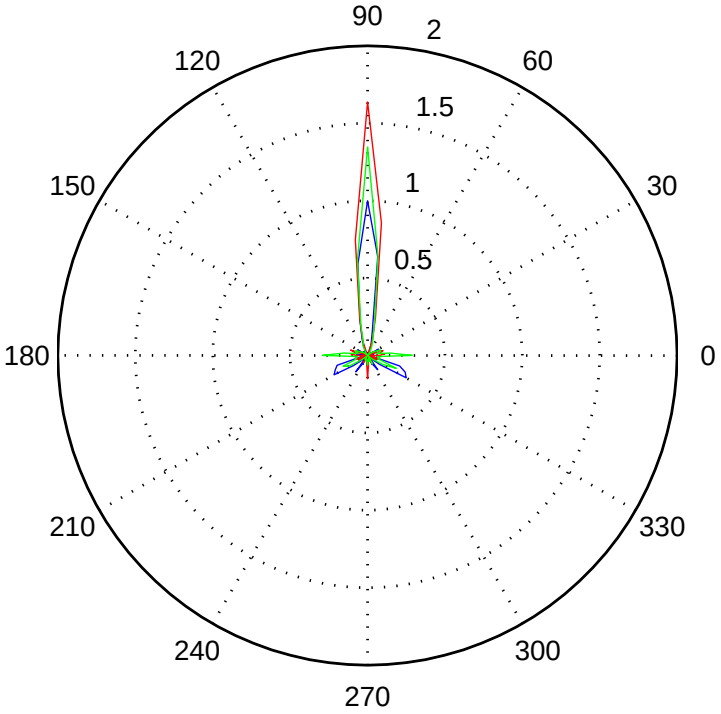

Figure 8.4: Scattered amplitude for $r = 2W$ and varying θ for the SF (blue), PAS (red) and 1-approximant (green) 21×21 lattices.

result to the previous example: the 4-approximant has a significantly lower error than the PAS at the majority of angles of observation.

For an array size of 55×55 scatterers the scattering from the lattices changes from that of a 34×34 array, see figure 8.9. In fact, in this sized array, the PAS demonstrates smaller errors in the comparison of scattered amplitude from the PAS. However, the 5-approximant still demonstrates a consistent ability at providing a good representation of the SF lattice. Note the smaller scale in this figure, as the errors have decreased.

It is of interest to continue to increase the accuracy of the approximant to see if the results continue to improve. However for larger n in the approximation of τ, the larger the approximant unit cell becomes. Therefore to ensure we are comparing different arrays of the SF and the approximant, the sample size must also continue to increase. This becomes computationally expensive. For example a 55×55 array of scatterers consists of 3025 scatterers. The multipole method accounts for the interaction between each and every scatterer and requires a numerical computation of the inverse of a

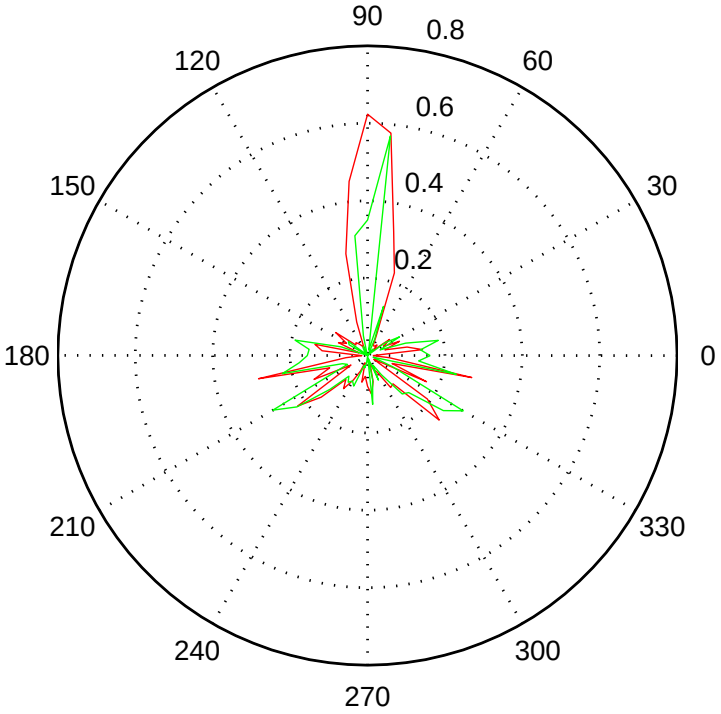

Figure 8.5: Absolute error in the scattered amplitude for the PAS (red) and 1-approximant (green) 21×21 lattices compared to the SF lattice, for $r = 2W$ and varying θ.

3025×3025 matrix, (2.136). This can take a long time.

One idea for future research would be to consider the strength of the interactions between scatterers. For scatterers at opposite sides of the array the interactions may be weak. Weak interactions could be considered to be negligible and thus it could be possible to make the matrix less dense. Another approach could be to use the sparse-matrix canonical grid method [46] as discussed in section 2.2.3.

For now we will continue to increase the approximant accuracy and consider varying sections of the SF lattice within one approximant unit lattice space, as we did in 1D in section 4.4.

Figure 8.10 shows the three arrays discretised into unit cells of the 5-approximant. The approximant lattice nodes are identical in each unit cell. The SF and PAS lattices will vary in different cells. Therefore we wish to analyse the average scattering properties of individual cells of the SF and PAS lattice nodes. It can be seen in figure

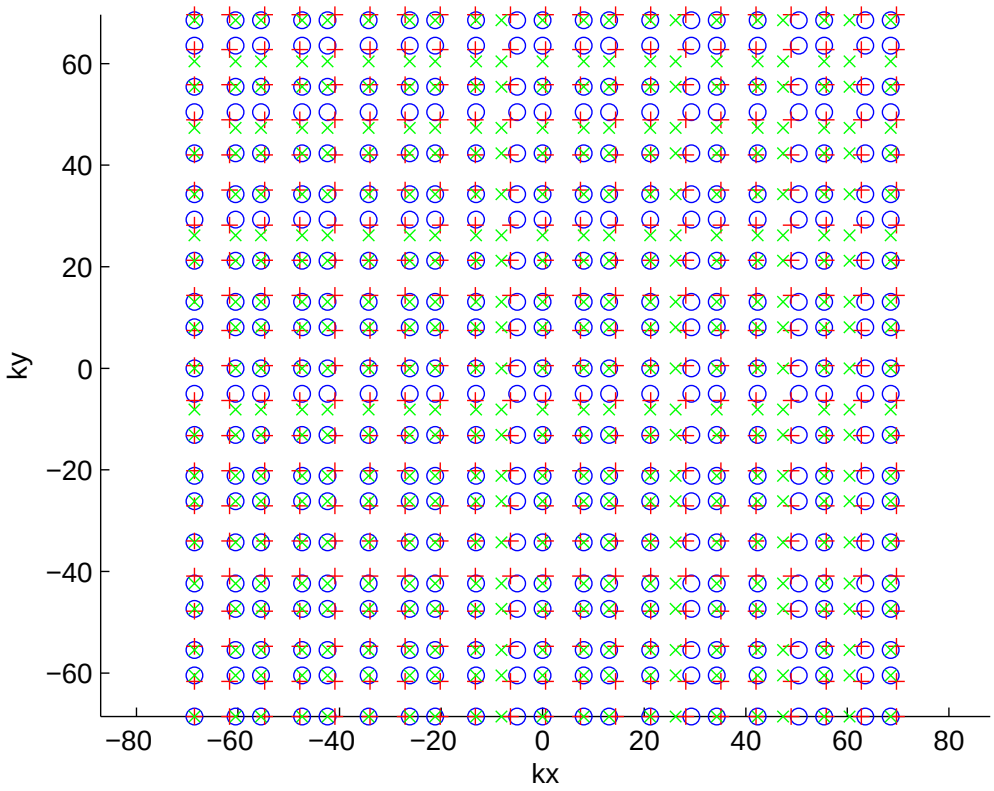

Figure 8.6: Node positions of the SF (blue), PAS (red) and 3-approximant (green) 21×21 lattices.

8.10 that the PAS lattice nodes hardly vary in each unit cell, thus the variation in the scattered fields of each unit cell are expected to be minimal.

We compute the scattered field for each of the unit cells depicted in figure 8.10, centring each at the origin. By taking the average amplitude for the SF and PAS lattices over the nine cells depicted we see how an average scattered field for the SF lattice compares to the average PAS and 5-approximant. Note here each unit cell is a 13×13 array since the period of the n-approximant for the Fibonacci chain has length $\mathrm{Fib}(n+2)$. Figure 8.11 shows how accurate the approximant is in comparison to the average SF chain within an approximant unit cell. The 5-approximant has marginal error at the majority of observation angles, whereas the PAS has three regions in which is provides a bad representation of the SF lattice.

Within each unit cell the lattice positions of the SF vary as it is not periodic. Therefore the scattering properties of each unit cell will vary. For unit cells further from the origin the SF nodes become more dissimilar to the approximant. To ensure

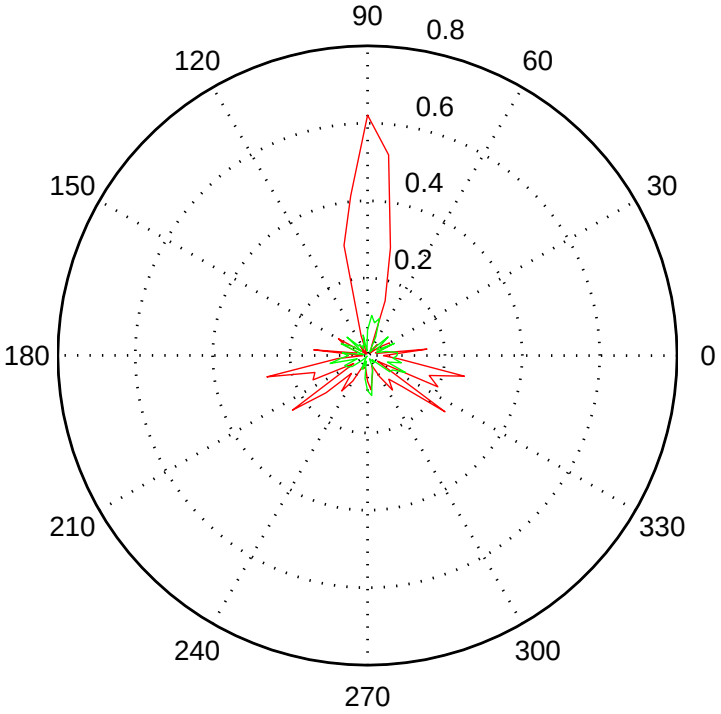

Figure 8.7: Absolute error in the scattered amplitude for the PAS (red) and 3-approximant (green) 21×21 lattices compared to the SF lattice, for $r = 2W$ and varying θ.

that the average scattered field over the nine unit cells in figure 8.10 provides an accurate representation any arbitrary unit cell, checks were completed to ensure that a unit cell taken far from the origin produced similar scattering patterns.

In summary it has been demonstrated that the approximant provides a better representation of the SF lattice than the PAS in terms of acoustic scattering from arrays of sound soft scatterers. There is no restriction on the angle at which the approximant provides a good representation. The similarity of amplitude of scattered field the approximant produces can continue to be improved dependent on the requirements.

As the approximant lattice has shown to provide a good representation of the SF lattice it is now of interest to apply the theory for 2D periodic structures to the infinite 2D approximant.

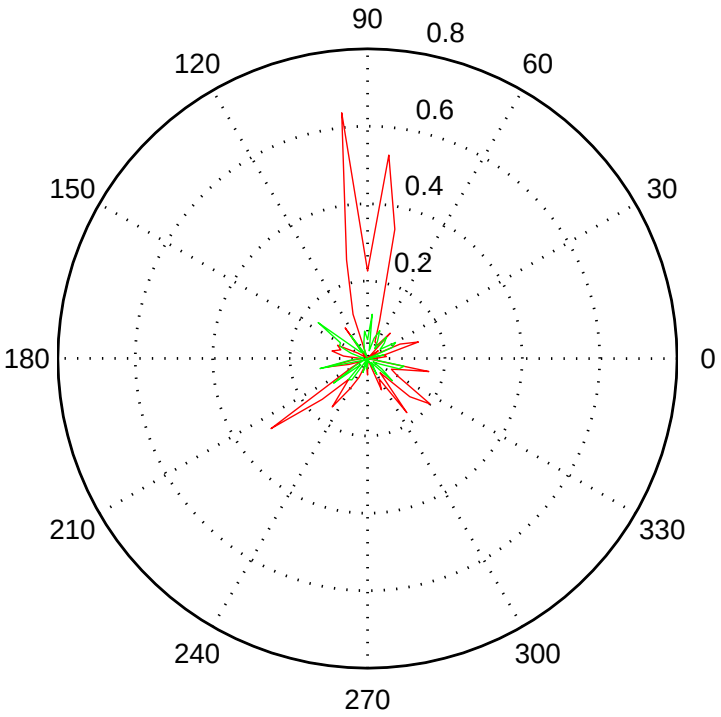

Figure 8.8: Absolute error in the scattered amplitude for the PAS (red) and 4-approximant (green) 34×34 lattices compared to the SF lattice, for $r = 2W$ and varying θ.

8.3 Wave scattering by an infinite approximant structure

In chapter 7 an expression to determine the effective wave propagation through a 2D array of small circular scatterers with distribution determined by the infinite periodic approximant lattice was derived. This enables the construction of a band diagram for the effective wave propagation, which portrays the pass and stop bands of the infinite approximant.

It was shown in the previous section that a finite array of scatterers with a SF approximant distribution provides similar scattering results to a finite array of scatterers with a SF distribution. Therefore by determining the effective properties of the infinite periodic approximant, it is possible to provide an estimate of the effective properties of the infinite aperiodic SF lattice. Because of the aperiodicity inherent in

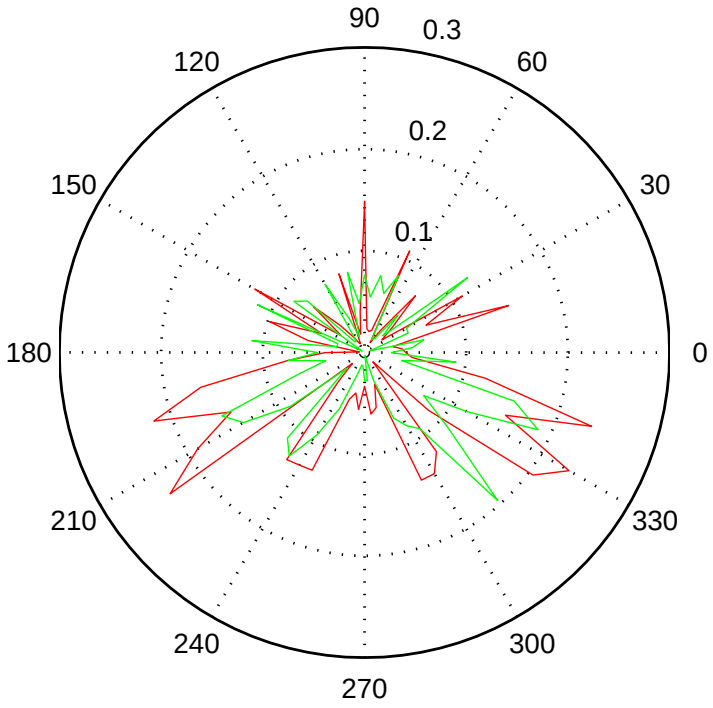

Figure 8.9: Absolute error in the scattered amplitude for the PAS (red) and 4-approximant (green) 55×55 lattices compared to the SF lattice, for $r = 2W$ and varying θ.

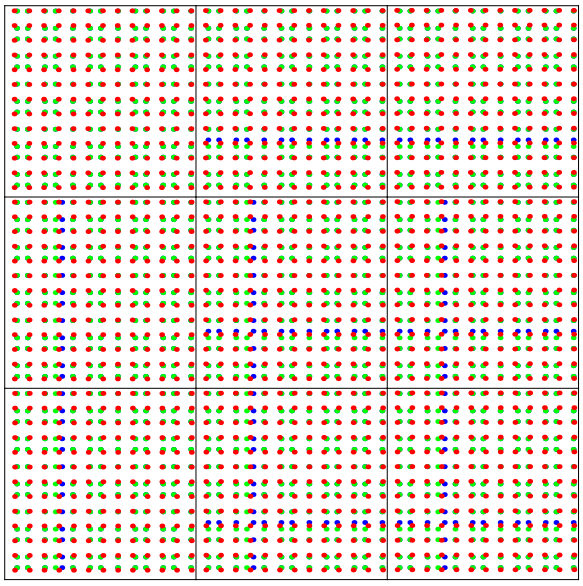

Figure 8.10: Lattice nodes for the SF (blue), PAS (red) and 5-approximant (green) lattices. The array has been discretised into the unit cell of the approximant.

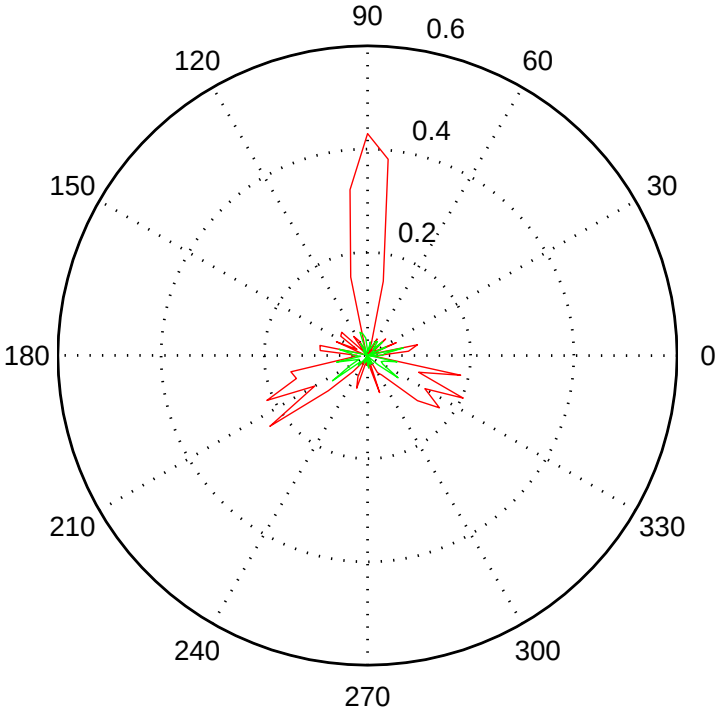

Figure 8.11: Absolute error in the scattered amplitude for the 5-approximant (green) and averaged PAS (red) lattices compared to the averaged SF lattices within an approximant unit cell, for $r = 2W$ and varying θ.

the SF lattice, such properties are currently unobtainable by other means.

When calculating the effective properties of a 2D infinite and periodic lattice it is common practice to only evaluate along the edges of the irreducible Brillouin zone, as discussed in section 2.2.2 and 7.3. For an infinite lattice with square periodic cell, as in the SF lattice, the irreducible Brillouin zone is as discussed in the previous chapter, depicted in figure 7.4. Define the irreducible Brillouin zone to be in the non-dimensional frequency space and so it has components $\gamma \cos\theta = \gamma_x$ and $\gamma \sin\theta = \gamma_y$ in the $\mathbf{e}_1$ and $\mathbf{e}_2$ directions, respectively. The coordinates of the vertices of the irreducible Brillouin zone in figure 7.4 are given by

$$0 = (0,0), \quad A = (\pi, 0), \quad B = (\pi, \pi). \tag{8.1}$$

As an example we show a section of the band diagram for varying n in the n-approximant. We consider the diagonal region along $0B$ in the irreducible Brillouin zone, i.e. $0 \leq \gamma \leq \sqrt{2}\pi$ and $\theta = \pi/4$. We disregard high non-dimensional host

frequencies $D = kd$ so that we can concentrate on the positions of the first bands. A small scatter of radius $a = 0.001$ is chosen. Figure 8.12 depicts the unit cell of the n-approximant for $n = 1, 2$.

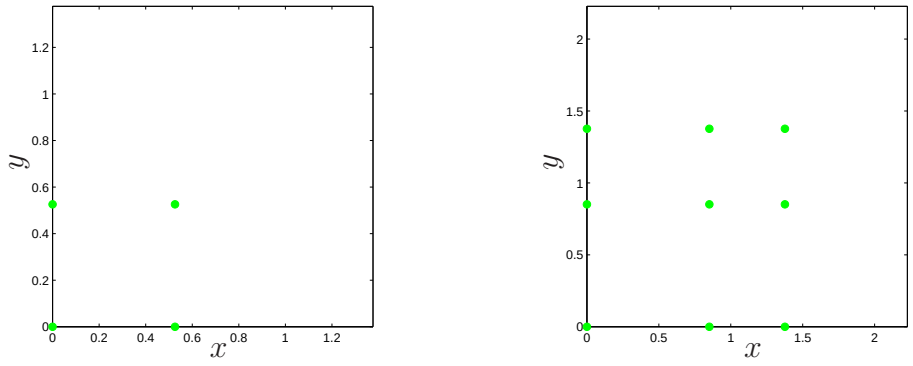

(a) 1-approximant. (b) 2-approximant.

Figure 8.12: Unit cell of the n-approximant.

We can apply these units cell node positions in the analysis conducted in chapter 7, to calculate the dimensional host wavenumber k at which waves can propagate along the diagonal $0B$. Figure 8.13 depicts the discrete nodes for which there exists values of k that allows for propagation of particular dimensional effective wavenumbers $\hat{\gamma}$. In our calculations we input θ and steps of $\gamma = k\hat{\gamma}$ into equation (7.86) to determine the allowed $D = kd$. To refine the image produced one can decrease the step increment size for γ. For the plots shown in 8.13, 20 steps were taken to give a clear image whilst keeping the computation time down. The band-diagram for the 1-approximant in 8.13a for the chosen frequency range shows three propagating modes. As we saw for the doubly-periodic lattice in figure 7.5 in the previous chapter, there is a stop band for the initial wavenumbers until just above $k = 1.5$. The band diagram for the 2-approximant 8.13b is more complex. Six modes of propagation can be seen, which can overlap. However, the cut-on wavenumber for the first pass band in this direction is similar to that of the 1-approximant, at just below $k = 1.5$. The more complicated mode behaviour for increasing n in the approximant is analogous to a trait we saw in the 1D case in figure 4.18.

We determine the cut-on wavenumber of n-approximants for greater n to validate that this is a continuing characteristic. Figure 8.14 illustrates the cut-on frequency k_0

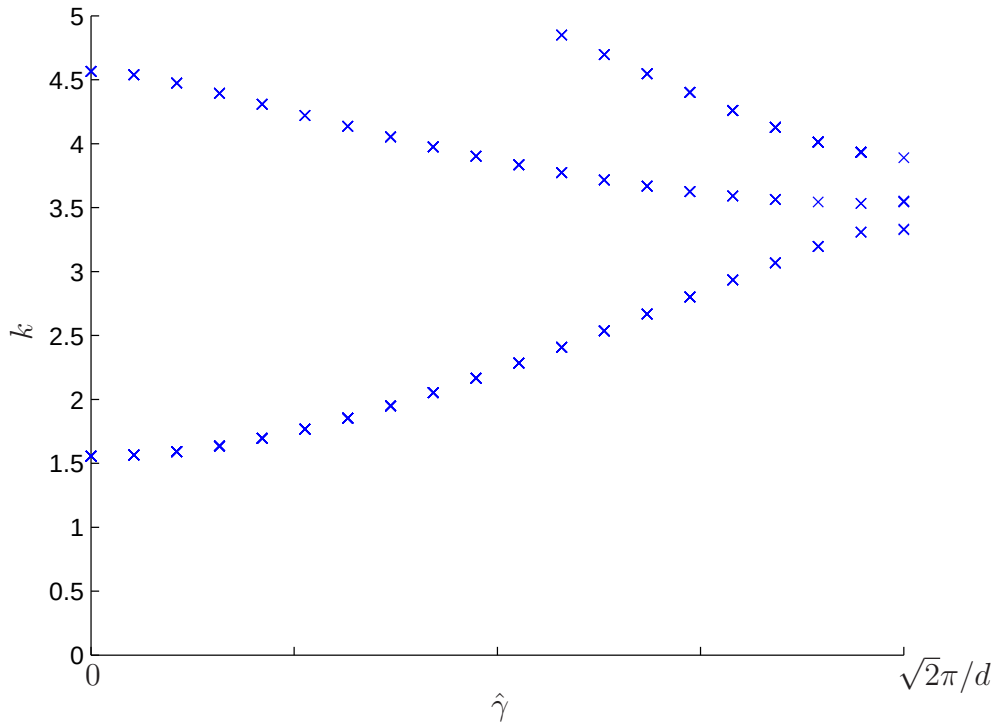

(a) 1-approximant.

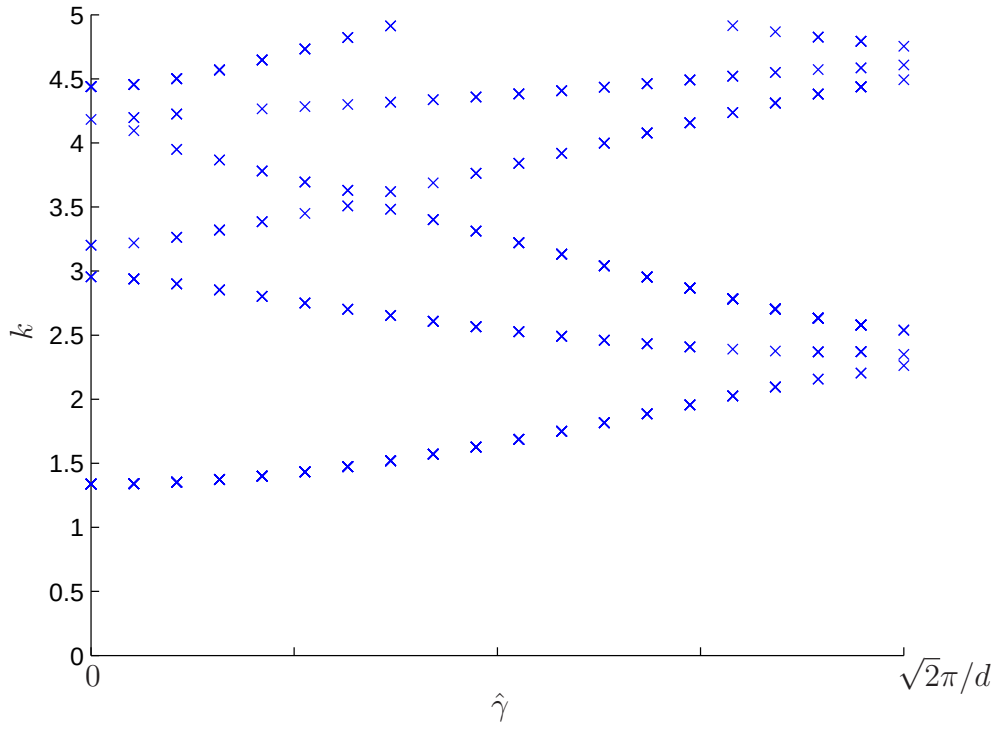

(b) 2-approximant.

Figure 8.13: Partial band diagram along $0B$ of the irreducible Brillouin zone, for the n-approximant.

for different n-approximants for $n = 1, \ldots, 5$. It can be seen that the cut-on wavenumber converges as n increases. In fact, a low value of $n = 4$ seems to find the converged cut-on wavenumber of the approximants. This suggests that a 4-approximant can represent the pass and stop band behaviour of an infinite SF lattice.

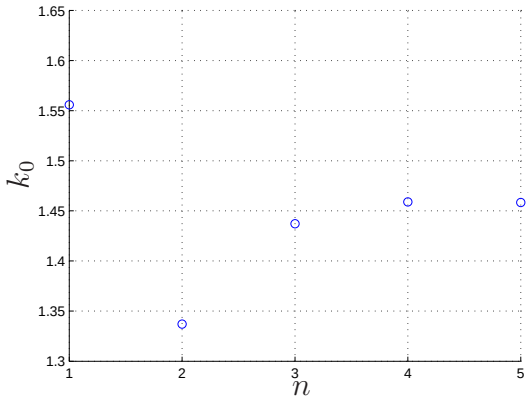

Figure 8.14: Cut-on wavenumber k_0 for increasing n in the n-approximant.

8.4 Conclusions

In this chapter we have applied the multipole method to evaluate the scattered fields from the SF lattice and its PAS and approximant. It was deduced that the PAS could not provide an accurate representation of the SF lattice for all angles of observation. However, the n-approximant proved to be a much better approximation, and for surprisingly low n. It was shown that the scattered field from arrays of the approximant and SF lattices were similar, as well as the scattering from a unit cell of the n-approximant compared to that of various sections of the SF lattice.

In view of the fact that the finite approximant could provide an appropriate approximation of the SF lattice, we considered the scenario of an infinite approximant lattice as an approximation of an infinite SF lattice. It was possible to calculate the effective wave propagation properties of the infinite approximant using the novel analysis set out in chapter 7. By considering an example direction of effective propagation and range of frequency it was demonstrated that the wavenumber associated with the cut on of the first pass band converged for increasing n in the n-approximant. Therefore, combined with the results for the finite approximant, we can postulate that using an infinite approximant as an approximation of an infinite SF lattice is a justified model.

Chapter 9

Two-dimensional wave scattering by a Penrose structure

9.1 Problem statement

This section presents the results for the multiple scattering from arrays of small circular cylinders with distributions determined by the 2D Penrose lattice, its periodic average structure (PAS) and its approximant. Comparisons are drawn between the three scattered fields for different selections of lattice nodes and different approximants.

The construction of the three lattices is discussed in chapter 6. The $(N_1, N_2)^{I/II}$-approximant can be altered by varying the scheme used (I or II) and the approximation of τ in two different dimensions, τ_{N_1} and τ_{N_2}. In this chapter scheme I is considered, since it was shown in (6.79) that the two schemes are related. As mentioned in section 2.2.3, previous studies have used the PAS to compare the wave scattering properties of the periodic lattice to the quasiperiodic lattice. In this section we provide further insight into these differences and also provide comparisons between the periodic approximant. It is shown that the approximant provides the better representation of the Penrose lattice and thus further analysis is completed to calculate effective properties of the infinite periodic approximant lattice.

The results in this section are determined in the same manner as in chapter 8 using the multipole method for a finite array of small circular scatterers. Measurements of the scattered field from the arrays of scatterers is restricted to a line of observation of constant distance $2W$ (W the width of the array in the $\mathbf{e}_1$ direction) away from the

array and varying angle θ as in figure 8.1c. It was shown in chapter 8 that this was an appropriate measurement to take.

It is desirable to see the effects of acoustic wave scattering when the wavelength of the incident wave is small enough to "see" the scatterer distribution. Therefore the results computed are for a wavelength λ such that $\lambda = a_r = \frac{2}{5}$, where a_r is the edge length of the rhombi in the Penrose lattice. Since $\lambda = \frac{2\pi}{k}$, this results in a wavenumber $k = 5\pi$. The radii of the cylinders is set to $a = 0.001$, satisfying the small scatterer assumption $0 < ka \ll 1$. An incident plane wave at angle $\alpha = \pi/2$ is assumed.

9.2 Comparison of wave scattering by a Penrose structure and its periodic approximations

Consider a section of the the 2D plane containing the lattice nodes of the three different lattices. For an initial comparison, consider a circular region A of scatterers where $A = \{(x, y) : x^2 + y^2 \leq R^2\}$ and R is the radius of the circle. In the results for the SF lattice a square section of the 2D plane was always taken. The choice of a square region for that lattice was made because of the square dimensions of the lattice itself. For the Penrose tiling there is no particular preferred shape in which the lattice fills, so we arbitrarily choose a circular region to work with the polar plot of the scattered field presented.

Figure 9.1 depicts the lattice nodes for the Penrose lattice (blue), the PAS (red) and the $(1, 2)^I$-approximant in a circular region with $R = 4$. A polar plot of the scattered field from the arrays shown in figure 9.1 is given in figure 9.2. It can be seen that the scattering from the Penrose lattice is most dominant at angles around $\theta = \pi/2$ and $\theta = 3\pi/2$. Both the PAS and the $(1, 2)^I$-approximant mimic this dominant scattering characteristic around $\theta = \pi/2$, although the PAS over estimates. The PAS also fails to represent the Penrose lattice for scattering at $\theta = 3\pi/2$, where the $(1, 2)^I$-approximant succeeds. The error (i.e. difference between the scattered amplitude from the Penrose lattice to the amplitudes due to the two approximations) is plotted in figure 9.3 to illustrate the differences more clearly. In this figure the quality of the $(1, 2)^I$-approximant as a representation of the Penrose lattice is obvious.

To investigate whether the scattering tendencies of the approximations continue in

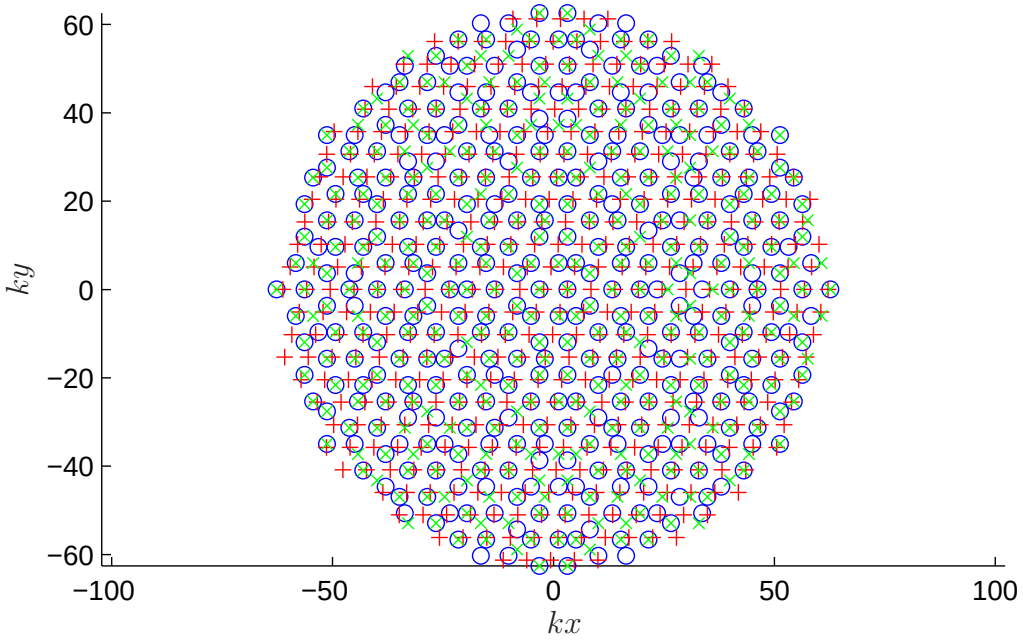

Figure 9.1: Lattice nodes for the Penrose (blue circle), PAS (red plus) and $(1,2)^I$-approximant (green cross) lattices.

this manner, consider another approximant with larger N_1 and/or N_2, i.e. a greater resemblance to the Penrose lattice. We also consider a larger circular region with $R = 5$. Figures 9.4 and 9.5 show the lattice nodes and error in scattered amplitude for an array of scatterers with a distribution determined by the Penrose lattice (blue), PAS lattice (red) and the $(2,2)^I$-approximant lattice (green), respectively. In comparison to figure 9.1, it can be seen that the Penrose and PAS nodes have the same positions, but the approximant nodes have varied slightly, and show more of a resemblance to the Penrose lattice. The error between the scattered pattern from the Penrose lattice and the PAS lattice is similar to that of the previous example, except it actually increases in error at the dominant angle $\theta = \pi/2$. The $(2,2)^I$-approximant provides a better representation, but is not as accurate around $\theta = 3\pi/2$. There is room for improvement of the accuracy, but for an approximant with N_1 and N_2 so low, this approximant appears to provide an excellent approximation to scattering from the Penrose lattice.

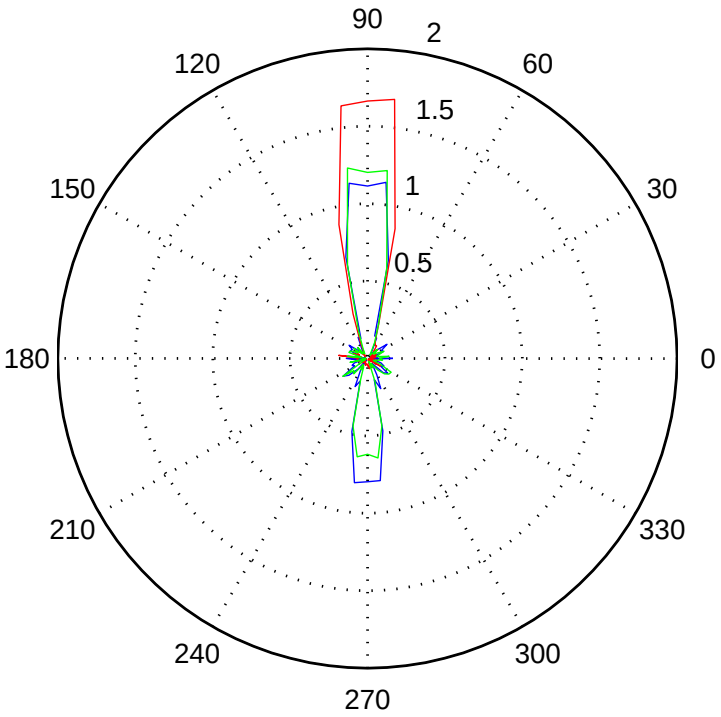

Figure 9.2: Scattered field amplitude from the Penrose (blue), PAS (red) and $(1,2)^I$-approximant (green) arrays for varying θ.

To further investigate the properties of the $(2,2)^I$-approximant consider the scattering from the periodic unit lattice of the approximant, as in chapter 8. The period of the approximant is determined by solving equation (6.97). For the $(2,2)^I$-approximant the period is a rectangular cell with edges of length in the x and y direction given by $L_x = \frac{2}{5}(7+11\tau)$ and $L_y = \frac{2}{5}\sqrt{3-\tau}(1+2\tau)$ and 152 lattice nodes. Note that these figures disagree with the statement of Florescu et al. [29], discussed in section 2.1.4. The L_y determined here is a factor 2/5 of the L_y^F stated by Florescu, which is to be expected due to the scaling applied in this thesis. However, their formulae lead to an edge length in the x direction of $L_x^F = 5(1+\tau)$ and only 80 lattice nodes. Unfortunately, Florescu et al. only state these formulae and give no derivation.

We continue to work with the period defined in this thesis. Figure 9.6 shows a section of the lattice nodes of the $(2,2)^I$-approximant (green) and the lattice nodes of the period (purple crosses). The repetition of the approximant nodes can be seen in each period, giving visual confirmation of the method applied in this thesis.

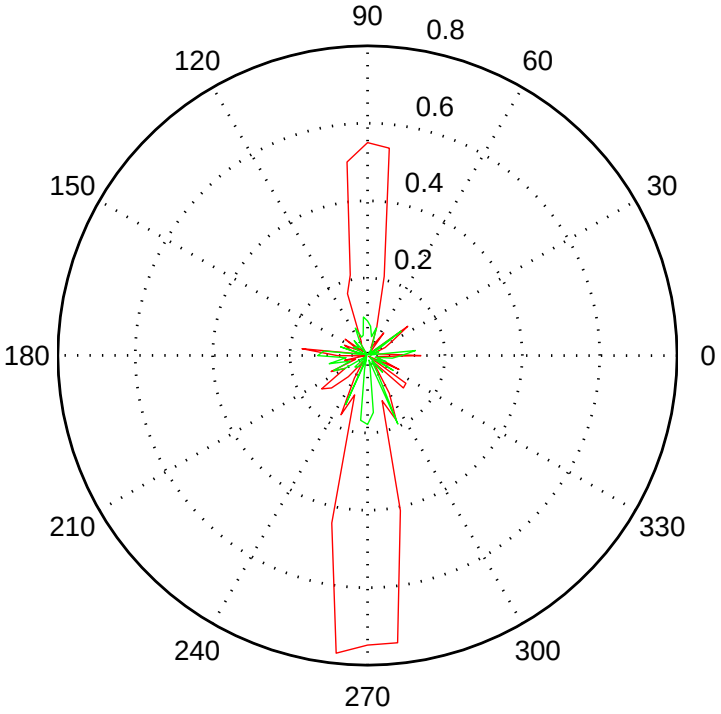

Figure 9.3: Absolute error in the scattered amplitude for the PAS (red) and $(1,2)^I$-approximant (green) lattices compared to the Penrose lattice, for a circle region of radius $R = 4$ for $r = 2W$ and varying θ.

The approximant lattice nodes are identical in each periodic cell, however the Penrose and PAS lattice nodes vary between cells. This is because the Penrose lattice is aperiodic and the PAS has a different period to the approximant. As in chapter 8, consider the multiple scattering associated with a number of different periodic cell configurations and thus a number of arrangements of the Penrose and PAS nodes. Figure 9.7 shows the lattice node positions for six different periods.

It was visually observed that the scattered fields associated with the Penrose or the PAS structures are similar for different periods, and thus we represent the scattered field for each lattice in a period cell by the average over six cells. Figure 9.8 presents the error between the average scattered field amplitude for the Penrose lattice and the two approximations: the $(2,2)^I$-approximant (green) and the average over six cells for the PAS (red) lattice. It can be seen that the scattered field from the PAS bears little resemblance to that from the Penrose array at certain angles, and therefore cannot

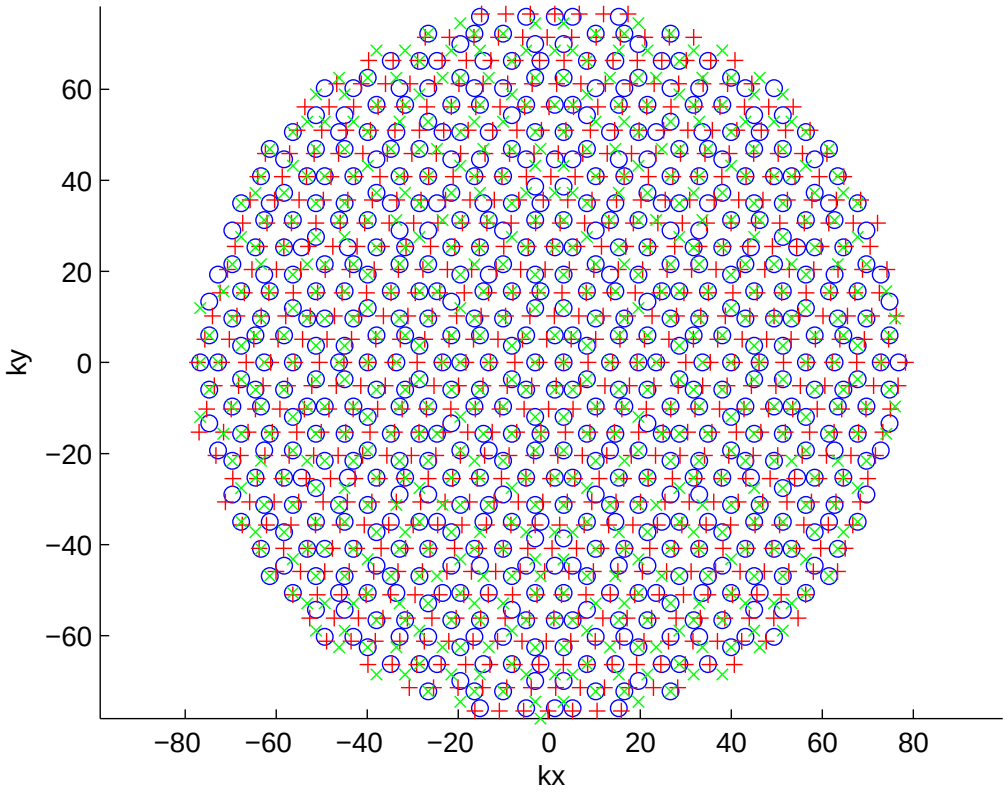

Figure 9.4: Lattice nodes for the Penrose (blue circle), PAS (red plus) and $(2,2)^I$-approximant (green cross) lattices.

represent the Penrose lattice for all directions of propagation. The $(2,2)^I$-approximant provides a very good approximation, with marginal error at all angles. As in the previous chapter, unit cells far from the origin were also considered to validate that the average field for the Penrose lattice was well-represented by the average taken over the six cells in figure 9.8. For the purposes of this thesis, the $(2,2)^I$-approximant provides strong support to the notion that the approximant can provide an excellent periodic representation of the Penrose lattice in the case of multiple scattering for small circular scatterers.

9.3 Wave scattering by an infinite approximant structure

In chapter 7 an expression to determine the effective wave propagation through a 2D array of small circular scatterers with distribution determined by the infinite periodic

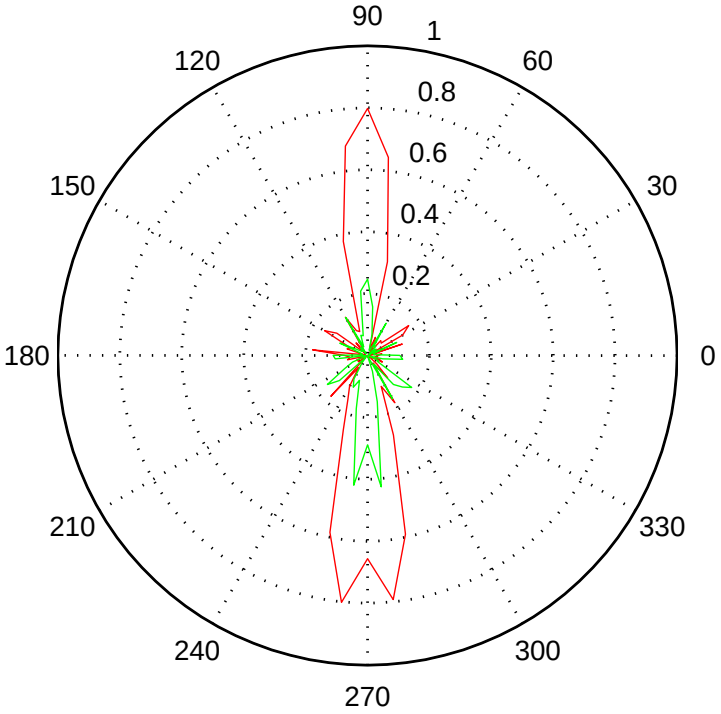

Figure 9.5: Absolute error in the scattered amplitude for the PAS (red) and $(2,2)^I$-approximant (green) lattices compared to the Penrose lattice, for a circle region of radius $R = 5$ for $r = 2W$ and varying θ.

approximant lattice was derived. This enables the construction of a band diagram for the effective wave propagation, which portrays the pass and stop bands of infinite approximants.

It was shown in the previous section that a finite array of scatterers with a periodic approximant distribution provides similar scattering results to a finite array of scatterers with a Penrose tiling distribution. Therefore by determining the effective properties of the infinite periodic approximant, it is possible to provide an estimate of the effective properties of the infinite (or very large finite) Penrose lattice. Because of the aperiodicity inherent in the Penrose lattice, such properties are currently unobtainable by other means.

We define the irreducible Brillouin zone to be in the non-dimensional frequency space and so it has components $\gamma\cos\theta = \gamma_x$ and $\gamma\sin\theta = \gamma_y$ in the $\mathbf{e}_1$ and $\mathbf{e}_2$ directions, respectively, where $\boldsymbol{\gamma} = \gamma(\cos\theta, \sin\theta)$ is the non-dimensional effective wavenumber as

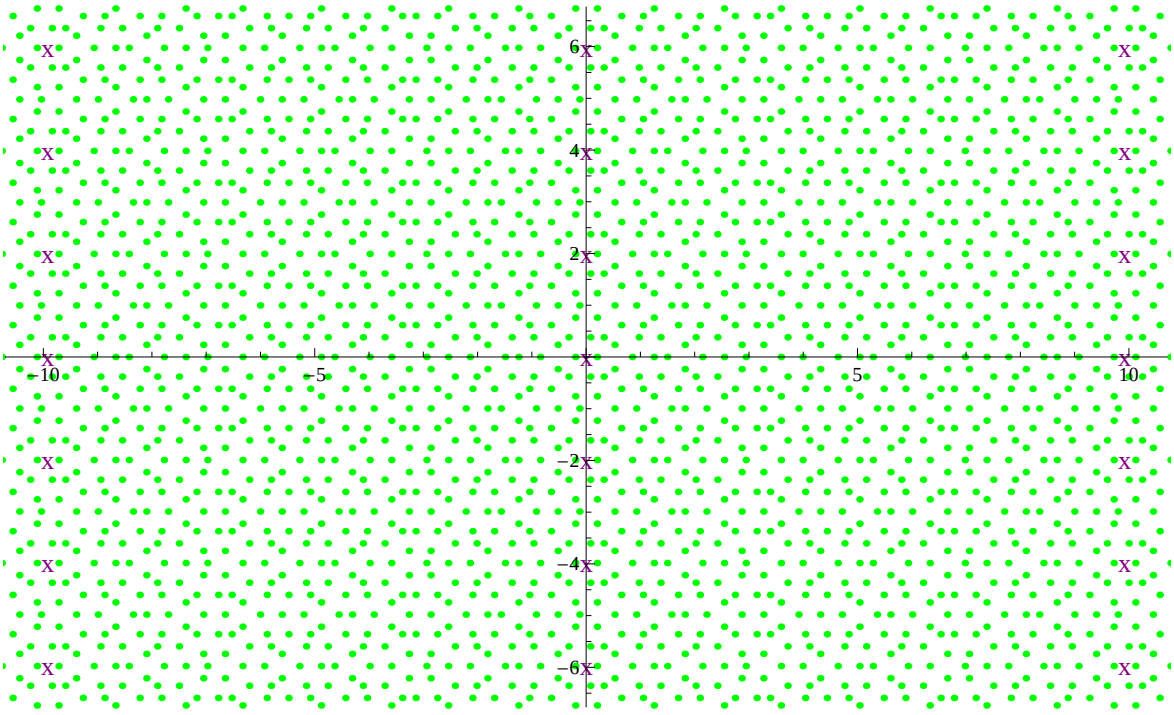

Figure 9.6: Lattice nodes for the $(2,2)^I$-approximant (green) lattices and the periodic cell (purple cross).

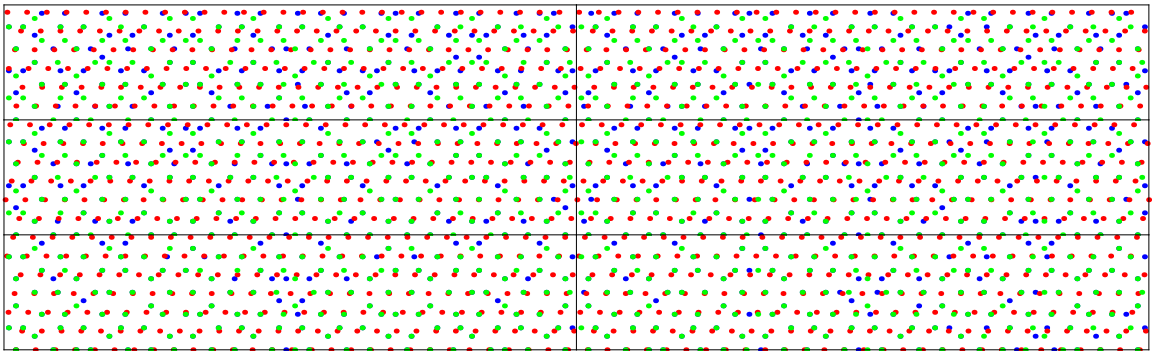

Figure 9.7: Lattice nodes for the Penrose (blue), PAS (red) and $(2,2)^I$-approximant (green) lattices. The array has been discretised into the unit cell of the approximant.

discussed in chapter 7. The coordinates of the vertices of the irreducible Brillouin zone, as in figure 7.4, are given by

$$0 = (0,0), \quad A = (\pi, 0), \quad B = (\pi, \pi/\lambda), \tag{9.1}$$

for the rectangular cell in physical space.

As an example we consider two approximants of the Penrose tiling: the $(1,1)^I$-approximant and the $(1,2)^I$-approximant. The notation $(n_1, n_2)^{I/II}$ refers to approximation made in the construction of the approximant and was discussed in detail in chapter 6. The unit cells of these two lattices are depicted in figure 9.9. The unit

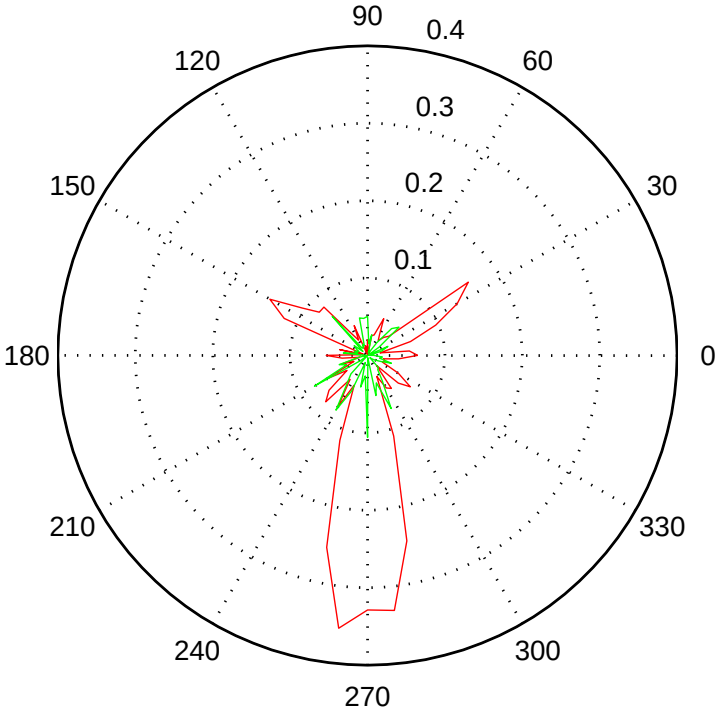

Figure 9.8: Absolute error in the scattered amplitude for the $(2,2)^I$–approximant (green) and averaged PAS (red) lattices compared to the averaged Penrose lattices within an approximant unit cell, for $r = 2W$ and varying θ.

cells contain many more points than the SF lattice examples given in the previous chapter in figure 8.12, and thus the computation times for the band structures are much longer. In the two examples here the cells contain 40 and 48 nodes, respectively.

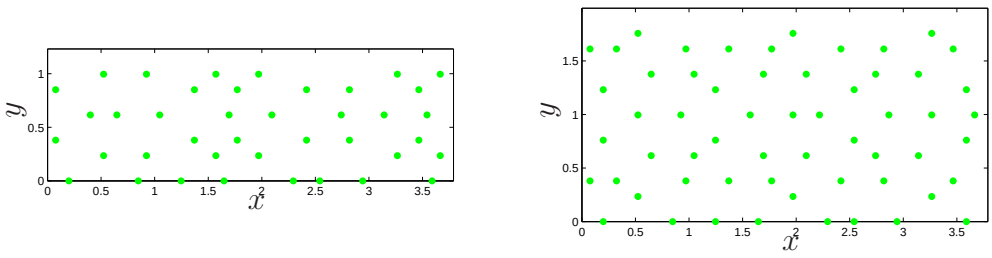

(a) $(1,1)^I$-approximant. (b) $(1,2)^I$-approximant.

Figure 9.9: Unit cell of the $(N_1, N_2)^I$-approximant.

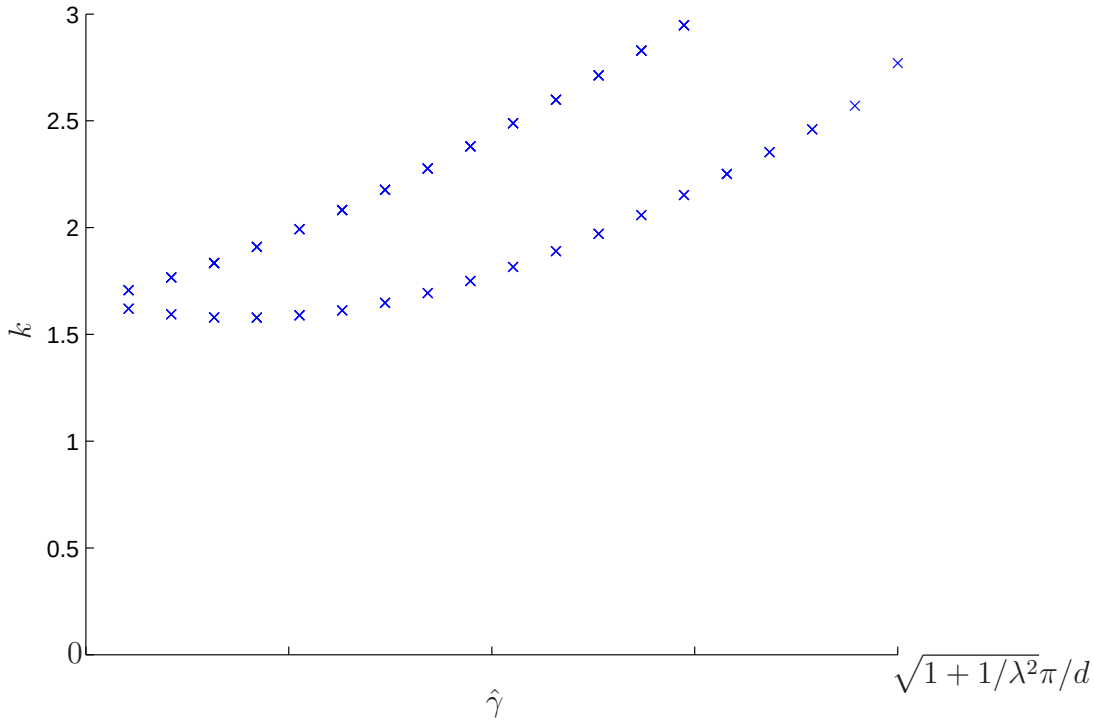

(a) $(1,1)^I$-approximant.

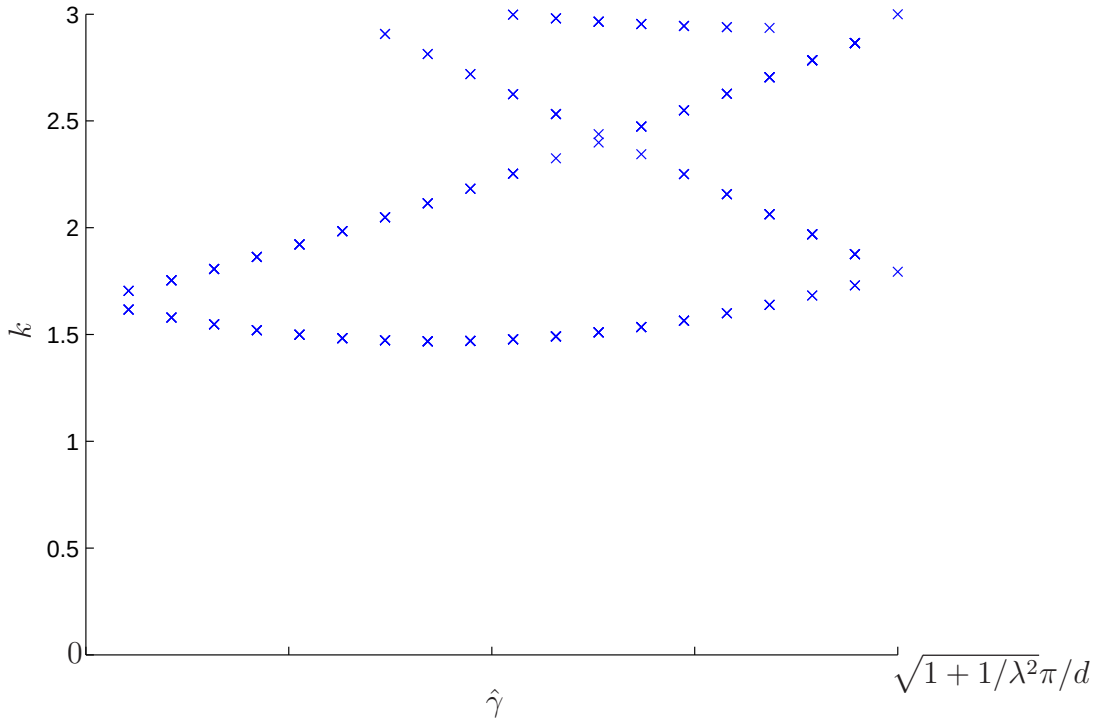

(b) $(1,2)^I$-approximant.

Figure 9.10: Partial band diagram along $0B$ of the irreducible Brillouin zone, for the $(n_1, n_2)^I$-approximant.

We have considered the partial band along the 0B section in the irreducible band diagram due to some interesting band structures that occur, see figure 9.10. It can be seen that, analogous to the SF examples, the first band cuts on at similar wavenumbers k_0 for $\gamma = 0$: $k_0 = 1.6504\ldots$ for the $(1,1)^I$-approximant and $k_0 = 1.6462\ldots$ for the $(1,2)^I$-approximant. This re-emphasises the justification for taking the infinite approximant as an approximation of the infinite Penrose tiling. What we then see in these partial band diagrams is a negative gradient in the first band. The negative gradient is subtle for the $(1,1)^I$-approximant in figure 9.10a but more obvious for the $(1,2)^I$-approximant in figure 9.10b. A negative gradient $dk/d\gamma$ relates to negative group velocity (see [14]) which means that, at these frequencies, the energy is propagating in the opposite direction to the wave crests. The negative gradient also means that the cut-on wavenumber k_0 determined for $\gamma = 0$ is **not** the cut-on wave number for the first band over the entire region; this should be determined by taking the value of k at the minimum of the curve. The two band diagrams depicted here, along 0B in the irreducible Brillouin zone, represent wave propagation in slightly different directions ($\theta = \arctan(1/\lambda)$) because of the variation in λ. Therefore, computing and comparing the positions of the minimum in the partial-band 0B, if at positions other than $\gamma \approx 0$, would not be beneficial in the validation of the approximant.

9.4 Conclusions

In conclusion, in this chapter it has been demonstrated that the approximant continues to provide a good representation of the quasiperiodic lattice as it has for previous investigation in chapters 4, 5 and 8. By considering different finite selections of the Penrose, PAS and approximant lattices it was shown that the PAS provided bad approximations of the scattering pattern at multiple angles, whereas the approximant could represent the Penrose lattice for arbitrary observation points. The $(N_1, N_2)^I$-approximant demonstrated good accuracy for values as low as $N_1 = 1$, $N_2 = 2$.

The partial band structure of the infinite approximant was also analysed using the methodology described in chapter 7. Two examples of the different approximants demonstrated similar cut-on wavenumbers for $\gamma = 0$, and negative group velocity for certain values of γ.

Chapter 10

Conclusions

10.1 Summary

This thesis has explored the time-harmonic acoustic multiple scattering from arrangements of small scatterers with quasiperiodic distributions. The motivation for which was to investigate the effects on the wave propagation due to aperiodicity in the structure. Quasiperiodic distributions were chosen over fully random distributions due to their deterministic nature and interesting physical properties.

The background, set out in chapter 2, introduced the concepts behind quasiperiodic media and discussed the existing influential literature in wave propagation in periodic, random and quasiperiodic media. The review demonstrated the existing established approaches for analysis of periodic media and the questions raised regarding the approximations of random media. It was shown that some existing investigations of quasiperiodic media in acoustics have been made but were incomplete. It was indicated that further analytic investigations of quasiperiodic media was required in order to gain a better understanding of the effects of its aperiodicity. In particular, the desire to determine periodic approximations of the quasiperiodic structures was demonstrated. The periodic approximations addressed in this thesis were the periodic average structure (PAS) and the approximant. The PAS has been investigated previously in acoustics with a mixture of successful and unsuccessful results. The approximant structure had mainly had prior consideration in terms of the atomic structure of a quasicrystal and had not been applied to acoustic multiple scattering.

The construction of the quasiperiodic lattices and their approximations is discussed

in numerous works, but the mathematical community lacks a mathematically rigorous and well-documented algorithm. It was one of the main intentions of this thesis to provide such a tool that could enable further mathematical investigations in the field of quasiperiodic media. In chapter 3, a comprehensive step-by-step algorithm for the construction of the 1D Fibonacci chain and its approximations was developed. The full mathematical formulae for each step of the algorithm were derived using specific notations, making it feasible to extend the algorithm to alternative quasiperiodic structures. The chapter also included visualisations of the steps taken in order to ensure full comprehension of the method. The visual approach is also referred to later when extending into higher dimensions for the construction of 2D quasiperiodic lattices, where the initial dimension of space is five and thus cannot be easily comprehended by graphical means.

Chapter 4 discussed the analytic approach to the multiple scattering in 1D for a propagating wave along an infinite string with distributions of point scatterers. When the distribution of scatterers is the finite Fibonacci chain, an initial benefit of the deterministic nature of quasiperiodic lattices is demonstrated. The deterministic and recursive nature of finite lengths of the 1D Fibonacci chain allows a recursive formulation of the transmission and reflection coefficients to be derived. The formulae we have derived allow the calculation of the reflection and transmission coefficients for Fib(n) point scatterers with only n iterations. The Fibonacci numbers are exponential in growth, therefore the computations are rapid for extremely large numbers of point scatterers.

A novel formulation of the effective wavenumber for a finite array of scatterers of arbitrary distribution was derived, exploiting the prior knowledge of the reflection and transmission coefficients determined via the recursive formulae. This allowed the modelling of arrays of scatterers on a string as a finite length of homogeneous string of a particular density.

Employing the recursive formulae for the three different distributions of scatterers (Fibonacci, PAS and approximant) allowed comparisons to be drawn between the scattering properties of each. It was demonstrated that the PAS failed to capture the essence of the scattering from the Fibonacci distribution of scatterers, but the approximant was much more successful. In particular, it was shown that n-approximants

determined by the approximation $\tau \approx \tau_n = \frac{\text{Fib}(n+1)}{\text{Fib}(n)}$ which have a unit cell containing $\text{Fib}(n+2)$ point scatterers, have capabilities of accurately mimicking the full scattering properties of Fibonacci chain distributions of point scatterers with $\text{Fib}(n+4)$ scatterers in total. Furthermore, the "near" stop band properties were replicated for larger distributions than this, especially with n as small as 6.

The results in chapter 4 motivated the analysis of 1D infinite periodic structures in which the basic unit cell contains a finite number of point scatterers with arbitrary position. The novel analytic solution derived enabled the calculation of effective properties of an infinite approximant which can be applied to approximate the properties of an infinite Fibonacci chain of point scatterers. Since the Fibonacci chain is aperiodic, no previous method has been available to predict such effective properties. It was shown that the first cut-off frequency for the infinite n-approximant converges as n increases, providing further evidence that the approximant is an appropriate lattice to employ as an approximation of the Fibonacci lattice.

Chapter 5 sought to extend the method and conclusions of chapter 4 by applying the 1D distributions to a 2D scenario. We considered infinite rows of small circular cylinders with periodic in-row spacing and quasiperiodic separation between the rows. It was demonstrated that by taking a 1D Fibonacci chain as the separation between the rows, then the same methodology could be applied to derive recursive formulae for the transmission and reflection coefficients in 2D. The transmission and reflection coefficients in this instance are the coefficients of propagating plane waves at particular scattering angles, thus the total scattered field is a sum of these plane waves. The derivation of these angles and propagating modes in chapter 5 is similar to that of previous existing literature in the field but with the simplification of a small radius of cylinder, which allows for an alternative form of solution. Similarly to the 1D scenario, comparative results for the scattering from the three different distributions demonstrated that the PAS was not a particularly good periodic representation of the Fibonacci chain but the approximant could be, even for multiple modes of propagation. We again derived analytic expressions to determine the effective properties of an infinite periodic distribution of rows of cylinders, where each period could contain an arbitrary distributions of the rows. The expression exploits prior knowledge of the transmission and reflection properties of the finite period gained from the recursive

formulae, as in 1D. The expression in 2D is of a similar form to that in 1D but is multi-dimensional, dependent on the array length parameters and the direction of effective wave propagation under consideration. This novel expression to determine the effective properties of an infinite periodic array was applied to the approximant of the Fibonacci chain in order to predict effective properties of the infinite Fibonacci chain in this 2D set up.

Chapter 6 extends the algorithm developed in chapter 3 to construct 2D quasiperiodic lattices. Firstly, we showed that by applying the derived formulae for the 1D lattice nodes of the Fibonacci chain and its approximations in two perpendicular directions, we can construct the 2D square Fibonacci (SF) lattice and its approximations fairly simply. Then, we developed a thorough step-by-step algorithm to construct a 2D Penrose lattice from 5D space. The 5D to 2D construction relies on the understanding and visualisations outlined in chapter 3, but still provides the full formulae and derivations for the 5D case. In order to clarify the approach and make it more intuitive, we choose to introduce a 4D space, an approach not often taken in the literature. This is the minimum dimension that the Penrose lattice can be projected from, and reduces the order of complexity. It also reduces the acceptance windows from being a complicated 3D polyhedron to simpler 2D polygons, making the visualisation of the intersection with the parallel plane much simpler.

In chapter 7 we developed novel analytic expressions to determine the effective properties of 2D wave propagation through 2D infinite doubly-periodic arrays of small circular scatterers. The expressions can be applied to arbitrary distributions of scatterers in the unit cell, but were sought with the intention of predicting effective propagation of acoustic waves in an infinite 2D approximant structure. As with chapters 4 and 5, the calculation of the effective properties exploits prior knowledge of wave propagation through a finite period and Bloch's theorem.

We compared the scattering properties of the SF lattice and its approximations in chapter 8 using the multipole method for finite arrays of small scatterers. It was shown that the PAS only captured scattering properties of the SF lattice at certain (and few) observation angles. The n-approximant however, was able to capture scattering properties of the SF lattice for all observation angles, and continued to improve in accuracy as we increased n.

Similarly, we compared the scattering properties of the Penrose lattice and its approximations in chapter 9. We again found that the PAS only produced accurate scattered fields at particular angles, whereas the $(n_1, n_2)^{I/II}$-approximant captured the full scattering behaviour of the 2D fully quasiperiodic Penrose lattice with good accuracy. As with all other comparisons throughout the thesis, it was shown how the accuracy of the $(n_1, n_2)^{I/II}$-approximant increased as n_1 and/or n_2 was increased.

Through existing and novel analytic techniques we have been able to predict the wave scattering due to multiple quasiperiodic structures and their approximations. We have shown that, contrary to previous investigations in approximations of quasiperiodicity, the PAS generally failed to provide a good representation of the quasiperiodic structure in question. However, the approximant was able to capture the full properties of the scattering from quasiperiodic structures, even for low values of n, or n_1 and n_2 in the approximation of $\tau \approx \tau_n = \frac{\mathrm{Fib}(n+1)}{\mathrm{Fib}(n)}$. This suggests that a small degree of quasiperiodicity within an approximant period can contain enough information of the full quasiperiodicity in a large array. With this in mind, we can justify the approximation of the effective wave propagation through an infinite quasiperiodic structure by the effective properties of the infinite approximant determined by our novel analytic expressions. In 1D we could further validate this approximation by comparing the approximant band structure to the transmission through an extremely large number (billions!) of point scatterers with a Fibonacci chain distribution, depicted in figure 4.20. The infinite approximant introduces an alternative outlook on acoustic wave propagation through some aperiodic structures, as they can in fact be modelled by periodic structures. With the ability of expressing the band structure of an infinite quasiperiodic medium by the band structure gained through analysis of the approximant, we demonstrate the occurrence of pass and stop frequency bands and lack of localisation as usually construed.

10.2 Future work

The conclusions of this thesis provide us with new insight into the scattering properties of quasiperiodic structures. However, we must be aware that the analysis in the thesis is restricted to small isotropic scatterers. It would be highly instructive to extend the

analysis to scenarios of more complex behaviours of scatterers to determine if the same conclusions can still be made.

For instance, further investigations should be made to consider small scatterers with sound-hard rather than sound-soft boundary conditions on the radius. As discussed in section 2.4, when applying the multipole method to determine the scattering from a finite array of scatterers, applying sound-hard or Neumann boundary conditions

$$\left.\frac{\partial u}{\partial r}\right|_{r=a} = 0 \tag{10.1}$$

results in coefficients that depend on the derivatives of the Bessel and Hankel functions (2.112). For small scatterers this results in the sound-hard scatterers that act as combined monopole and dipole sources, rather than just monopole sources for sound-soft. Therefore, all the analysis in this this thesis could be extended to the scenario of small sound-hard scatterers by considering scattering from each cylinder by an expression of the form

$$C_0 H_0^{(1)}(kr) + C_{-1} H_{-1}^{(1)}(kr) e^{-i(\theta-\alpha)} + C_1 H_1^{(1)}(kr) e^{i(\theta-\alpha)}, \tag{10.2}$$

where (r, θ) is the location of the observation point, expressed in polar coordinates.

Alternatively, one could extend the analysis of this thesis to consider instances of circular scatterers of arbitrary size. This results in more complicated expressions for the scattered field involving an infinite sum of Hankel functions over every integer order, since it is no longer the case that only the 0^{th} order of Hankel and Bessel functions provide significant contributions.

Further extensions of the work in this thesis could include the consideration of alternative quasiperiodic structures. This could involve quasiperiodic structures in 2D of different order of rotational symmetry, as considered in some of the literature discussed in section 2.2.3, e.g. [75]. For certain 2D quasiperiodic lattices, Sutter-Widmer found that the PAS could provide a good representation of the quasiperiodic structure, thus it would be of interest to investigate how the approximant would compare in these instances.

Extensions could also be made into three dimensions. The construction algorithms outlined in chapters 3 and 6 should be extended for the 6D to 3D construction of the 3D Penrose lattice [40]. This would involve a 6D hypercubic lattice, 3D parallel

and perpendicular spaces and 3D acceptance windows. The approximant and PAS lattices can be constructed in a similar manner in order to draw analogous comparisons. Multiple scattering from spheres in 3D space can be approached in a similar way to that of 2D multiple scattering, but employing spherical rather than cylindrical waves [50].

As well as the direct extensions of the work in this thesis, such as those just mentioned, there are also various concepts touched upon that could be investigated in further detail. Firstly, attempts to draw further comparisons between the quasiperiodic structures and their approximations could be made. As a supplement to the comparisons of the scattered fields one could endeavour to determine some statistical measures of the deviations of the quasiperiodic structure from its approximations. With the PAS this notion was discussed via the occupancy windows and the occupancy factor and packing density. With the time constraints of this research, it has not been possible to employ the statistical measures of the PAS and relate these to the quality of "fit" between the scattered fields. Nor has it been possible to provide similar properties for the approximant. With the approximant we have been able to demonstrate that an increase in the approximation of τ leads to a better fit between the quasiperiodic and approximant scattered fields, but not relate this to the deviation of its lattice positions from those of the quasiperiodic lattices. Related to this statistical measure of deviation, one could look to analyse periodic lattices with some added random perturbation and use these as approximations to the quasiperiodic structures. Allowing some random perturbation of lattice node location within a defined range could improve, or reduce, the quality of the approximations fit to the quasiperiodic structure, an investigation of which could be extremely instructive. If it was found that the perturbed lattice provided a better approximation of the quasiperiodic lattice, analysis of an infinite periodic lattice with some small random perturbation could be carried out to determine the effective wave propagation properties. Papers such as [60] or [51] propose approaches to this analysis.

In this thesis we analysed orthorhombic infinite periodic lattices in order to determine the effective properties of an infinite approximant structure. The analysis applied in chapter 7 could be employed to any arbitrary orthorhombic period, but also has the potential to be extended to consider instances in which the period cell

is not orthorhombic. This would require a slightly different form of Bloch condition and potentially an alternative form of integral representation of the Hankel function that was used in equation (5.41). In our investigations of the approximant we found that the periodic cell was always orthorhombic. However, periodic cells of other forms are possible, as discussed in section 2.1.4. Lord et al [49] and Subramaniam et al [49] investigated periodic cells with basis vectors subtended at angles of $2\pi/5$ as for a Penrose tile, as well as orthorhombic. For infinite approximant lattices, the cell shape should not affect the effective properties, and thus was not discussed in more detail in our investigations. However, in future investigations it would be of interest to determine whether varying the shape of the periodic cell would produce different results and conclusions when comparing finite arrays of scatterers.

When predicting the wave propagation through the 1D Fibonacci chain in 1D or 2D multiple scattering it was possible to rapidly determine the transmission due to the recursive nature of the Fibonacci chain. However for the more complex 2D quasiperiodic structures this is no longer possible and the numerical calculation of the scattering is much more expensive. It would be of interest in the future to consider weak interactions between scatterers that are far apart. If it is possible to neglect their interactions it would result in a more sparse matrix in equation (2.136), reducing computation time significantly. A similar approach was taken in [46] using a sparse-matrix and canonical grid method. Further improvements of the codes written in both Mathematica and Matlab for the computations in this thesis could also be made. This would enable them to run much faster should further investigations be conducted.

Finally, one further extension of the work in this thesis would be to relate the results with quasiperiodic media back to the original motivation of random media. It would be of interest to draw comparisons between the multiple scattering in random media and quasiperiodic. This would show whether the aperiodicity in quasiperiodic media results in similar scattering behaviour to that for random media, and thus whether or not understanding quasiperiodic media can provide new insight into the scattering properties of random media. The randomness could be fully random, or be considered as random perturbations from periodicity as mentioned above. It would also be extremely beneficial to apply the infinite periodic analysis, where the periodic cell can contain any arbitrary distribution of scatterers, to random media. That is,

can a repeating unit cell containing a random distribution of scatterers represent an infinite fully random structure? If so, what would be a reasonable size of unit cell as an RVE? The determination of the cell will not be as straightforward as for the quasiperiodic lattices, and so this potentially valuable concept topic will require a thorough investigation.

Bibliography

[1] Penrose tiling. http://en.wikipedia.org/wiki/Penrose_tiling. Accessed May 8, 2014.

[2] I. D. Abrahams. Effective mathematics, effective mathematicians. *IMA Mathematics Today*, 2010.

[3] I. D. Abrahams and G. R. Wickham. Scattering of elastic waves by an arbitrary small imperfection in the surface of a half-space. *Journal of the Mechanics and Physics of Solids*, 40(8):1683–1706, 1992.

[4] M. Abramowitz and I. Stegun. *Handbook of Mathematical Functions: With Formulas, Graphs, and Mathematical Tables*. Applied mathematics series. Dover Publications, 1964.

[5] C. M. Aegerter, M. Störzer, and G. Maret. Experimental determination of critical exponents in Anderson localisation of light. *EPL (Europhysics Letters)*, 75(4):562, 2006.

[6] P. W. Anderson. Absence of diffusion in certain random lattices. *Phys. Rev.*, 109(5):1492–1505, Mar 1958.

[7] H. Aoki. Anderson localisation in anisotropic systems. *Solid State Communications*, 37(8):677–680, 1981.

[8] D. Austin. Penrose tilings tied up in ribbons. http://www.ams.org/samplings/feature-column/fcarc-ribbons. Accessed August 12, 2011.

[9] E. Barnwell. *The propagation of waves and pulses in complex materials*. PhD thesis, The University of Manchester, Manchester, UK, In preparation.

[10] M. Bayindir, E. Cubukcu, I. Bulu, and E. Ozbay. Photonic band-gap effect, localization, and waveguiding in the two-dimensional penrose lattice. *Phys. Rev. B*, 63:161104, Apr 2001.

[11] M. Bayindir, E. Cubukcu, I. Bulu, T. Tut, E. Ozbay, and C. Soukoulis. Photonic band gaps, defect characteristics, and waveguiding in two-dimensional disordered dielectric and metallic photonic crystals. *Physical Review B*, 64(19):195113, 2001.

[12] L. G. Bennetts. Wave attenuation through multiple rows of scatterers with differing periodicities. *SIAM Journal on Applied Mathematics*, 71(2):540–558, 2011.

[13] L. G. Bennetts and V. A. Squire. Wave scattering by multiple rows of circular ice floes. *Journal of Fluid Mechanics*, 639:213–238, 2009.

[14] J. Billingham and A. King. *Wave Motion*. Cambridge Texts in Applied Mathematics. Cambridge University Press, 2000.

[15] L. Bindi, P. J. Steinhardt, N. Yao, and P. J. Lu. Natural quasicrystals. *Science*, 324(5932):1306–1309, 2009.

[16] F. Bloch. Über die quantenmechanik der elektronen in kristallgittern. *Zeitschrift für physik*, 52(7-8):555–600, 1929.

[17] L. Brillouin. *Wave propagation in periodic structures: electric filters and crystal lattices*. Dover books and science. Dover Publications, 1953.

[18] J. Carpenter. Nobel win for crystal discovery. http://www.bbc.co.uk/news/science-environment-15181187. Accessed October 6, 2011.

[19] Y. Chan, C. Chan, and Z. Liu. Photonic band gaps in two dimensional photonic quasicrystals. *Physical review letters*, 80(5):956, 1998.

[20] A.-L. Chen, Y.-S. Wang, Y.-F. Guo, and Z.-D. Wang. Band structures of fibonacci phononic quasicrystals. *Solid State Communications*, 145(3):103–108, 2008.

[21] J. H. Conway and K. M. Knowles. Quasiperiodic tiling in two and three dimensions. *Journal of Physics A: Mathematical and General*, 19(17):3645, 1986.

[22] N. G. De Bruijn. Algebraic theory of Penrose's non-periodic tilings of the plane. In *Indagationes Mathematicae Proceedings A 84*, pages 39–66, 1981.

[23] J.-M. Dubois. Properties and applications of quasicrystals and complex metallic alloys. *Chem. Soc. Rev.*, 41:6760–6777, 2012.

[24] A. Duclos, D. Lafarge, V. Pagneux, et al. Transmission of acoustic waves through 2d phononic crystal: visco-thermal and multiple scattering effects. *European physical journal. Applied physics*, 45(1):11302, 2009.

[25] V. Elser and C. L. Henley. Crystal and quasicrystal structures in Al-Mn-Si alloys. *Phys. Rev. Lett.*, 55:2883–2886, Dec 1985.

[26] O. Entin-Wohlman, M. Kléman, and A. Pavlovitch. Penrose tiling approximants. *Journal de Physique*, 49(4):587–598, 1988.

[27] A. Figotin and A. Klein. Localization of classical waves I: Acoustic waves. *Communications in mathematical physics*, 180(2):439–482, 1996.

[28] A. Figotin and A. Klein. Localization of classical waves II: Electromagnetic waves. *Communications in mathematical physics*, 184(2):411–441, 1997.

[29] M. Florescu, S. Torquato, and P. J. Steinhardt. Complete band gaps in two-dimensional photonic quasicrystals. *Phys. Rev. B*, 80:155112, Oct 2009.

[30] L. L. Foldy. The multiple scattering of waves. I. general theory of isotropic scattering by randomly distributed scatterers. *Phys. Rev.*, 67(3-4):107–119, Feb 1945.

[31] J.-P. Fouque, J. Garnier, G. Papanicolaou, and K. Solna. *Wave Propagation and Time Reversal in Randomly Layered Media*. Springer, 2007.

[32] M. Gei. Wave propagation in quasiperiodic structures: stop/pass band distribution and prestress effects. *International Journal of Solids and Structures*, 47(22):3067–3075, 2010.

[33] K. F. Graff. *Wave Motion in Elastic Solids*. Dover, London UK, 1991.

[34] B. Grunbaum and G. C. Shephard. *Tilings and patterns*. W.H. Freeman, New York, 1987.

[35] T. Hattori, N. Tsurumachi, S. Kawato, and H. Nakatsuka. Photonic dispersion relation in a one-dimensional quasicrystal. *Physical Review B*, 50(6):4220–4223, 1994.

[36] S. He and J. D. Maynard. Eigenvalue spectrum, density of states, and eigenfunctions in a two-dimensional quasicrystal. *Phys. Rev. Lett.*, 62:1888–1891, Apr 1989.

[37] C. H. Hodges, D. Weaire, and N. Papadopoulos. The recursion method and Anderson localisation. *Journal of Physics C: Solid State Physics*, 13(23):4311, 1980.

[38] D. Hundertmark. A short introduction to Anderson localization. http://www.math.uiuc.edu/d̃irk/preprints/localization3.pdf. Accessed August 21, 2011.

[39] C. Janot. *Quasicrystals: A Primer*. Monographs on the physics and chemistry of materials. OUP Oxford, 2012.

[40] M. Jarić. *Introduction to the mathematics of quasicrystals*. Aperiodicity and order. Academic Press, 1989.

[41] S. Jazbec and J. Dolinšek. The properties and applications of quasicrystals. *University of Ljubljana*, 2009.

[42] J. Joannopoulos, S. Johnson, J. Winn, and R. Meade. *Photonic Crystals: Molding the Flow of Light (Second Edition)*. Princeton University Press, 2011.

[43] P. King and T. Cox. Acoustic band gaps in periodically and quasiperiodically modulated waveguides. *Journal of applied physics*, 102(1):014902–014902, 2007.

[44] M. Kohmoto, B. Sutherland, and K. Iguchi. Localization of optics: Quasiperiodic media. *Physical review letters*, 58(23):2436, 1987.

[45] A. Krynkin and P. McIver. Approximations to wave propagation through a lattice of dirichlet scatterers. *Waves in Random and Complex Media*, 19(2):347–365, 2009.

[46] Y. Lai, Z. Zhang, C. Chan, and L. Tsang. Gap structures and wave functions of classical waves in large-sized two-dimensional quasiperiodic structures. *Physical Review B*, 74(5):054305, 2006.

[47] R. Lifshitz. The square Fibonacci tiling. *Journal of alloys and compounds*, 342(1):186–190, 2002.

[48] C. M. Linton. Schlömilch series that arise in diffraction theory and their efficient computation. *Journal of Physics A: Mathematical and General*, 39(13):3325, 2006.

[49] E. Lord, K. Ramakrishnan, and S. Ranganathan. An algorithm for generating quasiperiodic patterns and their approximants. *Bulletin of Materials Science*, 23:119–123, 2000.

[50] P. A. Martin. *Multiple Scattering: Interaction of Time-harmonic Waves With N Obstacles*. Encyclopedia of Mathematics and Its Applications 107. Cambridge University Press, 2006.

[51] P. A. Martin and A. Maurel. Waves around almost periodic arrangements of scatterers: Analysis of positional disorder. *Mathematical Methods in the Applied Sciences*, 33(18):2215–2224, 2010.

[52] J. D. Maynard. Wave propagation in arrays of scatterers tutorial: Part 1. *Acoustics Today*, 4(4):12–21, 2008.

[53] P. McIver. Approximations to wave propagation through doubly-periodic arrays of scatterers. *Waves in Random and Complex Media*, 17(4):439–453, 2007.

[54] R. McPhedran, A. Movchan, and N. Movchan. Platonic crystals: Bloch bands, neutrality and defects. *Mechanics of Materials*, 41(4):356–363, 2009.

[55] L. Mulholland and M. A. Heckl. Multi-directional sound wave propagation through a tube bundle. *Journal of Sound and Vibration*, 176(3):377 – 398, 1994.

[56] Y. Neve-Oz, T. Pollok, S. Burger, M. Golosovsky, and D. Davidov. Resonant transmission of electromagnetic waves through two-dimensional photonic quasicrystals. *Journal of Applied Physics*, 107(6):063105–063105, 2010.

[57] W. J. Parnell. Some details and thoughts on multiple scattering. Private communication.

[58] W. J. Parnell. *Homogenization Techniques for Wave Propagation in Composite Materials*. PhD thesis, University of Manchester, Manchester UK, 2004.

[59] W. J. Parnell and I. D. Abrahams. Dynamic homogenization in periodic fibre reinforced media. Quasi-static limit for SH waves. *Wave Motion*, 43(6):474–498, 2006.

[60] W. J. Parnell and I. D. Abrahams. Wave propagation in periodic and random inhomogeneous media: An overview. In *GDR 2051 Conference*, pages 92–99, 2007.

[61] S. Peng, X. Mei, P. Pang, M. Ke, and Z. Liu. Experimental investigation of negative refraction and imaging of 8-fold-symmetry phononic quasicrystals. *Solid State Communications*, 149(17):667–669, 2009.

[62] R. Penrose. The rôle of aesthetics in pure and applied mathematical research. *The Institute of Mathematics and its Applications Bulletin*, 10(7/8):266–271, July 1974.

[63] M. A. Peter and M. H. Meylan. Water-wave scattering by vast fields of bodies. *SIAM Journal on Applied Mathematics*, 70(5):1567–1586, 2009.

[64] M. A. Peter and M. H. Meylan. Band structures and band gaps in water-wave scattering by periodic lattices of arbitrary bodies. In *International Workshop on Water Waves and Floating Bodies 26*, 2011.

[65] A. Poddubny and E. Ivchenko. Photonic quasicrystalline and aperiodic structures. *Physica E: Low-dimensional Systems and Nanostructures*, 42(7):1871 – 1895, 2010.

[66] M. Senechal. *Quasicrystals and Geometry*. Cambridge University Press, Cambridge, UK, 1995.

[67] M. Senechal. Mathematical communities. *The Mathematical Intelligencer*, 26:10–21, 2004.

[68] D. Shechtman, I. Blech, D. Gratias, and J. W. Cahn. Metallic phase with long-range orientational order and no translational symmetry. *Phys. Rev. Lett.*, 53(20):1951–1953, Nov 1984.

[69] P. Sheng, B. White, Z.-Q. Zhang, and G. Papanicolaou. Minimum wave-localization length in a one-dimensional random medium. *Physical Review B*, 34(7):4757, 1986.

[70] W. Steurer and S. Deloudi. Higher-dimensional approach. In *Crystallography of Quasicrystals*, volume 126 of *Springer Series in Materials Science*, pages 61–188. Springer Berlin Heidelberg, 2009.

[71] W. Steurer and T. Haibach. The periodic average structure of particular quasicrystals. *Acta Crystallographica Section A*, 55(1):48–57, Jan 1999.

[72] W. Steurer and T. Haibach. Reciprocal-space images of aperiodic crystals. In *International Tables for Crystallography Volume B: Reciprocal space*, pages 486–532. Springer, 2001.

[73] W. Steurer and D. Sutter-Widmer. Photonic and phononic quasicrystals. *Journal of Physics D: Applied Physics*, 40(13):R229, 2007.

[74] A. Subramaniam and K. Ramakrishnan. Rational approximants to 5, 8 and 7-fold two-dimensional tilings. *Zeitschrift fr Kristallographie - Crystalline Materials*, 218(9):590–596, 2003.

[75] D. Sutter-Widmer. *Phononic Quasicrystals*. PhD thesis, ETH Zurich, Zurich Switzerland, 2007.

[76] D. Sutter-Widmer, S. Deloudi, and W. Steurer. Periodic average structures in phononic quasicrystals. *Philosophical Magazine*, 87(18-21):3095–3102, 2007.

[77] A.-P. Tsai, A. Inoue, and T. Masumoto. A stable quasicrystal in Al-Cu-Fe system. *Japanese Journal of Applied Physics*, 26(Part 2, No. 9):L1505–L1507, 1987.

[78] R. Twarock. Mathematical virology: a novel approach to the structure and assembly of viruses. *Philosophical Transactions of the Royal Society A: Mathematical, Physical and Engineering Sciences*, 364(1849):3357–3373, 2006.

[79] V. Twersky. On the scatttering of waves by an infinite grating. *Antennas and Propagation, IRE Transactions on*, 4(3):330–345, 1956.

[80] M. Van Der Baan. Acoustic wave propagation in one dimensional random media: the wave localization approach. *Geophysical Journal International*, 145(3):631–646, 2001.

[81] V. Velasco and J. Zárate. Elastic waves in quasiperiodic structures. *Progress in Surface Science*, 67(1):383–402, 2001.

[82] U. Vogg and P. Ryder. A general algorithm for generating quasiperiodic lattices by the strip projection method. *Journal of Non-Crystalline Solids*, 194(12):135 – 144, 1996.

[83] N. Willoughby. *Dynamic Homogenization for the Elastic Properties of Periodic and Random Composites*. PhD thesis, The University of Manchester, Manchester, UK, 2013.

[84] N. Willoughby, W. J. Parnell, A. L. Hazel, and I. D. Abrahams. Homogenization methods to approximate the effective response of random fibre-reinforced composites. *International Journal of Solids and Structures*, 49(13):1421–1433, 2012.

[85] K. Zong, O. Lenoir, and H. Franklin. Résonances de réseaux 2d de cylindres élastiques à gradients de propriété. *20ème Congrès Français de Mécanique, 28 août/2 sept. 2011-25044 Besançon, France (FR)*, 2011.

Appendix A

Proofs in one dimension

A.1 Projection method - angle of parallel plane

In the projection method for a 1D Fibonacci chain from a 2D square lattice the angle θ at which the 2D lattice is subtended from the parallel space determines the 1D pattern produced. For the Fibonacci chain with lengths L and S, where $L = \tau S$, for the golden ratio τ an angle θ such that $\tan\theta = 1/\tau$ is used. In this section a visual and geometrical derivation of the relationship between the angle θ and the properties of the 1D lattice is given. Figure A.1 depicts the geometry for the spacings L and S

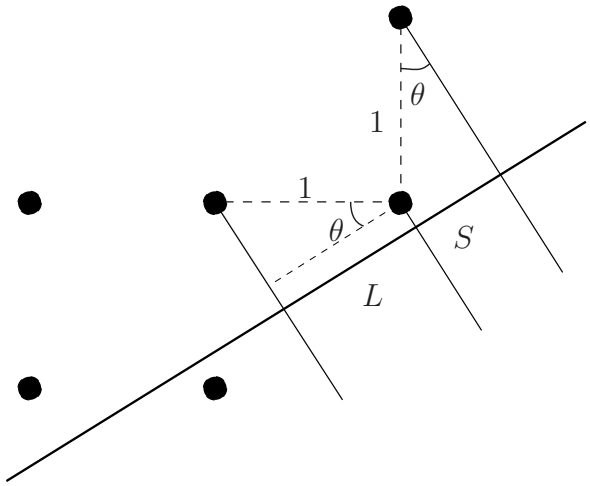

Figure A.1: Geometry of the 2D projection method in order to find the relation between L and S.

on the parallel space which is subtended at angle θ from the horizontal. The 2D unit square lattice is spanned by $\mathbf{e}_1$ and $\mathbf{e}_2$.

Using trigonometry, in the triangle with an edge of length L, it can be determined

that

$$\cos\theta = \frac{L}{1} = L, \tag{A.1}$$

and in the second triangle with an edge of length S,

$$\sin\theta = \frac{S}{1} = S. \tag{A.2}$$

Using these relations and the fact that θ is chosen such that $\tan\theta = \frac{1}{\tau}$, it is possible to show that

$$\tan\theta = \frac{S}{L} = \frac{1}{\tau}. \tag{A.3}$$

Rearranging gives the resulting relationship between S and L as

$$L = \tau S, \tag{A.4}$$

as required.

A.2 Projection method - width of strip

In sections 2.1.2 and 3.1 it was discussed how the selection of the 2D lattice nodes to project to the 1D Fibonacci lattice could be made in two ways. Firstly, using the concept of an acceptance window, which is the method employed in this thesis. Secondly, using a strip that cuts through the 2D lattice. In this section the derivation of the width of the strip to be used in the 2D to 1D projection method is given. The proof is given with no necessary knowledge of the acceptance window, but the results agree.

The value of the width of the strip that is needed to project the 1D Fibonacci chain comes from the geometry of the problem. Set the parallel space line to be at a slope of $\frac{1}{\tau}$ going through the origin to be the bottom of the strip. The upper line of the strip is set to run parallel to this and through the opposite diagonal lattice point of the origin square. With this set up it is possible to determine the required width of the strip from the visual geometrical set up, see figure A.2.

From the second part of the figure, using basic trigonometry and the fact that $1 + \frac{1}{\tau} = 1 + \tau - 1 = \tau$, it can be shown that

$$\cos\theta = \frac{h}{\tau}. \tag{A.5}$$

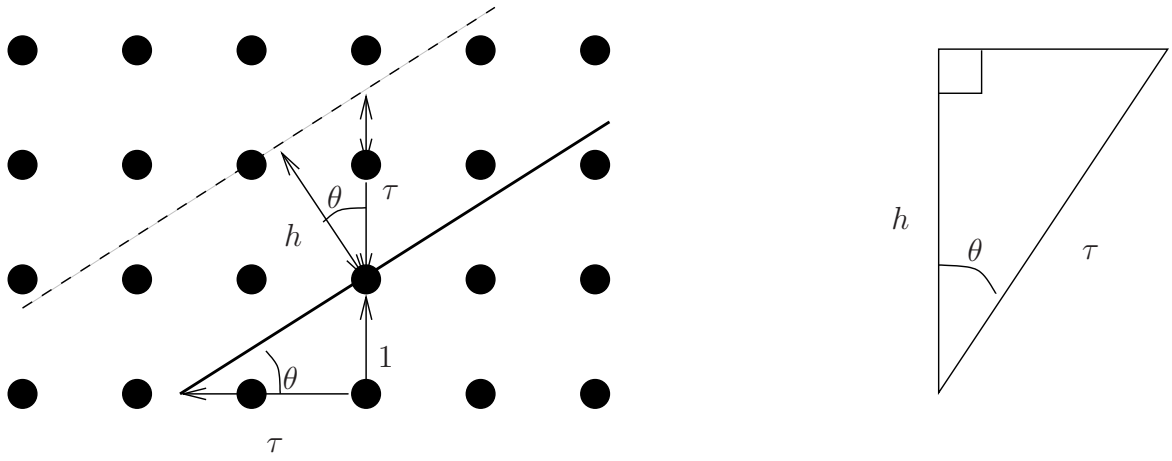

Figure A.2: Geometry of the 2D projection method in order to find the width of the strip.

Since $\tan\theta = \frac{1}{\tau}$, the cosine of θ can be expressed as

$$\cos\theta = \frac{\tau}{\sqrt{1+\tau^2}}. \tag{A.6}$$

Combining (A.5) and (A.6) gives the result

$$h = \frac{\tau^2}{\sqrt{1+\tau^2}}, \tag{A.7}$$

for the height of the strip

A.3 Inductive proof of the recursive formulation for wave propagation in a one-dimensional Fibonacci lattice

In this section an inductive proof is given for the recursive formulation used in section 4.3 for the transmission and reflection coefficients of a wave propagating along an infinite string with Fib(N) point scatterers with a Fibonacci chain distribution. The Nth distribution of Fib(N) scatterers is broken down into two subproblems: the $(N-1)$th distribution of Fib$(N-1)$ scatterers and the $(N-2)$th distribution of Fib$(N-2)$ scatterers. This is methodology applied in section 4.1.2. Figure A.3 depicts the set up and the break down.

First, it is necessary to provide a proof of the formula for the end position of the

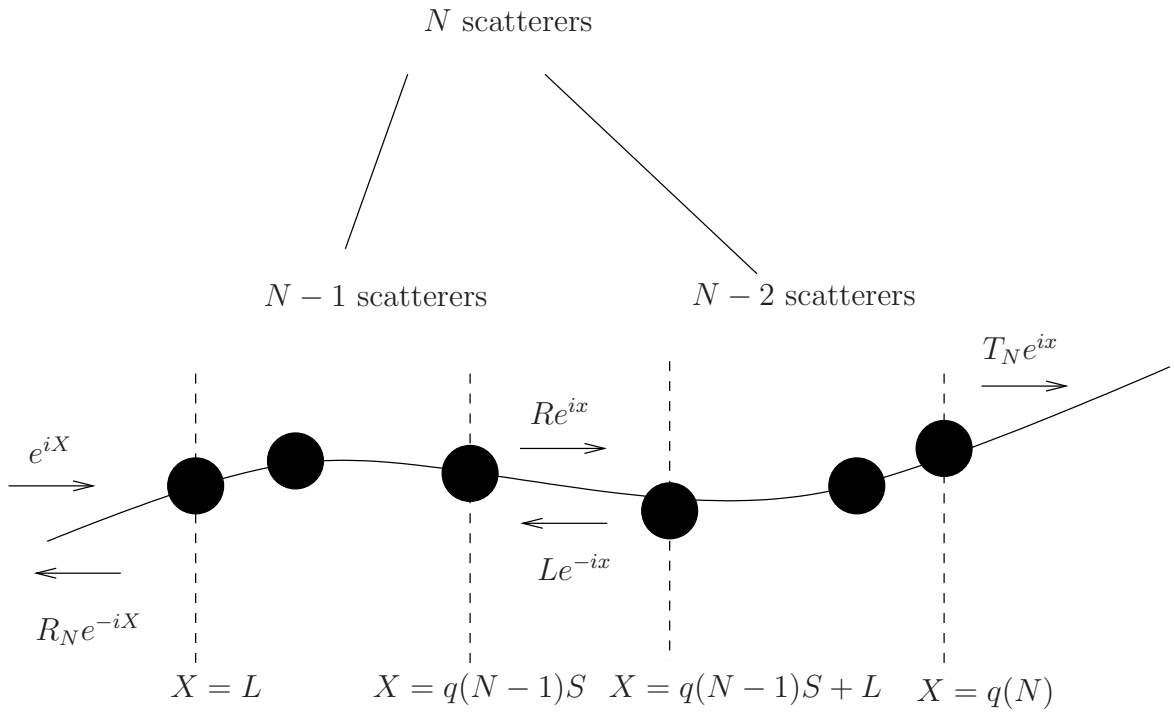

Figure A.3: Breakdown of the point masses for the Fibonacci chain problem.

Fibonacci Chain Problem, $N \geq 3$:

$$q(N)S = (\text{Fib}(N-1)\tau + \text{Fib}(N-2))S. \tag{A.8}$$

Inductively, begin with the base case, $N = 3$. It is known for $N = 3$ the chain is given by the two spacings LS, giving $q(3) = L + S$. Check this with the formula (A.8):

$$q(3)S = (\text{Fib}(2)\tau + \text{Fib}(1))S \tag{A.9}$$

$$= (1\tau + 1)S \tag{A.10}$$

$$= L + S \tag{A.11}$$

as required.

The inductive step is to assume true for $N = n-1$, $N = n-2$. Now consider $N = n$. The chain for n is given by adding the $n-2$ problem to the end of the $n-1$ problem, so

$$q(n) = q(n-1) + q(n-2) \tag{A.12}$$

$$= (\text{Fib}(n-2)\tau + \text{Fib}(n-3))S + (\text{Fib}(n-3)\tau + \text{Fib}(n-4))S \tag{A.13}$$

$$= ([\text{Fib}(n-2) + \text{Fib}(n-3)]\tau + [\text{Fib}(n-3) + \text{Fib}(n-4)])S \tag{A.14}$$

$$= (\text{Fib}(n-1)\tau + \text{Fib}(n-2)S, \tag{A.15}$$

completing the proof for the formulation of the end point.

It is now possible to complete a proof by induction for the transmission and reflection coefficients given in equations (4.35) and (4.37).

The base case is for $N = 3$ again, so plugging $N = 3$ into these equations gives

$$\begin{aligned} T_3 &= \frac{T_1 T_2}{1 - R_1 R_2^o}, \\ rR_3 &= R_2 + \frac{R_1 T_3 T_2^o e^{2iL}}{T_1}, \end{aligned} \tag{A.16}$$

which is the solution gained when working through the problem step by step in section 4.3.

The inductive step is to assume true for $N = n-2$ and $N = n-1$. Then, following previous techniques applied in section 4.1.2, see figure A.3, we get that

$$R_n = R_{n-1} + LT_{n-1}^o, \tag{A.17}$$

$$R = T_{n-1} + LR_{n-1}^o e^{-2iq(n-1)S}, \tag{A.18}$$

$$T_n = RT_{n-2}, \tag{A.19}$$

$$L = RR_{n-2} e^{2iq(n-1)S}, \tag{A.20}$$

which, on rearranging gives the R_n and T_n expected.

Appendix B

Proofs in two dimensions

B.1 Simplification of Graf's addition theorem for small scatterers

In section 2.4 the scattered field from two cylinders is determined using the multipole method. Evaluating the sound-soft boundary conditions on one cylinder at $r_1 = a$ gives equation (2.127). The method requires one to rewrite the $H_0^{(1)}(kr_2)$ component in terms of a different local coordinate system rather than the global one in relation to the origin. An alternative and more complete method to rewrite this expression than that used in section 2.4 is by using Graf's addition theorem (GAT) [4]. This transforms the current coordinate system to a local one and is used when there is not a small radii assumption. Using GAT gives

$$H_0^{(1)}(kr_2) = \sum_{n=-\infty}^{\infty} H_n^{(1)}(kb) J_n(k(r_1) e^{in(\pi-\theta_2-\beta)}, \tag{B.1}$$

refer to figure 2.21 for the notation.

It was shown in (2.114) that for $ka \to 0$, the only order of Bessel function which gives a significant value is order zero since

$$J_0(ka) \to 1, \tag{B.2}$$

$$J_n(ka) \to 0, \quad n \neq 0. \tag{B.3}$$

Thus it is no longer necessary to take the sum over all value of n, only the order $n = 0$ needs to be considered, i.e. equation B.1 becomes

$$H_0^{(1)}(kr_2) \approx H_0^{(1)}(kb) J_0(ka) \to H_0^{(1)}(kb). \tag{B.4}$$

The same approximation can be applied when considering greater numbers of cylinders. When evaluating the boundary conditions on the ith cylinder, it can be analogously shown that

$$H_0^{(1)}(kr_j) \to H_0^{(1)}(kb_{ij}), \quad \text{for } kr_i = ka \to 0. \tag{B.5}$$

B.2 Position of poles for the integral form of the Schlömilch series

In section 5.1.1 it is necessary to determine the positions of the poles of the integral forms of the Schlömilch series $S_0^{\pm}$ to ensure they do not lie on the contour, or in the path of any contour deformation. For $S_0^{\pm}$ (5.14) and (5.18), the poles are given by

$$\sinh t = \frac{i}{kd}(n\pi \mp kd\cos\alpha) + \frac{\epsilon}{kd} = Ai + \epsilon, \tag{B.6}$$

for

$$A = \frac{n\pi}{kd} \mp \cos\alpha \tag{B.7}$$

and just renaming the convergence parameter $\epsilon = \frac{\epsilon}{kd}$. Write $\sinh t$ in terms of exponentials to find

$$\frac{e^t - e^{-t}}{2} = Ai + \epsilon \tag{B.8}$$

$$\Rightarrow e^{2t} - 2(Ai+\epsilon)e^t - 1 = 0 \tag{B.9}$$

$$\Rightarrow e^t = Ai + \epsilon \pm \sqrt{(Ai+\epsilon)^2 + 1}. \tag{B.10}$$

This expression can be expanded and simplified using the assumption that $\epsilon \ll 1$,

$$e^t = Ai + \epsilon \pm \sqrt{1 - A^2 + 2A\epsilon i} \tag{B.11}$$

$$= Ai + \epsilon \pm \sqrt{1-A^2}\sqrt{1 + \frac{2A\epsilon i}{1-A^2}} \tag{B.12}$$

$$\approx Ai + \epsilon \pm \sqrt{1-A^2}\left(1 + \frac{A\epsilon i}{1-A^2}\right) \tag{B.13}$$

$$\approx Ai \pm \sqrt{1-A^2} + \epsilon\left(1 \pm \frac{Ai}{\sqrt{1-A^2}}\right). \tag{B.14}$$

Taking logs gives

$$t \approx \ln\left[Ai \pm \sqrt{1-A^2} + \epsilon\left(1 \pm \frac{Ai}{\sqrt{1-A^2}}\right)\right] + 2m\pi i \tag{B.15}$$

$$= \ln\left[(Ai \pm \sqrt{1-A^2})\left(1 + \frac{\epsilon}{Ai \pm \sqrt{1-A^2}}\left(1 \pm \frac{Ai}{\sqrt{1-A^2}}\right)\right)\right] + 2m\pi i \tag{B.16}$$

$$= \ln\left[Ai \pm \sqrt{1-A^2}\right] + \ln\left[1 + \frac{\epsilon}{\sqrt{1-A^2}}\frac{\sqrt{1-A^2} \pm Ai}{Ai \pm \sqrt{1-A^2}}\right] + 2m\pi i \tag{B.17}$$

$$= \ln\left[Ai \pm \sqrt{1-A^2}\right] + \ln\left[1 \pm \frac{\epsilon}{\sqrt{1-A^2}}\right] + 2m\pi i \tag{B.18}$$

$$\approx \ln\left[Ai \pm \sqrt{1-A^2}\right] \pm \frac{\epsilon}{\sqrt{1-A^2}} + 2m\pi i. \tag{B.19}$$

Now to understand the location of the poles from these equations, consider the different cases,

1. $|A| < 1$ and taking the top of the $\pm$, i.e. taking the 'plus',
2. $|A| < 1$ and taking the 'minus',
3. $|A| > 1$ and taking the 'plus',
4. $|A| > 1$ and taking the 'minus'.

Begin with **case 1**. For small $|A|$ the square root term can be expanded,

$$\sqrt{1-A^2} \approx 1 - \frac{A^2}{2}. \tag{B.20}$$

And thus the log term can be expanded too,

$$\ln\left[Ai + \sqrt{1-A^2}\right] \approx \ln\left[Ai + 1 - \frac{A^2}{2}\right] \tag{B.21}$$

$$\approx \left(Ai - \frac{A^2}{2}\right) - \frac{1}{2}\left(Ai - \frac{A^2}{2}\right)^2 \tag{B.22}$$

$$\approx Ai. \tag{B.23}$$

Therefore, for **case 1** the pole positions are given by

$$t \approx (A + 2m\pi)i + \epsilon. \tag{B.24}$$

Which means, for small ϵ the poles deviate from the imaginary axis slightly to the right, around even numbers of πi.

Case 2 is very similar, the pole positions are given by

$$t \approx \ln\left[Ai - 1 + \frac{A^2}{2}\right] \tag{B.25}$$

$$= (2m+1)\pi i + \ln\left[Ai + 1 - \frac{A^2}{2}\right] \tag{B.26}$$

$$\approx (2m+1)\pi i - Ai. \tag{B.27}$$

The pole positions for **case 2** relate to a finite number of poles just to the left of the imaginary axis, around odd numbers of πi. Care must be taken not to cross these poles when deforming the contour. However, because of the region that the contour lies in, only the case when $m = 0$ must be considered and, depending on the parameters chosen for k, d and α there will be a finite number of poles to worry about which satisfy $|A| < 1$.

For **case 3**, $|A| > 1$ and thus $1 - A^2 < 0$. Let

$$\sqrt{1-A^2} = \sqrt{-(A^2-1)} = i\sqrt{A^2-1}. \tag{B.28}$$

For $|A|$ very large

$$\sqrt{1-A^2} \to iA, \tag{B.29}$$

and thus

$$\ln\left[Ai + \sqrt{1-A^2}\right] \to \ln[2Ai] = \ln[2A] + i\pi/2. \tag{B.30}$$

So, for **case 3**, the poles are positioned at

$$t \approx \ln[2A] + i\left(\frac{\pi}{2} - \frac{\epsilon}{A} + 2m\pi\right). \tag{B.31}$$

Care must be taken here with the sign of A, so the two cases

(a) $A > 1$,

(b) $A < -1$,

must be considered separately. **Case 3 (a)** is straight forward, the log can be evaluated, and the poles are positioned just below the line from $i\pi/2 + 2m\pi i$ to $i\pi/2 + 2m\pi i + \infty$. **Case 3 (b)** needs a little more work. Let

$$A = -\bar{A}, \quad \bar{A} > 1, \tag{B.32}$$

then

$$\ln[2A] = \ln\left[-2\bar{A}\right] = i\pi + \ln\left[2\bar{A}\right]. \tag{B.33}$$

So the poles for **case 3 (b)** are given by

$$t \approx \ln\left[2\bar{A}\right] + i\left(\frac{3\pi}{2} + \frac{\epsilon}{\bar{A}} + 2m\pi\right), \tag{B.34}$$

and so are situated just above the line from $3i\pi/2 + 2m\pi i$ to $3i\pi/2 + 2m\pi i + \infty$.

Case 4 requires a bit more thought to begin with than **case 3**; higher order expansions of the expression in the log should be taken to avoid the singularity at $\ln 0$,

$$\sqrt{1-A^2} = \sqrt{A^2\left(\frac{1}{A^2} - 1\right)} \qquad = A\sqrt{\frac{1}{A^2} - 1} \tag{B.35}$$

$$= Ai\sqrt{1 - \frac{1}{A^2}} \qquad \approx Ai\left(1 - \frac{1}{2A^2}\right) \tag{B.36}$$

$$= Ai - \frac{i}{2A}. \tag{B.37}$$

This results in

$$\ln\left[Ai - \sqrt{1-A^2}\right] \approx \ln\left[\frac{i}{2A}\right] \tag{B.38}$$

$$= \frac{i\pi}{2} - \ln[2A]. \tag{B.39}$$

Therefore the poles are positioned at

$$t \approx -\ln[2A] + \left(\frac{\pi}{2} + \frac{\epsilon}{A} + 2m\pi\right)i \tag{B.40}$$

for **case 4 (a)**, and

$$t \approx -\ln\left[2\bar{A}\right] + \left(-\frac{\pi}{2} - \frac{\epsilon}{\bar{A}} + 2m\pi\right)i \tag{B.41}$$

for **case 4 (b)**, which are just below the lines from $i\pi/2 + 2m\pi i - \infty$ to $i\pi/2 + 2m\pi i$ and $-i\pi/2 + 2m\pi i - \infty$ to $-i\pi/2 + 2m\pi i$ respectively.

B.3 Scattering angles for infinite rows of cylinders with constant periodic separation

In section 5.1.1 it was shown that the transmission of an incident plane wave through an infinite periodic row of cylinders could be defined by a set of propagating plane waves at a finite number of angles ψ_m. For an angle of incidence α, the ψ_m satisfy

$$|\cos\psi_m| = \left|\cos\alpha + \frac{m\pi}{kd}\right| < 1, \quad m \in \mathbb{Z}. \tag{B.42}$$

Say, for a certain α, k and d the integers m which satisfy equation (B.42) and determine the scattering angles ψ_m, are denoted $m_1, ..., m_M$. Consider what happens when one of these plane waves is incident on the next array, i.e. there is an incident plane wave at an angle ψ_{m_i}, $1 \leq i \leq M$. Then the scattering angles from this are

$$|\cos\phi_n| = |\cos\psi_{m_i} + \frac{n\pi}{kd}| \tag{B.43}$$

$$= |\cos\alpha + \frac{(m_i + n)\pi}{kd}| < 1. \tag{B.44}$$

This is comparable to equation (B.42), and thus we know that $m_i + n \in \{m_1, ..., m_M\}$, and so the scattering angles, ϕ_n are just the same set as the ψ_m. The same result would be reached for all $1 \leq i \leq M$ in ψ_{m_i}.

Therefore when each row has the same periodic spacing between the cylinders, the transmitted propagating plane waves propagate at the same set of scattering angles between each row.

B.4 Five-dimensional hypercubic lattice basis vectors for the projection of the Penrose tiling

In order to employ the projection method to construct the Penrose tiling, a quasiperiodic lattice with 5-fold symmetry, an appropriate 5D lattice must be defined. First, it is necessary to define isometries and representative matrices. Senechal [66] discusses such concepts, and mentions that Engel was the first to prove such higher dimensional representatives in 1986.

Firstly, an *isometry* ϕ of the space $\mathbb{E}^n$ can be defined as any transformation that preserves the distances between points in the space. The isometry can be used to define any transformations in space, i.e. the rotational symmetry of a lattice. Isometries can be easily visualised and written down in two or even three dimensions but until Engel's descriptions it was much harder in higher dimensions. For the 5D space required to project to the Penrose tiling, any linear isometry can be represented by a 5×5 reducible

matrix of the form

$$\mathcal{A} = \begin{pmatrix} A_1 & & & \\ & A_2 & & \\ & & \ddots & \\ & & & A_m \end{pmatrix}, \tag{B.45}$$

where each A_j is either 1, -1 or a 2×2 rotation matrix of the form

$$\begin{pmatrix} \cos\theta & -\sin\theta \\ \sin\theta & \cos\theta \end{pmatrix}, \tag{B.46}$$

and all other entries are zero.

For the 5-fold symmetry required for the Penrose lattice it is necessary to have two A_j's that are of the form (B.46) with $\theta = 2\pi/5$ and $4\pi/5$, and the third simply being 1. The components give a 5×5 matrix,

$$\Gamma_5(5) = \begin{pmatrix} \cos 2\pi/5 & -\sin 2\pi/5 & 0 & 0 & 0 \\ \sin 2\pi/5 & \cos 2\pi/5 & 0 & 0 & 0 \\ 0 & 0 & \cos 4\pi/5 & -\sin 4\pi/5 & 0 \\ 0 & 0 & \sin 4\pi/5 & \cos 4\pi/5 & 0 \\ 0 & 0 & 0 & 0 & 1 \end{pmatrix} = \left(\begin{array}{c|c} \Gamma_5^{||} & 0 \\ \hline 0 & \Gamma_5^{\perp} \end{array}\right). \tag{B.47}$$

These three A_j matrices are irreducible and represent three subspaces of $\mathbb{E}^5$: two 2D planes with rotations of angle $2\pi i/5$ and $4\pi i/5$, $1 \leq i \leq 5$; and a 1D representative space along the 5-fold axis. $\Gamma_5^{||}$ represents the 2D space with the rotation $2\pi i/5$, and $\Gamma_5^{\perp}$ represents the other 2D space with the rotation $4\pi i/5$ and the 1D space.

The angles $2\pi/5$ and $4\pi/5$ are determined from the fifth roots of unity,

$$1, \xi, \xi^2, \xi^4, \xi^4, \quad \xi^j = e^{j2\pi i/5}, \tag{B.48}$$

see [66] and [74].

Senechal shows that from this it it is possible to deduce a reciprocal and a direct basis for a 5D hypercubic lattice with the required 5-fold symmetry built in,

$$\mathbf{d}_i^* = \sqrt{\frac{2}{5}} \begin{pmatrix} \cos 2\pi i/5 \\ \sin 2\pi i/5 \\ \cos 4\pi i/5 \\ \sin 4\pi i/5 \\ 1/\sqrt{2} \end{pmatrix}, \quad 1 \leq i \leq 5, \tag{B.49}$$

$$\mathbf{d}_i = \sqrt{\frac{2}{5}} \begin{pmatrix} \cos 2\pi i/5 \\ \sin 2\pi i/5 \\ \cos 4\pi i/5 \\ \sin 4\pi i/5 \\ 1/\sqrt{2} \end{pmatrix}, \quad 1 \leq i \leq 5. \tag{B.50}$$

Here the definition for the relationship between reciprocal and direct basis vectors

$$\mathbf{d}_i^* \cdot \mathbf{d}_j = \delta_{ij}, \tag{B.51}$$

is applied, and the fact that an orthogonal bases is required.

B.5 Four-dimensional hyperrhombic lattice basis vectors for the projection of the Penrose tiling

The 4D lattice for the projection of the Penrose tiling can be formed in a similar way to the 5D lattice in section B.4, using the higher dimension description of an isometry (B.45). In this instance, only the two 2D spaces with rotations related to $2\pi/5$ are required,

$$\Gamma_4(5) = \begin{pmatrix} \cos 2\pi/5 & -\sin 2\pi/5 & 0 & 0 \\ \sin 2\pi/5 & \cos 2\pi/5 & 0 & 0 \\ 0 & 0 & \cos 4\pi/5 & -\sin 4\pi/5 \\ 0 & 0 & \sin 4\pi/5 & \cos 4\pi/5 \end{pmatrix} = \left(\begin{array}{c|c} \Gamma_4^{||} & 0 \\ \hline 0 & \Gamma_4^{\perp} \end{array}\right). \tag{B.52}$$

$\Gamma_4^{||}$ represents the 2D space with the rotation $2\pi i/5$, and $\Gamma_4^{\perp}$ represents the 2D space with the rotation $4\pi i/5$.

The reciprocal and direct basis vectors can therefore be given by

$$\mathbf{f}_i^* = \begin{pmatrix} \cos 2\pi i/5 \\ \sin 2\pi i/5 \\ \cos 4\pi i/5 \\ \sin 4\pi i/5 \end{pmatrix}, \quad 1 \leq i \leq 4, \tag{B.53}$$

and

$$\mathbf{f}_i = \frac{2}{5}\begin{pmatrix} \cos 2\pi i/5 - 1 \\ \sin 2\pi i/5 \\ \cos 4\pi i/5 - 1 \\ \sin 4\pi i/5 \end{pmatrix}, \quad 1 \leq i \leq 4. \tag{B.54}$$

Appendix C

One-dimensional wave scattering

The recursive method for finding the reflection and transmission coefficients for distributions of point scatterers on an infinite string, as described in section 4, can easily be extended to other distributions. In this appendix some examples of other applications are given.

C.1 Periodically distributed point scatterers

Consider an infinite string with density ρ, tension F and a finite number of point scatterers with a periodic distribution. Recursive formulae for the transmission and reflection coefficients for Fib(N) point scatterers with periodic distribution can be derived in a similar manner to that of section 4.3. This enables a rapid computation of the coefficients as the number of scatterers with each recursion is increased by Fib(N), of exponential growth. Denote the Nth scenario by D_N. For D_1 and D_2, let the string have one point scatterer on. The D_N problem will have Fib(N) point scatterers and can be composed of the D_{N-1} and $D_N - 2$ problems. It is possible to find R_N and T_N in terms of R_{N-1} and T_{N-1} very quickly.

In section 2.3.1 it was shown that for one point scatterer the reflection and transmission coefficients are given by

$$R_1 = R_2 = \frac{M\epsilon i}{2 - M\epsilon i}, \tag{C.1}$$

$$T_1 = T_2 = \frac{2}{2 - M\epsilon i}, \tag{C.2}$$

where $\epsilon = kp$, the non-dimensional spacing. Then using the same technique as in

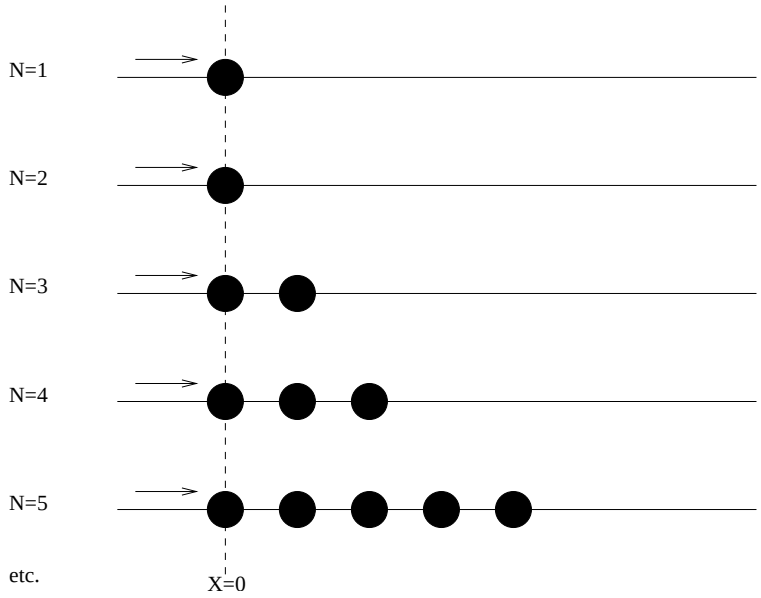

Figure C.1: Fibonacci sequence of the point scatterers as N increases.

section 4.1.1, letting the scatterers be at $X = 0$ and $X = \epsilon$,

$$T_3 = \frac{T_2 T_1}{1 - R_2 R_1 e^{2i\epsilon}}, \tag{C.3}$$

$$R_3 = \frac{R_2 + (T_2^2 e^{2i\epsilon} - R_2^2) R_1 e^{2i\epsilon}}{1 - R_2 R_1 e^{2i\epsilon}}. \tag{C.4}$$

For D_4 there are three scatterers at $X = 0, X = \epsilon$ and $X = 2\epsilon$, which, on decomposing into D_3 followed by the D_2 case on the right, and considering the phase changes, gives

$$T_4 = \frac{T_3 T_2}{1 - R_3 R_2 e^{2i\epsilon}}, \tag{C.5}$$

$$R_4 = \frac{R_3 + (T_3^2 e^{4i\epsilon} - R_3^2) R_2 e^{2i\epsilon}}{1 - R_3 R_2 e^{2i\epsilon}}. \tag{C.6}$$

Continuing like this the pattern emerges for $N > 2$, $N \in \mathbb{Z}$,

$$T_N = \frac{T_{N-1} T_{N-2}}{1 - R_{N-1} R_{N-2} e^{2i\epsilon}}, \tag{C.7}$$

$$R_N = \frac{R_{N-1} + (T_{N-1}^2 e^{2i\epsilon} - R_3^2 e^{2i\epsilon Fib(N)}) R_2}{1 - R_{N-1} R_{N-2} e^{2i\epsilon}}, \tag{C.8}$$

$$= \frac{R_{N-1}(1 - R_{N-2} R_{N-1} e^{2i\epsilon}) + R_{N-2} T_{N-1}^2 e^{2i\epsilon Fib(N)}}{1 - R_{N-1} R_{N-2} e^{2i\epsilon}}, \tag{C.9}$$

$$= R_{N-2} + \frac{R_{N-2} T_{N-1} T_N e^{2i\epsilon Fib(N)}}{T_{N-2}}, \tag{C.10}$$

which can be proved by induction.

C.2 Randomly distributed point scatterers

Consider an infinite string with a finite number of point scatterers with random separations. The computation of the reflection and transmission coefficients for N randomly distributed scatterers takes longer than for a deterministic distribution of scatterers as only one scatterer can be added per recursion, however, it can still work fast.

Determine the spacing S_n between two point scatterers by selecting at random a variable with Uniform distribution in some range. As more scatterers are introduced, scale all the spacings so that the entire distribution of scatterers always lies within a certain length A. Once the position of all the point scatterers are determined, e.g. in figure C.2, then calculate R_N and T_N recursively using the general formulae given in section 4.1.2. Figure C.3 shows the transmission coefficients for different random distributions as the number of scatterers is increased. This shows what a variation in transmission one can get due to the randomness. Such results are as expected due to the physical differences in the distributions, shown in figure C.2. As the number of scatterers is increased, the transmission coefficients converge, due to set length of the distribution; as more scatterers are introduced the wave will be less likely to be able to 'see' the spacing variations. For smaller numbers of scatterers, when there is a great variation in the transmission coefficients, it would be difficult to find a periodic distribution, or an average transmission coefficient which would represent all the different distributions. It is possible to determine the effective wavenumber for realisations of random distributions using the formula (4.29). Figure C.4 shows an example of this.

C.3 Periodically distributed point scatterers with varying mass

The Fibonacci chain can be introduced to a distribution of point scatterers on an infinite string through the mass of the scatterers. Consider a finite number of point scatterers distributed periodically with spacing ϵ. Let the masses of the scatterers vary according to the Fibonacci chain, with large and small masses M_L and M_S. Taking the Fibonacci chain as described in chapter 3, for the initial scenario D_1, consider a

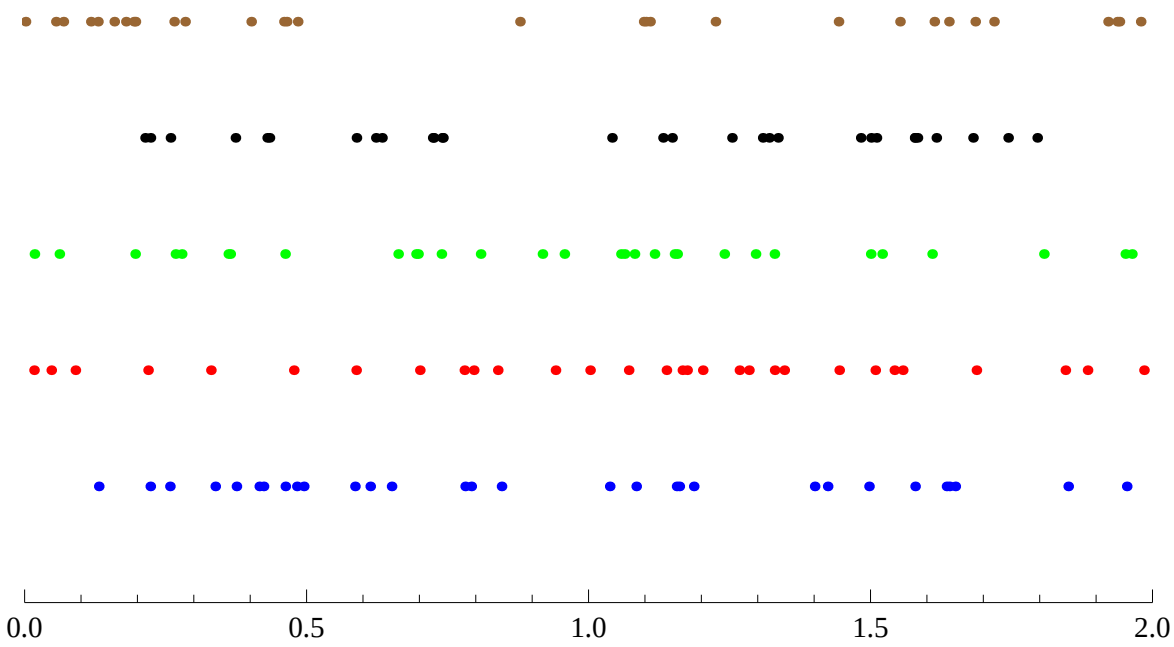

Figure C.2: 5 different distributions of 30 point scatterers on a string section of length 2.

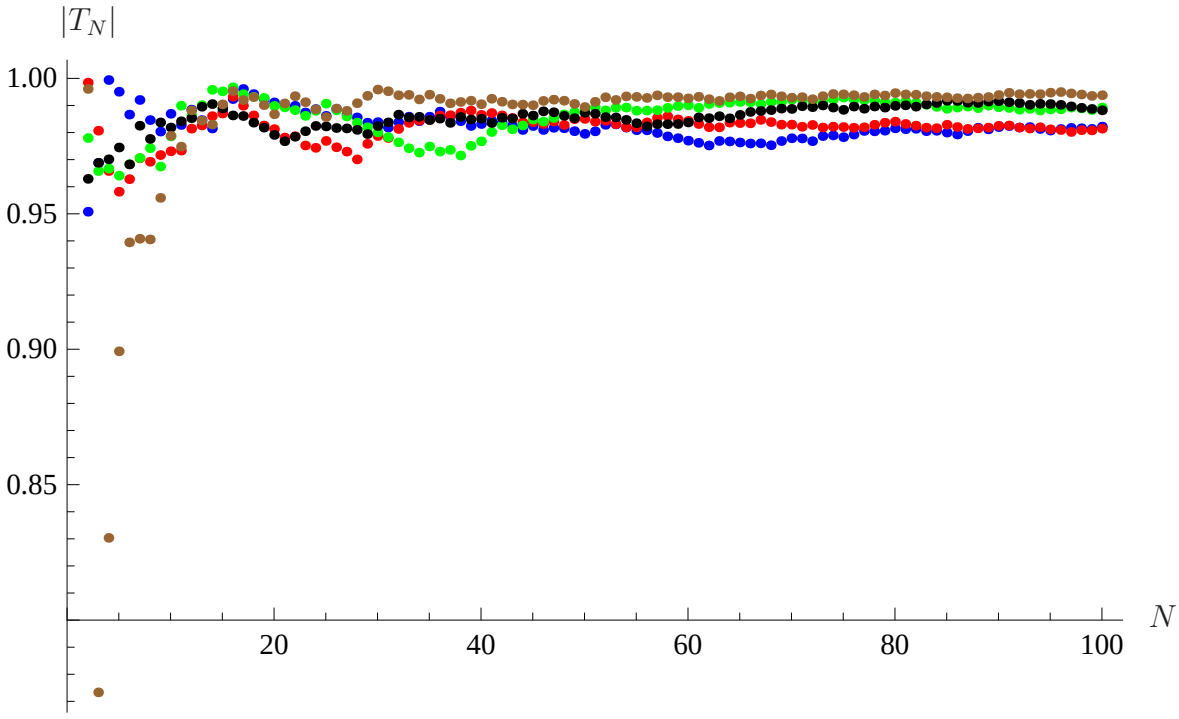

Figure C.3: Transmission coefficients for different random distributions, for $M = 0.7$, $S \in \mathcal{U}[0, 2]$, $A = 2$.

scatterer of mass M_S at $X = 0$, for D_2 consider a scatterer of mass $M_L = \tau M_S$ at $X = 0$, for D_3 scatterers of mass M_L at $X = 0$ and M_S at $X = \epsilon$, etc.

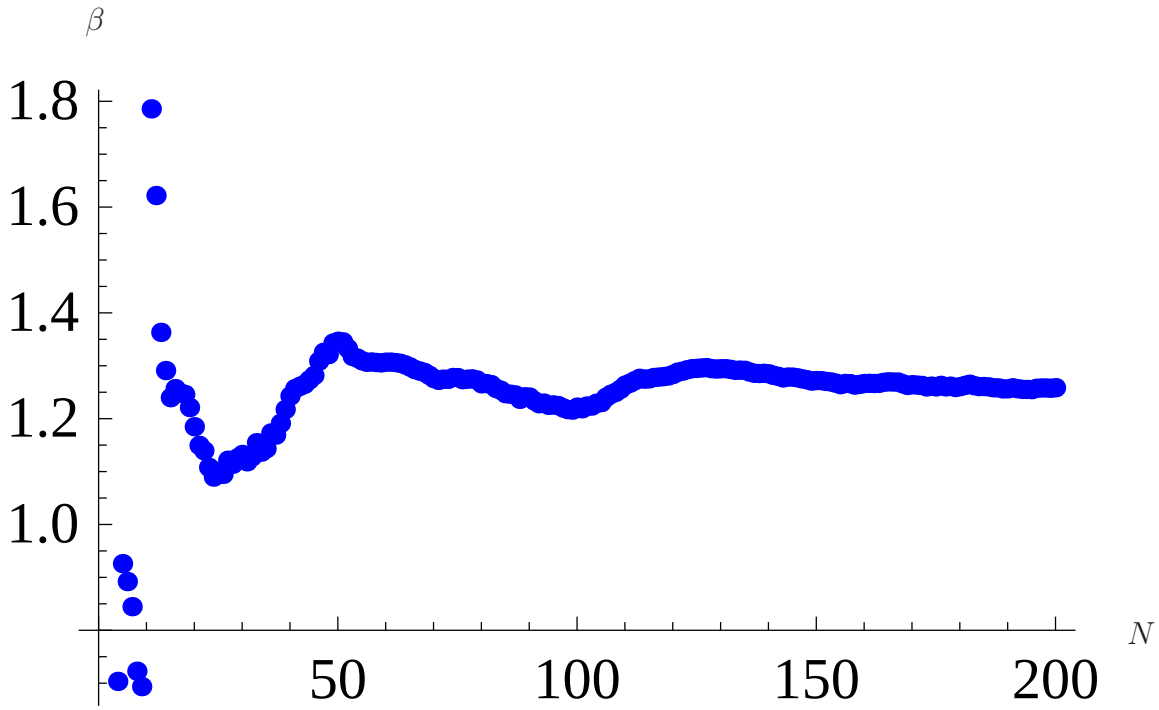

Figure C.4: Effective wavenumber against N, for $M = 0.7$, $S \in \mathcal{U}[0, 2]$, $A = 2$.

Working through analogously to previous problems, it is found that

$$
\begin{aligned}
T_1 = T_1^o &= \tfrac{2}{2-M_S\epsilon i}, \\
R_1 = R_1^o &= \tfrac{M_S\epsilon i}{2-M_S\epsilon i}, \\
T_2 = T_2^o &= \tfrac{2}{2-M_L\epsilon i}, \\
R_2 = R_2^o &= \tfrac{M_L\epsilon i}{2-M_L\epsilon i}, \qquad \text{(C.11)} \\
T_N &= \tfrac{T_{N-2}T_{N-1}}{1-R_{N-2}R_{N-1}^o e^{2i\epsilon}}, \\
R_N = R_{N-1} &+ \tfrac{R_{N-2}T_{N-1}^o T_N e^{2i\epsilon Fib(N-1)}}{T_{N-2}}, \qquad \text{(C.12)} \\
T_N^o &= \tfrac{T_{N-2}^o T_{N-1}^o}{1-R_{N-2}R_{N-1}^o e^{2i\epsilon}}, \\
R_N^o = R_{N-2}^o &+ \tfrac{R_{N-1}^o T_{N-2}T_N^o e^{2i\epsilon Fib(N-2)}}{T_{N-1}^o}. \qquad \text{(C.13)}
\end{aligned}
$$

Figure C.5 shows an example of the transmission coefficients for two scenarios: one of constant mass, thus each scatterer is identical; and one of varying mass, where the relationship $M_L = \tau M_S$ has been applied.

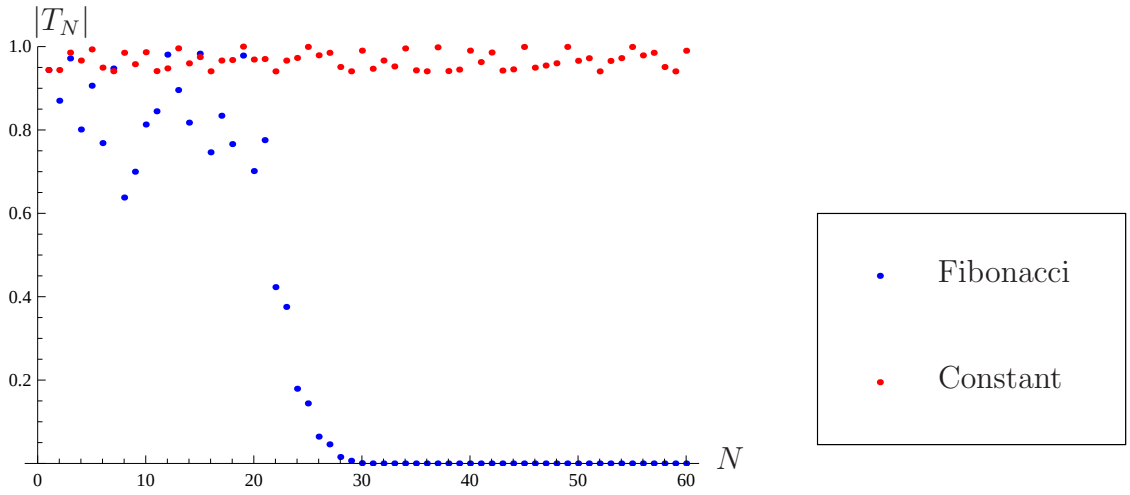

Figure C.5: Transmission for Fib(N) periodic point scatterers with constant mass (red) and for varying mass (blue) using the Fibonacci chain with $\tau = \frac{1+\sqrt{5}}{2}$, the golden ratio.

Figure C.6: Infinite string with sections of different density and separation determined by the Fibonacci chain.

C.4 Fibonacci(N) density changes

Consider an infinite host string of density ρ_1, with sections of length A of density ρ_2. Let these different density sections be separated with a spacing determined by the Fibonacci chain. This problem can be solved using the same recursive method applied in other 1D problems in this thesis. The reflection and transmission coefficients gained for $N \geq 4$ are

$$T_1 = \frac{4\beta e^{iA(\beta-1)}}{(1+\beta)^2-(1-\beta)^2 e^{2iA\beta}}, \tag{C.14}$$

$$R_1 = e^{2iS}\frac{(1-\beta^2)(1-e^{2iA\beta})}{(1+\beta)^2-(1-\beta)^2 e^{2iA\beta}}, \tag{C.15}$$

$$T_2 = \frac{4\beta e^{iA(\beta-1)}}{(1+\beta)^2-(1-\beta)^2 e^{2iA\beta}}, \tag{C.16}$$

$$R_2 = e^{2iL}\frac{(1-\beta^2)(1-e^{2iA\beta})}{(1+\beta)^2-(1-\beta)^2 e^{2iA\beta}}, \tag{C.17}$$

$$T_3 = \frac{T_1 T_2}{1-R_1 R_2^o e^{2iS}}, \tag{C.18}$$

$$R_3 = R_2 + \frac{R_1 T_2^o T_3 e^{2i(L+A+S)}}{T_{N-2}}, \tag{C.19}$$

$$T_N = \frac{T_{N-2}T_{N-1}}{1-R_{N-2}R_{N-1}^o e^{2iL}}, \tag{C.20}$$

$$R_N = R_{N-1} + \frac{R_{N-2}T_{N-1}^o T_N e^{2i(r(N-1)+L)}}{T_{N-2}}, \tag{C.21}$$

where $r(N) = Fib(N-1)L + Fib(N-2)S + Fib(N)A$ and $\beta = k_2/k_1$, the ratio of the wavenumbers in the inclusion and host strings.

For an incident wave from the right, the reflection and transmission coefficients are given by

$$T_1^o = \frac{4\beta e^{iA(\beta-1)}}{(1+\beta)^2-(1-\beta)^2 e^{2iA\beta}}, \tag{C.22}$$

$$R_1^o = \frac{(1-\beta^2)(1-e^{2iA\beta})}{(1+\beta)^2-(1-\beta)^2 e^{2iA\beta}}, \tag{C.23}$$

$$T_2^o = \frac{4\beta e^{iA(\beta-1)}}{(1+\beta)^2-(1-\beta)^2 e^{2iA\beta}}, \tag{C.24}$$

$$R_2^o = \frac{(1-\beta^2)(1-e^{2iA\beta})}{(1+\beta)^2-(1-\beta)^2 e^{2iA\beta}}, \tag{C.25}$$

$$T_3^o = \frac{T_1^o T_2^o}{1-R_1 R_2^o e^{2iS}}, \tag{C.26}$$

$$R_3^o = R_1^o + \frac{T_1 R_2^o T_3^o e^{2i(A+S)}}{T_{N-2}^o}, \tag{C.27}$$

$$T_N^o = \frac{T_{N-2}^o T_{N-1}^o}{1-R_{N-2} R_{N-1}^o e^{2iL}}, \tag{C.28}$$

$$R_N^o = R_{N-2}^o + \frac{T_{N-2} R_{N-1}^o T_N^o e^{2ir(N-2)}}{T_{N-1}^o}. \tag{C.29}$$